Alma Mater Studiorum - Università di Bologna
Dipartimento di Astronomia
Corso di dottorato di ricerca in Astronomia
Ciclo XXIII (2008-2010)
Esame finale anno 2011

A panchromatic view of the evolution of supermassive black holes

Tesi di Dottorato
di
Elisabeta Lusso

Relatore:
Chiar.mo Prof. Luca Ciotti

Coordinatore:
Chiar.mo Prof. Lauro Moscardini

Co-Relatore:
Dr. Andrea Comastri

Scuola di Dottorato in Scienze Matematiche, Fisiche e Naturali
Settore Scientifico Disciplinare: Area 02 - Scienze Fisiche
FIS/05 Astronomia e Astrofisica

Sail away from the safe harbor.
Catch the trade winds in your sails.
Explore. Dream. Discover.
Mark Twain

Abstract

This PhD Thesis is devoted to the accurate analysis of the physical properties of Active Galactic Nuclei (AGN), and the study of the interplay between AGN and host-galaxy using a twofold approach: observational and theoretical. Since the AGN emission is a broad-band phenomenon (from radio to hard X–ray), a multi-wavelength approach is mandatory to better understand the physics and evolutionary properties of these sources. The analysis is carried out in the context of the XMM–*Newton* wide-field survey in the COSMOS field. The COSMOS field is so far a unique area for deep and wide comprehensive multi-wavelength coverage: radio with the VLA, infrared with *Spitzer*, optical bands with *Hubble*, *Subaru* and X-rays with XMM–*Newton* and *Chandra*. The spectroscopic coverage with VIMOS/VLT and IMACS/Magellan, coupled with the reliable photometric redshifts derived from multiband fitting, allows us to build a large and homogeneous sample of AGN over a wide range of redshifts, luminosities and obscuring column densities.

The systematic study of the SEDs of bright, unobscured X–ray selected AGN provide a first indication about the nature of the central engine powering the AGN. The correlation between the X–ray to optical-UV index, $\alpha_{\rm ox}$, with the optical luminosity is fully confirmed using the largest and complete sample of X–ray selected AGN to date. A very tight relation between $\alpha_{\rm ox}$ and the hard X–ray bolometric correction, $k_{\rm bol}$, is found, suggesting that the AGN bolometric output is well traced by $\alpha_{\rm ox}$ over a broad range of redshifts and luminosities. Moreover, it could be used as a practical tool to estimate reliable bolometric corrections, providing the rest-frame 2500 Å and 2 keV luminosities. A fairly significant correlation is found, between both $\alpha_{\rm ox}$ and $k_{\rm bol}$ with the Eddington ratio, indicating that AGN with high mass accretion rate onto the SMBH are characterized by a steeper $\alpha_{\rm ox}$ and a high $k_{\rm bol}$.

On the one hand, for obscured AGN the host-galaxy light is the dominant component in the optical/near-infrared SED, making difficult recover the intrinsic emission. On the other hand, it is possible to obtain robust constraints on colors, stellar masses and star-formation rates of the host galaxies. A multicomponent SED-fitting code is developed to disentangle the emission associated to the galaxy stellar population from that due to mass accretion, and to estimate both host-galaxy parameters (such as stellar mass and star formation rate), and nuclear intrinsic bolometric luminosities and accretion rates. On average, bolometric corrections for obscured AGN tend to be considerably lower than those for unobscured AGN. Host-galaxies morphologies and stellar masses indicate that obscured AGN are preferentially harbored in bulge-dominated galaxies with $M_* \gtrsim 10^{10} M_\odot$. Furthermore, $\sim 50\%$ of AGN hosts are likely to be passive galaxies, the remaining objects have colors consistent with the presence of young stellar populations.

Finally, a physical motivated model for the evolution of spheroidal galaxies with a central SMBH is developed. The model is able to reproduce two important phases of galaxy evolution, namely an obscured-cold-phase followed by a quiescent hot phase. An extended exploration of the parameters space is performed and, interestingly, only models with relatively low initial black hole masses ($M_{\rm BH} \lesssim 10^6 M_\odot$) and high radiative accretion efficiencies ($\epsilon \sim 0.01 - 0.1$) are found to reproduce the observed Magorrian relation.

Acknowledgements

I was wondering about the language to use for these acknowledgements, however the people that I would like to thank are only italians. Therefore, I prefer switch on italian from now on.

Sarà banale, ma la prima persona che vorrei ringraziare è il Capo. Posso dire, sembra ombra di dubbio, che un guida come la tua sarà estremamente difficile ritrovarla nel proseguo della mia carriera. Hai investito così tanto in me. Tra scuole di dottorato e conferenze ho non solo girato il mondo, ma imparato molto. Devo solo a te se sono stata tre mesi alle Hawaii, è stata una esperienza meravigliosa e decisamente istruttiva.
Grazie. Spero di non averti deluso.

Come potrei non ringraziare anche te, Luca, per la pazienza che hai avuto sia durante la tesi di laurea che il dottorato, quando, nei ritagli di tempo, si lavorava al codice che non ne voleva sapere di dare risultati sensati. Sembrava che quell'articolo non dovesse mai vedere la luce, ma alla fine ci siamo riusciti.

Gianni, un ringraziamento particolare anche per te, che ti sei letto tutta la Tesi in meno di due giorni, credo sia un record. Per tutte le volte che con un semplice righello ed una matita riuscivi a trovare errori in un grafico.

Le caramelle ed i cioccolatini sono stati una costante in questo periodo, grazie Cristian.

Alla mia famiglia, che mi è stata sempre vicino, che si è sempre prodigata per me, che ha sempre creduto in me. Laura non so come avrei fatto se non ci fossi stata tu, avere una sorella come te é una fortuna che poche persone hanno, io sono stata fortunata...

Ci sono molte persone che vorrei ringraziare, ma dovró semplicemente elencarne (e non in ordine d'importanza) i nomi. Mi scuso anticipatamente se mi sono dimenticata qualcuno.
Micol, Francesca, Marcella, Roberto e Preethi.

Da tutti voi ho imparato molto, ed ancora molto ho da imparare...
Grazie.

Contents

Chapter 1

Introduction

This Chapter aims at providing a very brief introduction to the physics of Active Galactic Nuclei (AGN), which is the topic of this Thesis*. The AGN definition and the origin of the continuum emission are presented, and also the connection between AGN and host galaxy in the context of AGN/galaxy co-evolution is briefly addressed. The motivations of the project and the outline of the Thesis are discussed at the end of this Chapter.

1.1 Active Galactic Nuclei

In general, we consider "active galactic nuclei", or AGN, galaxies with energetic phenomena in their nuclei, or central regions, which cannot be directly attributed to stellar phenomena. They constitute a heterogeneous class of objects and represent a few percent of the whole galaxy population. A galaxy can be defined as an AGN if some of these characteristic features are present (not necessarily all of them at the same time):

- a compact nuclear region, more luminous with respect to the corresponding region in a normal, inactive Hubble-type galaxy;
- nuclear continuum emission, both thermal and/or non-thermal radiation over a wide portion of the electromagnetic spectrum;
- nuclear emission lines observed mainly at the near-infrared and optical-UV wavelengths, indicating excitation by the continuum emission;
- variable continuum and/or variable emission lines. Variability is present especially in the X–rays.

Historically, AGN are classified on the basis of their optical spectra, and they can be broadly divided into two main groups: broad-line emission galaxies and narrow-line emission galaxies.

*The interested reader may refer to Peterson (1997); Mo et al. (2010); Carroll & Ostlie (1996) for a more detailed discussion.

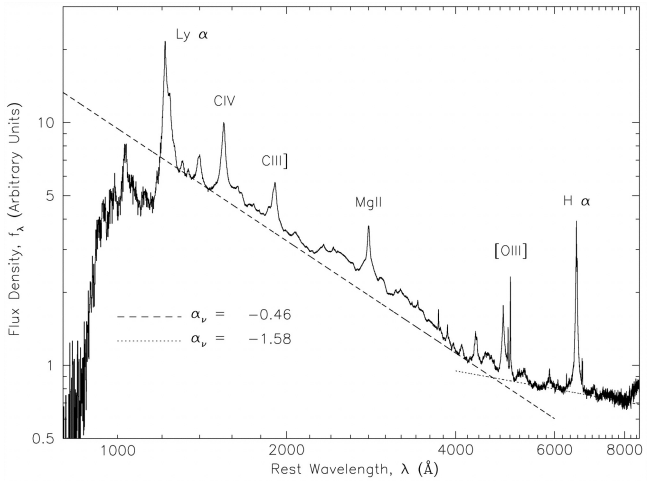

Figure 1.1: Composite quasar spectrum for Type-1 AGN taken from the SDSS. Power-law fits to the estimated continuum flux are shown with the dashed and dotted lines (from Vanden Berk et al. 2001).

Broad-line emission galaxies (or Type-1 AGN) are characterized by broad (FWHM of 2000 – 10000 km s^{-1}) permitted lines (e.g., Lyα, C IV, Mg II, Balmer hydrogen lines) and narrow (typically with FWHM of $\sim$ 500 km s^{-1}) forbidden lines[†] (e.g., [Ne IV], [Ne V], [O II], [O III]). An example of a typical spectrum of a Type-1 AGN is shown in Fig. 1.1, where the continuum is well-fitted with a broken power-law and the most important emission lines arising from the continuum radiation are marked.
Narrow-line emission galaxies (or Type-2 AGN) are characterized by relatively narrow, both permitted and forbidden, emission lines. The continuum in the Type-2 AGN spectrum is nearly flat, reddened and extinguished by the dust within the galaxy. An example of a typical spectrum for a Type-2 AGN is shown in Fig. 1.2, in which the host-galaxy contribution has been properly removed in order to reveal weak emission lines.
These AGN classes can be further divided in radio-quiet or radio-loud depending on the radio properties: approximately 10% of the AGN population is radio-loud. These two classes will be discussed in some more detail in Sect. 1.2.

1.1.1 The central engine

AGN produce very high bolometric luminosities, of the order of 10^{46} – 10^{48} erg s^{-1}, four order of magnitudes higher than the luminosity of a typical galaxy, in a concentrated volume (of the order of the size of the solar system up to the Oort cloud, $\sim$ pc size). The fundamental question is how the AGN energy detected as radiation is produced. Nowadays it is widely accepted that the central engine of an AGN is an accreting supermassive black hole (SMBH) at the center of the galaxy. Accretion is the principal source of energy in high-energy astrophysics and is responsible for most of the observed emission. The basic idea is that during accretion a decrease of potential energy (the absolute value) of a fluid element has to be compensated with an increase of kinetic energy (energy conservation). If part of the kinetic energy becomes internal energy (which means an increase of the gas temperature), there are a lot of processes that can dissipate this internal

[†]Forbidden lines involve low-probability transitions in atoms and indicate the presence of low gas density regions.

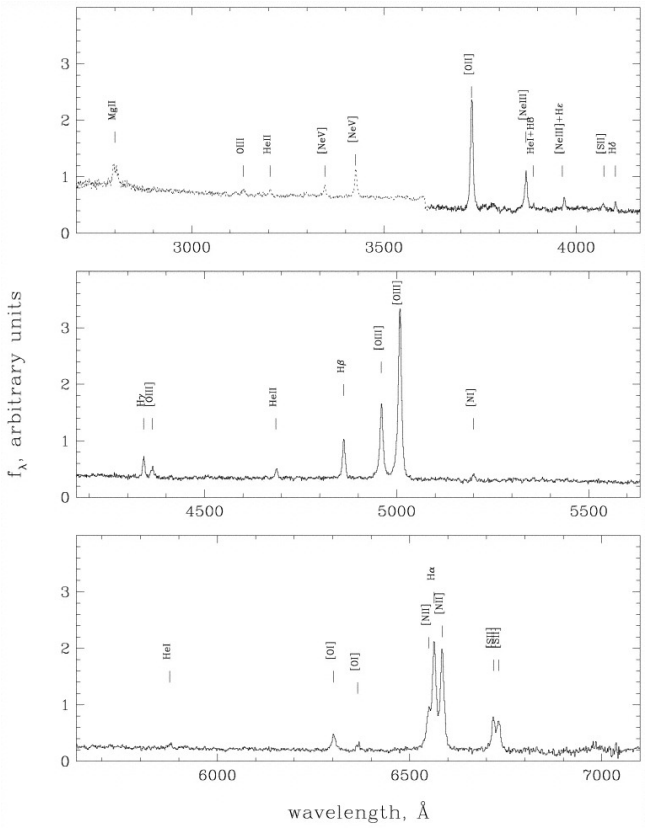

Figure 1.2: Expanded view of the composite quasar spectrum for Type-2 AGN taken from the SDSS, where the host-galaxy contribution is subtracted (from Zakamska et al. 2003).

energy and emit radiation (such as bremsstrahlung, synchrotron, Compton processes, etc). In a simple model the luminosity of the central object can be estimated assuming a stationary, spherically symmetric fully-ionized accreting material mainly composed by hydrogen. The effects of the radiation pressure due to Thomson electron scattering become important on the accreting gas. In this scenario the accreting flow has an upper limit, the well-known *Eddington accretion rate* $\dot{M}_{\rm Edd}$. The inward (only the radial component is considered) gravitational force on an element of fluid m is

$$F_{\rm g} = n_{\rm e}\mu m_{\rm p}\frac{GM}{r^2}, \tag{1.1}$$

where $n_{\rm e}$ is the electron density, μ is the mean molecular weight and $m_{\rm p}$ is the proton mass; and it must be balanced by the outward force due to the radiation pressure

$$F_{\rm rad} = n_{\rm e}\sigma_{\rm T}\frac{L}{4\pi r^2 c} \tag{1.2}$$

where $\sigma_{\rm T}$ is the Thomson scattering cross-section ($\sigma_{\rm T} = 6.65 \times 10^{-25}$ cm^2), c is the light speed ($c \simeq 3 \times 10^{10}$ cm s^{-1}) and M is the central mass that generates the luminosity L. Therefore, the force balance is obtained when

$$\mu m_{\rm p}\frac{GM}{r^2} = \sigma_{\rm T}\frac{L}{4\pi r^2 c}. \tag{1.3}$$

The maximum luminosity allowed is called *Eddington luminosity*

$$L_{\rm Edd} = \frac{4\pi c G M \mu m_{\rm p}}{\sigma_{\rm T}} \simeq 1.3 \times 10^{46} \frac{M}{10^8 M_\odot} \ [\rm erg\ s^{-1}] \tag{1.4}$$

and this is an upper limit for a stationary source (if $L \gg L_{\rm Edd}$, the radiation pressure stops accretion). The minimum mass of the central object that emits at the Eddington limit is

$$M = 8 \times 10^5 \frac{L_{\rm Edd}}{10^{44} \rm erg\ sec^{-1}} M_\odot. \tag{1.5}$$

For sources with luminosities of $10^{46} - 10^{48}$ erg s^{-1}, a central mass of the order of $10^8 - 10^{10}\ M_\odot$ is required. Another important question concerns the efficiency in the conversion of the accreted mass into energy in AGN. One of the key parameters of the accretion is the radiative accretion efficiency ϵ (i.e., the fraction of mass that is converted into radiation). The rate at which energy is emitted from a mass M is

$$L = \epsilon \dot{M} c^2 \tag{1.6}$$

where $\dot{M}$ is the mass accretion rate. The value of the efficiency is very uncertain, and depends on the details of how accretion actually occurs. In general, an average value often used in the literature is $\epsilon = 0.1$. The luminosity produced by the central mass M, under the assumption that it is powered by the gravitational potential $\Phi = -GM/r$, can be written as

$$L = \frac{GM\dot{M}}{r}. \tag{1.7}$$

As the Schwarzschild radius of a black hole of mass M is

$$R_{\rm S} = \frac{2GM}{c^2} \simeq 3 \times 10^{13} \frac{M}{10^8 M_\odot} \ [\rm cm], \tag{1.8}$$

by combining Eqs. (1.6) and (1.7), the radiative efficiency is

$$\epsilon = \frac{R_{\rm S}}{2r}. \tag{1.9}$$

The bulk of the accretion disk emission is expected to be originated within $r \sim 5\ R_{\rm S}$, therefore it follows that $\epsilon \sim 0.1$. In Section 5.3 we will address the problem of accretion considering a modified version of the accretion process presented by Bondi (1952), taking into account also the radiation pressure effects.

1.1.2 The continuum emission

The continuum spectrum of AGN spans a wide range of wavelengths: from radio to hard X-ray. The AGN Spectral Energy Distribution (SED), as a first-order approximation, can be described as a power-law over a wide range of wavelengths

$$F_\nu \propto \nu^{-\alpha} \tag{1.10}$$

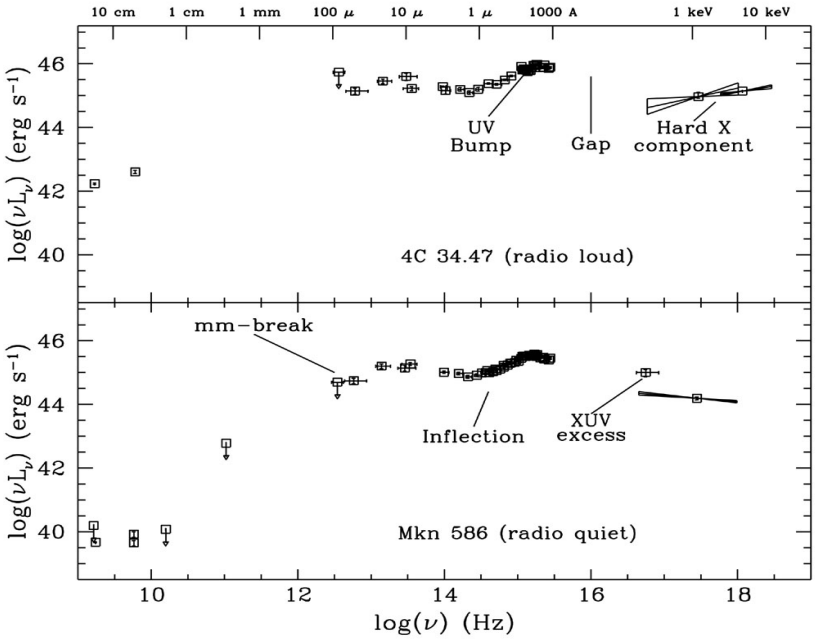

Figure 1.3: SED from radio to X-ray of radio-loud (upper) and radio-quiet (lower) quasar (from Elvis et al. 1994).

where α is fairly flat, $0 < \alpha < 1$. We consider in this analysis also the quantity νF_ν representing the total energy emitted per unit time in a band $\Delta\nu \sim \nu$. The SED of an AGN is now known to be more complicated, but the parametrization given in Eq. (1.10) is a useful approximation widely used in the literature. Fig. 1.3 shows the average broad-band SED for luminous radio-quiet and radio-loud AGN as compiled in Elvis et al. (1994, hereafter E94). They are referred to as the typical quasar SED and thought to be representative of the *intrinsic* properties of AGN. These SEDs are based on a sample of predominantly "UV-blue excess" selected quasars from the Bright Quasar Survey sample. The E94 sample is limited by the low number of sources (29 radio-quiet and 18 radio-loud quasars), the large number of upper limits in the far-infrared, ultraviolet and X-ray, and the selection criteria biased toward very luminous X-ray sources. Average SEDs of X-ray selected AGN show significant differences, and we will address this issue in Sect. 3.3 for X–ray selected Type-1 AGN. Nevertheless, in the following the main features in the average E94 SED will be discussed in order to facilitate the comparison between our findings and those on optically selected samples.

The SEDs in Fig 1.3 present two significant gaps in the extreme ultraviolet and in the millimiter-region where data are not available. The far-ultraviolet gap is due to absorption by neutral hydrogen at the wevelengths between 912 Å and ~ 100 Å by our own Galaxy, the so called *Lyman continuum edge*. The interstellar medium in our Galaxy makes impossible any detection at these wavelengths. The gap at frequencies smaller than 10^{12} Hz ($\lambda > 300\mu$m) is mostly due to the lack of sensitive detectors in this range at the epoch of publication of the E94 paper.

The shape of the SED in the optical-UV shows a bump called "big-blue bump" with a peak around the Lyman edge. This bump is attributed to thermal black-body emission at temperature

of $10^4 - 10^5$ K and is usually ascribed to the emission from the accretion disk surrounding the SMBH. Another feature in this region of the SED is the "small-blue bump" around 2200 Å, which is associated to a forest of emission lines from Fe II and the Balmer recombination continuum. At 1μm there is a local minimum in the SED, which is thought to represent the transition region between the thermal spectrum at $T \gtrsim 2000$ K and the cool thermal emission ($T < 2000$ K) in the infrared due to presence of dust grains that, at $T \sim 2000$ K, are completely sublimated.
The bump at wavelengths longer than 1μm is called "infrared-bump" with a peak at $\sim 10\mu$m. This bump is associated to the presence of dust grains in the AGN environment and is well represented with a grey body radiation at temperature $T \sim 2000 - 1500$ K or cooler.
The radio part of the SED is not believed to be thermal. The radio emission is about 3 orders of magnitude lower than the optical-UV region of the SED in radio-loud AGN, while it is 5 orders of magnitude lower than the radio region in the SED of radio-quiet AGN. The emission is associated to synchrotron radiation from particles accelerated in shocks with a spectral index of ~ 0.7. The region that is emitting at the radio wavelengths is often associated to the presence of powerful jets and compact cores in radio-loud AGN. Albeit the importance of the radio emission is crucial for understanding AGN physics, the description of the SED at the radio wavelengths needs a separate discussion, and is beyond the purposes of this Thesis.
The X–ray region of the SED contributes for $\sim 10\%$ to the bolometric luminosity of an AGN, and can be divided in "soft X-rays" ($\sim 0.1 - 2$ keV) and "hard X-rays" (from 2 keV to a few hundreds keV[‡]). Moreover, the rapid X–ray variability, with timescales of the order of a day, gives hints of the innermost region of the AGN. In X-ray astronomy the SEDs are usually fitted considering photons per keV rather than energy per unit of frequency

$$P \propto E^{-\Gamma} \propto \nu^{-\Gamma} \qquad [\text{photons s}^{-1}\text{keV}^{-1}], \tag{1.11}$$

while in units of energy flux we have

$$F_\nu \propto P \times h\nu \,[\text{erg/photon}] \propto \nu^{-\Gamma+1} \propto \nu^{-\alpha}, \tag{1.12}$$

where α is called "energy index" and $\Gamma = \alpha + 1$ is called "photon index". X–ray observations revealed that, on average, the soft part of the spectrum is well fitted with $\alpha \gtrsim 1$, while in the hard region a flatter slope $\alpha \sim 0.7 - 0.9$ is required. The fit of the X–ray spectrum of Seyfert galaxies suggests also a high-energy cut-off around few hundreds keV. However, given the large scatter in AGN X–ray spectra, both in the energy index and high energy cut-off, these values have to be considered as average values. The origin of the X–ray spectra is probably related to inverse-Compton scattering of low-energy photons by high-energy electrons. Photons emitted from the accretion disk (in the optical-UV) are scattered (inverse-Compton) by hot-electrons (probably also relativistic electrons are involved) in a corona surrounding the accretion disk (the process is called "Comptonization"). The very soft part of the spectrum can, instead, be associated to the high energy part of the thermal distribution of photons emitted in the accretion disk.
The relative amount of X–ray and optical emission is parameterized by the ratio of the optical-UV and X–ray flux (or luminosity). The distribution of X-ray to optical–UV ratio in quasars, as a

[‡]The very high-energy region above hundreds keV (γ-rays) is not treated in this Thesis.

function of optical and X-ray luminosity and redshift, has been the subject of active investigations for more than 30 years (Tananbaum et al. 1979). The ratio is parameterized by the optical to X-ray spectral index ($\alpha_{\rm ox}$) defined as:

$$\alpha_{\rm ox} = -{\rm Log}\left[\frac{L_{2\ {\rm keV}}/L_{2500\ \text{Å}}}{\nu_{2{\rm keV}}/\nu_{2500\ \text{Å}}}\right] = -\frac{{\rm Log}\ [L_{2\ {\rm keV}}/L_{2500\ \text{Å}}]}{2.605}, \tag{1.13}$$

where $L_{2500\ \text{Å}}$ and $L_{2\ {\rm keV}}$ are the rest-frame monochromatic luminosities at 2500 Å and 2keV, respectively. The AGN $\alpha_{\rm ox}$ distributions typically cover the range 1.2–1.8, with a mean value of about 1.5.

1.2 The unified model for AGN

Unified models for AGN have been proposed by several authors (e.g., Antonucci 1993; Urry & Padovani 1995) in order to explain the difference between Type-1 and Type-2 AGN. In Sect. 1.1 we have divided Type-1 and Type-2 AGN on the basis of the optical features in their spectra. The linewidths are related to different velocities of gas clouds, and also to different emission regions. Broad emission lines are thought to be originated in regions nearby the central engine ($\sim$ 1 pc from the center), so that the gas emitting clouds are more influenced by the gravitational field of the central source, the gas density is higher ($\sim 10^9 - 10^{10}$ cm^{-3}) with gas temperature of the order of $\sim 10^4$ K. The radius of the broad emitting gas cloud can be estimated using the *reverberation technique*. If the time delay between the continuum emission and the line variation is measured, this time delay can be used to estimate the size of the emitting region (i.e., $t = r/c$). The measured time-delays are typically of the order of several light days, confirming that these clouds are near the central source. Narrow lines are produced in regions far from the central region (from $\sim$ 10 pc up to few hundreds pc from the center), where the gas is not only more rarefied ($\sim 10^4 - 10^6$ cm^{-3}), with gas temperature of the order of $\sim 1.6 \times 10^4$ K (Koski 1978), but also less gravitationally influenced by the central source. In Figure 1.4 a simplified description of the phenomenological model for the AGN is shown, while in Figure 1.5 a summary of the different kinds of photon emission originated from different locations are highlighted. Briefly, the basic idea is that the central engine, an accreting SMBH, is surrounded by a dense optically thick obscuring gas and dust with a toroidal geometry. An observer looking at the AGN through the torus (edge-on perspective) has the view of the accretion disk (optical-UV and soft X–ray continuum) and of the broad-line regions obstructed by the intercepting material. Only the narrow-emission lines, ionized from the continuum emission, are visible. On the other hand, at any other viewing angles the observer has a direct view on both broad-line and narrow-line regions, as well as the accretion disk emission. The Seyfert dichotomy could be explained in this way. Seyfert galaxies (Carl Seyfert 1943) are low-luminous AGN ($L_{\rm bol} \lesssim 10^{44}$ erg s^{-1}) and are characterized by the presence of strong high-ionization emission lines and almost all of them are morphologically classified as a spiral galaxies. At the beginning, Seyfert galaxies were classified 1 or 2 on the basis of the presence or absence of broad emission lines in their spectra. The spectrum of Seyfert 1 galaxies is characterized by permitted broad emission lines, mostly from hydrogen, and narrow forbidden

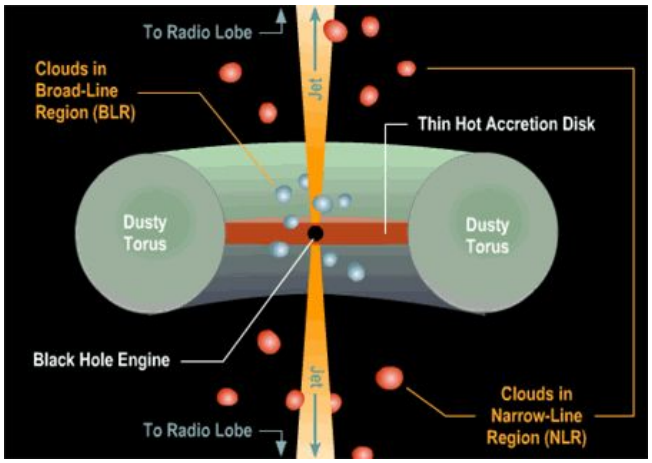

Figure 1.4: Phenomenological model for AGN (image credit: Brooks/Cole Thomson Learning).

lines. The only difference between the spectrum of Seyfert 2 galaxies and Seyfert 1 galaxies is that only narrow lines are present (both permitted and forbidden) in the Seyfert 2 class. The continuum and the X–ray emission is much stronger in Seyfert 1 galaxies than in Seyfert 2. One possible explanation for the difference between these two classes is that Seyfert 2 galaxies are intrinsically Seyfert 1 sources, but the broad line region is hidden by the presence of intercepting material along the line of sight. Narrow lines are thought to be ionized by the strong continuum arising from the central region, which is collimated in ionization cones. Indeed, there are many observational evidence for ionization cones observed, for example, in Seyfert 2 galaxies (e.g., Tadhunter & Tsvetanov 1989; Wilson et al. 1993). Therefore, Seyfert 1 and 2 can be associated to the same sources, but seen at different viewing angles. Accordingly, in the proposed unified scheme obscuration is strongly orientation- and geometry-dependent. The amount of obscuring gas is parameterized by the column density, $N_{\rm H}$, which represents the number of hydrogen atoms per unit area along the line of sight. The observed absorbed flux, F_o, can be written as

$$F_o(\lambda) = F_i(\lambda)e^{-\tau}, \tag{1.14}$$

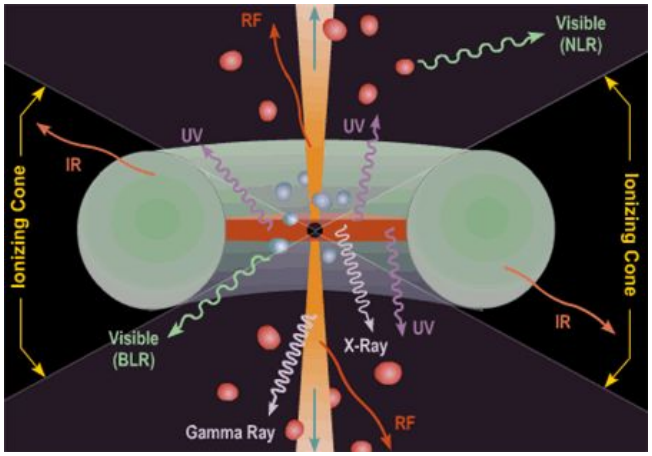

Figure 1.5: The AGN emission depends on the orientation, and the energy of the emitted photons is determined by the source location (image credit: Brooks/Cole Thomson Learning).

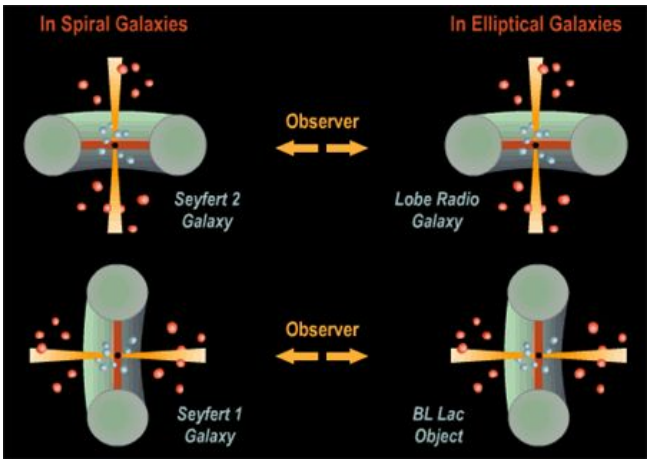

Figure 1.6: Schematic description of the "Unified model for AGN". AGN have a common structure and appear different depending on the observer viewing angle (image credit: Brooks/Cole Thomson Learning).

where F_i is the unabsorbed flux and τ is the optical depth

$$\tau = \int \sigma_{\rm T} \cos\theta \, n(r) {\rm d}r = N_{\rm H} \sigma_{\rm T}, \tag{1.15}$$

defined as the integral along the optical path of the number density $n(r)$, while θ is the angle to the normal. If $\tau = 1$, the intrinsic flux is diminished by a factor $1/e$, while for $\tau > 1$ the source is optically-thick and thus $N_{\rm H} > 1/\sigma_{\rm T}$ ($\sim 10^{24}$ cm^{-2}). As a consequence, the source is opaque to the optical-UV and X–ray photons (i.e., Compton-thick).
Also radio galaxies can be divided in broad-line radio galaxies (BLRGs) and narrow-line radio galaxies (NLRGs) in a similar way as Seyfert galaxies. If the jet is present, BLRGs and NLRGs dichotomy can be also explained considering an orientation dependence (see Fig. 1.6). If a source is seen directly face-on, the relativistic jet is pointing to the observer, therefore the AGN spectrum in completely dominated by the synchrotron emission continuum and no lines (or very weak lines) are visible in the SED (e.g., Blazar, BL Lacs). At intermediate angles, both radio emission and broad-lines are visible (BLRGs), while if the source is seen edge-on a NLRG is detected. In principle, BLRGs and NLRGs can be regarded as radio emitting Seyfert 1 and 2 galaxies, respectively. One important difference is that radio sources appear to occur mainly in ellipticals rather than spiral galaxies.

1.3 Current evolutionary scheme of AGN/galaxy co-evolution

The formation and growth of SMBHs and their host-galaxies are related processes. This is supported by many observational evidences: the SMBH mass correlates with the mass of the bulge of the host-galaxy (Magorrian et al. 1998a; Marconi & Hunt 2003), with the bulge velocity dispersion (Ferrarese & Merritt 2000a; Tremaine et al. 2002a), and also with the bulge luminosity (Kormendy & Richstone 1995). Additionally, almost all spheroids are observed to harbour a SMBH and this strongly indicates that probably all galaxies have experienced an active phase

in their past. Moreover, there is a remarkable evidence for a connection between the AGN and host-galaxy which is given by the similarity between the cosmic evolution of the star formation rate (SFR) density and SMBH accretion rate density. Both processes peak at $z \approx 2$ and decline rapidly at lower (e.g. Dickinson et al. 2003; Merloni et al. 2004) and higher (e.g. Wilkins et al. 2008; Brusa et al. 2009b) redshifts. All of these observational results suggest that feedback between accretion onto SMBH and host-galaxy may play an important role in galaxy formation and evolution. A simple way to quantity whether the energy output from an AGN can have an impact on the environment is to compare the energy amount from the AGN with the binding energy of the host galaxy. The rate at which energy is emitted from a mass M (see Eq. [1.6]) can be expressed as

$$\frac{dE}{dt} = \epsilon c^2 \frac{dM_{\rm BH}}{dt}. \tag{1.16}$$

Integrating over the AGN lifetime it follows that

$$E = \epsilon c^2 M_{\rm BH}, \tag{1.17}$$

which is the total amount of energy released by an AGN along the cosmic time. This energy can be compared with the total binding energy (U) of the galaxy hosting the SMBH, which is related, by the virial theorem, to the galaxy kinetic energy T, $U = -2T$. The kinetic energy can be written as $T = 1/2 M_{\rm g}\sigma^2$, where $M_{\rm g}$ and σ are the galaxy mass and the virial velocity dispersion, respectively. The galaxy binding energy is therefore

$$U \backsimeq -M_{\rm g}\sigma^2. \tag{1.18}$$

Comparing the total energy output of the AGN with the binding energy of the host-galaxy we finally have

$$\frac{E}{|U|} \backsimeq \epsilon \left(\frac{c}{\sigma}\right)^2 \frac{M_{\rm BH}}{M_{\rm g}}. \tag{1.19}$$

From observations $M_{\rm BH}/M_{\rm g}$ is of the order of 10^{-3} and for a massive galaxy $\sigma \simeq 300$ km s^{-1}, so that the ratio $E/|U|$ is roughly $10^3\epsilon$, where ϵ ranges between 0.01 and 0.1 approximately. This indicate that the energy output from the AGN can exceed the total binding energy of the host-galaxy and, consequently, energy feedback should play a key role in the galaxy formation and evolution. However, the value of ϵ depends also on the feedback processes involved. There are, at least, two possible energy mechanisms that may release energy in the surrounding gas:

(1) radiative feedback: optical-UV and X–ray photons emitted by the AGN can ionize and heat the surrounding medium through photoionization. The radiative output could be extremely large in bright AGN ($\epsilon \sim 0.1$) and, therefore, have an important effect in the galaxy such as suppressing star-formation and gas cooling. If dust is present, part of the radiation from the AGN can be absorbed by dust grains and re-emitted in the infrared; this does not produce feedback, however, radiation pressure can transfer momentum into the dust grains (which are coupled with the gas of the galaxy) and, if the radiation pressure is high enough, this can also suppress accretion onto the SMBH and produce gas winds. Hence, part of the gas can be blown out from the galaxy. We will describe the effects of the radiation pressure on

mass accretion and gas surrounding the SMBH in Chapter 5;

(2) mechanical feedback: during episodes of low-accretion onto the SMBH, the AGN is believed to release energy via mechanical processes in collimated jets. Observational evidence comes from radio-loud spheroidal galaxies, mainly found in clusters. Jets can inflate the surrounding gas originating cavities and bubbles that can be observed in the X–rays. The typical energy released by this process is of the order of $\sim 10^{60}$ erg s^{-1}, which is enough to quench star-formation and heat the gas (Böhringer et al. 2002).

It is also possible that energetic particles, such as cosmic rays, are produced, although there is no clear evidence that the energy amount produced by such particles is high enough to contribute significantly to the pressure of the gas enclosing the AGN.
As described above, galaxy evolution involves a variety of complex hydrodynamical processes related to gas heating and cooling, shocks, star-formation, energy feedback from stellar mass loss and from the nuclear activity of the galaxy. Semi-analytical models and hydrodynamical simulations have to deal with these processes, some of which poorly understood. From the theoretical side, a number of models have been proposed to link the formation and evolution of SMBHs to the structure formation over cosmic time (e.g., Kauffmann & Haehnelt 2000; Hopkins et al. 2006). One of the key issues towards understanding the formation of AGN is to identify physical mechanisms to bring gas into the center of the galaxy, fueling the central SMBH. Part of these semi-analytical models and hydrodynamical simulations (e.g., Springel et al. 2005) invoke major mergers of gas-rich galaxies as the mechanism enabling the fueling of the central SMBHs and the building of the galaxy bulges. Alternative fueling mechanisms have been discussed in the literature, including minor-mergers (e.g., Corbin 2000), bars (e.g., Jogee et al. 2004), disk instabilities (e.g., Genzel et al. 2008), recycled gas from dying stars (e.g., Ciotti et al. 2010).
Several works consider also radiative feedback able to reproduce two important phases of galaxy evolution, namely an obscured-cold-phase, when the bulk of star formation and black hole accretion occur, and the following quiescent hot phase in which accretion remains highly sub-Eddington and unobscured (e.g., Sazonov et al. 2005; Lusso & Ciotti 2011). These studies consider AGN activity without involving galaxy mergers (e.g., Ciotti & Ostriker 1997). AGN activity can be triggered simply considering the recycled gas from evolving stellar populations. The total amount of mass gas lost in a Hubble time is about 20% of the total stellar mass (e.g., $M_* \sim 10^{11} M_\odot$), hence a factor of hundreds more than the BH mass observed today in massive galaxies (e.g., $M_{\rm BH} \sim 10^9 M_\odot$). Necessarily, the AGN produce a substantial amount of feedback even without any merger in the whole galaxy lifetime, preventing also the formation of very high BH mass.
At the first order, the galaxy evolution can be broadly divided into three phases. Firstly, an early phase in which the galaxy has strong interactions with other galaxies. Gas-rich mergers are expected to drive nuclear inflows of gas, triggering a, possibly very large, enhancement in the star formation rate in the merging system and fueling the growth of SMBHs. This phase is associated to heavily obscured quasars. Secondly, the galaxy starts to coalesce. In this phase the bulk of star-formation and mass accretion onto the SMBH occurs. AGN became optically visible blowing out the gas from the galaxy. In the final phase there is not left gas available to feed the SMBH and to form stars, so that star-formation and accretion are quenched and the galaxy passively evolves

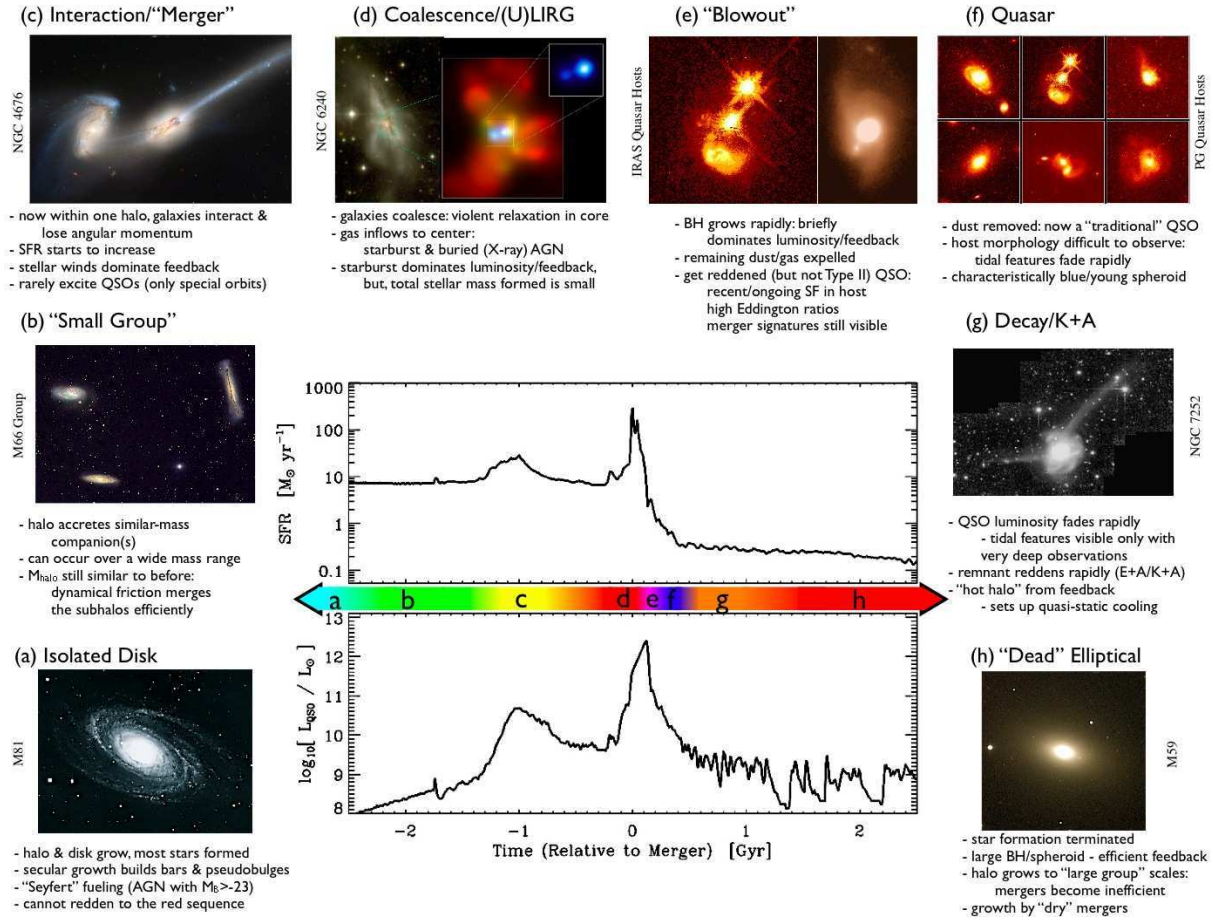

Figure 1.7: Schematic outline of the phases of growth in a "typical" galaxy. Image credit: *(a)* NOAO/AURA/NSF; *(b)* REU program/NOAO/AURA/NSF; *(c)* NASA/STScI/ACS Science Team; *(d)* optical *(left)*: NASA/STScI/R. P. van der Marel & J. Gerssen; X-ray *(right)*: NASA/CXC/MPE/S. Komossa et al.; *(e) left*: J. Bahcall/M. Disney/NASA; *right*: Gemini Observatory/NSF/University of Hawaii Institute for Astronomy; *(f)* J. Bahcall/M. Disney/NASA; *(g)* F. Schweizer (CIW/DTM); *(h)* NOAO/AURA/NSF (from Hopkins et al. 2008).

becoming a red spheroid. In Figure 1.7 a schematic representation of these phases is presented. In the central panel both the QSO luminosity evolution and the SFR evolution are considered with respect to the time at which merger occurred. These physical parameters are linked with different stages of AGN/host galaxy co-evolution. Observational evidence supporting the above scenario comes from the bimodality of the rest-frame color distribution of the host-galaxies (e.g., Strateva et al. 2001; Bell et al. 2004), the so called "red-sequence" and "blue-cloud" in color-magnitude or color-mass diagrams. Galaxies in the blue-cloud present ongoing star-formation and AGN activity. Once the gas is depleted, galaxies then move in the red-sequence becoming red spheroids (e.g., Rovilos & Georgantopoulos 2007). It is, however, well known that not all

galaxies in the red-sequence are passive galaxies. A significant fraction of them, especially at relatively high redshift ($z > 1$), are red because of dust extinction associated to still ongoing star formation (Cimatti et al. 2002; see also Brusa et al. 2009c).

1.4 Aims of the project and Thesis outline

Understanding the properties and the formation of AGN is an important issue in galaxy formation and evolution studies. AGN represent a not negligible fraction (a few %, see Lilly et al. 2007) of magnitude selected samples of galaxies and, additionally, their energy feedback may have critical effects in the intergalactic medium and a crucial role in galaxy formation and evolution. Therefore, any theory of galaxy formation has to take into account the formation of AGN. Furthermore, AGN are powered by an accreting SMBH, as already discussed in Sect. 1.1.1, and the correlation of the SMBH mass with the host-galaxy bulge mass suggests that formation and growth of SMBHs and their host-galaxies are tightly linked. Feedback between accretion onto SMBH and host-galaxy may also play an important role in galaxy formation and evolution. But how does the feedback actually work? Understanding this is a challenging problem for both observers and theorists.

In this vein, the work presented in this Thesis is aimed at a detailed characterization of a large sample of Type-1 and Type-2 AGN over a wide range of frequencies using a twofold approach, both observational and theoretical. The AGN structure is reflected in the shape of the SED; therefore a densely sampled SED over a broad wavelength interval is mandatory to extract useful information from SED-fitting procedures, allowing to tightly constrain physical parameters from multicomponent modeling and, in particular, to properly disentangle the emission associated to stellar light from that due to accretion. An obvious complication in the study of host galaxy properties in Type-1 AGN is that the emission of the central AGN outshines the galaxy light; hence it becomes extremely difficult to derive constraints on the colors, stellar populations, and morphologies of the host. On the other hand, for obscured AGN the host-galaxy light is the dominant component in the optical/near-infrared SED, while it is difficult to recover the intrinsic emission, and the lack of a proper knowledge of the nuclear SED of obscured Type-2 AGN is the major limitation. As a consequence, the relations between stellar masses, SFR, morphologies and accretion luminosity remain poorly known. In particular, in order to address these topics, the analysis has been divided into three parts. Chapter 2 is dedicated to a general presentation of the multi-wavelength data-set. The method adopted to compute the broad-band SEDs, the average SED and the SED-fitting code used to disantangle the nuclear light from the host-galaxy emission are also discussed.

The first part of this Thesis, discussed in Chapter 3, concerns the study of the X-ray to optical properties of a sample of X-ray selected Type-1 AGN, from the XMM-COSMOS survey, over a wide range of redshifts and hard X-ray luminosities. This part of the Thesis is mainly focused on the relationship between UV and X-ray luminosity, as parameterized by the optical to X-ray spectral index, $\alpha_{\rm ox}$, and its dependence on redshift and luminosity. Understanding how $\alpha_{\rm ox}$ evolves with luminosity and redshift may provide a first hint about the nature of the energy generation mechanism in AGN. It is also a first step towards an estimate of the AGN bolometric

luminosity function (Hopkins et al. 2007) and the mass function of SMBHs (e.g. Marconi et al. 2004), and towards the understanding of the structure of the AGN accretion disk and X-ray corona. The broad-band information contained in the COSMOS database is well suited for a detailed study of AGN SEDs, bolometric luminosities and bolometric corrections. The black hole mass is also available for a subsample of sources. Therefore, it is possible to compute the Eddington ratio, $\lambda_{\rm Edd}$ (see Eq. [2.35] in Sect. 2.5.1), and investigate any possible dependence of $\lambda_{\rm Edd}$ on the SED shape.

In Chapter 4 the second part of the Thesis is presented, aimed at a detailed analysis of the SEDs of about 250 hard X-ray selected obscured AGN from the XMM-COSMOS survey, the largest Type-2 sample to date. The SEDs, bolometric luminosities and bolometric corrections for the sample of Type-2 AGN are discussed. A comparison between Type-1 and Type-2 results on bolometric corrections is also presented. The morphology of the host-galaxies, star-formation rates, stellar masses, and colors are analyzed in the context of galaxy formation and evolution.

Chapter 5 addresses the co-evolution of SMBHs and their host galaxies, as a function of the accretion radiative efficiency, dark matter content, and cosmological infall of gas, from the theoretical point of view, using a one-zone evolutionary model. This last part of the Thesis focuses on a scenario where the mass of the central SMBH and that of the host galaxy grow in a dark matter halo replenished by accretion of gas of cosmological origin. The evolution of star formation is followed, as well as the mass return from the evolving stellar populations. The length of the so-called "obscured accretion phase", defined as the period of time when a high column density is associated with a high accretion rate onto the central SMBH, and the corresponding "cold phase" defined by a low mass-weighted gas temperature, is investigated. The relation between the duration of the obscured and cold phase and how they depend on the adopted physical parameters is studied. In the last Chapter the main findings are reviewed, underlining the future perspectives of this work.

Chapter 2

Data handling

One of the main goals of this Thesis is to constrain the AGN and host-galaxy physical parameters and to properly disentangle the emission associated to stellar light from that due to accretion. Since the relative contribution of the different components is dominant at different wavelengths, a proper decomposition can be obtained by an SED-fitting approach, possibly complemented by morphological analysis. This will provide a robust estimate of the nuclear emission (bolometric luminosities and bolometric corrections, absorption column density distributions, etc) and their relation with the host galaxy properties (mass, star formation rates, morphological classification). The AGN structure is reflected in the shape of the SED; therefore a densely sampled SED over a broad wavelength interval is mandatory to extract useful information from SED-fitting procedure. In this Chapter we present the data and describe the methodology used to derive the rest-frame broad-band SED (from the far-infrared to the hard X–ray); to compute the mean and median SED and the SED-fitting code adopted for the multicomponent modeling.

2.1 Multiwavelength data-set

The XMM–*Newton* wide-field survey in the COSMOS field (hereafter XMM-COSMOS; Hasinger et al. 2007) is a ~ 2 deg^2 area of the HST/ACS COSMOS Treasury program (Scoville et al. 2007; Koekemoer et al. 2007), it has been surveyed with XMM–*Newton* for a total of$\sim$ 1.55 Ms during AO3, AO4, and AO6 cycles of XMM observations (Cappelluti et al. 2007, 2009, hereafter C07, C09, respectively). XMM-COSMOS provides an unprecedently large sample of point-like X-ray sources ($\geq$ 1800), detected over a large, contiguous area, with complete ultraviolet to mid-infrared (including Spitzer data) and radio coverage, and extensive spectroscopic follow-up granted through the zCOSMOS (Lilly et al. 2007, 2009) and Magellan/IMACS (Trump et al. 2007, 2009) projects. The excellent multi-band photometry available in this area allows a robust photometric redshift estimate for the faint sources not reachable by optical spectroscopy (Salvato et al. 2009), thus allowing a virtually complete sample of X-ray sources. The XMM-COSMOS project is described in Hasinger et al. (2007), while the X-ray point source catalog and source counts are presented in C09.

The catalog used in this Thesis is an extension of the work on the optical identification of a sample of X–ray sources detected in the first 1.3 deg^2 in the XMM-COSMOS survey (Brusa et al.

2007), over the entire 2 deg^2 in the XMM-COSMOS survey (Brusa et al. 2010, hereafter B10). The association of the correct optical counterpart has been performed using the "likelihood ratio" technique (Sutherland & Saunders 1992; Ciliegi et al. 2003) complemented by an extensive collection of multiwavelength data from 24μm to UV, available from the COSMOS survey, for each of the X-ray sources. The optical positions are then cross-correlated with the I-band, K-band and IRAC catalogs and visually checked. The catalog includes 1848 point-like sources detected in at least one of the soft (0.5 – 2 keV), hard (2 – 10 keV), or ultra-hard (5 – 10 keV) bands down to nominal limiting fluxes of $\sim 5 \times 10^{-16}$, $\sim 3 \times 10^{-15}$, and $\sim 7 \times 10^{-15}$ erg s^{-1}cm^{-2}, respectively (i.e., the flux of the faintest source detected in the band; see C09). The adopted likelihood threshold corresponds to a probability $\sim 4.5 \times 10^{-5}$ that a catalog source is a spurious background fluctuation (see Cappelluti et al. 2007; C09 for more details). In B10 the source list has been created from 53 out of the 55 XMM-COSMOS fields; for the additional 65 sources detected when the pointings obtained in AO6 are included, the identification is not completed yet. For this reason, the number of XMM-COSMOS sources is slightly lower than that discussed in C09. Twenty-six faint sources in this catalog are coincident with diffuse XMM sources (Finoguenov et al. (2007)). These sources are flagged as "possibly extended" in the point-like catalog and are excluded from the following analysis. The inner part of the COSMOS field has been imaged for a total of 1.8 Ms by Chandra (Elvis et al. 2009), with 36 pointings of $\sim$ 50 ks each in a 6×6 array. The mosaic covers an area of ~ 0.92 deg^2 (about half of the XMM-COSMOS field) down to a limiting flux of $\sim 2 \times 10^{-16}$ erg s^{-1}cm^{-2} in the soft band and $\sim 7.3 \times 10^{-16}$ erg s^{-1}cm^{-2} in the hard band, i.e., 3 – 4 times deeper than XMM-COSMOS. Of the 1822 XMM sources, 945 ($\sim$ 52%) have been observed by Chandra with an exposure larger than 30 ks, and 875 of them are present in the C-COSMOS point-like source catalog (Puccetti et al. 2009; Elvis et al. 2009). Of the 70 sources not recovered by Chandra, more than half are in regions with relatively low exposure (between 30 and 50 ks) and are detected at faint XMM fluxes, mostly in the hard band ($\leq 6 \times 10^{-15}$ erg s^{-1}cm^{-2}). The remainder are either sources with only hard XMM detections (14) or, after a visual inspection, they can be associated with spurious sources (15), consistent with the expected fraction in the XMM-COSMOS field (see Elvis et al. 2009). Twenty-five of the 875 XMM-COSMOS sources with Chandra detection (2.8%) are resolved in two different Chandra sources, lying at distances between 2 and 10 arcsec from each other and therefore being likely blurred in the XMM large point-spread function (PSF; see discussion in C09). B10 further discard these 25 sources from the final sample. The XMM-COSMOS sample used in this Thesis consists therefore of 1797 X-ray sources, 850 with Chandra detection (47.3%).

Spectroscopic redshifts for the proposed counterparts are compiled by Brusa et al. (2009b, 2010) from the Magellan/IMACS and MMT observation campaigns ($\sim$ 530 objects, Trump et al. 2009), from the zCOSMOS project ($\sim$ 500 objects, Lilly et al. 2007), or were already present either in the SDSS survey catalog ($\sim$ 100 objects, Adelman-McCarthy & et al. 2005, Kauffmann et al. 2003a*), or in the literature ($\sim$ 95 objects, Prescott et al. 2006). Additional $\sim$ 40 objects have redshifts from ongoing spectroscopic campaigns designed to target high-redshift, faint objects with the DEIMOS instrument at Keck-II telescope (PI: P. Capak, M. Salvato, N. Scoville). In summary, good-quality spectroscopic redshifts are available for 853 sources, corresponding to a

*These sources have been retrieved from the Nasa Extragalactic Database (NED) and from the SDSS archive.

substantial fraction ($\sim$ 47%, 853/1797) of the entire XMM–*Newton* sample.
Photometric redshifts for almost all XMM-COSMOS sources have been obtained exploiting the COSMOS multi-wavelength database and are presented in Salvato et al. (2009, hereafter S09). Since the large majority of the XMM-COSMOS sources are AGN, in addition to the standard photometric redshift treatments for normal galaxies, a new set of SED templates has been adopted, together with a correction for long–term variability and luminosity priors for point-like sources (see below and S09 for further details). The availability of the intermediate band *Subaru* filters (Taniguchi et al. 2007) is crucial in picking up emission lines (see also Wolf et al. 2004). This led, for the first time for an AGN sample, to a photometric redshift accuracy comparable to that achieved for inactive galaxies ($\sigma_{\Delta z/(1+z)} \sim 0.015$ and $\sim$ 5% outliers) down to $i \simeq 22.5$. At fainter magnitudes ($22.5 < i < 24.5$), the dispersion increases to $\sigma_{\Delta z/(1+z)} \simeq 0.023$ with $\sim$ 10% outliers, still remarkably good for an AGN sample. A photometric redshift is available for all but 32 objects out of 1797.
In addition to the photometric redshifts, S09 provide also a photometric classification based on the best-fit broad-band SED template. Briefly, each AGN SED has been fitted with a total of 30 different templates including both normal galaxies (early type, late type and ULIRG galaxies), low-and-high luminosity QSOs (both Type 1 and 2) and hybrids created assuming a varying ratio between the AGN and a galaxy templates (90:10, 80:20,..., 10:90; see S09 for details and Polletta et al. 2007). About 40% of the sources are best-fitted by AGN-dominated SED, while the remaining sources are reproduced by host galaxy-dominated SED. The photometric classification is also confirmed a posteriori (see Fig.10 in S09) with the distribution of the XMM sources in the X-ray hardness ratio plane (Cappelluti et al. 2009; Hasinger et al. 2007).
We divided the extragalactic sources with available optical spectra in the XMM-COSMOS counterpart sample into three classes, on the basis of a combined X-ray and optical classification (see also Szokoly et al. 2004):

(1) **Broad-line AGN** (Type-1 hereafter). All the objects having at least one broad ($FWHM > 2000\,\mathrm{km\ s^{-1}}$) optical emission line in the available spectrum (421 sources out of 1797).

(2) **Non-broad-line AGN** (Type-2 hereafter). All the objects with unresolved, high-ionization emission lines, exhibiting line ratios indicating AGN activity, and, when high-ionization lines are not detected, or the observed spectral range does not allow to construct line diagnostics, objects without broad lines in the optical spectra (330 sources out of 1797).

(3) **"Normal" galaxies**. All the objects with unresolved emission lines consistent with spectra of star-forming galaxies or with a typical galaxy spectrum showing only absorption lines (86 sources out of 1797).

We used all the multi-color information as compiled by Brusa et al. (2009b, 2010)[†]. The catalog includes multi-wavelength data from radio to hard X-rays: VLA-COSMOS Deep project (see Schinnerer et al. 2010; Bondi et al. 2008), MIPS 160 μm, 70 μm and 24 μm GO3 data (Le Floc'h

[†]The multi-wavelength XMM-COSMOS catalog can be retrieved from: http://www.mpe.mpg.de/XMMCosmos/optical_cp/.

et al. 2009), IRAC flux densities (Sanders et al. 2007), near-infrared CFHT/K-band data (McCracken et al. 2008), J UKIRT (Capak et al. 2008), HST/ACS F814W imaging of the COSMOS field (Koekemoer et al. 2007) and optical multiband photometry (SDSS, Subaru, Capak et al. 2007).
The observations are not simultaneous, as they span a time interval of about 5 years: 2001 (SDSS), 2004 (Subaru and CFHT) and 2006 (IRAC). In order to reduce variability effects, expecially for the Type-1 AGN sample presented in Chapter 3, we selected the bands closest in time to the IRAC observations (i.e., we excluded SDSS data). Some variability may be still present in the Type-1 AGN sample.
We adopted a flat model of universe with an Hubble costant $H_0 = 70$ Km s^{-1} Mpc^{-1}, $\Omega_{\rm M} = 0.3$, $\Omega_\Lambda = 1 - \Omega_{\rm M}$ and $\Omega_{\rm k} = 0$ ($\Omega_M + \Omega_\Lambda + \Omega_k = 1$, Komatsu et al. 2008). The data in the SED computation were blueshifted to the rest frame and no K-correction has been applied.

2.1.1 X-rays

Assuming a power law spectrum

$$S(\nu) = A\nu^{-\alpha}, \tag{2.1}$$

the band flux $S(\nu_2 - \nu_1)$ is :

$$S(\nu_2 - \nu_1) = A \int_{\nu_1}^{\nu_2} \nu^{-\alpha} d\nu \tag{2.2}$$

where A is a constant. Integrating the previous formula using $\alpha \neq 1$ we have

$$S(\nu_2 - \nu_1) = \frac{A(\nu_2^{-\alpha+1} - \nu_1^{-\alpha+1})}{(-\alpha + 1)}. \tag{2.3}$$

Deriving A by Eq. (2.3) and putting it into (2.1) we have

$$S(\nu) = \frac{S(\nu_2 - \nu_1)(-\alpha + 1)\nu^{-\alpha}}{(\nu_2^{-\alpha+1} - \nu_1^{-\alpha+1})}. \tag{2.4}$$

Integrating Eq. (2.2) using $\alpha = 1$ we have

$$S(\nu_2 - \nu_1) = A \ln(\nu_2/\nu_1). \tag{2.5}$$

Deriving A and putting it into Eq. (2.1) we have

$$S(\nu) = \frac{S(\nu_2 - \nu_1)\nu^{-1}}{\ln(\nu_2/\nu_1)}. \tag{2.6}$$

We calculate, from the fluxes in the soft 0.5-2 keV and hard 2-10 keV band, monochromatic fluxes in the observed frame using $\alpha = 1$ for the soft band, and $\alpha = 0.7$ in the hard band. The *observed* monochromatic soft flux at 1 keV is

$$S(\nu_{\rm 1keV}) = \frac{S([0.5 - 2]{\rm keV})}{\ln(4)\nu_{\rm 1keV}} \qquad [{\rm erg\ s^{-1}cm^{-2}Hz^{-1}}] \tag{2.7}$$

while, for hard flux at 4 keV we use Eq. (2.4)

$$S(\nu_{4\mathrm{keV}}) = \frac{S([2-10]\mathrm{keV})(1-\alpha)\nu_{4\mathrm{keV}}^{-\alpha}}{(\nu_{10\mathrm{keV}}^{1-\alpha} - \nu_{2\mathrm{keV}}^{1-\alpha})} \qquad [\mathrm{erg\ s^{-1}cm^{-2}Hz^{-1}}] \tag{2.8}$$

The *intrinsic* luminosity for each source, is derived from

$$\nu_{\mathrm{e}} L(\nu_{\mathrm{e}}) = S(\nu_{\mathrm{o}})\nu_{\mathrm{o}} 4\pi \mathrm{d}_{\mathrm{L}}^2 \tag{2.9}$$

$$\nu_{\mathrm{e}} = \nu_{\mathrm{o}}(1+z), \tag{2.10}$$

where ν_{o} and ν_{e} are the frequencies observed and emitted by a source a redshift z, respectively; and $\mathrm{d_L}$ is the luminosity distance. Then, monochromatic fluxes (Eqs. [2.7] and [2.8]) are multiplied for the frequency correspondent to 1 keV and 4 keV for the soft and hard band respectively. Luminosities at 1 keV and 4 keV were calculated using Eq. (2.9) then plotted at the rest-frame 1 keV and 4 keV, respectively in the Log ν – Log (νL_ν) plane.

Intrinsic absorption correction for the X-ray luminosity

Column densities, N_{H}, are estimated from spectral analysis (see Mainieri et al. 2007a for details) and, therefore, the de-absorbed X–ray luminosity at 0.5–2 keV and 2–10 keV can be computed. For the sources without an estimate of the column density, the 2–10 keV luminosity is computed from the correspondent X–ray flux density without the absorption correction. The integrated intrinsic luminosity, L_{int}, is defined as

$$L_{\mathrm{int}} = A \int_{\nu_{\mathrm{min}}}^{\nu_{\mathrm{max}}} E^{-\Gamma+1} e^{-E/E_{\mathrm{cut}}}\, \mathrm{d}E \tag{2.11}$$

where Γ is the X-ray slope fixed to 2 and 1.7 for 0.5-2 keV and 2-10 keV, respectively; and ν_{min} and ν_{max} are the boundaries of the soft and hard X–ray bands. E_{cut} is the energy cut-off fixed to 200 keV and A is the normalization. The observed integrated X-ray luminosity is absorbed by a column density N_{H} and can be written as

$$L_{\mathrm{abs}} = A \int_{\nu_{\mathrm{min}}(1+z)}^{\nu_{\mathrm{max}}(1+z)} E^{-\Gamma+1} e^{-E/E_{\mathrm{cut}}} e^{-N_{\mathrm{H}}\sigma(E)}\, \mathrm{d}E \tag{2.12}$$

where $\sigma(E)$ is the effective photoelectric absorption cross-section per hydrogen atom and its value depends on the energy range (see Table 2 in Morrison & McCammon 1983). The X-ray luminosity L_{abs} is computed from the observed X-ray density flux, so that we can substitute A into the Eq. (2.12) and finally have intrinsic X-ray luminosity

$$L_{\mathrm{int}} = L_{\mathrm{abs}} \frac{\int_{\nu_{\mathrm{min}}}^{\nu_{\mathrm{max}}} E^{-\Gamma+1} e^{-E/E_{\mathrm{cut}}}\, \mathrm{d}E}{\int_{\nu_{\mathrm{min}}(1+z)}^{\nu_{\mathrm{max}}(1+z)} E^{-\Gamma+1} e^{-E/E_{\mathrm{cut}}} e^{-N_{\mathrm{H}}\sigma(E)}\, \mathrm{d}E}. \tag{2.13}$$

Table 2.1: Effective wavelength, width, systematic offset (s_f) in magnitude of the adopted photometric bands.

Filter	Telescope	Effective λ	FWHM	s_f
u^*	CFHT	3911.0	538.0	-0.054
B_J	Subaru	4439.6	806.7	0.242
g_+	Subaru	4728.3	1162.9	-0.024
V_J	Subaru	5448.9	934.8	0.094
r_+	Subaru	6231.8	1348.8	-0.003
i_+	Subaru	7629.1	1489.4	-0.019
i^*	CFHT	7628.9	1460.0	0.007
z_+	Subaru	9021.6	955.3	0.037
J	UKIRT	12444.1	1558.0	-0.124
K	CFHT	21480.2	3250.0	0.051
IRAC1	Spitzer	35262.5	7412.0	-0.002
IRAC2	Spitzer	44606.7	10113.0	-0.000
IRAC3	Spitzer	56764.4	13499.0	-0.013
IRAC4	Spitzer	77030.1	28397.0	0.171

2.1.2 Optical and Ultraviolet

All magnitudes in the XMM-COSMOS catalog are in the AB system and are aperture magnitudes. The total magnitudes are computed using the corrections tabulated in the multiwavelength catalog for each source:

$$m_{\mathrm{AB,tot}} = m_{\mathrm{AB,aper}} + \text{apert. corr.} \tag{2.14}$$

In addition, for each band a sistematic offset, s_f, which is tabulated in Table 2.1, is added to the magnitude. Thie sistematic offset is usually small, of the order of few percent in almost all bands, with the exception of the B_J band (which has known calibration problems) where the offset is about 0.2 with an error of about ±0.05 mag. For a complete description of the observations, data reduction and of the photometry in the catalog refer to Capak et al. (2007, 2008). These total magnitudes are converted into observed monochromatic fluxes using the following formula (see Fukugita et al. 1996)

$$S(\nu) = 10^{-(m_{\mathrm{AB,tot}}+48.6)/2.5} \qquad [\mathrm{erg\ s^{-1}cm^{-2}Hz^{-1}}], \tag{2.15}$$

and the corresponding flux error, $\mathrm{d}S(\nu)$, is

$$\mathrm{d}S(\nu) = \frac{\ln(10)}{2.5}\, \mathrm{d}m\, S(\nu), \tag{2.16}$$

where $\mathrm{d}m$ is the magnitude error. The median 5σ depths for the catalog including PSF matching, deblending, background subtraction, and photon noise are given in Table 2.2. These numbers are for total magnitudes and should be used when choosing signal-to-noise ratio cuts and magnitude limits for the COSMOS catalog (the numbers reported here are updated values and they are slightly different from those in Table 7 of Capak et al. 2007)
The observed flux is then corrected for the Galactic extinction using Eq. (2.17) and it has been

Table 2.2: 5σ depths of the adopted photometric bands.

Filter	Telescope	5σ depth (3″ aperture)
u^*	CFHT	26.50
B_J	Subaru	27.00
g_+	Subaru	27.00
V_J	Subaru	26.60
r_+	Subaru	26.80
i_+	Subaru	26.20
i^*	CFHT	24.00
z_+	Subaru	25.20
J	UKIRT	23.70
K	CFHT	21.20

multiplied by the corresponding observed frequency. Finally, using Eq. (2.9), the intrinsic luminosity for each optical band is obtained.
The Galactic extinction correction is made using a single extinction law for each band based on the standard notation:

$$F_{\rm obs}(\lambda) = F_{\rm intr}(\lambda) 10^{-0.4\ E(B-V)\ k(\lambda)} \tag{2.17}$$

where $F_{\rm obs}$ and $F_{\rm intr}$ are the observed and intrinsic fluxes respectively. The selective attenuation of the stellar continuum $k(\lambda)$ is taken by Capak et al.(2007) Table 11; while the estimated Galactic extinction, $E(B-V)$, is provided for each object in the XMM-COSMOS catalog (Schlegel et al. 1998). The Galactic extinction curve used is from Bolzonella et al. (2000), originally taken from Allen (1976) for the Milky Way. The values adopted for the Galactic extinction correction are tabulated in Table 2.3.

2.1.3 Infrared

The four IRAC channels: 3.6 μm, 4.5 μm, 5.8 μm, and 8.0 μm; and the *deep* 160 μm, 70 μm and 24 μm MIPS observations (GO3) are considered. IRAC fluxes (computed using an aperture radius of 1.5 arcsec) in the XMM-COSMOS catalog are in μJy. After conversion in the cgs system the aperture flux is divided by 0.759 to have the total infrared flux (Surace et al. 2005[‡]):

$$S(\nu_i)_{\rm tot} = \frac{S(\nu_i)_{\rm aper}\, 10^{-29}}{0.759} \qquad [\rm erg\ s^{-1} cm^{-2} Hz^{-1}], \tag{2.18}$$

where i corresponds to 4 IRAC channels: 3.6, 4.5, 5.8, 8.0 μm, and $S(\nu_i)_{\rm tot}$ is multiplied for the observed frequency to have the integrated observed fluxes. If a source is not detected with a 1.5 arcsec radius, the values of the 1.9 arcsec radius aperture flux is considered, and converted to total fluxes dividing it by the wavelength dependent correction factors: 0.765, 0.740, 0.625, 0.580 for 3.6 μm, 4.5 μm, 5.8 μm, and 8.0 μm, respectively. The total flux is then corrected for the galactic extinction using Eq. (2.17) and multiplied by the corresponding observed frequency.

[‡]SWIRE Data Release 2 (Pasadena,CA: Cal Tech): http://swire.ipac.caltech.edu/swire/astronomers/publications/SWIRE2_doc_083105.pdf

Table 2.3: Values of $k(\lambda)$ for the Galactic extinction correction.

λ	$k(\lambda)$
u^*	4.690237
B_J	4.038605
g_+	3.738239
V_J	3.147140
r_+	2.586050
i_+	1.922693
i^*	1.922912
z_+	1.435914
J	0.965000
K	0.340677

For the undetected sources the 5σ upper limits are considered (see Table 2.4). The intrinsic luminosity for each IRAC channel is computed using Eq. (2.9). MIPS 160 μm, 70 μm and 24 μm fluxes are already reported as total fluxes in the catalog. After conversion from mJy in the cgs system, the intrinsic luminosities are computed as already done for the IRAC channels (for MIPS fluxes the correction for galactic extinction is negligible).

2.1.4 Radio

The radio fluxes are from the VLA observations at 1.4 GHz in the 2 deg^2 COSMOS field (see for more details Bondi et al. 2008; Schinnerer et al. 2010). All sources listed in the catalog have peak flux densities $\geq 5\sigma$ at 1.5″ and/or 2.5″ resolution to account for the fact that a significant fraction of sources at these low flux levels are expected to be slighty resolved at 1.5″ resolution. All properties listed in the catalog, such as peak flux density, integrated flux density and source size are determined in the 2.5″ resolution Deep image. The peak flux densities (in mJy) are considered and the intrinsic luminosities at 1.4 GHz are computed as already described in the previous Sections. For the undetected sources a 5σ upper limit flux of 0.075 mJy (Schinnerer et al. 2010) is adopted. The radio luminosities are used to estimate "radioloudness" for Type-1 and Type-2 AGN. Historically, radio-loudness is defined as the ratio between the rest-frame monochromatic luminosity at 5 GHz, $L_{5\,\mathrm{GHz}}(\nu)$, and in the optical B band, $L_{\mathrm{B}}(\nu)$

$$R = \left[\frac{L_{5\,\mathrm{GHz}}(\nu)}{L_{\mathrm{B}}(\nu)}\right], \tag{2.19}$$

sources are considered radio-loud if $R \geq 10$ (Kellermann et al. 1989). The monochromatic flux at 1.4 GHz is converted to $L_{5\,\mathrm{GHz}}(\nu)$ assuming $f(\nu) \propto \nu^{-\alpha}$ with $\alpha = 0.7$, and the rest-frame luminosity is computed as usual.

Table 2.4: S-COSMOS measured sensitivities.

Filter	5σ depth [mJy]
IRAC1	0.001
IRAC2	0.0017
IRAC3	0.0110
IRAC4	0.0145
24 μm	0.08
70 μm	8.5
160 μm	65

2.2 The Spectral Energy Distribution computation

The SEDs for the individual sources considered in this Thesis have been assembled. First of all, the information for all the sources, from 24 μm to the hard X-ray band (upper limits in the optical and near-infrared are not included), is plotted in the rest-frame Log ν – Log (νL_ν) plane. For each source the rest-frame luminosity and corresponding frequency in each of the available bands are considered. A first order polynomial between two adjacent points is determined, and the resulting function is then sampled with a step of $\Delta\mathrm{Log}\,\nu = 0.085$. In this way a "first order" SED, where every point is separated by 0.085 in Log frequency, is created. The resulting SED is "smoothed" using a fourth order polynomial interpolation and re-sampled with a step of $\Delta\mathrm{Log}\,\nu = 0.01$. This choice is motivated by the fact that a single interpolation with a high-order polynomium could introduce spurious features in the final SED. This procedure allows us to build densely sampled SEDs at all frequencies, to extract accurate rest-frame monochromatic luminosities at all redshifts, and to estimate bolometric luminosities and bolometric corrections for Type-1 AGN (see Sect. 2.5).

For the computation of the bolometric luminosity for Type-1 AGN, the data need to be extrapolated in the UV to X-ray gap and at high X-ray energies. From the rest-frame UV luminosity data point at the highest frequency in each SED, a power law spectrum, as measured by HST observations for AGN ($f_\nu \propto \nu^{-1.8}$ for radio-quiet Type-1 AGN, $f_\nu \propto \nu^{-2.2}$ for radio-loud Type-1 AGN; see Zheng et al. 1997), is assumed to extrapolate the SED up to 500Å. The UV luminosity at 500 Å is then linearly connected to the 1 keV luminosity (see Fig. 2.3 for an example of the SED). The X-ray data points are extrapolated to the luminosity at 1 keV computing the slope, $\alpha_x = \mathrm{Log}\,(f_{4\,keV}/f_{1\,\mathrm{keV}})/\mathrm{Log}\,(\nu_{4\,keV}/\nu_{1\,keV})$ ($\alpha_x = \Gamma_x - 1$). Finally, the X-ray spectrum is extrapolated at higher energies using the observed slope α_x, and introducing an exponential cut-off at 200 keV, $f(E) \sim E^{-\alpha_x} e^{-E/200\mathrm{keV}}$ (Gilli et al. 2007).

2.3 Average Spectral Energy Distribution

After having estimated the rest-frame SEDs for all the sources in our sample, they are then normalized at 1μm. The frequency interval is divided from $\mathrm{Log}\,\nu_{\mathrm{min}} = 12$ to $\mathrm{Log}\,\nu_{\mathrm{max}} = 20$ using a fixed step $\Delta\mathrm{Log}\,\nu = 0.02$. Hence, data are averaged in each given interval $\mathrm{Log}\,\nu_l \leq \mathrm{Log}\,\nu \leq \mathrm{Log}\,\nu_{l+1}$. It is important to note that sources at different redshift contribute to the same

bin. Then, the arithmetic mean is calculated as

$$\overline{\text{Log } L} = \frac{\sum_l^{l+1} \text{Log } L_l}{n}, \tag{2.20}$$

where n is the dimension of the vector that contains the values of luminosity in one bin. The scatter around $\overline{\text{Log } L}$ is characterized by the standard deviation

$$\sigma_{\text{Log } L_n} = \sqrt{\frac{1}{n-1}\sum_{i=1}^{n}\left(\text{Log } L_i - \overline{\text{Log } L}\right)^2}, \tag{2.21}$$

while the standard error of the mean is

$$\sigma_{\overline{\text{Log } L}} = \sigma_{\text{Log } L_n}/\sqrt{n}. \tag{2.22}$$

The median of the luminosity distribution is evaluated from the vector (Log L_1, Log L_2,..., Log L_n), by finding the value Log L_i which has equal number of values above and below it, Log $L_{(n+1)/2}$, if the number of values is odd. If the number is even the mean of the central values Log $L_{n/2}$ and Log $L_{(n/2)+1}$ is considered. Considering the values sorted into ascending (or descending) order, the median of logarithmic luminosities, Log L_{med}, is estimated as

$$\text{Log } L_{\text{med}} = \begin{cases} \text{Log } L_{(n+1)/2} & n \text{ odd} \\ \\ \dfrac{1}{2}\left(\text{Log } L_{n/2} + \text{Log } L_{(n/2)+1}\right) & n \text{ even.} \end{cases} \tag{2.23}$$

Due to the relatively wide range of redshifts, the frequency bins close to the boundaries of the observed data points are populated by a variable, typically small, number of points. This effect may introduce relatively high fluctuations in the average luminosity in those bins. In order to minimize these effects the following approach is adopted:

(1) use in the analysis only bins which contains a minimum number of SEDs, this threshold depends on the total number of sources in the sample (e.g., if the sample is composed of 257 sources, as for the Type-2 sample, at least 200 SEDs in each bin to average are considered).

(2) select the mean reference frequency of the bin as

$$\overline{\text{Log } \nu} = \frac{\text{Log } \nu(i) + \text{Log } \nu(i+1)}{2} \tag{2.24}$$

(3) for each source use a `binary-search` algorithm to find all luminosities that correspond at $\overline{\text{Log } \nu}$

(4) if a source does not have a frequency that correspond to $\overline{\text{Log } \nu}$, choose the luminosity with the frequency closer to $\overline{\text{Log } \nu}$

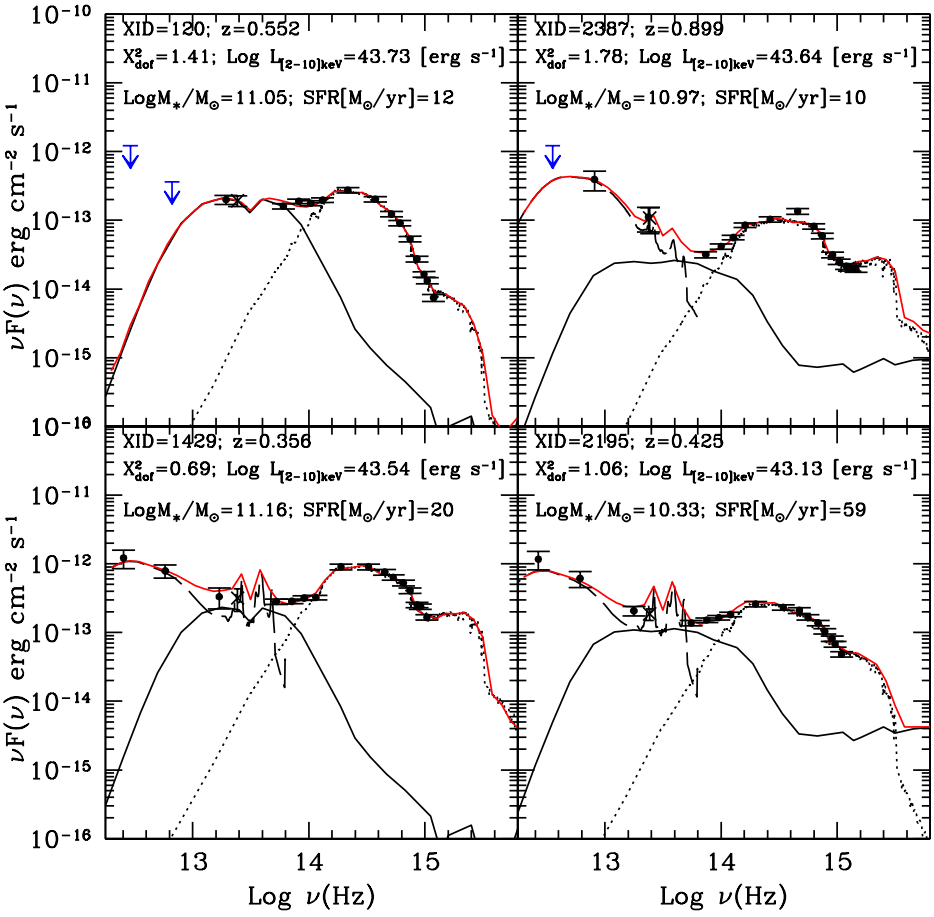

Figure 2.1: Examples of SED decompositions. Black circles are the observed photometry in the rest-frame (from the far-infrared to the optical-UV). The long-dashed, solid and dotted lines correspond respectively to the starburst, AGN and host-galaxy templates found as the best fit solution. The red line represents the best-fit SED. The stellar mass and the SFR derived from the galaxy template are reported.

(5) all selected luminosities in the bin are used to compute mean and median.

Finally, all adjacent luminosities in each bin are connected to compute the final mean and median SED. The median is a robust estimator of the central value, if the luminosity distribution inside the bin is strongly peaked and/or the number of sources inside each bin is high (at least 30 sources in each bin are considered, but this strongly depends on the distribution). The mean, instead, is a robust estimator of the central value if the luminosity distribution is similar to a normal distribution.

2.4 SED-fitting

The purpose of the SED-fitting code is to properly disentangle the emission associated to stellar light from that due to accretion and constrain physical parameters (e.g., stellar masses, SFR, bolometric luminosites) from multi-component modeling. Since the relative contributions of the different components are different at different wavelengths, a proper decomposition can be obtained through a SED-fitting approach providing a robust estimate of the nuclear emission (bolometric luminosities and bolometric corrections, absorption column density distributions, etc) and its relation with the host-galaxy properties (mass, star formation rates, morphological classification). A well sampled SED is mandatory; in particular, far-infrared observations are fundamental to sample the star-formation activity, while mid-infrared observations are necessary to sample the region of the SED where most of the bolometric luminosity of obscured AGN is expected to be re-emitted. In Fig. 2.1 the broad-band SEDs of four XMM-Newton Type-2 AGN are plotted as examples. The lower two panels are representative of a full SED with all detections from the far-infrared to the optical. Unfortunately, there are very few detections at 160 and 70μm, so that the more representative situation is shown in the upper left panel of Fig. 2.1. The three components adopted in the SED-fitting code, *starburst*, *AGN torus* and *host-galaxy* templates, are shown as a long-dashed line, solid line and dotted line, respectively. All the templates used in the SED-fitting code will be described in the following Sections. The red line represents the best-fit, while the black points represent the photometric data used in the code, from low to high frequency: MIPS-Spitzer (160μm, 70μm and 24μm if available), 4 IRAC bands, K CFHT, J UKIRT, optical Subaru and CFHT bands.
The observed data points from infrared to optical are fitted with a combination of various SED templates (see Sect. 2.4.1) using a standard χ^2 minimization procedure

$$\chi^2 = \sum_{i=1}^{n_{\rm filters}} \left[\frac{F_{obs,i} - A \times F_{gal,i} - B \times F_{agn,i} - C \times F_{ir,i}}{\sigma_i} \right]^2 \tag{2.25}$$

where $F_{obs,i}$ and σ_i are the monochromatic observed flux and its error in the band i; $F_{gal,i}$, $F_{agn,i}$ and $F_{ir,i}$ are the monochromatic template fluxes for the host-galaxy, the AGN and the starburst component, respectively; A, B and C are the normalization constants for the host-galaxy, AGN and starbust component, respectively. The starburst component is used only in the case of detections in the 160μm and 70μm band. When detections in these bands are not available, a two components SED-fit is used. Sixteen is the maximum number of bands used (only detection are considered): 160μm, 70μm, 24μm, 8.0μm, 5.8μm, 4.5μm, 3.6μm, K_S, J, z^+, i^*, r^+, g^+, V_J, B_J and u^*.

2.4.1 Template libraries

Optical template library

A set of 75 galaxy templates built from the Bruzual & Charlot (2003, BC03 hereafter) code for spectral synthesis models are used, considering the version with the "Padova 1994" tracks, solar metallicity and Chabrier IMF (Chabrier 2003). For the purposes of this analysis a set of galaxy

templates representative of the entire galaxy population from ellipticals to starbursts is selected. To this aim, 10 exponentially decaying star formation histories with characteristic times ranging from $\tau = 0.1$ to 30 Gyr and a model with constant star formation are included. For each SFH, a subsample of ages available in BC03 models is selected, to avoid both degeneracy among parameters and speed up the computation. In particular, early-type galaxies, characterised by a small amount of ongoing star formation, are represented by models with values of τ smaller than 1 Gyr and ages larger than 2 Gyr, whereas more actively star forming galaxies are represented by models with longer values of τ and a wider range of ages from 0.1 to 10 Gyr. For each source, the age has to be smaller than the age of the Universe at the source redshift. Each template is reddened with the reddening law taken from Calzetti et al. (2000);

$$k(\lambda) = \begin{cases} 2.659\left(-2.156 + \dfrac{1.509}{\lambda} - \dfrac{0.198}{\lambda^2} + \dfrac{0.011}{\lambda^3}\right) + R_V & 0.12\mu\text{m} \leq \lambda \leq 0.63\mu\text{m}, \\ 2.659\left(-1.857 + + \dfrac{1.040}{\lambda}\right) + R_V & 0.63\mu\text{m} < \lambda \leq 2.2\mu\text{m}. \end{cases} \tag{2.26}$$

Outside the validity range of the law, the slope of $k(\lambda)$ is obtained by interpolating between 1300 Å and 1200 Å; while at $\lambda > 22000$ Å the slope is computed interpolating between 21900 Å and 22000 Å, and then extrapolated to lower and higher wavelengths. The law derived by Calzetti and collaborators is the most used in the literature, particularly in high-z and star-forming galaxies studies. The ultraviolet region of the SED is more affected by the presence of dust, and this correction becomes important for galaxies at $z \gtrsim 3$, when the optical data are "moved" to the UV region. The extinction at a wavelength λ is related to the colour excess $E(B-V)$ and to the reddening curve $k(\lambda)$ by $A_\lambda = k(\lambda)E(B-V) = k(\lambda)A_V/R_V$, with $R_V = 4.05$ for the Calzetti's law. The setting for $E(B-V)$ ranges between 0 and 1 with a step of 0.05. Using different extinction laws (e.g., Milky Way, Large and Small Magellanic Clouds) does not change significantly our results.

The normalization of the BC03 templates is as follows:

- For burst and exponentially declining SFR models, it is given in solar luminosities per solar mass.
- For continuous star-forming models, it is given in solar luminosities units and assuming SFR= 1 $M_\odot$/yr. The total stellar mass, M_*, for a model of a given age is SFR×age.

The observed flux, F_o, from the best-fit galaxy template, is evaluated as

$$F_o = A\, F_{\text{model}} \qquad [\text{erg s}^{-1}\text{cm}^{-2}], \tag{2.27}$$

where A is the normalization as defined in Eq. (2.25) and F_{model} is the monochromatic best-fit template flux. The total luminosity is

$$L = A\, F_{\text{model}}\, 4\pi \text{d}_\text{L}^2 \qquad [\text{erg sec}^{-1}] \tag{2.28}$$

where d_L is in cm. The total luminosity computed from the BC03 model is defined as

$$L_{\rm model} = \frac{M_*}{M_\odot} F_{\rm model} L_\odot, \tag{2.29}$$

Therefore, the stellar mass in solar units is

$$M_* [M_\odot] = A \frac{4\pi d_L^2}{(1+z) M_\odot L_\odot}, \tag{2.30}$$

where $L_\odot = 3.90 \times 10^{33}$erg/s, and $(1 + z)$ takes into account the fact that the normalization is computed from the rest-frame template.
Absolute magnitudes in the AB photometric system are computed, for each source, from the best-fit galaxy template in the following filters: I, R, V, B and U (but different filters can be also considered by adding the files with the transmission function, $R(\nu)$, in the code) in the Johnson and Kron-Cousins photometric system (hereafter JKC). The apparent magnitude, $m_{\rm AB}$, of a source observed through a photometric bandpass, $R(\nu)$, is defined as

$$m_{\rm AB} = -2.5 \, {\rm Log} \frac{\int R(\nu) F(\nu) {\rm d}\nu}{\int R(\nu) {\rm d}\nu} - 48.60. \tag{2.31}$$

The absolute magnitude $M_{\rm AB}$, in the emitted-frame bandpass, is

$$M_{\rm AB} = m_{\rm AB} - 5 \, {\rm Log} \left[\frac{d_L}{10 \, {\rm pc}} \right]. \tag{2.32}$$

AGN template library

The nuclear SED templates are taken from Silva et al. (2004). They were constructed from a large sample of Seyfert galaxies selected from the literature for which clear signatures of non-stellar nuclear emission were detected in the near-IR and mid-IR. After a proper subtraction of the stellar contribution, the nuclear infrared data were interpolated with a radiative transfer code for dust heated by a nuclear source with a typical AGN spectrum, and including different geometries, distribution of the dust, variation of the radii, density and dust grain sizes to account for possible deviation from a standard ISM extinction curve (see for more details Granato & Danese 1994; Maiolino et al. 2001).
The infrared SEDs were then normalized by the intrinsic, unabsorbed X-ray flux in the 2–10 keV band, and are divided into 4 intervals of absorption in terms of $\langle N_{\rm H} \rangle$: $\langle N_{\rm H} \rangle < 10^{22}$ cm^{-2} for Sy1, while $10^{22} < \langle N_{\rm H} \rangle < 10^{23}$ cm^{-2}, $10^{23} < \langle N_{\rm H} \rangle < 10^{24}$ cm^{-2} and $\langle N_{\rm H} \rangle > 10^{24}$ cm^{-2} for Sy2. In Fig. 2.2 the average nuclear SEDs in the infrared are presented. The main differences between the SEDs of Sy1s and Sy2s with $10^{22} < \langle N_{\rm H} \rangle < 10^{23}$ cm^{-2} are the absorption in the near-IR at about $\lambda < 2\mu$m and the silicate absorption at $\lambda = 9.7\mu$m, which are present in the Sy2 template. The shape of the SED with $10^{23} < \langle N_{\rm H} \rangle < 10^{24}$ cm^{-2} is quite similar to the SED with $10^{22} < \langle N_{\rm H} \rangle < 10^{23}$ cm^{-2}. The Compton-thick SED ($\langle N_{\rm H} \rangle > 10^{24}$ cm^{-2}) shows conspicuous absorption also at $\lambda \sim 1.3\mu$m. If a source has the $N_{\rm H}$ value available, this is used as a prior in the

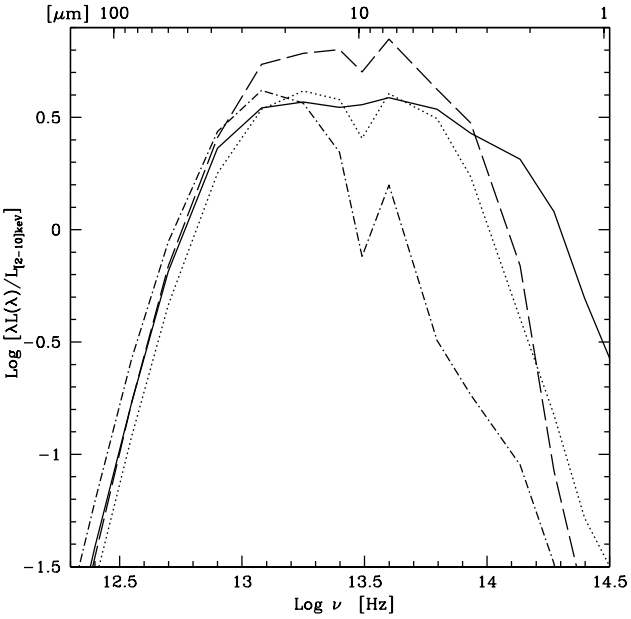

Figure 2.2: Nuclear infrared SED of Seyfert galaxies by Silva et al. (2004), normalized to $L_{[2-10]\mathrm{keV}}$ and binned in column densities $\langle N_\mathrm{H}\rangle$. The solid line is the SED for Sy1s, the dotted line for Sy2s with $10^{22} < \langle N_\mathrm{H}\rangle < 10^{23}$ cm^{-2}, the short-dashed line for Sy2s with $10^{23} < \langle N_\mathrm{H}\rangle < 10^{24}$ cm^{-2} and the long-dashed line is for Sy2s with $\langle N_\mathrm{H}\rangle > 10^{24}$ cm^{-2}.

selection of the best-fit AGN template.

Starburst template library

Two different starburst template libraries are used in the SED-fitting code: Chary & Elbaz (2001) and Dale & Helou (2002). These template libraries represent a wide range of SED shapes and luminosities and they are widely used in the literature.
The Chary & Elbaz (2001) template library consists of 105 templates based on the SEDs of four prototypical starburst galaxies (Arp220 (ULIRG); NGC 6090 (LIRG); M82 (starburst); and M51 (normal star-forming galaxy)). They were derived using the Silva et al. (1998) models with the mid-infrared region replaced with ISOCAM observations between 3 and 18μm (verifying that the observed values of these four galaxies were reproduced by the templates). These templates were then divided into two portions (4–20μm and 20–1000μm) and interpolated between the four to generate a set of libraries of varying shapes and luminosities. The Dale et al. (2001) templates are also included in this set to extend the range of shapes.
The Dale & Helou (2002) templates are updated versions of the Dale et al. (2001) ones. This model considers three components: large dust grains in thermal equilibrium, small grains semistochastically heated, and stochastically heated PAHs. They are based on IRAS/ISO observations of 69 normal star-forming galaxies in the wavelength range 3–100μm. Dale & Helou (2002) improved upon these models at longer wavelengths using SCUBA observations of 114 galaxies from the Bright Galaxy Sample (BGS, see Soifer et al. 1989), 228 galaxies observed with ISOLWS (52–170μm; Brauher 2002), and 170μm observations for 115 galaxies from the ISOPHOT Serendipity Survey (Stickel et al. 2000). All together, these 64 templates span the IR luminosity range 10^8 – $10^{12} L_\odot$. The total infrared template sample used in our analysis is composed of 168 templates.

2.5 Bolometric luminosities and bolometric corrections

The determination of AGN physical parameters such as bolometric luminosity and bolometric correction, accretion rate and Eddington ratio, if the black hole mass is known, needs a proper QSO SED modelling. In fact, the mean quasar SED (e.g., Sanders et al. 1989; Elvis et al. 1994; Hatziminaoglou et al. 2005; Richards et al. 2006) contains important information on the AGN structure. The big-blue bump and the infrared-bump are related to the torus that surrounds the accretion disk on to the central SMBH, respectively. Bolometric corrections and bolometric luminosities are determined assuming that the AGN emits isotropically. From observations we know that this is not the case. The AGN can be seen at different viewing angles, and the bolometric luminosity of the same source seen face-on or edge-on can be significantly different. For a typical viewing angle of $\sim 30^{\circ}$ to the quasar central engine, the value of $L_{\rm bol}$ resulting from the isotropy assumption is systematically higher by $\sim 30\%$ if compared to the value of Lbol which incorporates the anisotropic emission of the accretion disc (see Nemmen & Brotherton 2010). The energy emitted is the same, but not necessarily equally distributed along different line of sights. The SEDs computed as described in Sect. 2.2, do not take into account orientation effects. However, the isotropy assumption is widely used in the literature and, in order to compare our findings with previous work, the same assumption is considered.

2.5.1 Bolometric luminosities and bolometric corrections for Type-1 AGN

In general, the bolometric luminosity in the rest-frame Log ν − Log (νL_{ν}) plane can be written as:

$$L_{\rm bol} = \ln(10) \int_{\rm Log\ \nu_i}^{\rm Log\ \nu_j} \nu L_{\nu}\ {\rm dLog}\ \nu \tag{2.33}$$

where νL_{ν} is the broad-band rest-frame SED. The bolometric luminosity for Type-1 AGN is computed integrating the SED, as described in Sect. 2.2, in the Log ν − Log (νL_{ν}) rest-frame plane from 1μm to 200 keV. The choice to neglect the infrared bump is motivated by the fact that nearly all photons emitted at these wavelengths by the AGN are reprocessed optical/UV/soft X-ray photons; in this way we avoid to count twice the emission reprocessed by dust (see Fig. 2.3 as example). In order to compute hard X–ray bolometric correction the standard definition is used

$$k_{\rm bol} = \frac{L_{\rm bol}}{L_{\rm [2-10]keV}}, \tag{2.34}$$

where $L_{\rm [2-10]keV}$ is evaluated as in Sect. 2.1.1. If the black hole mass is available, the Eddington ratio can be also estimated as

$$\lambda_{\rm Edd} = \frac{L_{\rm bol}}{L_{\rm Edd}} \propto \frac{L_{\rm bol}}{M_{\rm BH}}, \tag{2.35}$$

which represents the accretion rate relative to the Eddington accretion rate

$$\lambda_{\rm Edd} = \frac{L_{\rm bol}}{L_{\rm Edd}} = \frac{\epsilon c^2 \dot{M}_{\rm BH}}{\epsilon c^2 \dot{M}_{\rm Edd}} = \frac{\dot{M}_{\rm BH}}{\dot{M}_{\rm Edd}}. \tag{2.36}$$

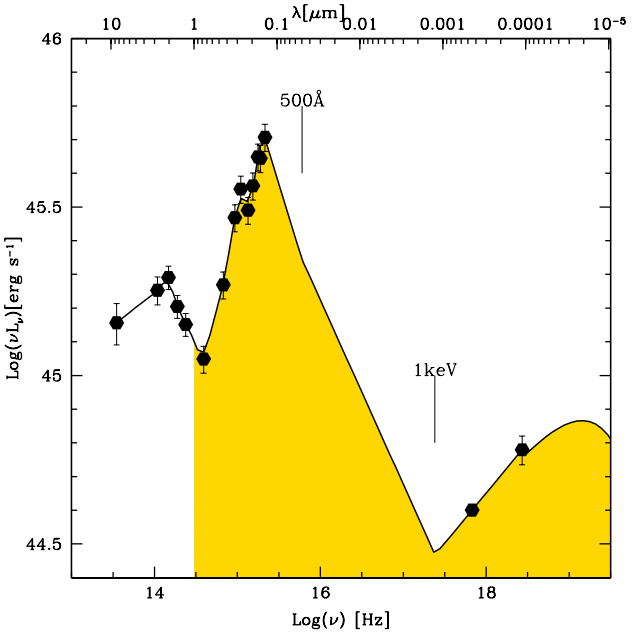

Figure 2.3: Rest-frame SED for an X–ray selected Type-1 AGN. Black points represent the data used to construct the rest-frame SED (*black solid line*). The yellow shaded area represents the integrated area considered for the computation of the bolometric luminosity (from 1μm to the X–ray).

2.5.2 Bolometric luminosities and bolometric corrections for Type-2 AGN

As already pointed out at the beginning of this Section, most of the emission of obscured AGN in the optical-UV is dominated by the host-galaxy, which outshines the nuclear absorbed light. The nuclear bolometric luminosities and bolometric corrections are estimated, using an approach similar to Pozzi et al. (2007, see also Vasudevan et al. 2010; Pozzi et al. 2010), whereas the infrared luminosity is used as a proxy of the intrinsic nuclear luminosity. The appropriate nuclear template from Silva et al. (2004) is selected based on the absorbing column density $N_{\rm H}$, when available, or from the best-fit nuclear infrared template. The bolometric luminosity is computed as the sum of the total infrared and X–ray luminosity:

$$L_{\rm bol} = L_{\rm IR} + L_{\rm X}. \tag{2.37}$$

After performing the SED-fitting, only the nuclear component of the best-fit is integrated. Hence, the total IR luminosity $L_{\rm IR}$ is obtained integrating the nuclear template between 1 and 1000μm. To convert this IR luminosity into the nuclear accretion disk luminosity, we applied the correction factors to account for the geometry of the torus and the anisotropy of the torus emission (see Pozzi et al. 2007). The first correction is parameterized by the covering factor f. The covering factor is related to the geometry of the torus that obscures the accretion disk emission in the optical-UV along the line of sight, and its value is estimated from the ratio of obscured/unobscured quasars found by the X–ray background synthesis models (Gilli et al. 2007). This correction factor is ~ 1.5. This value correspond to a typical covering factor of $f \sim 0.67$, consistent with the results

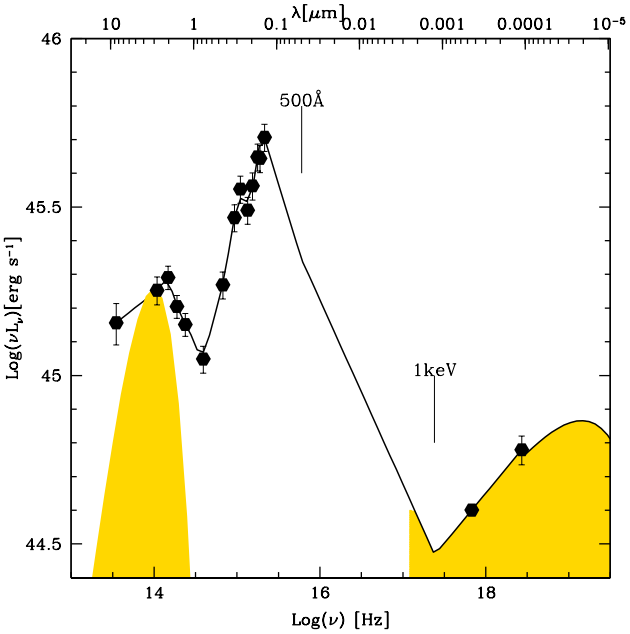

Figure 2.4: Rest-frame SED as in Fig. 2.3. The yellow shaded area represents the integrated area considered for the computation of the bolometric luminosity. The yellow shaded area in the infrared represents a black-body spectrum at $T = 1700$ K (note that it has to be corrected for the geometry of the torus in order to have the correspondent nuclear disk emission).

based on clumpy torus models (Nenkova et al. 2008).
The anisotropy factor is defined as the ratio of the luminosity of face-on versus edge-on AGN, where the obscuration is a function of the column density $\langle N_{\rm H} \rangle$. Therefore, SEDs in Silva et al. (2004) have been integrated in the 1–30μm range, after normalizing these SEDs to the same luminosity in the 30–100μm range. The derived anisotropy values are 1.2–1.3 for $10^{22} < \langle N_{\rm H} \rangle < 10^{24}$ and 3–4 for $\langle N_{\rm H} \rangle > 10^{24}$. The same values as in Vasudevan et al. (2010) are adopted: 1.3 for $10^{22} < \langle N_{\rm H} \rangle < 10^{24}$ and 3.5 for $\langle N_{\rm H} \rangle > 10^{24}$.
The total X–ray luminosity $L_{\rm X}$ is estimated integrating in the 0.5-100 keV range the X–ray SED using the de-absorbed soft and hard X–ray luminosities. The X–ray SED is estrapolated at higher energies using the estimated X–ray slope, and introducing an exponential cut-off at 200 keV (see Fig. 2.4 as example).

2.5.3 Robustness of the method

The robustness of the method used to estimate nuclear bolometric luminosities and bolometric corrections from SED-fitting, for the sample of Type-2 AGN, has been tested against an updated version of the soft X–ray selected sample of Type-1 AGN. The Type-1 AGN sample described in Chapter 3 was composed of 361 spectroscopically classified broad-line AGN. The recent work by Brusa et al. (2010) has updated the spectroscopic classification and increased the number of Type-1 AGN with spectroscopic redshift, so that the final sample is composed of 395 Type-1 AGN in the redshift range $0.103 \leq z \leq 4.255$ with X–ray luminosities $42.20 \leq \mathrm{Log}\, L_{[2-10]\rm keV} \leq 45.23$. Bolometric and X–ray luminosities, and bolometric corrections have been computed using the same approach as in Sect. 2.5.1 for the Type-1 sample. In order to compare bolometric luminosities computed using the "standard" method (integrating the rest-frame SEDs from 1μm up to the UV-bump), with the results from the SED-fitting code (IR+X-

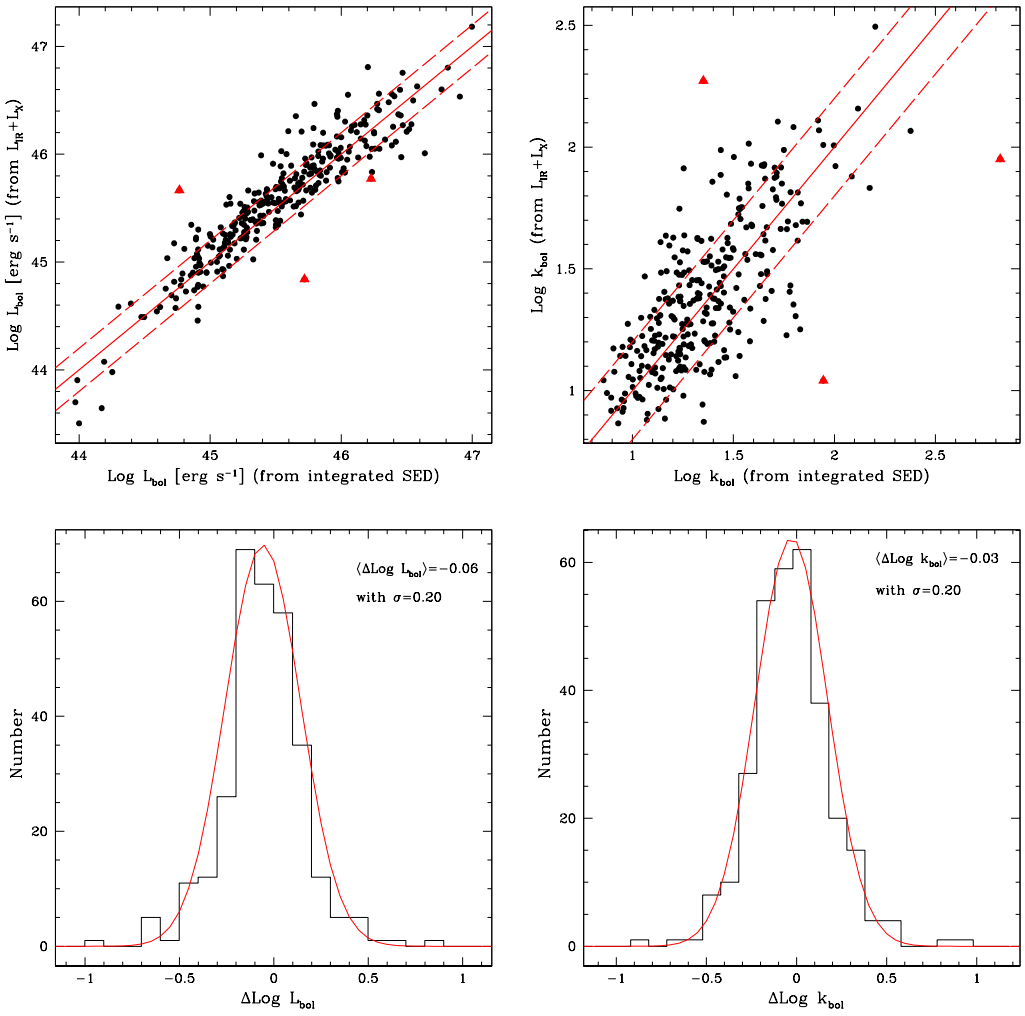

Figure 2.5: Upper panel: Comparison between the values of bolometric luminosity and bolometric correction from the "standard" approach and from the SED-fitting for Type-1 AGN. Lower panel: Distribution of the differences between the values of bolometric luminosity and bolometric correction from the "standard" approach (integrating the rest-frame SEDs from 1μm up to the UV-bump) and from the SED-fitting.

ray luminosity, Eq. [2.37]), we have applied, to the Type-1 sample, the approach described in Sect. 2.4 to estimate bolometric parameters. To be consistent with the selection criteria of the sample discussed in this paper, only AGN with X–ray detection in the hard band are considered (87 Type-1 AGN are removed from the main sample). Moreover, for 2 sources the best-fit does not consider an AGN component, so we cannot compute the bolometric luminosities for them. The final test sample is composed of 306 Type-1 AGN in the redshift range $0.103 \leq z \leq 3.626$ and X–ray luminosities $42.20 \leq \mathrm{Log}\, L_{[2-10]\mathrm{keV}} \leq 45.04$.

In order to select the appropriate nuclear template from Silva et al. (2004), we consider the SED for Sy1 AGN (no correction for anisotropy is necessary in this case) and the Sy2 SED with $10^{22} < \langle N_{\mathrm{H}} \rangle < 10^{23}$ for 20 Type-1 AGN that have N_{H} in this range.

The comparison between the values of $L_{\rm bol}$ and $k_{\rm bol}$ from the two different approaches (1μm-UV versus infrared SED-fitting), are presented in Fig. 2.5. Three outliers are shown as red triangles in the two upper panels. The outlier in the bottom side of the plot, XID=357 at redshift 2.151 has Log $k_{\rm bol}$ = 1.95 from the 1μm-UV rest-frame SED and Log $k_{\rm bol}$ = 1.04 using the infrared luminosity, and presents large error bars at 24μm, so that the total bolometric luminosity, computed using the infrared luminosity, is probably underestimated. The outlier in the right end of the distribution, XID=5114 at redshift 0.212 (Log $k_{\rm bol}$ = 2.82 from the 1μm-UV rest-frame SED and Log $k_{\rm bol}$ = 1.95 using the infrared luminosity) is detected at 160μm, 70μm and 24μm, Log $\langle N_{\rm H} \rangle$ = 22.68 from X–ray and Log $L_{[2-10]\rm keV}$ = 42.89. Probably this source is a star-forming galaxy, so that using the integrated rest-frame SED the stellar emission in the estimate of the bolometric luminosity is included, thus overestimating the bolometric luminosity and, therefore, the bolometric correction. The last notable outlier in the top/left side of the distribution, XID=2152 at redshift 0.627 (Log $k_{\rm bol}$ = 1.35 from the 1μm-UV rest-frame SED and Log $k_{\rm bol}$ = 2.27 using the infrared luminosity) presents a significant host-galaxy contribution in the optical-UV and, therefore, the bolometric luminosity is likely to be underestimated in the integrated rest-frame SED approach.

Although the two methods are rather different, the estimates of bolometric luminosities agree remarkably well, with a 1σ dispersion of 0.20 dex after performing a 3.5σ clipping method in order to avoid outliers. Bolometric luminosities from SED-fitting are, on average, slightly larger than those computed integrating the rest-frame SED from 1μm to the X–ray (see the lower left side in Fig. 2.5). This effect is also present in the Vasudevan et al. (2010) work and they attribute this effect to a number of factors. For example, it is possible that SED-fitting underestimates the host-galaxy contribution, or that the anisotropy and geometry corrections are too large for some objects. In conclusion, the agreement between the two methods is overall quite satisfactory.

Chapter 3

Properties of X–ray selected Type-1 AGN

In this Chapter we present the analysis of the X-ray to optical properties of a sample of 545 X-ray selected Type-1 AGN, from the XMM-COSMOS survey, over a wide range of redshifts ($0.04 < z < 4.25$) and X-ray luminosities ($40.6 \leq \mathrm{Log}\ L_{[2-10]\mathrm{keV}} \leq 45.3$). About 60% of them are spectroscopically identified Type-1 AGN, while the others have a reliable photometric redshift and are classified as Type-1 AGN on the basis of their multi-band SEDs. The average SED for Type-1 AGN with spectroscopic redshift are derived, while the relationship between UV and X-ray luminosity (α_{ox}), and its dependence on redshift and luminosity are discussed for the entire sample. A highly significant correlation between α_{ox} and $L_{2500\ \text{Å}}$ is found, in agreement with previous investigations of optically selected samples. The bolometric corrections, k_{bol}, for the whole sample are calculated using hard X-ray luminosities ($L_{[2-10]\mathrm{keV}}$), and the Eddington ratios for a subsample of 150 objects for which black hole mass estimates are computed. The trend of increasing bolometric correction with increasing Eddington ratio as proposed in previous works is confirmed. A tight correlation is found between α_{ox} and k_{bol}, which can be used to estimate accurate bolometric corrections using only optical and X-ray data. We find a significant correlation between α_{ox} and Eddington ratio, in which the ratio between X-ray and optical flux decreases with increasing Eddington ratio. This Chapter is mainly based on: "*The X-ray to optical-UV luminosity ratio of X-ray selected type 1 AGN in XMM-COSMOS*"; Lusso E., Comastri A., Vignali C., Zamorani G., et al.; 2010; A&A; 512, A34.

3.1 The Data Set

3.1.1 Type-1 AGN Sample

The analysis is restricted to the X-ray sources detected in the soft band at a flux larger than 10^{-15}erg s^{-1}cm^{-2} (Cappelluti et al. 2009). The parent sample consists of 1312 sources* (hereafter

*In this analysis we used the version of the catalog presented in Brusa et al. 2009a,b; hence, the numbers of sources that we will give in this Section are slightly different from those reported in Brusa et al. 2010. However, the main results discussed in this Chapter do not change significantly.

Table 3.1: Selection criteria from 1312-XMM catalog.

Catalog	BL[a]	Photoz	Total[b]
1312XMM[c]	361	613*	974
Class ≥ 19 [d]	(361)[f]	236	597
Radio quiet[e]	322	223	545

[a] Broad-line sources from optical spectroscopy (FWHM >2000 km s^{-1}).

[b] This column gives the sum of the objects with spectroscopic or photometric redshifts.

[c] $F_{[0.5-2]\mathrm{keV}} \geq 10^{-15}$ erg $s^{-1}cm^{-2}$ and secure optical association. The 1312-XMM catalog also comprises: 241 sources which are not broad-line AGN; 34 sources which are spectroscopically classified as stars; 49 sources which are best-fitted with a stellar template and 14 sources for which the photometric redshift is not reliable.

[d] According to Table 2 in Salvato et al. (2009).

[e] $R \leq 10$. Radio loudness is defined in Eq. (2.19). We exclude 51 radio-loud sources: 39 with spectroscopic redshift and 12 with photometric redshift.

[f] All spectroscopically identified broad-line AGN are included, even if the classification flag is less than 19.

* Only extragalactic sources are considered.

1312-XMM) for which a secure optical counterpart can be associated (see discussion in Brusa et al. 2009a,b).

From the 1312-XMM catalog 361 spectroscopically classified broad-line AGN[†] are selected on the basis of broad ($FWHM > 2000\,\mathrm{km\,sec^{-1}}$) emission lines in their optical spectra. We will refer to this sample as the "spectro-z" sample. As a comparison, in the 1312-XMM catalog there are 241 objects spectroscopically classified as not broad-line AGN (Type-2 or emission-line or absorption-line galaxies, see Sect. 2.1).

The spectroscopic completeness of the X-ray selected sample quickly decreases towards faint optical magnitudes. A sizable fraction of Type-1 AGN may be present among optically faint X-ray sources; not to use them in our analysis would significantly bias the distribution of X-ray to optical flux ratios. In order to extend the Type-1 AGN sample to fainter magnitude, we proceed as follows.

First, we looked at the distribution of the best-fit photometric classifications for the spectroscopically identified sample. Figure 3.1 shows the distribution separately for the 361 spectroscopically identified Type-1 AGN (*hatched histogram*) and for the 241 sources which are not broad-line AGN (*filled histogram*). The dashed line at the SED Type=19 marks the division between galaxy-dominated and AGN-dominated SED (see Table 2 in S09 for details). The large majority of the broad emission line AGN in the spectro-z sample (> 90%) are classified as Type-1 AGN by the SED fitting. The distribution of the 241 not broad-line sources is in agreement with the SED-based classification (∼ 83% have Class<19), and the number of not-Type-1 which have

[†]The origin of spectroscopic redshifts for the 361 sources is as follows: 63 objects from the SDSS archive, 75 from MMT observations (Prescott et al. 2006), 112 from the IMACS observation campaign (Trump et al. 2007), 93 from the zCOSMOS bright 10k sample (see Lilly et al. 2007) and 18 from the zCOSMOS faint catalog.

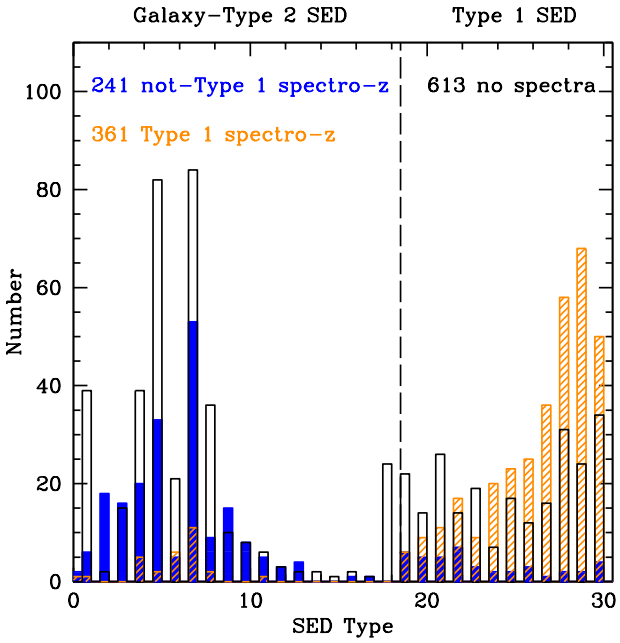

Figure 3.1: Distribution of the photometric classification (see Table 2 in Salvato et al. 2009) for the spectroscopically identified Type-1 AGN sample (*hatched histogram*), for the photometric sample (*open histogram*) and for the not-Type-1 AGN sample (*filled histogram*). The dashed line at SED Type=19 marks our adopted separation between sources with photometric redshift that are defined as Type-1 AGN (236 sources on the right) and not-Type-1 (377 sources on the left) on the basis of the best-fitting SED template.

Class≥19 is relatively small (42 sources, about 17%). Then, the remaining 613 X-ray sources in the 1312-XMM sample for which only a photometric redshift is available from S09 are considered, and all sources which are best-fitted with a galaxy template are excluded. The distribution of the best-fit templates for this photometric sample is also shown in Fig. 3.1 (*open histogram*). In the following, the 236 X-ray sources, classified by the SED fitting with an AGN-dominated SED (i.e., SED Type ≥ 19), are assumed to be Type-1 AGN. We will refer to this sample as the "photo-z" sample.

In Figure 3.2 we plot the soft X-ray flux as a function of i^* CFHT magnitude. Points and crosses represent sources in the spectro-z and photo-z sample, respectively. The dashed lines delimit the region typically occupied by AGN along the X-ray to optical flux ratio $\log(X/O) = \pm 1$[‡] (Maccacaro et al. 1988). The 236 sources in the photo-z sample increase the completeness of the data-set at fainter magnitudes. While some Type-1 AGN may have been missed (about 10%, with SED Type<19 in Fig. 3.1), we are confident that the described choice minimizes the selection bias against optically faint Type-1 AGN. Only sources that have optical-UV data in order to compute monochromatic luminosities at 2500Å and the SED are included in the main sample. This selection criterium only excludes the photometric source with XID=5120.

It is well known that radio-loud AGN have an enhanced X-ray emission mechanism linked to the jets, which can provide an increment in the X-ray emission with respect to radio-quiet AGN with similar optical luminosities (e.g., Zamorani et al. 1981, Wilkes & Elvis 1987, Cappi et al. 1997). Radio-loud AGN are excluded from the total sample using the "standard" definition of radio-loudness, R ≥ 10 (see Sect. 2.1.4). Fiftyone radio-loud Type-1 AGN (39 AGN from the spectroscopic sample and 12 sources with photometric redshift) with a value of radio-loudness $R \geqslant 10$ are removed from the sample .

[‡] $\log(X/O) = \log f_x + i^*/2.5 + 5.6$

The final Type-1 AGN sample used in our analysis, therefore, comprises 545 X-ray selected AGN (322 from the spectro-z sample and 223 from the photo-z sample) spanning a wide range of redshifts ($0.04 < z < 4.25$) and X-ray luminosities ($40.6 \leq \mathrm{Log}\, L_{[2-10]\mathrm{keV}} \leq 45.3$). The selection criteria are summarized in Table 3.1.

Assuming that the fraction of misclassified sources in the spectro-z sample (17%) and the fraction of missing Type-1 sources (10%) can be applied to the photometric sample, we are able to estimate the uncertainties associated to the photo-z sample. If this were the case, the incompleteness and the contamination on the total sample are very low, namely about 4% and 7%, respectively.

The redshift distributions of the total, spectroscopic and photometric samples are presented in Figure 3.3. The median redshift of the total sample is 1.57 (the mean redshift is 1.66, with a dispersion of 0.75). The median redshift of the spectro-z sample is 1.54, while the median of the photo-z sample is 1.66.

3.2 Rest-frame monochromatic fluxes and SEDs for Type-1 AGN

To obtain rest-frame monochromatic luminosities at 2 keV and 2500Å and estimate bolometric luminosities, we used all the multi-color information as compiled by Brusa et al. (2009b). The catalog includes multi-wavelength data from mid infrared to hard X-rays (see Sect. 2.1).

More specifically, the number of detections at 24 μm is 472; for the 73 undetected sources, we consider 5σ upper limits of 0.08 mJy. Most of the sources are detected by IRAC: 545, 543, 544 and 543 at 3.6 μm, 4.5 μm, 5.8 μm and 8.0 μm band, respectively (all Type-1 AGN were

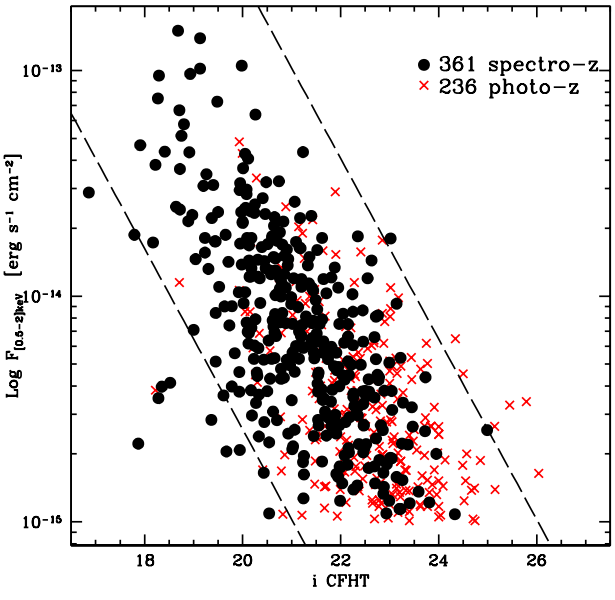

Figure 3.2: Plot of the [0.5 − 2]keV flux versus the total i^* CFHT magnitude for the spectroscopically identified (*black points*) and the photo-z classified (*red crosses*) broad line AGN. The dashed lines represent the constant X-ray to optical flux ratio $\log(X/O) = \pm 1$.

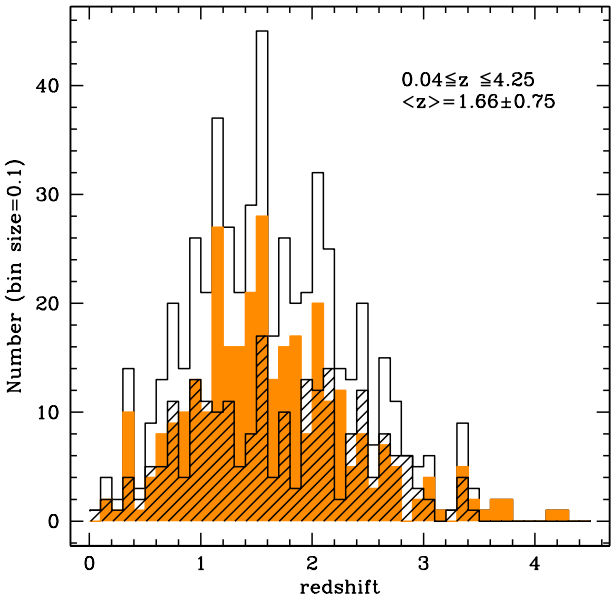

Figure 3.3: Redshift distribution of the 545 Type-1 AGN considered in this work (*open histogram*). The filled histogram shows the redshift distribution for the sample of 322 spectroscopically identified sources, while the hatched histogram is the redshift distribution for the 223 sources without spectroscopic redshift.

detected in the 3.6μm IRAC band). For the undetected sources we consider 5σ upper limits of 1.7 μJy, 11.3 μJy and 14.6 μJy at 4.5 μm, 5.8 μm and 8.0 μm, respectively (see Table 2.4 described in Sect. 2.1.3). Only very faint objects went undetected in the optical and near infrared bands: only 2 upper limits in the z^+ band; 1 upper limit in the B_J, V_J and r^+ bands; 8 upper limits in both i^* and u^* CFHT bands; 9 in the K_S CFHT band and 31 in the J UKIRT band. In Table A.1 we list the main X-ray and optical properties of the sample. Count rates in the 0.5-2 keV and 2-10 keV are converted into monochromatic X-ray fluxes in the observed frame at 1 and 4 keV, respectively, using a Galactic column density $N_H = 2.5 \times 10^{20}\, cm^{-2}$ (see Cappelluti et al. 2009), and assuming a photon index $\Gamma_x = 2$ and $\Gamma_x = 1.7$, for the soft and hard band, respectively (see Sect. 2.1.1).

SEDs for 545 Type-1 AGN are assembled using the procedure described in Sect. 2.2. In Figure 3.4 and 3.5, two examples of SED used for the calculation of the bolometric luminosities and the rest-frame monochromatic luminosities of the Type-1 AGN sample are presented. Given the selection criteria, the SEDs of the objects in our sample are quite different, ranging from blue QSO with an SED close to that reported by Elvis et al. (1994) for radio-quiet AGN (see Fig. 3.4), to objects with a red SED possibly due to intrinsic absorption and/or host-galaxy contamination (see Fig. 3.5). We will discuss in Sections 3.5.1 and 3.5.2 how we take the possible effects of reddening and host-galaxy contamination into account in our analysis. A complete Type-1 AGN SED atlas will be presented in Elvis et al. (2011), in preparation. However, in the following Section we will present a preliminary analysis of the average SEDs and bolometric corrections for the Type-1 AGN in XMM-COSMOS.

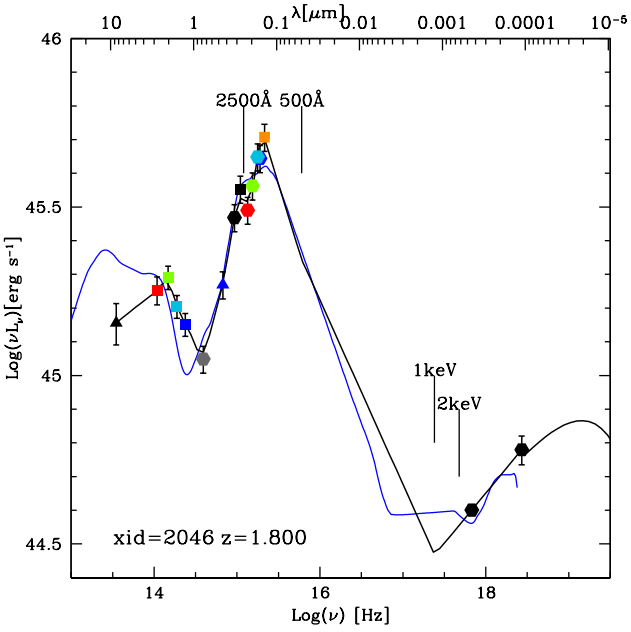

Figure 3.4: The SED of a spectroscopically identified QSO at $z = 1.8$ (XID=2046, *black line*), compared with the mean SED of Elvis et al. (1994, *blue line*). The rest-frame data, used to construct the SED of XID=2046 are, from left to right: black triangle, 24 μm MIPS; red square, 8.0 μm IRAC; green square, 5.8 μm IRAC; cyan square, 4.5 μm IRAC; blue square, 3.6 μm IRAC; gray hexagon, K CFHT; blue triangle, J UKIRT; black, red, green, cyan and blue hexagons represent z^+, r^+, g^+, V_J and B_J Subaru bands, respectively; black and orange squares represent i^* and u^* CFHT bands, respectively; black hexagons soft X-ray and medium-hard X-ray luminosity.

3.3 The average SEDs for Type-1 AGN

The mean and median SEDs are obtained by taking the arithmetic mean and the median of logarithmic luminosities as described in Sect. 2.3. Since there are only slightly differences in the mean and in the median SEDs, only the median SEDs are discussed in the following discussion. The Type-1 AGN sample considered in this Chapter is composed of 361 spectroscopically classified broad-line AGN. The recent work by Brusa et al. (2010) has updated the spectroscopic classification and increased the number of Type-1 AGN with spectroscopic redshift, so that the final sample is composed of 395 Type-1 AGN in the redshift range $0.103 \leq z \leq 4.255$ with X-ray luminosities $42.20 \leq \mathrm{Log}\, L_{[2-10]\mathrm{keV}} \leq 45.23$. In the following analysis we do not distinguish between radio-quiet and radio-loud AGN, since in this sample the fraction of radio-emitters is about 10% (see Sect. 3.1.1) and their inclusion does not affect the main results. In order to keep under control the contribution of host-galaxy stellar light a subsample of 162 sources is considered, which have a host-galaxy contribution less than 10% (hereafter 162PL) in the F814W ACS band. The selection has been made using the MPI Heidelberg group morphological analysis results (Jahnke private communication): all objects which have a host-to-nucleus galaxy flux ratio less 0.1 in the ACS image, could be considered marginally resolved or unresolved. The 162PL sample is used to create a "pure" nuclear Type-1 SED with a minimum host-galaxy contribution. This sample has X–ray luminosities in the range $44.05 \leq \mathrm{Log}\, L_{[2-10]\mathrm{keV}} \leq 45.16$ and redshift typically between 1 and 2. The sample is further divided in four luminosities intervals sorted by hard X–ray luminosity calculated at 4 keV (see Table 3.2 for details). The median SEDs of all the spectroscopic sources and the 162PL sample are shown in Fig 3.6, and the mean SED of the total Type-1 sample and the dispersion around the mean are also plotted. Additionally, the average SEDs for the radio-quiet Type-1 AGN sample by Elvis et al. (1994) (hereafter E94) and for the SDSS quasar sample by Richards et al. (2006) (hereafter R06) are presented as a comparison.

The median SED of all AGN in X–ray selected spectroscopic sample is flat both in the infrared and in the ultraviolet region, showing no evidence for a "big blue-bump" or an inflection point at about 1μm, as commonly seen in quasars. The bars (gray area) show the large dispersion of the SEDs going from "galaxy-like" SEDs at low luminosities, to "quasar-like" SEDs at higher luminosities, similar to those considered in the E94 and R06 analysis. From this large dispersion it is apparent the variety of SEDs that characterize this sample with respect to the E94 or R06 sample. E94 sample was composed mainly by bright PG quasar in the optical-UV, typically at low redshift ($\langle z \rangle \sim 0.206$); while in the SDSS sample of R06, even if the sample covers a wider redshift ($\langle z \rangle \sim 1.525$) and luminosity range, all sources present a prominent big-blue bump. The lack of the 1μm inflection point in our sample may be due to host-galaxy contamination. Typically, the SED of a galaxy peaks around 1μm, which is associated with the emission from the evolving stellar population in the galaxy, so if the luminosity of the galaxy is comparable with the AGN luminosity the combination of these two SEDs can result in a flat SED from the infrared to the UV region. Another possible factor that has to be taken into account in the SED flatness may be the intrinsic obscuration, especially at low luminosity AGN (Lawrence & Elvis 1982) producing both X–ray absorption and reddening in the optical-UV. Intrinsic obscuration could be the cause for large variation of SED's shapes, in particular depressing the strength of the big-blue bump. The differences could be also due to the different ranges of redshift and X–ray luminosities probed by the XMM-COSMOS survey compared to the E94 and R06 samples. The median SED considering the 162PL sample, for which the contribution of the host-galaxy light is less than the 10%, shows a more prominent infrared and big-blue bump, although, also in this case, the resulting average SED is flatter than the median SED by E94 or by R06.

The 162PL sample is further binned in X–ray luminosity and the resulting median SEDs are reported in Fig. 3.7. The luminosity at 4 keV is used to divide the total sample in four bins with

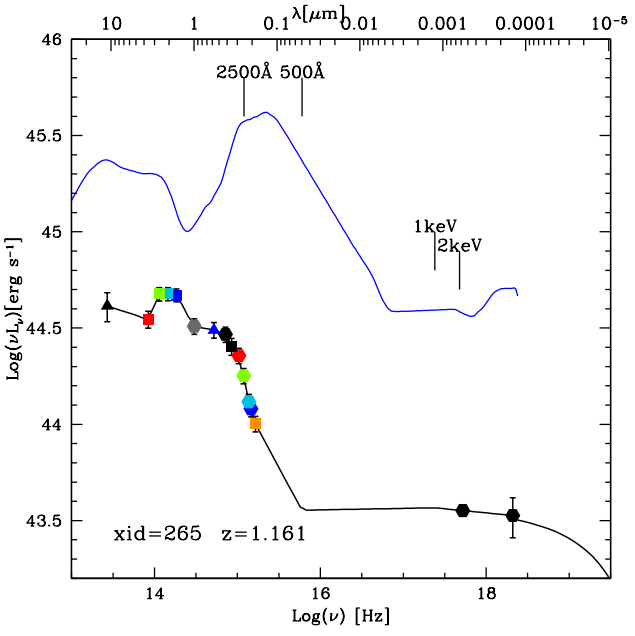

Figure 3.5: The SED of a spectroscopically identified QSO at $z = 1.161$ (XID=265, *black line*). Keys are as in Fig. 3.4.

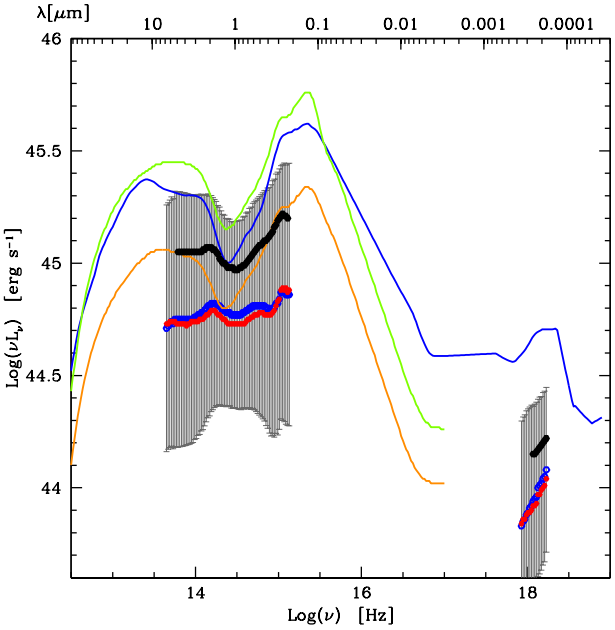

Figure 3.6: The median (*red points*) and the mean (*blue points*) SEDs for the total spectroscopic sample. The mean SED for the 162PL sample is represented with black points. The error bars (gray area) represent the dispersion of the total spectroscopic sample around the mean SED. The average SEDs are compared with the mean SED of Elvis et al. (1994, *blue line*), the mean SEDs of Richards et al. (2006) using all the SDSS quasar sample (*green line*) and the near-IR dim SDSS quasar sample (*orange line*).

the same number of sources in each bin. The shapes of the average SEDs are approximately the same in all luminosity bins. However, at higher X–ray luminosities the median SEDs are characterized by a more pronounced big-blue bump. Bolometric luminosities and bolometric corrections are computed averaging all values in the main spectroscopic sample, in the 162PL sample and in the binned samples. These average parameters are evaluated from the median SEDs extrapolating the SED in the ultraviolet/soft X–ray region and at higher X–ray energies as described in Sect. 2.2. All values are reported in Table 3.2 and compared to the average parameters estimated from the median SED for radio-quiet AGN by E94. The average bolometric correction values seem to show a trend going from lower to higher hard X–ray luminosities. Low hard X–ray luminosity sources seem to have low bolometric correction. However, this trend is not statistically significant given the errors. The significance of the difference between the first and the fourth hard X–ray luminosity bin computed as the median of the values in each bin is $\sim 1.7\sigma$, while there is no trend if we consider the median $k_{\rm bol}$ computed directly from the median SEDs. This is consistent with the findings discussed in Sect. 4.4.1 (see Fig. 4.11) for both Type-1 and Type-2 AGN.

3.4 Statistical Analysis

To study the possible correlations between $\alpha_{\rm ox}$, $L_{2500\ \text{Å}}$, $L_{2\ \rm keV}$ and redshift, we used the Astronomy Survival Analysis software package (ASURV rev. 1.2; Isobe et al. 1990; Lavalley et al. 1992). ASURV implements the bivariate data-analysis methods and also properly treats censored data using the survival analysis methods (Feigelson & Nelson 1985; Isobe et al. 1986). We have employed both full parametric estimate and maximized (EM) regression algorithm and semiparametric Buckley-James regression algorithm (Buckley & James 1979) to perform the lin-

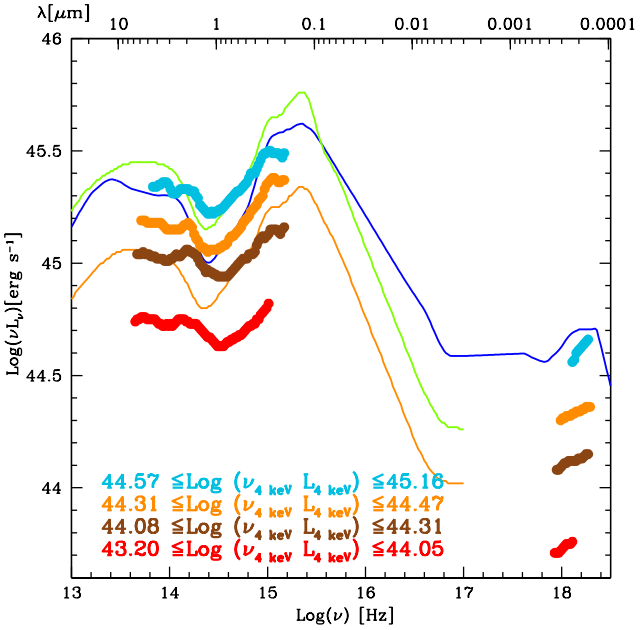

Figure 3.7: The median SEDs computed binning the 162PL sample in X–ray luminosity at 4 keV.

ear regression of the data. The EM regression algorithm is based on the ordinary least-squares regression of the dependent variable Y against the independent variable X (OLS[Y|X]). The regression line is defined in such a way that it minimizes the sum of the squares of the Y residuals. Since in our analysis the choice of the independent variable is not straightforward, we have also used the inverse of OLS(Y|X) (OLS[X|Y]) and we then calculated the bisector of the two regression lines (see Isobe et al. 1990). We only present the findings from the EM regression algorithm, since in all cases the results from the Buckley-James regression algorithm agreed within the errors; we also report the findings from OLS bisector. Moreover, we used the partial-correlation analysis method to compute the correlation between two variables, checking the effect of an additional parameter which the two variables depend on. This method is implemented in the FORTRAN program PARTIAL_TAU, available from the Penn State Center of Astrostatistics, and uses the methodology presented in Akritas & Siebert (1996). The procedure is based on Kendall τ-statistic that properly handles censored data. The results for the partial-correlation analysis are summarized in Table 3.3.

3.4.1 L_{2500} vs $L_{2\,\mathrm{keV}}$

Previous studies on optically selected AGN reported a relationship between $L_{2\,\mathrm{keV}}$ and $L_{2500\,\text{Å}}$ in the form $L_{2\,\mathrm{keV}} \propto L^{\beta}_{2500\,\text{Å}}$, with the best-fit values of the exponent between $0.7 \div 0.8$ (e.g. Avni & Tananbaum 1982, 1986; Chanan 1983; Kriss & Canizares 1985; Anderson & Margon 1987; Wilkes et al. 1994; Yuan et al. 1998;Vignali et al. 2003; Strateva et al. 2005; S06; J07; see also La Franca et al. (1995), who found $\beta \sim 1$). For the best-fit parameters using OLS(Y|X) (i.e. treating $L_{2500\,\text{Å}}$ as the independent variable) we find

$$\mathrm{Log}\, L_{2\,\mathrm{keV}} = (0.599 \pm 0.027)\mathrm{Log}\, L_{2500\,\text{Å}} + (8.275 \pm 0.801) \quad (3.1)$$

Table 3.2: Bolometric properties of Type-1 AGN: average bolometric and hard X–ray luminosities and bolometric corrections.

Sample	Number	$\langle \mathrm{Log}\, k_{\mathrm{bol}} \rangle^a$	σ^b	$\langle k_{\mathrm{bol}} \rangle^a$	$L_{\mathrm{bol},1\mu\mathrm{m}}{}^c$ [erg s^{-1}]	$L_{[2-10]\mathrm{keV}}{}^c$ [erg s^{-1}]	$\langle k_{\mathrm{bol}} \rangle^c$
All	395	1.38	0.30	24 ± 1	3.17×10^{45}	1.34×10^{44}	24 ± 1
162PL	162	1.47	0.29	29 ± 2	5.04×10^{45}	2.17×10^{44}	23 ± 1
Bin 1	39	1.42	0.22	26 ± 2	1.92×10^{45}	8.75×10^{43}	22 ± 2
Bin 2	41	1.44	0.20	28 ± 2	4.65×10^{45}	2.02×10^{44}	23 ± 2
Bin 3	39	1.49	0.33	31 ± 4	7.39×10^{45}	3.29×10^{44}	22 ± 3
Bin 4	43	1.50	0.32	32 ± 3	1.27×10^{46}	5.43×10^{44}	23 ± 3
E94[d]	29	—	—	—	1.33×10^{46}	7.10×10^{44}	19

[a] Median bolometric correction computed from the average of single values.
[b] σ = MAD/ $\sqrt{N}$ where MAD is the median of the absolute deviation between data and the median of data multiplied by 1.4826 and N is the number of sources.
[c] Bolometric and hard X–ray luminosities and bolometric corrections computed from the median SEDs.
[d] Bolometric and hard X–ray luminosities and bolometric correction computed from the median SEDs for radio-quiet AGN by Elvis et al. (1994).

while treating $L_{2500\ \text{Å}}$ as the dependent variable (i.e., OLS(X|Y)) and inverting the resulting best-fit, it follows that

$$\mathrm{Log}\, L_{2\ \mathrm{keV}} = (0.952 \pm 0.033)\mathrm{Log}\, L_{2500\ \text{Å}} - (2.138 \pm 0.975). \tag{3.2}$$

Accordingly, the bisector of the two regression lines is computed as described by Isobe et al. (1990), finding that

$$\mathrm{Log}\, L_{2\ \mathrm{keV}} = (0.760 \pm 0.022)\mathrm{Log}\, L_{2500\ \text{Å}} + (3.508 \pm 0.641) \tag{3.3}$$

with a dispersion of 0.37. The difference of the best-fit β with respect to a linear correlation (i.e., $\beta = 1$) is highly significant ($11\,\sigma$). This result confirms the non linear correlation between $L_{2\ \mathrm{keV}} - L_{2500\ \text{Å}}$. This implies not only that α_{ox} must be dependent on optical luminosity, but also that optically bright AGN emit less X-ray (per unit UV luminosity) than optically faint AGN. Comparing our results with those obtained from optically selected samples, we find that our slope is consistent within $2\,\sigma$ with those of S06 sample ($\beta_{S06} = 0.721 \pm 0.011$) and J07 sample ($\beta_{J07} = 0.709 \pm 0.010$), while it is significantly smaller than the slope of 1.117 ± 0.017 found by Green et al. (2009). Moreover, our slope is similar to the value found by Stalin et al. (2009) who used an X-ray selected sample composed by 267 broad-line AGN ($\beta = 0.870$). Treating separately the spectro-z and photo-z samples, we found that the best-fit slope for the bisector is 0.782 ± 0.033 with a normalization 2.815 ± 0.989 and 0.786 ± 0.033 with a normalization 2.824 ± 0.958, respectively. The spectro-z sample is limited to relatively bright 2500 Å luminosities, while the photo-z sample extends the luminosity range of about 1.5 dex towards lower $L_{2500\ \text{Å}}$ values. The percentual difference between the predicted $L_{2\ \mathrm{keV}}$ using the best-fit relation for the total sample and the best-fit for the spectro-z sample is $\sim 10\%$. Moreover, considering only the

Table 3.3: Correlations and their significance from Kendall-τ statistics (K-τ) and from Partial Kendall-τ.

Correlation	K-τ (σ)	Controlling variable	Partial K-τ (σ)
		Total	
$\alpha_{ox} - L_{2500\,Å}$	17	z	21
$\alpha_{ox} - L_{2\,keV}$	1.2	z	1.5
$\alpha_{ox} - z$	7	$L_{2500\,Å}$	< 0.1
		Spectro-z	
$\alpha_{ox} - L_{2500\,Å}$	12	z	14
$\alpha_{ox} - L_{2\,keV}$	0.2	z	2.3
$\alpha_{ox} - z$	5	$L_{2500\,Å}$	< 0.1
		Photo-z	
$\alpha_{ox} - L_{2500\,Å}$	10	z	12
$\alpha_{ox} - L_{2\,keV}$	0.2	z	3
$\alpha_{ox} - z$	5	$L_{2500\,Å}$	0.7

results from the spectro-z sample, we would slightly underestimate the dispersion in the bisector. These considerations justified the choice of adding the photo-z sample in order to reduce possible biases associated to the spectro-z sample. In Figure 3.8 monochromatic X-ray luminosities as a function of monochromatic UV luminosities are shown for the X-ray selected sample. For comparison, we plot the $L_{2\,keV} - L_{2500\,Å}$ relations from S06 and J07. In the bottom panel, we report residuals from Eq. (3.1), while on the right panel, residuals from Eq. (3.2) with the mean and the 1σ dispersion computed for each bin with $\Delta\mathrm{Log}\,L = 1$ are reported.

3.4.2 α_{ox} vs L_{2500}

Previous X-ray studies of AGN using optically selected samples (e.g.; Vignali et al. 2003, Strateva et al. 2005, S06, J07) revealed a highly significant correlation between α_{ox} and the 2500 Å monochromatic luminosity, with a slope of ~ 0.14. We apply EM regression to our X-ray selected Type-1 sample and confirm the $\alpha_{ox} - L_{2500\,Å}$ correlation at the $17\,\sigma$ significance level. The correlation becomes stronger when taking into account the effect of redshift using Kendall-τ partial-correlation analysis ($\sim 21\,\sigma$). The best-fit relation for $\alpha_{ox} - L_{2500\,Å}$, using OLS(Y|X) (i.e. treating $L_{2500\,Å}$ as the independent variable), is

$$\alpha_{ox}(L_{2500\,Å}) = (0.154 \pm 0.010)\mathrm{Log}\,L_{2500\,Å} - (3.176 \pm 0.223), \tag{3.4}$$

with a dispersion of 0.18. For the spectro-z sample, we found a slope of 0.166 ± 0.011 with a normalization of -3.541 ± 0.335, while for the photo-z sample the best-fit slope is 0.142 ± 0.012 with a normalization -2.831 ± 0.345. In Figure 3.9 we plot α_{ox} versus $L_{2500\,Å}$ for our sample. For comparison, we plot the best-fit linear regression found in S06 (*short-dashed line*) and J07 (*long-dashed line*). Our slope is statistically consistent within $\sim 1.5\sigma$ with the slopes of the S06 and J07 best-fits. Moreover, our slope is consistent, within 1.6σ and 1σ, with those published

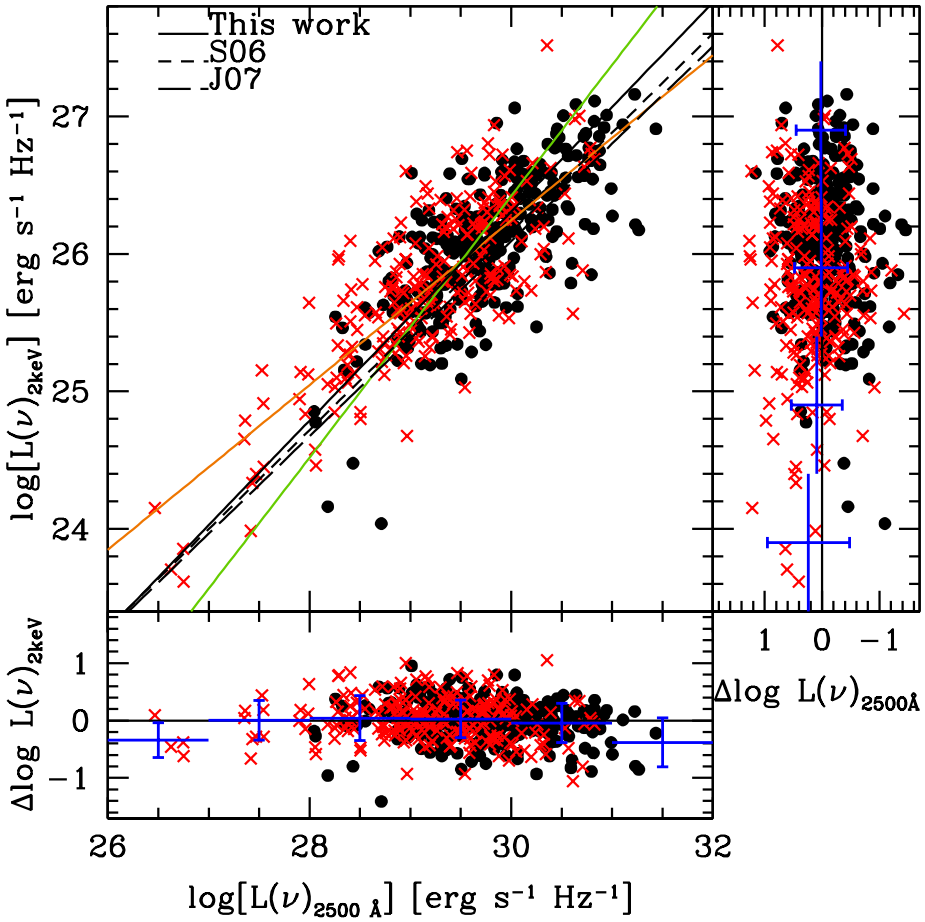

Figure 3.8: Values of the rest-frame monochromatic luminosity $L_{2\,\mathrm{keV}}$ plotted versus the rest-frame $L_{2500\,\text{Å}}$ monochromatic luminosity for our X-ray selected sample: 322 spectroscopic sources (*circles*) and 223 sources with photometric redshift (*crosses*). The solid black line shows the best-fit relation that we found using the OLS bisector algorithm (see Eq. [3.3]). For comparison, the best-fit derived by S06 (*short-dashed line*) and the best-fit from J07 (*long-dashed line*) are also shown. The orange and the green line represent equations (3.1) and (3.2), respectively. The lower panel and the panel on the right show the residuals of log $L_{2\,\mathrm{keV}}$ and log $L_{2500\,\text{Å}}$ with respect to the best-fit lines given by Eq. [3.1] and [3.2]), respectively. The error bars represent the mean and the 1σ dispersion of the residuals for each $\Delta\mathrm{Log}\,(L_{2500\,\text{Å}}) = 1$ bin.

recently by Kelly et al. (2008) (0.12 ± 0.02) and Young et al. (2009) (0.153 ± 0.012), respectively. Differently, Green et al. (2009) and Stalin et al. (2009) found a flatter slope of 0.061 ± 0.009 and 0.065 ± 0.019, respectively. The residual $\Delta\alpha_{\mathrm{ox}}$, defined as

$$\Delta\alpha_{\mathrm{ox}} = \alpha_{\mathrm{ox}} - \alpha_{\mathrm{ox}}(L_{2500\,\text{Å}}), \tag{3.5}$$

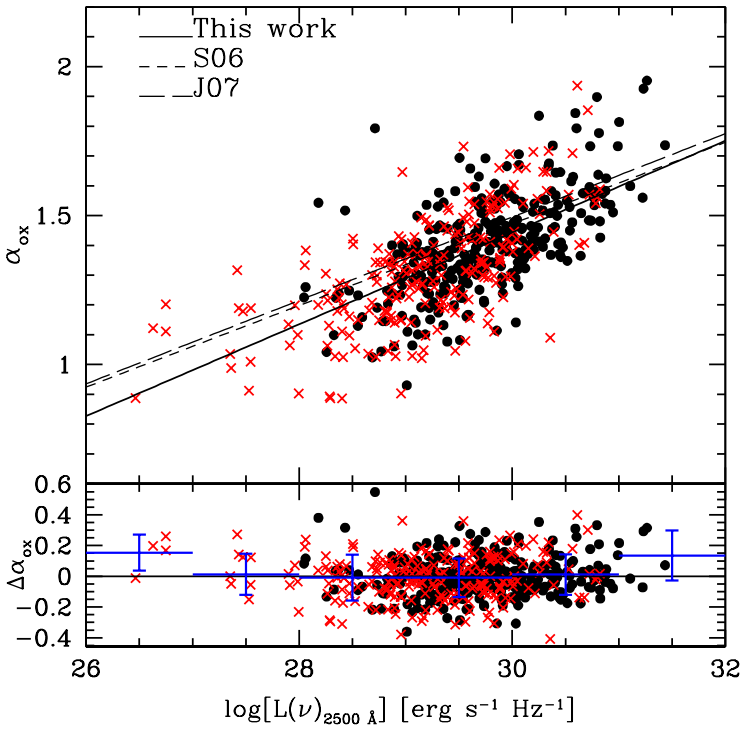

Figure 3.9: Plot of the α_{ox} vs. the rest-frame monochromatic luminosity $L_{2500\ Å}$ for our X-ray selected sample: 322 spectroscopic sources (*circles*) and 223 sources with photometric redshift (*crosses*). The solid line represents our best-fit given by Eq. (3.4). For comparison, the best-fit derived by S06 (*short-dashed line*) and from J07 (*long-dashed line*) are shown. The lower panel shows the residuals ($\Delta\alpha_{ox}$) of our best-fit relation. The error bars represent the mean and the 1σ standard deviation of the mean of the residuals for each ΔLog ($L_{2500\ Å}$) = 1 bin.

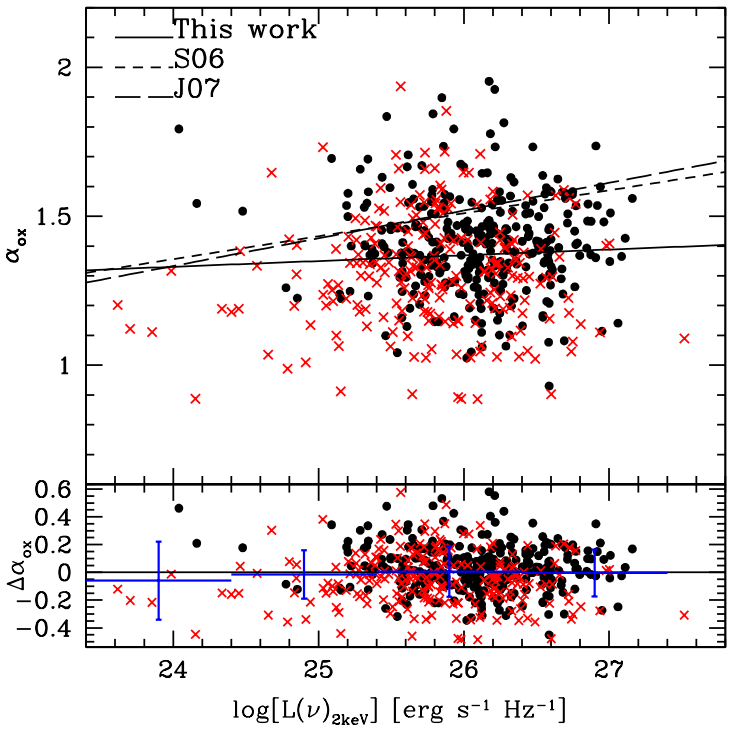

Figure 3.10: Plot of α_{ox} vs. the rest-frame monochromatic luminosity $L_{2\ keV}$ for our X-ray selected sample: 322 spectroscopic sources (*circles*) and 223 sources with photometric redshift (*crosses*). The solid line represents our best-fit given by Eq. (3.6). For comparison, the best-fit derived by S06 (*short-dashed line*) and from J07 (*long-dashed line*) are also shown. The lower panel shows residuals ($\Delta\alpha_{ox}$) from our best-fit relation, while error bars represent the mean and the 1σ dispersion of the residuals for each Δ[Log $L_{2\ keV}$] = 1 bin.

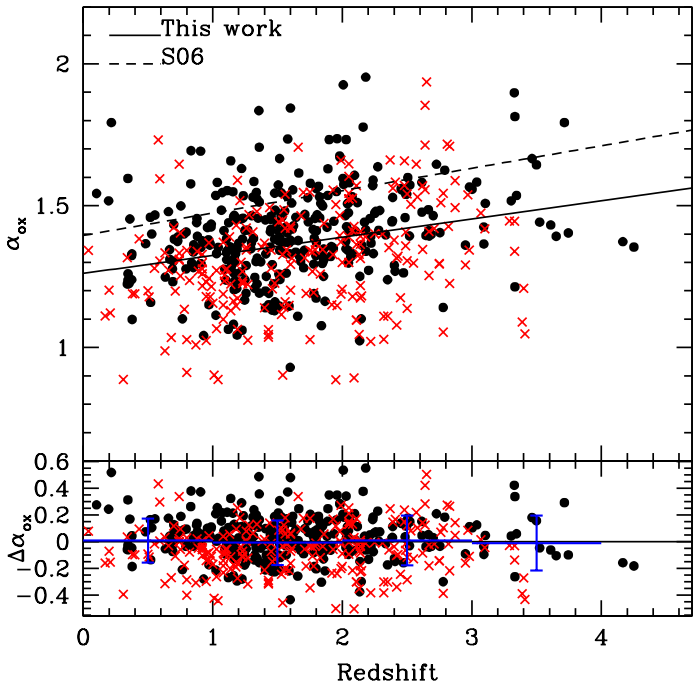

Figure 3.11: Plot of α_{ox} vs. redshift for our X-ray selected sample: 322 spectroscopic sources (*circles*) and 223 sources with photometric redshift (*crosses*). The solid line represents our best-fit given by Eq. (3.7). For comparison, also the best-fit derived by S06 (*short-dashed line*) is shown. The lower panel shows residuals ($\Delta\alpha_{ox}$) from our best-fit relation, while error bars represent the mean and the 1σ dispersion of the residuals for each $\Delta z = 1$ bin.

where α_{ox} values are measured from the observations, are shown in the bottom panel of Fig. 3.9. The bars represent the mean and the $1\,\sigma$ dispersion for $\Delta\mathrm{Log}\,(L_{2500\,\text{Å}}) = 1$ bins.

3.4.3 α_{ox} vs $L_{2\,\mathrm{keV}}$ and vs redshift

We find no significant correlation between α_{ox} and $L_{2\,\mathrm{keV}}$ (e.g.; Kriss & Canizares 1985; Avni & Tananbaum 1986; Wilkes et al. 1994 and Yuan et al. 1998). For comparison with S06 and J07, the EM regression method is performed and the best-fit parameters for the $\alpha_{ox} - L_{2\,\mathrm{keV}}$ relation (i.e. treating $L_{2\,\mathrm{keV}}$ as the independent variable) are

$$\alpha_{ox}(L_{2\,\mathrm{keV}}) = (0.019 \pm 0.013)\mathrm{Log}\,L_{2\,\mathrm{keV}} + (0.863 \pm 0.344). \tag{3.6}$$

For the spectro-z sample the slope is 0.012 ± 0.020, while for the photo-z sample it is -0.020 ± 0.019. Analyzing in the same way the $\alpha_{ox} - z$ relation (i.e. treating z as the independent variable), we find

$$\alpha_{ox}(z) = (0.064 \pm 0.010)\,z + (1.261 \pm 0.018). \tag{3.7}$$

The significance of the correlation between α_{ox} and redshift is $7\,\sigma$. This may suggest a not negligible evolution of α_{ox} with redshift, but if we account for the effect of the optical luminosity using partial Kendall-τ statistics, the significance of the correlation disappears ($< 0.1\,\sigma$). In Figure 3.10 and 3.11 α_{ox} as a function of $L_{2\,\mathrm{keV}}$ and redshift are shown, respectively, where the solid line represents the best-fit relation (Eqs. [3.6] and [3.7]). In the bottom panel of each plot the residuals and the 1σ dispersion in bins of $\Delta z = \Delta\mathrm{Log}\,L_{2\,\mathrm{keV}} = 1$ are shown. The absence of a correlation between α_{ox} and $L_{2\,\mathrm{keV}}$ is consistent with the fact that the correlation between $L_{2500\,\text{Å}}$

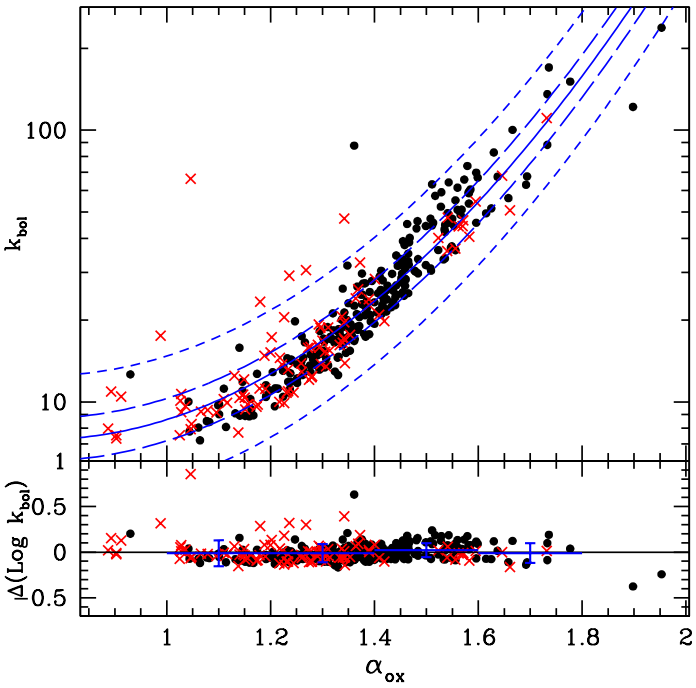

Figure 3.12: Plot of the hard X-ray bolometric corrections against α_{ox} for the 343 Type-1 AGN with detection in both soft and hard bands. The blue solid line represents the best-fit relation from Eq. (3.8), while the long and the short dashed lines represent the 1σ and the 3σ dispersion in the distribution of bolometric correction, respectively. The bottom panel shows residuals (Δ[Log $k_{bol,\,1\mu m}$]) from the best-fit relation, while error bars represent the mean and the 1σ dispersion of the residuals for each Δ(Log $k_{bol,\,1\mu m}$) = 0.2 bin.

and $L_{2\,\mathrm{keV}}$, treating $L_{2\,\mathrm{keV}}$ as the independent variable (Eq. [3.2]), is very close to be linear (i.e., $\beta \sim 1$). From the partial correlation analysis it is apparent that there is no correlation between α_{ox} and redshift, once the effect of optical luminosity is properly removed. The energy mechanisms that generate the broad-band emission in AGN do not vary, in an appreciable way, over cosmic time. This is in agreement with most of previous works (but see Yuan et al. (1998) and Bechtold et al. (2003) who claimed that the primary correlation comes out upon redshift). The difference in the normalization between our $\alpha_{ox} - z$ best-fit relation and S06 best-fit relation is probably due to the different optical luminosity range spanned by our data and S06 data. The average optical luminosity of the S06 sample is more than 1 decade higher than ours. Because of the correlation between α_{ox} and $L_{2500\,\text{Å}}$, this implies a stepeer α_{ox} at any given redshift. For the spectro-z sample we found that the slope is 0.058 ± 0.012, while for the photo-z sample it is 0.079 ± 0.016.

3.4.4 Relations between α_{ox}, bolometric corrections and Eddington ratios

In Figure 3.12 α_{ox} vs. k_{bol} are plotted. In order to better estimate the bolometric correction values, a subsample of 343 AGN with detections in both soft and hard bands has been selected. The best-fit relation is computed using a second-degree polynomial:

$$\mathrm{Log}\, k_{bol} = 1.561 - 1.853\alpha_{ox} + 1.226\alpha_{ox}^2. \tag{3.8}$$

The 1σ (~ 0.078) and the 3σ (~ 0.234) dispersion in the Log $k_{bol} - \alpha_{ox}$ relation is quantified using a 3.5σ clipping method. A linear correlation is not a good description of the observed

data points. The addition of a quadratic term significantly improves the fit quality ($\Delta\chi^2 \sim 140$, significant at $\gtrsim 8\sigma$ confidence level according to an F-test). A visual inspection of the individual SED of the sources which mostly deviate from a linear fit (i.e. those with $\alpha_{ox} \leqslant 1.2$) indicate that their SEDs are not significantly different from those of the rest of the sample. Also note that the dispersion around the best-fit is very small. For 150 Type-1 AGN in our sample in the redshift range $0.196 \leq z \leq 4.251$, an estimate of the BH mass is available from virial estimators (Peterson et al. 2004) using the Mg II line width (63 sources from Merloni et al. 2010; 63 sources from Trump et al. 2009); the Hβ line width (16 sources from Trump et al. 2009) and the C IV line width (8 sources from Trump et al. 2009).

The bolometric luminosity which enters in the calculation of the Eddington ratio, λ_{Edd}, is computed by integrating the individual SEDs from $1\mu m$ to 200 keV (see Sect. 2.5.1). By neglecting the IR bump we avoid counting twice the UV emission reprocessed by dust. The hard X-ray bolometric correction, k_{bol}, is computed as the ratio between $L_{bol,1\mu m}$ and the X-ray luminosity, $L_{[2-10]keV}$.

A remarkably good correlation is found between k_{bol} and the Eddington ratio. Since the choice of the independent or dependent variable is not straightforward, here the OLS bisector is computed for the $k_{bol} - \lambda_{Edd}$ relation as already done for the $L_{2500\ \text{Å}} - L_{2\ keV}$ relation. We found that the best-fit parameters for the $k_{bol} - \lambda_{Edd}$ relation using OLS(Y|X) (i.e. treating λ_{Edd} as the independent variable) are

$$\text{Log}\ k_{bol}(\lambda_{Edd}) = (0.273 \pm 0.045)\text{Log}\ \lambda_{Edd} + (1.656 \pm 0.056), \tag{3.9}$$

while the relation using OLS(X|Y) is

$$\text{Log}\ k_{bol}(\lambda_{Edd}) = (1.200 \pm 0.170)\text{Log}\ \lambda_{Edd} + (2.600 \pm 0.180). \tag{3.10}$$

Then, the bisector of the two regression lines is computed finding that

$$\text{Log}\ k_{bol}(\lambda_{Edd}) = (0.643 \pm 0.043)\text{Log}\ \lambda_{Edd} + (2.032 \pm 0.053). \tag{3.11}$$

The absence of a correlation is excluded at the 15σ level.

Figure 3.13 shows k_{bol} as a function of λ_{Edd} for our sub-sample of Type-1 AGN and for the sample of local Seyferts by VF09, where radio-loud objects and low X-ray flux observations are removed. Points with error bars are obtained averaging the values of bolometric correction in each bin of λ_{Edd}, and standard errors at 1σ are plotted for comparison (see Section 4.3 of VF09 for details). The VF09 sample contains AGN with simultaneous optical, UV and X-ray data retrieved from the XMM-*Newton* EPIC-pn and Optical Monitor (OM) archives, while the virial M_{BH} is estimated using the reverberation mapping method (Peterson et al. 2004). It is worth noting that, although the methods to construct the SEDs and measure M_{BH} are completely different from those adopted by VF09, the trend of increasing bolometric correction with Eddington ratio is confirmed, with mean $\langle k_{bol}\rangle \sim 22$ for $\lambda_{Edd} \leq 0.1$, $\langle k_{bol}\rangle \sim 27$ for $0.1 < \lambda_{Edd} \leq 0.2$ and $\langle k_{bol}\rangle \sim 53$ for $\lambda_{Edd} > 0.2$.

Equation (3.9) is in agreement, within the errors, with the VF09 results, which are shown in Figure 3.13. The Eq. (3.9), represented by the orange dashed line, and red bins are directly comparable, because of the treatment of the independent variable.

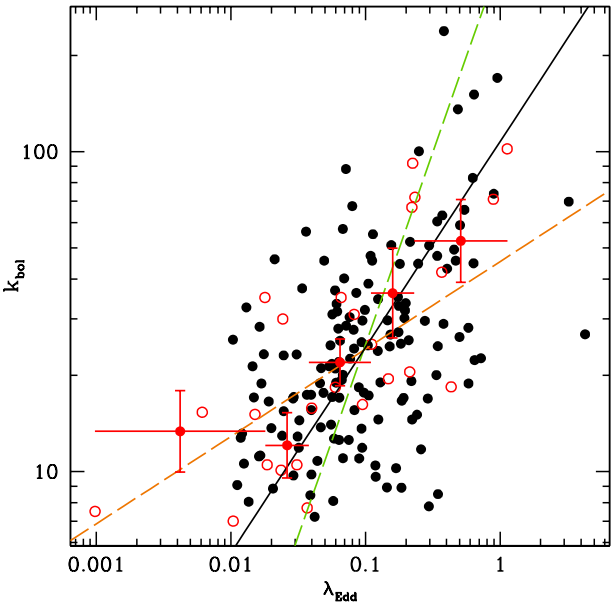

Figure 3.13: Hard X-ray bolometric correction versus Eddington ratio for the 150 Type-1 AGN with BH mass estimate. The solid black line shows the best-fit relation that we found using the OLS bisector algorithm (see Eq. [3.11]), while the orange and the green dashed lines represent equations (3.9) and (3.10), respectively. Red open circles represent the sample by VF09 (25 sources, see their Fig. 6 for details) and the corresponding bins with error bars.

Differently from VF09, a correlation is found also between α_{ox} and the Eddington ratio. In the same interval of λ_{Edd} we have a larger number of sources, hence the presence of the correlation could be simply due to the better statistic, although the dispersion is rather large. In Fig. 3.14 α_{ox} against λ_{Edd} is presented, where the best-fit relation using OLS(Y|X) is

$$\alpha_{ox}(\lambda_{Edd}) = (0.133 \pm 0.023)\mathrm{Log}\ \lambda_{Edd} + (1.529 \pm 0.028), \tag{3.12}$$

while the best-fit relation using OLS(X|Y) is

$$\alpha_{ox}(\lambda_{Edd}) = (0.719 \pm 0.127)\mathrm{Log}\ \lambda_{Edd} + (2.124 \pm 0.132). \tag{3.13}$$

Finally, the bisector of the two regression lines is

$$\alpha_{ox}(\lambda_{Edd}) = (0.397 \pm 0.043)\mathrm{Log}\ \lambda_{Edd} + (1.797 \pm 0.047). \tag{3.14}$$

The absence of a correlation is excluded at $\sim 9\sigma$ level.

3.5 Effects of reddening and host-galaxy light

As mentioned in Sect. 3.2 and discussed at length in Elvis et al. (2011, in prep.), the objects used in this analysis show a large variety of SEDs. In addition to objects with a "typical" Type-1 AGN SED (see Fig. 3.4), there is also a not negligible number of objects which show a red optical-UV SED (see Fig. 3.5). While some of them may be intrinsically red AGN, it is likely that for most of them this red optical-UV SED is due either to intrinsic absorption or to a significant contribution of emission from the host-galaxy, or both (see Richards et al. 2003, hereafter R03). In the analysis presented in the previous Sections, the "observed" $L_{2500\ \text{Å}}$ is used.

If intrinsic absorption or contribution from the host-galaxy are not negligible, the used $L_{2500\,\text{Å}}$ would be biased. In particular, the intrinsic $L_{2500\,\text{Å}}$ would be higher in presence of reddening, while it would be smaller in presence of a significant contribution from the host-galaxy. In the following we try to estimate the size of the effect of extinction and/or host-galaxy contribution to the relations between $L_{2500\,\text{Å}} - L_{2\,\text{keV}}$ and $\alpha_{\text{ox}} - L_{2500\,\text{Å}}$ discussed in Section 3.4.1 and 3.4.2.

3.5.1 Intrinsic Extinction

Following the procedure described in R03, the underlying continuum color is estimated by subtracting the median colors of AGN in redshift bins of $\Delta z = 0.2$ from the observed color of each source in that bin. We refer to $\Delta(g^+ - i^*) = (g^+ - i^*) - \langle g^+ - i^* \rangle$ as the *relative color* (see Richards et al. 2001), where the average $\langle g^+ - i^* \rangle$ is computed in each redshift bin. All sources have been detected in the Subaru g^+ band, only 8 sources do not have i^* CFHT magnitude. For these AGN the detection in the i^+ Subaru band is considered. In Figure 3.15 the redshift of the sources as a function of their relative color are plotted (see Fig. 6 in R03). The $\Delta(g^+ - i^*)$ distribution shows a large scatter with respect to the SDSS sample in R03. Given the quality of the COSMOS photometric data, this is not due to photometric errors, but likely to the different selection criteria: SDSS quasar candidates are selected using optical color-color selection, so the scatter in $\Delta(g^+ - i^*)$ is smaller than in our X-ray selected sample. However, the same plot can be still used in order to identify possibly reddened sources. Under the assumption that all Type-1 AGN have the same continuum shape, the dashed lines show the expected change in relative color as a function of redshift for an SMC reddening law (Prevot et al. 1984) with E(B-V) = 0.04, 0.12 and 0.20 moving from left to right in the $\Delta(g^+ - i^*)$ axis. Following R03, dust-reddened Type-1 AGN are defined as all the sources that lie to the right of the dashed line at E(B-V)=0.12. Using this

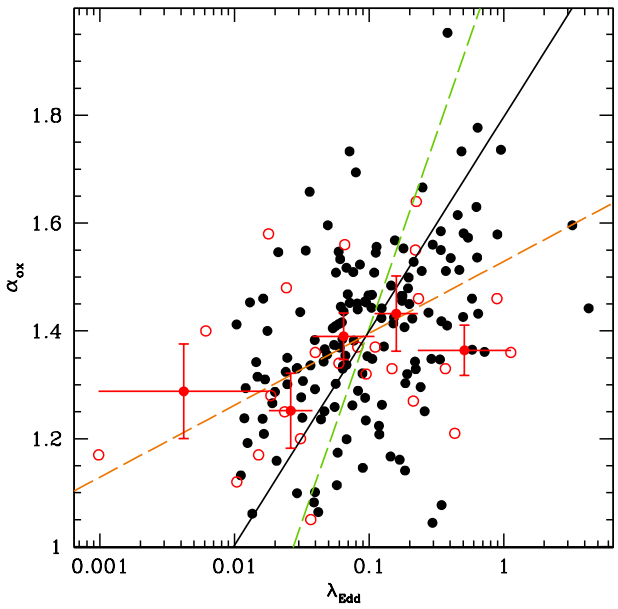

Figure 3.14: Plot of α_{ox} as a function of Eddington ratio for the 150 Type-1 AGN and the corresponding bins with error bars. Key as in Figure 3.13. The solid black line shows the best-fit relation that we found using the OLS bisector algorithm (see Eq. [3.14]), while the orange and the green dashed lines represent equations (3.12) and (3.13), respectively.

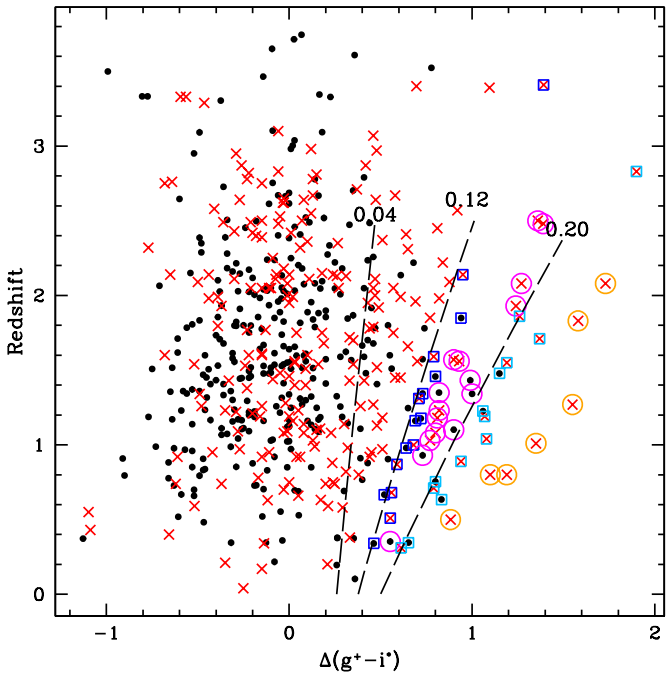

Figure 3.15: Distribution of redshifts versus the relative $\Delta(g^+ - i^*)$ color for the sample with $z < 4$. The dashed lines represent, from left to right, the expected loci for E(B-V)=0.04, 0.12, 0.20, respectively. Open circles and squares mark *reddened* AGN: blue corresponds to E(B-V)~0.12 (16 AGN), magenta to E(B-V)~0.16 (16 AGN), cyan to E(B-V)~0.20 (14 AGN) and yellow to E(B-V)~0.24 (7 AGN).

definition, about 10% of the total sample is affected by intrinsic absorption. For about 80% of the sample, reddening is negligible, with E(B-V) less than 0.04. The 53 reddened Type-1 AGN have been divided in 4 subsamples which correspond to an average E(B-V) value of about 0.12, 0.16, 0.20 and 0.24 (see caption in Fig. 3.15). Monochromatic luminosities at 2500 Å of these objects were corrected using the SMC reddening law and the corresponding average value of E(B-V) in each bin. Figure 3.16 shows the distribution of the optical luminosities before and after dereddening. The $L_{2500\ \text{Å}}$ distribution of the reddened AGN is significantly different (i.e. lower luminosity) from that of the total sample. This would suggest that extinction is more important for lower luminosity AGN (see Gaskell et al. 2004). The average shift induced by the correction for the intrinsic extinction in the 10% of the total sample is $\langle \Delta\text{Log}\ L_{2500\ \text{Å}} \rangle = 0.28 \pm 0.07$.

X-ray absorption is generally negligible in Type-1 AGN; however, it is known that a fraction of the order of 10% of broad-line AGN may be obscured by column densities up to 10^{22} cm^{-2} (see Brusa et al. 2003; Mainieri et al. 2007b). Unabsorbed X-ray fluxes can be computed if the absorption column density (N_H) is known, which is not the case for most of the sources in our sample. Hardness ratios may be used instead, but they are almost insensitive to column densities of the order of 10^{22}cm^{-2} or slightly higher at the average redshifts of the XMM-COSMOS sources, and they tend to over-estimate N_H (e.g. Perola et al. 2004). In order to quantify the average impact of X-ray absorption on the $\alpha_{\rm ox}$ distribution and bolometric corrections, 10% of the sources in our sample are assumed to be obscured by a column density of 10^{22} cm^{-2}. Note that this assumption is likely to overestimate X-ray absorption in Type-1 AGN (see Fig. 13 in Mainieri et al. 2007b). By correcting X-ray monocromatic fluxes at 2 keV for randomly chosen 10% of the sources, the unobscured X-ray fluxes are 10% higher. The shift induced by this

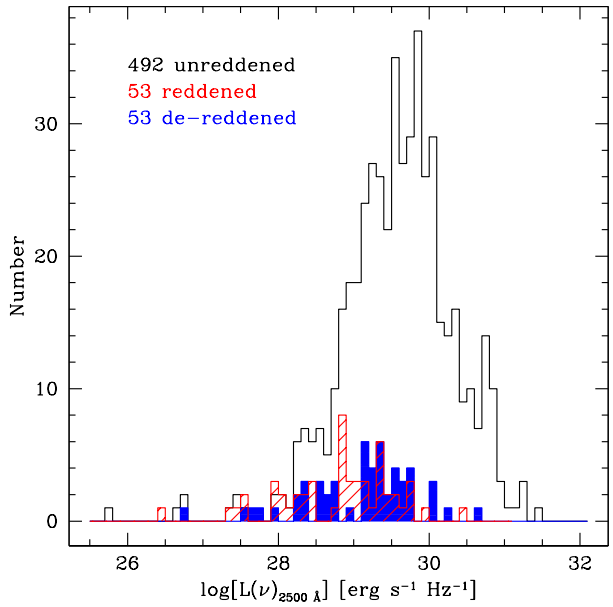

Figure 3.16: Distribution of $L_{2500\,\text{Å}}$ for the unreddened sample (*open histogram*) and for the 53 sources with E(B-V)≥ 0.12, before (*red hatched histogram*) and after reddening correction (*blue filled histogram*).

correction in the 10% of the total sample is $\langle \Delta\text{Log}\, L_{2\,\text{keV}} \rangle = 0.04$.

Broad absorption-line quasars (BAL QSOs) are known to be X-ray obscured (e.g., Green et al. 1995, Gallagher et al. 1999, Brandt et al. 2000), and are not included in previous studies of optically selected samples because they can cause an artificial steepening of the $\alpha_{\text{ox}} - L_{2500\,\text{Å}}$ and $L_{2500\,\text{Å}} - L_{2\,\text{keV}}$ correlations. Due to the lack of a systematic analysis of the optical spectra of broad-line AGN in the zCOSMOS and IMACS spectroscopic surveys and the inclusion of photometric Type-1 AGN, an estimate of the BAL fraction in our sample is not available. Assuming they constitute about 10–15% of the entire quasar population (e.g. R03, Hewett & Foltz 2003), BAL QSO may be numerous among red sources in Fig.3.16 and/or X-ray obscured AGN. Therefore, we expect that the effects of dust reddening and X-ray absorption considered and quantified in the previous paragraphs take into account, at least in a statistical sense, the BAL QSO contamination. Moreover, the considered fraction of BAL QSOs comes from optically selected samples, so that the same fraction should be smaller (and possibly redshift dependent) for soft X-ray selected samples.

Applying these corrections for absorption in the optical and in the X-ray, we find that the slopes of the $L_{2500\,\text{Å}} - L_{2\,\text{keV}}$ and $\alpha_{\text{ox}} - L_{2500\,\text{Å}}$ relations become $\beta_{corr} = 0.782 \pm 0.021$ (OLS bisector algorithm) and 0.147 ± 0.008. Both these "corrected" slopes are within one sigma from those derived with no correction for absorption (see Eq. [3.3] and Eq. [3.4]). The slight steepening of the $L_{2500\,\text{Å}} - L_{2\,\text{keV}}$ relation is due to the fact that the fraction of optically extincted AGN is higher at lower optical luminosity (see Fig. 3.16). The corrections for absorption increase the mean value of α_{ox} by only 0.01. We therefore conclude that the absorption corrections do not change significantly our main results.

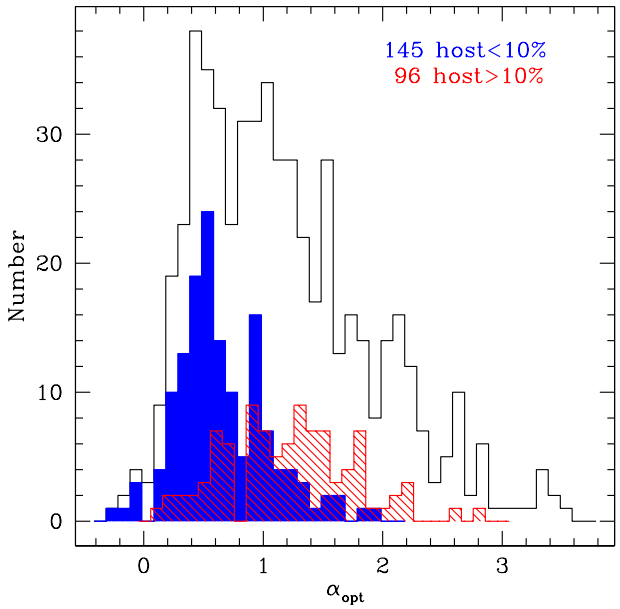

Figure 3.17: Distribution of the optical index for the total sample (*open histogram*), for the 145 AGN which have a host-galaxy contribution less than 10% (*filled histogram*) and for the 96 AGN which have a host-galaxy contribution greater than 10% (*hatched histogram*).

3.5.2 Host-Galaxy Contamination

In order to estimate the possible effect of the contribution of the host-galaxy stellar light to the 2500 Å luminosity, we have considered a subsample of 241 sources for which we have a host-galaxy contribution computed subtracting a point-spread-function scaled to a central 4 pixel aperture, and measuring the extended flux in ACS F814W (Jahnke et al. 2004, Jahnke et al. 2009): 145 sources have an extended host-galaxy contribution of less than 10%, while for 96 AGN the contamination of the host-galaxy light is greater than 10%. This is a robust, model independent measure to determine whether substantial extended flux is present or not. A useful parameter that we can compute for the total sample is the optical spectral index, $\alpha_{\rm opt}$. By linking it with the morphological information we can try to quantify the host-galaxy contribution for each AGN.

Following Vanden Berk et al. (2001), we compute the optical spectral index using the monochromatic luminosities at 2000Å and 5000Å

$$\alpha_{\rm opt} = -2.5\,{\rm Log}\,\frac{L_{2000\text{Å}}}{L_{5000\text{Å}}}. \tag{3.15}$$

Figure 3.17 shows the distribution of $\alpha_{\rm opt}$ for the total sample, for the 145 sources for which the stellar light contribution to the total flux is less than $\sim$ 10% and for the 96 sources for which this contribution is greater than 10%. These two samples have significantly different distributions of $\alpha_{\rm opt}$. Unresolved quasars have an average $\alpha_{\rm opt}$ of $\sim$ 0.5, which is consistent with previous results from the SDSS samples, while the sample with a significant galaxy contribution has a range of $\alpha_{\rm opt}$ from 0 to $\sim$ 3 (typical of a spiral Sc template) with an average of $\sim$ 1.2.

We then tried to estimate the fraction of galaxy light at 2500 Å assuming a typical slope $\alpha_{\rm opt} = 0.5$ for the nucleus component and $\alpha_{\rm opt} = 3$ for the galaxies. We further assume that the monochro-

matic luminosity in the range 2000 − 5000Å is due to the contribution of two power laws:

$$L_\nu = A\nu^{-0.5} + G\nu^{-3}, \tag{3.16}$$

where A and G are the normalization constants we want to estimate. With this assumption the observed $\alpha_{\rm opt}$ is a function only of the ratio between A and G, therefore, at any given $\alpha_{\rm opt}$ value, the expected relative contribution of the nuclear and host-galaxy emission can be computed. We divided the total sample in 5 bins of $\alpha_{\rm opt}$, with $\Delta\alpha_{\rm opt} \sim 0.5$, and corrected the observed $L_{2500\ \text{Å}}$ using an average value of A/G in each bin. The shift in the monochromatic luminosities at 2500 Å induced using this correction is $\langle \Delta\text{Log}\ L_{2500\ \text{Å}} \rangle = -0.15 \pm 0.01$, with a dispersion of 0.21. Applying this correction, we find that the slopes of the $L_{2500\ \text{Å}} - L_{2\ \text{keV}}$ and $\alpha_{\rm ox} - L_{2500\ \text{Å}}$ become 0.660 ± 0.022 (OLS bisector algorithm) and 0.197 ± 0.011, respectively. Both these slopes corrected for the possible host-galaxy contribution are different at about 3σ from those derived with no correction (see Eq. [3.3] and [3.4]). In this case, the flattening of the $L_{2500\ \text{Å}} - L_{2\ \text{keV}}$ relation is due to the fact that $\alpha_{\rm opt}$ tends to be steeper (i.e. with a possibly higher contribution from the host-galaxy) for lower luminosity AGN. This correction decreases the mean value of $\alpha_{\rm ox}$ by ~ 0.06.

At face value, the possible effects of host-galaxy contribution estimated above are not negligible. However, we stress that these estimates have to be taken as upper limits, for at least two reasons. First, in our derivation of the constants A and G we have assumed that all AGN have the same intrinsic $\alpha_{\rm opt}$; in presence of a dispersion of $\alpha_{\rm opt}$ distribution of AGN, the contribution from the host-galaxy would be smaller than that we have derived. Secondly, the same would happen also if, as it is likely to be the case, both effects (extinction and host-galaxy contribution) are at work at the same time.

3.6 Discussion

3.6.1 Sample biases and systematics

We used the COSMOS multi-wavelength database to build a large X-ray selected sample of Type-1 AGN and study their optical to X-ray properties. The sample size is comparable to that of optically selected samples previously reported in the literature (e.g., Gibson et al. 2008), but to our knowledge this is the largest complete X-ray selected sample for which the study of the $\alpha_{\rm ox}$ distribution is performed. In order to keep the selection criteria as clean as possible and to cope with the lack of spectroscopic information at faint optical magnitudes, the Type-1 classification is based on both spectroscopic and photometric redshifts. This choice guarantees a well defined and relatively simple selection function, but it is not completely free from other biases. In particular, contamination from photometrically misclassified Type-1 AGN cannot be excluded (see Section 3.1.1). Other possible biases and systematics include the contribution of the effect of dust reddening and gas absorption at UV and X-ray frequencies and the host-galaxy light to the 2500 Å nuclear flux. Even though we tried to estimate and quantify the impact of the above mentioned biases (see Section 3.5.1 and 3.5.2), some residual contamination due to either one or more of these biases cannot be completely excluded. However, we are confident that the

most important results of our analysis, and especially those concerning the average properties of the total sample, are not significantly affected.
The correlations between optical and X-ray luminosities obtained from the analysis of the spectroscopic sample are recovered, if only photo-z are considered. Even though the best fit parameters of the correlations are slightly different, the inclusion of photo-z sources allows us to extend the study of optical and X-ray properties to much lower luminosities.

3.6.2 Constraints on the X-ray emission models

The optical to X-ray spectral index $\alpha_{\rm ox}$ connects the two portions of the AGN broad-band spectrum dominated by the accretion power and thus it is expected to be a reliable tracer of the accretion properties and, in particular, of the relation between disk emission, peaking in the UV, and coronal X-ray emission. Previous studies have shown a non linear dependence of the X-ray versus UV luminosity, which implies a correlation between the optical–UV to X-ray luminosity ratio on monochromatic luminosity and/or redshift. Based on extensive analysis of large samples of optically selected AGN (i.e. Vignali et al. 2003, Strateva et al. 2005, S06, J07) it is concluded that $\alpha_{\rm ox}$ is primarily dependent on optical luminosity at 2500 Å. The results presented in this study confirm and extend the previous findings to a large sample of X-ray selected AGN, suggesting that band selection does not significantly modify the current observational picture. The observed $L_{2500\,\text{Å}} - L_{2\,\rm keV}$ (or $\alpha_{\rm ox} - L_{2500\,\text{Å}}$) correlation implies that more optical luminous AGN emit less X-rays per unit UV luminosity than less luminous AGN. The predicted UV to X-ray luminosity ratio depends on the hot corona covering factor, optical depth and electron temperatures. The optical–UV and X-ray emission of radio-quiet AGN can be explained by the interplay between hot electrons in a coronal gas and a colder accretion flow. Soft photons from the accretion disk are Comptonized by hot electrons and lead to the formation of a power law spectrum in the hard X-rays accompanied by a high energy cut-off at the electrons' temperature (Haardt & Maraschi 1991, 1993). If only a fraction of the accretion power is released in the hot phase, as in the patchy corona model (Haardt et al. 1994), the $L_{\rm UV}/L_{\rm X}$ ratio is higher than the value computed using a model with more uniform corona. The observed correlation suggests that disk-corona parameters are depending on UV luminosity.

3.6.3 Using $\alpha_{\rm ox}$ as a bolometric correction estimator

An accurate determination of bolometric quantities is essential to compute AGN accretion rates and, more in general, for all the arguments related to the accretion onto SMBH at large. These parameters require to sample the AGN SED over a broad range of wavelengths from near-infrared to hard X-rays. Owing to the excellent quality of the multi-wavelength COSMOS database, this is becoming possible for large AGN samples. Because the optical–UV to X-ray portion of the spectrum contains about 60% of the total bolometric luminosity, we have investigated to what extent the UV to X-ray luminosity ratio can be considered a reliable proxy of the bolometric correction.
We computed bolometric corrections from the 2–10 keV energy range for all the objects in our sample with detection in both soft and hard bands. Given the strong luminosity dependence

of α_{ox} upon UV luminosity which is close to the SED maximum, it is not surprising to find a significant correlation between α_{ox} and k_{bol}. However, it is important to note that the correlation, best-fitted by a second order polynomial, has a small dispersion around the best-fit (see Fig. 3.12). The existence of such a tight relation between these two parameters suggests that the AGN bolometric output is well traced by α_{ox} over a broad range of redshifts and luminosities. Moreover, it offers the opportunity to estimate reliable bolometric corrections, for large AGN samples, provided that rest-frame 2500Å and 2 keV luminosities are known.

3.6.4 Bolometric corrections and Eddington ratios

Accretion rates are then estimated using the previously computed bolometric corrections. A correlation is found between the 2–10 keV bolometric correction and the Eddington ratio for a sizable subsample of 150 objects (see Fig. 3.13), for which black hole masses are computed from the broad emission lines FWHM (see Merloni et al. 2009, Trump et al. 2009 for a detailed discussion). The presence of this correlation was originally suggested by Vasudevan & Fabian (2007) using broad-band observations of nearby Seyfert galaxies and confirmed in a subsequent paper (VF09) using simultaneous optical-UV and X-ray data. A similar trend is reported by Bianchi et al. (2009) from a multi-wavelength analysis of archival XMM-*Newton* observations. Although we do not have simultaneous data or M_{BH} estimate from reverberation mapping, our findings are consistent with the $k_{bol} - \lambda_{Edd}$ relation by VF09. This correlation may, in principle, be induced by the fact that both parameters depend on the bolometric luminosity. However, if we look for the effect of the bolometric luminosity using the Kendall-τ partial correlation analysis, we found that the correlation is still significant. This suggests that the systematic effects introduced by the presence of bolometric luminosity on both axes are not relevant (see also Section 5.1.4 in VF07).
A fairly significant correlation, albeit with a large scatter, is also found between α_{ox} and the Eddington ratio. In the framework of the disk-corona models discussed above, sources with steep α_{ox} are explained by a patchy corona where the number of blobs or their covering factor decreases for increasing values of α_{ox}. For a given BH mass, bright UV emission is due to a high accretion rate. If in highly accreting sources most of the power is dissipated in the disk, rather than in the hot corona, then a correlation between α_{ox} and Eddington ratio is expected.

3.7 Summary and conclusions

In this first part of our study we have presented the analysis of the UV to X-ray properties of 545 radio-quiet X-ray selected Type-1 AGN, in the multi-wavelength COSMOS survey. The full data-set covers a large range of redshifts ($0.04 < z < 4.25$) and X-ray luminosities ($40.6 \leq \mathrm{Log}\, L_{[2-10]\mathrm{keV}} \leq 45.3$). It is mostly composed by spectroscopically selected Type-1 AGN (322 sources, $\sim$ 60% of the total sample), with the addition of 223 Type-1 AGN classified on the basis of the best-fitting SED procedure provided by S09. We constructed single SEDs for the full sample and, from these, we computed optical and X-ray rest-frame luminosities at 2500 Å and 2 keV, respectively; we also investigated the dependence of α_{ox} upon redshift, $L_{2\,\mathrm{keV}}$ and $L_{2500\,\text{Å}}$

using the fully parametric EM (estimated and maximized) regression algorithm and Kendall-τ partial correlation analysis. Moreover, we estimated bolometric correction and bolometric luminosities for a subsample of 343 AGN for which we have detections in both soft and hard bands. Our principal results are the following:

(1) The $L_{2\,\mathrm{keV}} - L_{2500\,\text{Å}}$ correlation parametrized by $L_{2\,\mathrm{keV}} \propto L^{\beta}_{2500\,\text{Å}}$, where $\beta = 0.760 \pm 0.022$, is fully confirmed. The best-fit slope agrees with previous studies based on optically selected samples, which found a value of β inconsistent with unity.

(2) The mean value of α_{ox} for the full X-ray selected sample is $\langle \alpha_{\mathrm{ox}} \rangle \sim 1.37 \pm 0.01$ with a dispersion around the mean of 0.18. The correlation between α_{ox} and $L_{2500\,\text{Å}}$ is confirmed at the $17\,\sigma$ significance level. The correlation becomes stronger if we take into account the effect of redshift using the partial correlation analysis ($\sim 21\,\sigma$). The slope of our the best-fit relation between α_{ox} and $L_{2500\,\text{Å}}$ is consistent within $\sim 1.6\sigma$ with that obtained for an optically selected sample.

(3) From the EM regression method, a weak correlation has been found between α_{ox} and redshift; however, if the effect of $L_{2500\,\text{Å}}$ is taken into account, the correlation disappears.

(4) No significant correlation between α_{ox} and $L_{2\,\mathrm{keV}}$ has been observed ($\sim 1.5\,\sigma$ significance level if we take into account the effect of the optical luminosity).

(5) A tight correlation between the α_{ox} values and the hard X-ray bolometric correction values is found. The $\alpha_{\mathrm{ox}} - k_{\mathrm{bol}}$ relation could be used as a practical tool to provide an accurate estimate ($\sim 20\%$ at 1σ) of the bolometric correction using only the α_{ox} value.

(6) A correlation for both α_{ox} and k_{bol} with Eddington ratio is found. Our results for the $k_{\mathrm{bol}} - \lambda_{\mathrm{Edd}}$ relation and for $\alpha_{\mathrm{ox}} - \lambda_{\mathrm{Edd}}$ suggest that there is a connection between the broad-band emission, mostly in the UV, and the Eddington ratio, which is directly linked to the ratio between mass accretion rate, $\dot{M}_{\mathrm{acc}}$, and Eddington accretion rate, $\dot{M}_{\mathrm{Edd}}$.

(7) The possible effects of intrinsic absorption and/or contribution of the host-galaxy on the $L_{2500\,\text{Å}} - L_{2\,\mathrm{keV}}$ and $\alpha_{\mathrm{ox}} - L_{2500\,\text{Å}}$ relations have been estimated. If the main reason for the red optical-UV SEDs in the sample were intrinsic extinction, the resulting $L_{2500\,\text{Å}} - L_{2\,\mathrm{keV}}$ relation would be slightly steeper ($\beta = 0.782 \pm 0.021$); if, instead, the host-galaxy contribution were important in determining the red optical-UV SEDs, the resulting $L_{2500\,\text{Å}} - L_{2\,\mathrm{keV}}$ relation would be flatter ($\beta = 0.660 \pm 0.022$). Neither effect can produce a linear correlation ($\beta = 1$).

Chapter 4

Properties of X–ray selected Type-2 AGN

In this Chapter a study of the multi-wavelength properties, from the mid-infrared (24μm) to the hard X–rays (10 keV), for a sample of 257 X–ray selected Type-2 AGN from the XMM-COSMOS survey is presented. All of them are spectroscopically identified Type-2 AGN and for 112 of them an estimate of the column density from their X–ray spectra is available. Average SEDs are builded for the total sample and for different bins of redshift, X–ray luminosites and infrared luminosites. The shape of the average SEDs in the optical shows a strong host-galaxy contribution, which is maximum in the lower luminosity/redshift bins. There is also a trend between X–ray and mid-infrared luminosity: the contribution in the infrared is higher at higher X–ray luminosities. Bolometric luminosities, bolometric corrections, stellar masses and SFR for these sources are estimated using a multicomponent SED-fit technique to properly disentangle the emission associated to stellar light from that due to accretion. For 90% of the sample the morphological classification is obtained with an upgraded version of the Zurich Estimator of Structural Types (ZEST), known as ZEST+.

4.1 The Data Set

The parent sample consists of 1078 X–ray sources detected in the 2–10 keV band at fluxes $> 2.5 \times 10^{-15}$erg s^{-1}cm^{-2} (see Table 2 in Cappelluti et al. 2009). The objects for which no secure optical counterpart could be assigned are often affected by severe blending problems, so that in this analysis the 971 sources (hereafter 971-XMM), for which a secure optical counterpart can be associated (see discussion in Section 2.1), are considered.

From the 971-XMM catalog 257 sources are selected requiring the absence of broad (FWHM< 2000 km s^{-1}) emission lines in their optical spectra*: 225 are classified “not-broad-line AGN”

*The origin of spectroscopic redshifts for the 257 sources is as follows: 13 objects from the SDSS archive, 2 from MMT observations (Prescott et al. 2006), 70 from the IMACS observation campaign (Trump et al. 2007), 156 from the zCOSMOS bright 10k sample (see Lilly et al. 2007), 7 from the zCOSMOS faint catalog and 9 from the Keck/DEIMOS campaign.

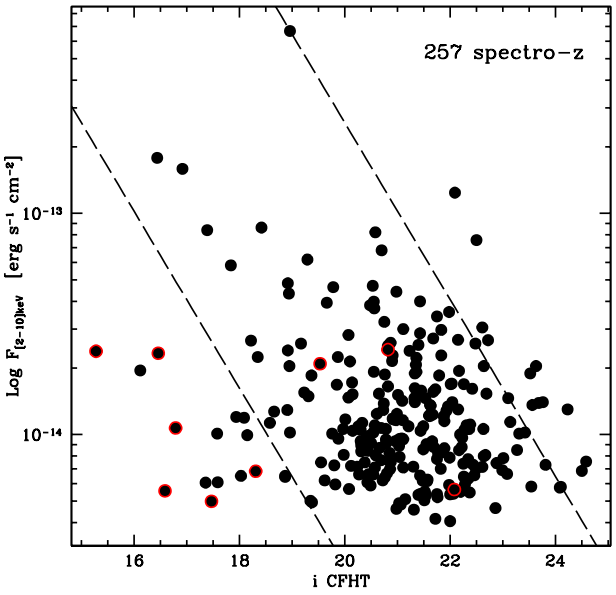

Figure 4.1: Plot of the 2 − 10keV flux versus the total i^* CFHT magnitude for the objects spectroscopically classified as Type-2. The red circles represent sources with a de-absorbed 2–10 keV luminosity lower than 10^{42} erg s^{-1}. The dashed lines represent a constant X–ray to optical flux ratio of Log $(X/O) = \pm 1$.

(bona fide either Type-2 AGN or emission line galaxies), while 32 are absorption-line galaxies (hereafter the Type-2 AGN sample).

In Figure 4.1 the 2–10 keV X–ray flux is plotted as a function of i^* CFHT magnitude. The dashed lines limit the region typically occupied by AGN in between constant X–ray to optical flux ratio Log $(X/O) = \pm 1$[†]. Nine sources have a de-absorbed 2–10 keV luminosity lower than 10^{42} erg s^{-1}, the conventional threshold below which the X–ray sources can plausibly be explained by moderate-strength starbursts, hot gas in elliptical galaxies, or other sources besides accretion onto a nuclear SMBH (Hornschemeier et al. 2001). The three sources inside the dashed lines have X–ray luminosities close to 10^{42} erg s^{-1}, while six AGN (6/257, 2%) lie in the part of the diagram usually occupied by star-forming galaxies, and have X–ray luminosities $< 10^{42}$ erg s^{-1}. Their inclusion in the analysis does not affect the main results.

The final Type-2 AGN sample used in our analysis, comprises 257 X–ray selected AGN spanning a wide range of redshifts ($0.045 < z < 3.524$) and X–ray luminosities ($41.6 \leq$ Log $L_{[2-10]\mathrm{keV}} \leq 45.0$). The redshift distribution of the total sample and the distribution of the de-absorbed hard X–ray luminosities are presented in Figure 4.2. The mean redshift is $\langle z \rangle = 0.761$, while the mean Log $L_{[2-10]\mathrm{keV}}$ is 43.32 with a dispersion of 0.64.

4.1.1 Absorption correction

For a sub-sample of 112 AGN an estimate of the column density N_{H} from spectral analysis (hereafter 112XMM; see Mainieri et al. 2007a for details) is available and, therefore, the de-absorbed X–ray luminosity at 0.5–2 keV and 2–10 keV can be computed (see Sect. 2.1.1). In Figure 4.4 the distribution of the column densities is shown, for this sub-sample, ranging from

[†]Log (X/O) = Log $f_x + i^*/2.5 + 5.6$

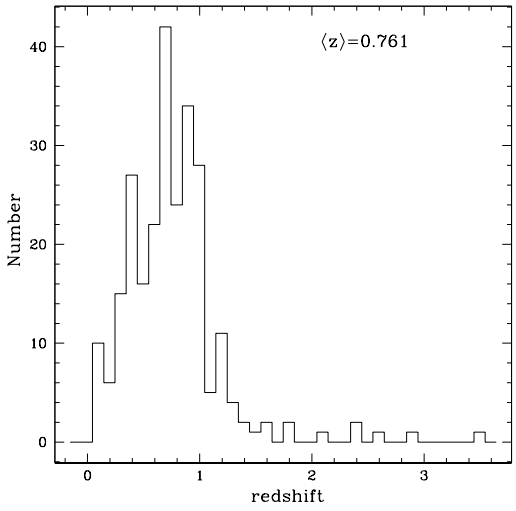

Figure 4.2: Redshift distribution of the 257 Type-2 AGN considered in this work.

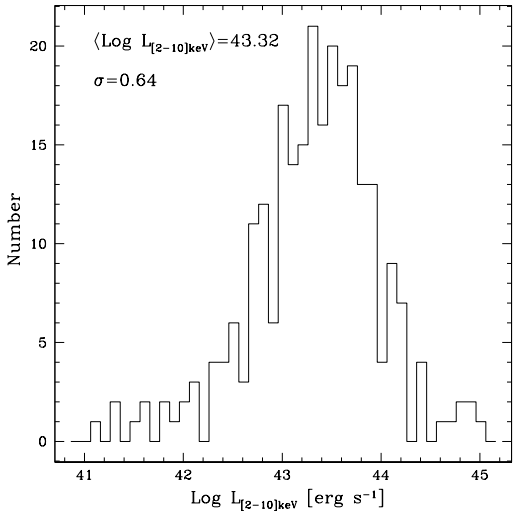

Figure 4.3: Hard X–ray luminosity distribution of the 257 Type-2 AGN considered in this work.

3×10^{20} cm^{-2} to 1.5×10^{24} cm^{-2}. The mean $N_{\rm H}$ value is 1.4×10^{22} cm^{-2} with a dispersion of 0.73 dex. For the sources without an estimate of the column density, the 2–10 keV luminosity is computed from the corresponding X–ray flux density without the absorption correction (only the Galactic correction is applied, see Sect. 3.2). Figure 4.5 shows the distribution of the hard X–ray luminosities before and after the absorption correction. The average shift induced by the correction for absorption in the 112XMM sample is $\langle \Delta \mathrm{Log}\, L_{[2-10]\mathrm{keV}} \rangle = 0.04 \pm 0.006$.

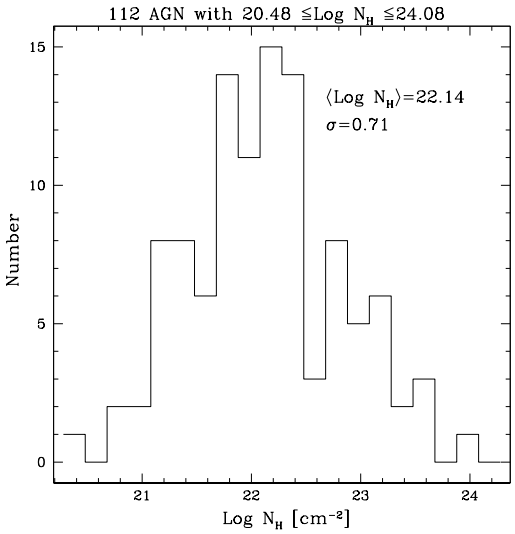

Figure 4.4: Column density distribution of the 112 Type-2 AGN with an $N_{\rm H}$ estimate from spectral analysis.

4.2 Rest-frame monochromatic fluxes and SEDs for Type-2 AGN

All the available multi-wavelength data are retrieved from the Brusa et al. (2010) catalog (see Sect. 2.1). More specifically, the number of detections at 160 μm and 70 μm is 18 and 43, respectively; for the undetected sources in these band 5σ upper limits are: 65 mJy and 8.5 mJy at 160 μm and 70 μm, respectively. At 24 μm the number of detected sources is 239; for the 18 undetected sources at 24 μm, the 5σ upper limits is 0.08 mJy. All sources are detected in the infrared IRAC bands, and only very faint objects went undetected in the optical and near infrared bands: we have only 8 upper limits in the z^+ band; 1 upper limit in the B_J and i^* bands; 2 upper limits in both u^*; 4 upper limits in the K_S CFHT band and 2 in the J UKIRT band. The observations

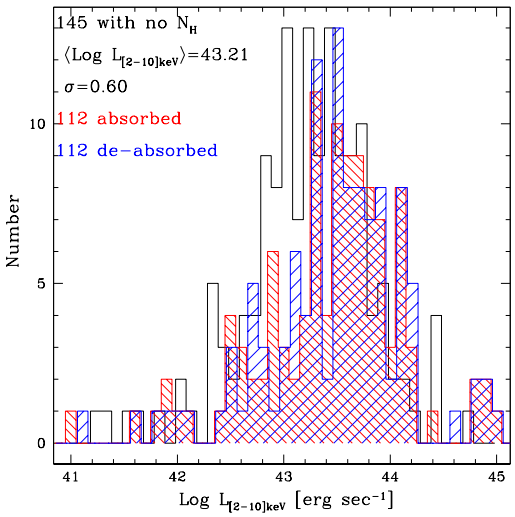

Figure 4.5: Distribution of the $L_{[2-10]\rm keV}$ for the sample without $N_{\rm H}$ value available (*open histogram*), and for the 112XMM sample before (*red hatched histogram*) and after absorption correction (*blue hatched histogram*).

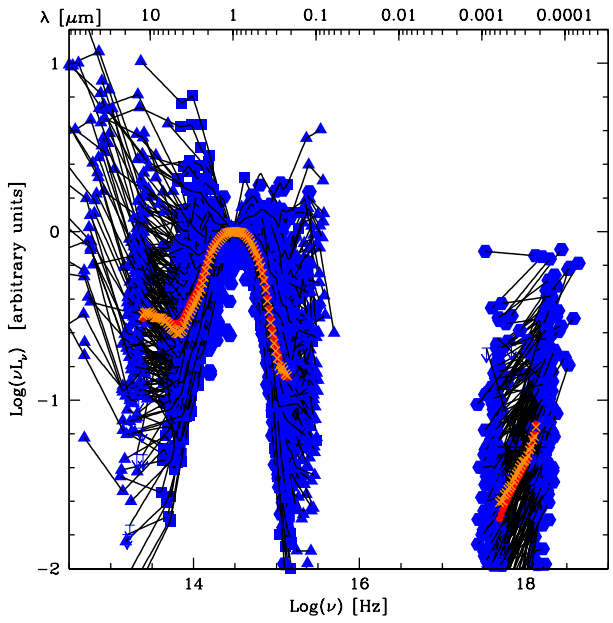

Figure 4.6: Mean (*orange crosses*) and median (*red points*) SED from the total sample of 257 Type-2 AGN. The blue points represent the rest-frame data, from infrared to X–ray, used to construct the average SED, while the black lines represent the interpolated SED.

in the various bands are not simultaneous, as they span a time interval of about 5 years: 2001 (SDSS), 2004 (Subaru and CFHT) and 2006 (IRAC). Variability for Type-2 AGN is likely to be negligible, but, in order to further reduce it, observations closest in time to the IRAC data are considered. GALEX bands are not taken into account because, given the large aperture, they can include light from close companions. All the data for the SED computation were blueshifted to the rest-frame wavelength, and no K-correction was therefore needed (see Sect. 2.2). Galactic reddening is included: using the selective attenuation of the stellar continuum $k(\lambda)$ taken from Table 2.3 (see Sect. 2.1.2). Galactic extinction is estimated from Schlegel et al. (1998) for each object in the 971-XMM catalog. Count rates in the 0.5-2 keV and 2-10 keV are converted into monochromatic X–ray fluxes in the observed frame at 1 and 4 keV, respectively, using a Galactic column density $\langle N_{\rm H} \rangle = 2.5 \times 10^{20}\ cm^{-2}$ (see Cappelluti et al. 2009), and assuming a photon index $\Gamma_x = 2$ and $\Gamma_x = 1.7$, for the soft and hard band, respectively (see Sect. 2.1.1). These X–ray fluxes are not corrected for the intrinsic column density. All sources are detected in the 2-10 keV band by definition, while in the soft band there are 70 upper limits.

4.3 Average SED

The single rest-frame SEDs for all sources in our sample are computed, following the approach in Sect. 2.2. The resulting mean and median SEDs, both normalized at 1μm, are reported in Figure 4.6 with orange crosses and red points, respectively. In order to show the dispersion, individual SEDs are also plotted. The average SED is characterized by a flat X–ray slope, $\langle \Gamma \rangle = 1.12$, while in the optical-UV the observed emission appears to be consistent with that from the host-galaxy. The flat X–ray slope could be due to the fact that the fluxes at 1 and 4 keV are not corrected for the intrinsic absorption. The average SED in the mid-infrared is most likely a combination of

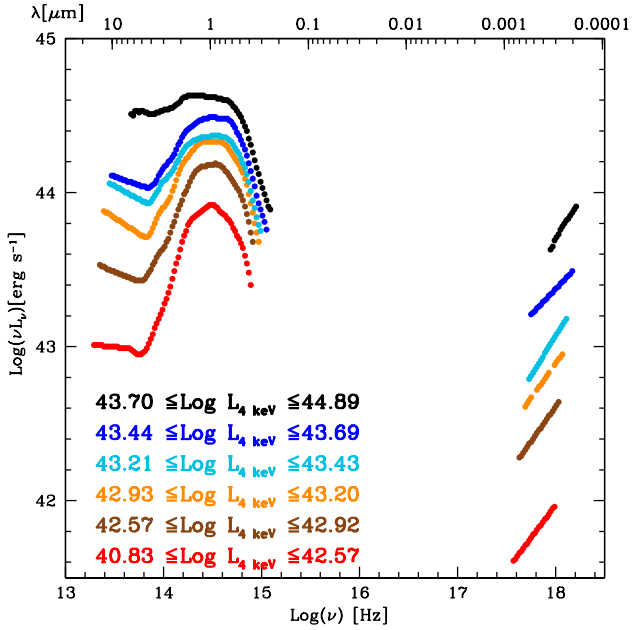

Figure 4.7: Average SEDs in the rest-frame Log $(\nu L_\nu) -$ Log ν plane. Mean SEDs computed binning in X–ray luminosity at 4 keV. The color code refers to the different bins as labeled.

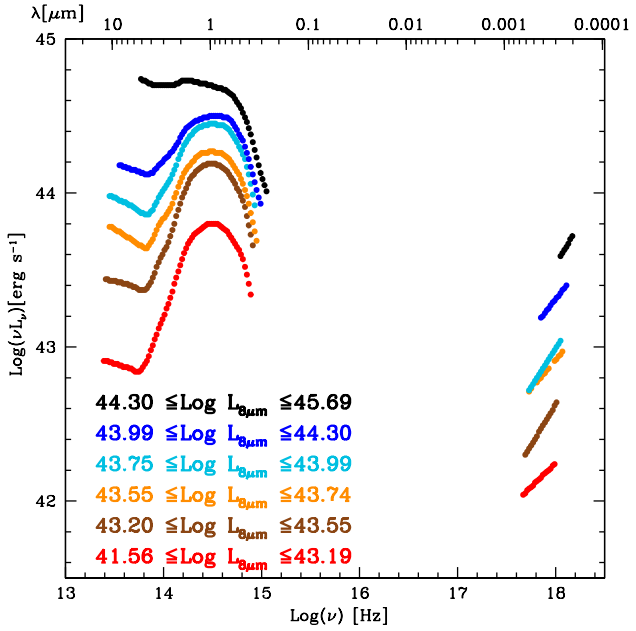

Figure 4.8: Average SEDs in the rest-frame Log $(\nu L_\nu) -$ Log ν plane. Mean SEDs computed binning in infrared luminosity at 8μm. The color code refers to the different bins as labeled.

dust emission from star-forming region and AGN emission reprocessed by the dust.

The total sample is also binned in X–ray and infrared luminosites and redshift. The luminosity at 4 keV and 8μm is used to divide the total sample in 6 bins with the same number of sources in each bin. The two wavelengths are chosen to minimize the contribution of the host-galaxy. The results are shown in Figs. 4.7, 4.8 and 4.9. There is a trend in luminosity from lower to higher redshifts, but this is due to a selection effect: at higher redshifts we are looking to the most luminous sources. The shapes of the average SEDs in the optical bands are approximately the same

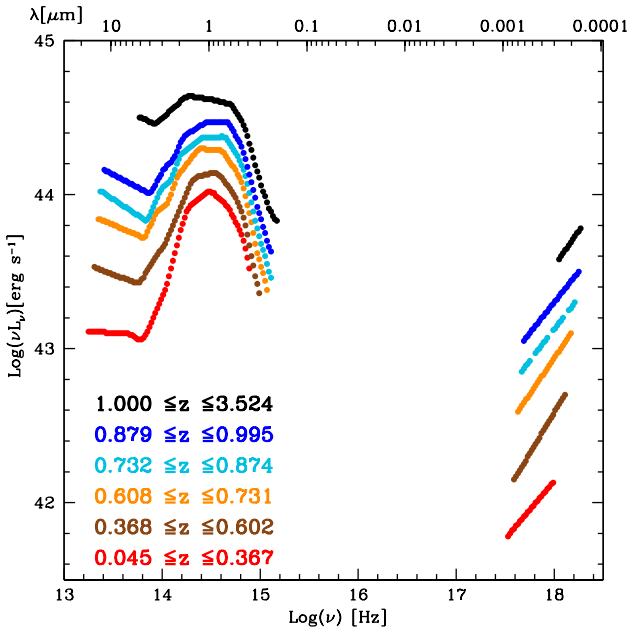

Figure 4.9: Average SEDs in the rest-frame Log (νL_ν) – Log ν plane. Mean SEDs computed binning in redshift. The color code refers to the different bins as labeled.

in all luminosity and redshift bins. As expected, there is a stronger host-galaxy contribution at lower luminosity/redshift bins, where the average SEDs have a typical galaxy shape. Moreover, there is a trend between X–ray and mid-infrared luminosity: the contribution in the infrared is higher at higher X–ray luminosities. This correlation is not new, and there are several works that analyzed this correlation for both Type-1 and Type-2 AGN using the intrinsic (non-stellar) emission from the AGN (e.g., Lutz et al. 2004, Gandhi et al. 2009). The change in the average

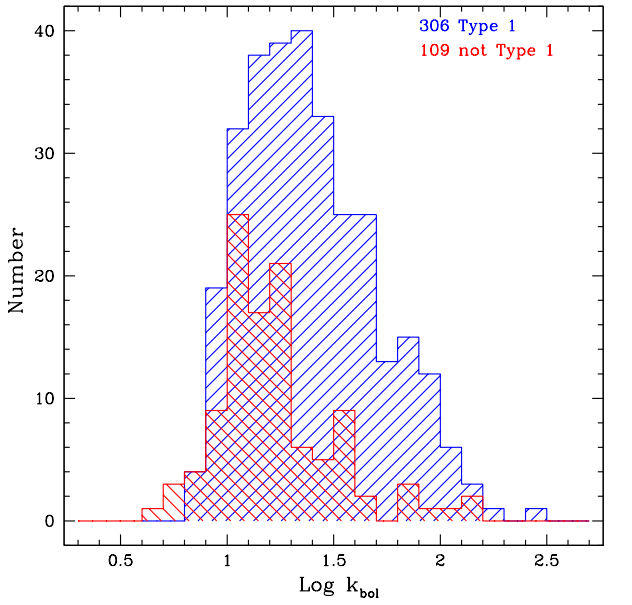

Figure 4.10: Distribution of the bolometric correction for the 109 Type-2 AGN sample (*red hatched histogram*) and for the 306 Type-1 AGN (*blue hatched histogram*).

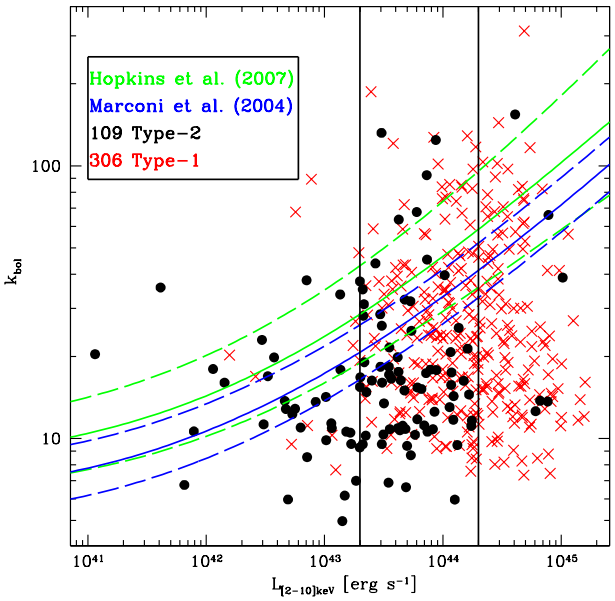

Figure 4.11: Hard X–ray bolometric correction against the intrinsic 2–10 keV luminosity for 109 Type-2 AGN with N_H detection and AGN best-fit (*black points*). The crosses represent the bolometric correction for 306 Type-1 AGN, computed with the approach described in Sect. 2.5. The green and blue lines represent the bolometric correction and the 1σ dispersion obtained by Hopkins et al. (2007) and Marconi et al. (2004), respectively.

shape in the mid-infrared as a function of the X–ray suggests an increased AGN contribution in the most luminous sources.

4.4 Results and discussion

4.4.1 Bolometric correction and luminosites for Type-2 AGN

Individual SED-fits have been performed as described in Sect. 2.4. Bolometric luminosities and bolometric corrections were computed for the 112XMM Type-2 AGN sample, for which intrinsic soft and hard X–ray luminosities are estimated as described in Chapter 2 (see Sect. 4.1.1). For 3 sources we do not have an estimate of the AGN luminosity from the SED-fitting (the best-fit involves only the starburst and galaxy components), and we cannot compute the bolometric luminosity for them. In Fig. 4.10 the distribution of the bolometric correction for the 109 Type-2 AGN sample and for the 306 Type-1 AGN are presented.

Figure 4.11 shows bolometric corrections for both the Type-1 and the Type-2 AGN samples as a function of the hard X–ray luminosity. For both samples bolometric parameters are estimated from the SED-fitting as discussed in Sect. 2.4. The green and blue curves represent the bolometric corrections and their 1 σ dispersion as derived by Hopkins et al. (2007) and Marconi et al. (2004), respectively. Type-2 AGN have, on average, smaller bolometric corrections than Type-1 AGN at comparable hard X–ray luminosity. For example, at $43.30 \leq \mathrm{Log}\, L_{[2-10]\mathrm{keV}} \leq 44.30$, where both AGN types are well represented, the median bolometric correction for the Type-2 AGN (69 objects) is $\langle k_{\mathrm{bol}} \rangle \sim 16 \pm 1$, to be compared with a median bolometric correction $\langle k_{\mathrm{bol}} \rangle \sim 23 \pm 1$ for the Type-1 AGN (167 objects). The two averages are statistically different at $\sim 5\ \sigma$ level and this is consistent with the results in Vasudevan et al. (2010). The mean $L_{[2-10]\mathrm{keV}}$

for the Type-1 and Type-2 AGN within this luminosity range are different by a factor 1.6, and this could in principle explain at least part of the difference in the average bolometric corrections for the two samples of AGN. However, the significance of the difference is still present if we split this luminosity range in two equal Log $L_{[2-10]\mathrm{keV}}$ bins and perform a Kolmogorov–Smirnov test for the Type-1 and Type-2 AGN luminosity distributions in each bin.
Vasudevan & Fabian (2009) and Lusso et al. (2010, see Chapter 3 of this Thesis) have shown that hard X–ray bolometric corrections are correlated with the Eddington ratios ($\lambda_{\mathrm{Edd}} = L_{\mathrm{bol}}/L_{\mathrm{Edd}}$) for Type-1 AGN. The $k_{\mathrm{bol}} - \lambda_{\mathrm{Edd}}$ relation suggests that there is a connection between the broad-band emission, mostly in the optical-UV, and the Eddington ratio, which is directly linked to the ratio between mass accretion rate and Eddington accretion rate. A high λ_{Edd} corresponds to an enhanced optical-UV emission, which means a prominent big-blue bump and therefore a higher k_{bol}. The difference between the average bolometric corrections for Type-1 and Type-2 AGN could be due to lower mass accretion rates in Type-2 AGN, assuming the same black hole mass distribution for the two AGN populations. This would be at variance with the current theoretical framework of AGN/host-galaxy co-evolution, where obscured AGN are highly accreting objects and their black hole is rapidly growing. Besides, even if most of the Type-2 AGN in the present sample are relatively luminous ($42.37 \leq \mathrm{Log}\, L_{\mathrm{bol}} \leq 46.80$), they are at moderately low redshift ($0 < z < 1$), so that the 112XMM sample is likely to represent a different stage in AGN evolution history.

4.4.2 Infrared emission: indication of AGN activity

The re-processed infrared emission can be used as a proxy of the intrinsic disc emission, since the timescale for transfer of energy from the disk to the outer edge of the torus into infrared emission is of the order of several years in standard AGN picture; whereas optical, UV and X–ray variability in AGN is known to occur on shorter timescales. The correlation between the 2–10 keV X–ray emission and IR emission at 12.3μm for a sample of Seyfert nuclei has been discussed in Gandhi et al. (2009). Using X–ray data from the literature and new IR data from the Very Large Telescope's Imager and Spectrometer for mid-Infrared (VISIR/VLT), taken specifically for addressing the issue of nuclear emission in local Seyferts, they found a tight correlation between intrinsic, uncontaminated IR luminosity and X–ray luminosity in the 2–10 keV range

$$\mathrm{Log}\,\frac{L_{12.3\ \mu m}}{10^{43}} = (0.19 \pm 0.05) + (1.11 \pm 0.07)\mathrm{Log}\,\frac{L_{[2-10]\mathrm{keV}}}{10^{43}}. \tag{4.1}$$

The relation is characterized by a small scatter with a standard deviation of 0.23 dex. The mid-infrared continuum is a good proxy for the intrinsic power of AGN, and Gandhi et al. results re-inforce and improve constraints on previous determinations of the correlation (Horst et al. 2006, 2008). For the 112XMM sample the expected nuclear mid-infrared luminosity is computed from Eq. (4.1) using the estimate of the intrinsic unabsorbed X–ray luminosity. From the observed rest-frame SED (AGN+host-galaxy) the luminosity at 12.3 μm is computed. A comparison of the total observed luminosity at 12.3 μm and that predicted by Eq. (4.1) is plotted in Figure 4.12. The distribution of the ratio $r = \mathrm{Log}\left(L_{12.3\ \mu m,\mathrm{obs}}/L_{12.3\ \mu m,\mathrm{predicted}}\right)$ has a mean which is shifted from zero by ~ 0.2. However, if we consider a gaussian distribution with $\sigma = 0.23$, i.e. the same

dispersion observed by Gandhi et al. (2009) in their local sample, the majority of the objects are found within 2σ of the r distribution. The tail outside 2σ and extending to high r includes 28 sources (with $r \gtrsim 0.5$) for which the predicted mid-infrared luminosity is significantly lower than observed. The hard X–ray luminosities of these 28 AGN are in range Log $L_{[2-10]\mathrm{keV}} \sim 42.5 - 44$, where the local correlation is well-sampled. There are two possible explanations for a significant ($\sim 25\%$ of the objects) tail toward high-r values: either the Gandhi relation, which was derived for a sample of local Seyfert galaxies, cannot be extended to all the sources in our sample or the SED-fitting procedure may overestimate, in a fraction of these objects, the nuclear contribution. In order to study the properties of these outliers, bolometric corrections, morphologies, stellar masses and SFR are discussed in following. We call "low-r" AGN all sources within 2σ of the r distribution, while the "high-r" AGN sample is populated by the sources deviating more than 2σ (see Fig. 4.13 for some examples).

A clear separation in bolometric corrections for these two sub-samples is found, and this is shown in Figure 4.14 in which bolometric corrections are plotted as a function of the 2–10 keV luminosity for 109 Type-2 AGN with N_{H} detection and AGN best-fit (see Table 4.1). At a given hard X–ray luminosity ($43 \leq \mathrm{Log}\, L_{[2-10]\mathrm{keV}} \leq 44$) the low-$r$ sample has a median bolometric correction of $\langle k_{\mathrm{bol}} \rangle \sim 12 \pm 1$ (52 objects), to be compared with a median bolometric correction for the high-r sample of $\langle k_{\mathrm{bol}} \rangle \sim 36 \pm 3$ (17 objects). The two median values for k_{bol} are statistically different at $\sim 7.6\sigma$ level.

Furthermore, in the high-r sample 13 Type-2 AGN out of 28 have a detection at 70μm ($\sim 46\%$, significantly higher than those for the low-r sample, $\sim 8\%$) and 4 of these 13 have also a detection at 160μm ($\sim 14\%$ considering the total high-r sample, and only $\sim 4\%$ for the low-r sample). This denotes that the difference in the average bolometric corrections between the low-r and high-r samples is probably due to the fact that a significant fraction of the infrared emission is

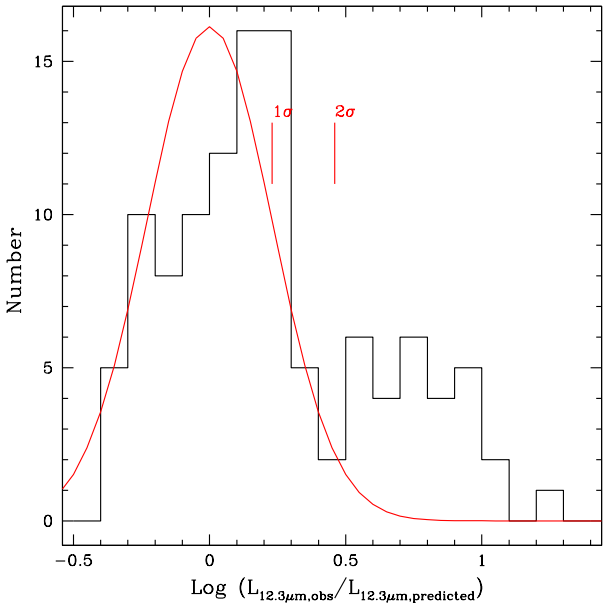

Figure 4.12: Histogram of the ratio between the total observed luminosity at 12.3 μm and the mid-infrared luminosity predicted by Eq. (4.1). The red curve represents a gaussian with mean equal to zero and standard deviation 0.23. The 1σ and 2σ standard deviations of the correlation are also reported.

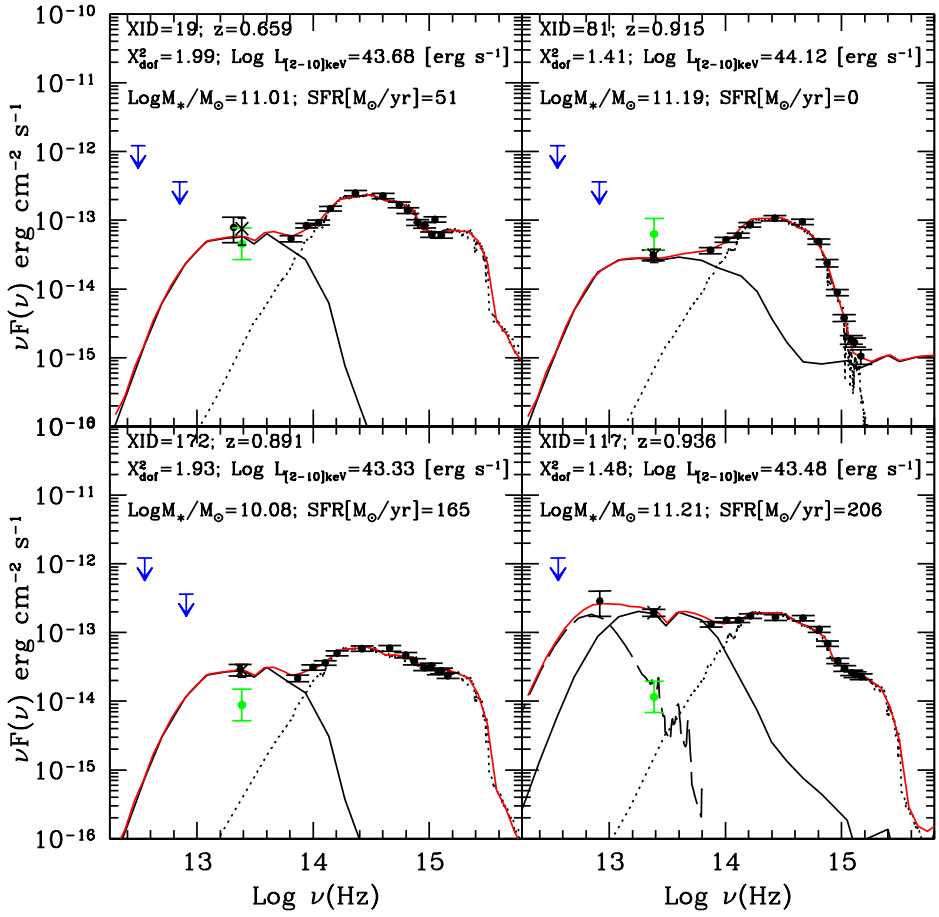

Figure 4.13: Examples of SED decompositions. Black circles are the observed photometry in the rest-frame (from the far-infrared to the optical-UV). The long-dashed, solid and dotted lines correspond respectively to the starburst, AGN and host-galaxy templates found as the best fit solution. The red line represents the best-fit SED. The stellar mass and the SFR derived from the galaxy template are reported. The green point represents the nuclear mid-infrared luminosity using Eq. (4.1), while the cross represents the total observed luminosity at 12.3 μm computed from the rest-frame SED. XID=19 and 81 are examples of low-r AGN, while XID=172 and 117 represent high-r AGN.

attributable to an incorrect modeling of the star-formation process, or the AGN contribution is somehow overestimated by the SED-fitting procedure.

There is no significant difference in the average stellar masses, nor in nuclear absorption between the low-r and the high-r sample, while there is a possibly significant difference in SFR. The average stellar mass in the high-r sample is $\langle \mathrm{Log}\, M_* \rangle \sim 10.85 M_\odot$ with a dispersion of 0.32, while for the low-r sample is $\langle \mathrm{Log}\, M_* \rangle \sim 10.69 M_\odot$ with $\sigma = 0.42$. The two averages are not statistically different. The average SFR, as derived from the SED-fit, for the high-r sample is $\langle \mathrm{Log}\, SFR \rangle \sim 1.57 M_\odot$/yrs with a $\sigma = 0.81$, while for the low-r sample is $\langle \mathrm{Log}\, SFR \rangle \sim$

Table 4.1: Summary of the different subsamples in the X–ray selected 112XMM AGN sample.

All	257
$N_{\rm H}$ available	112
low-r	high-r
84	28
low-r & AGN best-fit	high-r & AGN best-fit
83	26

$0.45 M_{\odot}$/yrs with a $\sigma = 1.46$ and the two averages are statistically different at 4 σ level.

Concluding, the SED-fitting for the 28 Type-2 AGN is likely to overestimate the AGN emission in the infrared, which is probably due to the infrared emission from star-forming regions. The average bolometric correction for Type-2 AGN, excluding these sources, would be even lower than what we have computed in the previous Section. This reinforces the idea of lower bolometric corrections for Type-2 AGN with respect to Type-1 AGN. However, if part of the bolometric accretion disk power is not re-emitted in the mid-infrared, but rather dissipated (e.g., AGN-feedback), this would not be accounted for the bolometric luminosity, and could be the cause for having such low bolometric corrections in the low-r sample. At this stage, this is just a speculation, and more work is needed to verify this possibility.

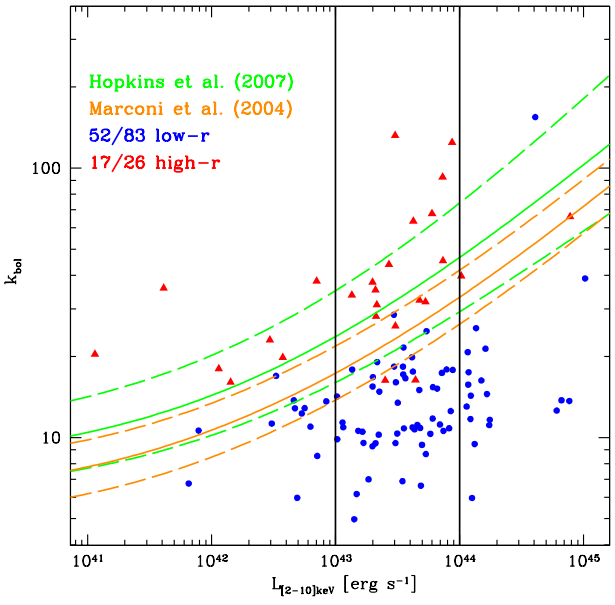

Figure 4.14: Hard X–ray bolometric correction against 2–10 keV luminosity for 109 Type-2 AGN with $N_{\rm H}$ detection and AGN best-fit. The 109 Type-2 sample is divided into subsamples: low-r AGN sample (*blue points*) and high-r AGN sample (*red triangles*). The green and orange lines represent the bolometric correction and 1σ dispersion obtained by Hopkins et al. (2007) and Marconi et al. (2004), respectively. In the de-absorbed hard X–ray luminosity range highlighted by the solid lines, we have 52 low-r and 17 high-r (in the infrared) sources.

4.4.3 Galaxy morphologies

Galaxies show a colour bi-modality both in the local Universe and at higher redshift (up to $z \sim 2$; e.g., Strateva et al. 2001; Bell et al. 2004). This bi-modality (red-sequence and blue-cloud galaxies) has been interpreted as an evidence for a dicothomy in the star formation and merging histories of galaxies (e.g., Menci et al. 2005). Color-magnitude and color-mass diagrams (e.g., rest-frame $(U-V)$ colors versus stellar mass) have been used as tools in galaxy evolution studies, and since many models invoke AGN feedback as an important player in such evolution, it is interesting to locate the hosts of Type-2 quasars in those diagrams. Using the galaxy component obtained from the best fit of the Type-2 AGN, it is possible to derive rest-frame colors for the host that, linked to the stellar mass and possibly to the morphologies, can provide hints on AGN feedback. Several studies found that the hosts of obscured AGN tend to be redder than the overall galaxy population in the rest-frame $(U-V)$ color (e.g., Nandra et al. 2007). There are at least two possible and significantly different interpretations for this observational result: the observed red colors are mainly due to dust extinction, so that a significant fraction of obscured AGN would live in massive, dusty star-forming galaxies with red optical colors (e.g., Brusa et al. 2009c); or red sources are linked with early-type passive systems (e.g., Rovilos & Georgantopoulos 2007). Therefore, accurate stellar mass and SFR estimates, together with detailed galaxy morphologies, are of particular importance to discriminate between the two alternative possibilities.

Galaxy morphologies were obtained with an upgraded version of the Zurich Estimator of Structural Types (ZEST; Scarlata et al. 2007), known as ZEST+ (Carollo et al. 2011, in prep). Relative to its predecessor, ZEST+ includes additional measurements of non-parametric morphological indices for characterising both structures and substructures. For consistency with the earlier versions, ZEST+ uses a Principal Component Analysis (PCA) scheme in the 6-dimensional space of concentration, asymmetry, clumpiness, M20 , Gini coefficient, and ellipticity. ZEST+ classifies galaxies in seven morphological types located in specific regions of the 6-dimensional space: elliptical, S0, bulge-dominated disk, intermediate-bulge disk, disk-dominated, irregular, compact. The different types were then visually inspected. For 19 objects ZEST+ is unable to give any information on morphology because these sources lie off the edge of the ACS tiles and 4 sources are blended. As a result of the ZEST+ procedure and visual inspection of the other 234 galaxies in our sample, we find that 16 are ellipticals (Ell), 54 are S0s, 74 are bulge-dominated (BD) disks, 27 are intermediate-bulge (IB) disks, just 1 is disk-dominated (DD), 19 are irregular galaxies (Irr), 15 are compact galaxies (i.e. the structural parameters computed for these galaxies from the HST-ACS images are highly affected by the instrumental PSF) and 18 are unresolved compact galaxies (UC, i.e. essentially point-like sources). Ten galaxies show distortions and potential signatures of ongoing or recent mergers (PM). Examples of morphological classes of the AGN hosts are shown in Figs. 4.15, 4.16 and 4.17. In Table B.1 we list the main properties of the sample.

With the aim of discussing and exploring the properties of AGN host-galaxies, the rest-frame $(U-V)$ colors are adopted (e.g., Sandage & Visvanathan 1978; Bell et al. 2004; Borch et al. 2006; Cardamone et al. 2010). This rest-frame $(U-V)$ color encompasses the 4000Å break, and it is particularly sentitive to age and metallicity variations of stellar population in galaxies. In Fig. 4.18 the distribution of the rest-frame $(U-V)$ colors, which are computed directly from

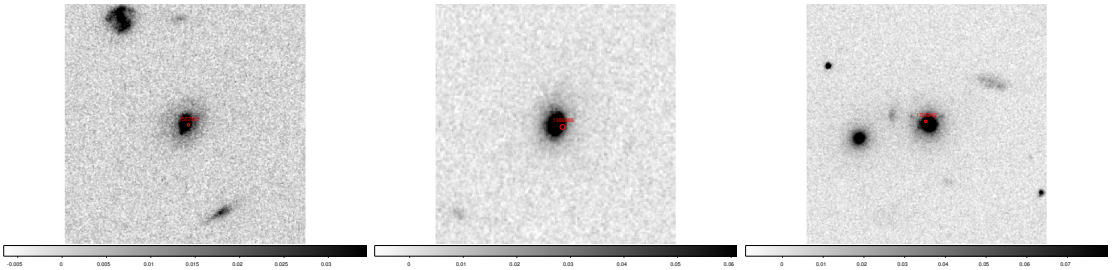

Figure 4.15: Type-2 AGN hosts classified as *ellipticals* and *S0s* using the ZEST+ code on ACS F814W images. From left to right XID: 2210, 5288 and 54514.

the best-fit galaxy template, and stellar masses (output of the SED-fitting code) are reported for the entire Type-2 AGN sample. In the same figure, the background contours for a sample of $\sim$ 18000 galaxies in zCOSMOS ($i_{\rm acs} < 22.5$, 240 Type-2 are detected in the $i_{\rm acs}$ band, 183/240 Type-2 AGN (76%) have $i_{\rm acs} < 22.5$) are also plotted, where colours and stellar masses are computed using the Hyperz code (Bolzonella et al. 2000). The distribution of AGN in this plane is significantly different from that of normal galaxies over a comparable redshift range, and this is also clear in Fig. 4.19 where we have plotted the distribution of stellar masses as a function of redshift for the zCOSMOS galaxies and for the Type-2 AGN sample.

AGN are known to reside in massive galaxies (e.g., Silverman et al. 2009; Brusa et al. 2009c) and this is fully confirmed by the present analysis. By selecting all sources with M_* larger than $2.5 \times 10^{10} M_{\odot}$, in order to have meaningful statistic for a comparison, it is clear that AGN host-galaxies are bluer than the inactive galaxy population (see also Koss et al. 2010 for a local sample of hard (*Swift*-BAT) X–ray selected AGN). The morphologies of the host-galaxies and the stellar masses indicate that there is a preference for these obscured AGN to be hosted in bulge-dominated and S0 galaxies ($\sim$ 50%) with stellar masses greater than $10^{10} M_{\odot}$. This result is consistent with the previous studies on Type-2 AGN by Silverman et al. (2008, see also Kauffmann et al. 2003b; Bundy et al. 2008).

It should be noted that no correction for the internal extinction has been applied to the $(U - V)$ colors of both background galaxies in zCOSMOS and Type-2 AGN hosts. This correction could be important as shown in Cowie & Barger (2008). In that work the star formation and galactic stellar mass assembly are analyzed using a very large and highly spectroscopically complete sample selected in the rest-frame NIR bolometric flux in the GOODS-N. They found that applying extinction corrections is critical when analyzing galaxy colors; nearly all of the galaxies in the green valley are $24\mu m$ sources, but after correcting for extinction, the bulk of the $24\mu m$ sources lie in the blue cloud. This correction introduces an average shift in color of $\sim$ 0.2 mag for the most extincted/star-forming galaxies. However, as a consistency with the colors of the background galaxies, we decided to consider the $(U - V)$ colors without the correction for the intrinsic extinction.

AGN host-galaxies belong to the red-sequence if their $(U-V)$ color is above the threshold (Borch et al. 2006):

$$(U - V)_{\rm AB,rest-frame} > 0.277 {\rm Log}\ M_* - 0.352z - 0.39 \qquad (4.2)$$

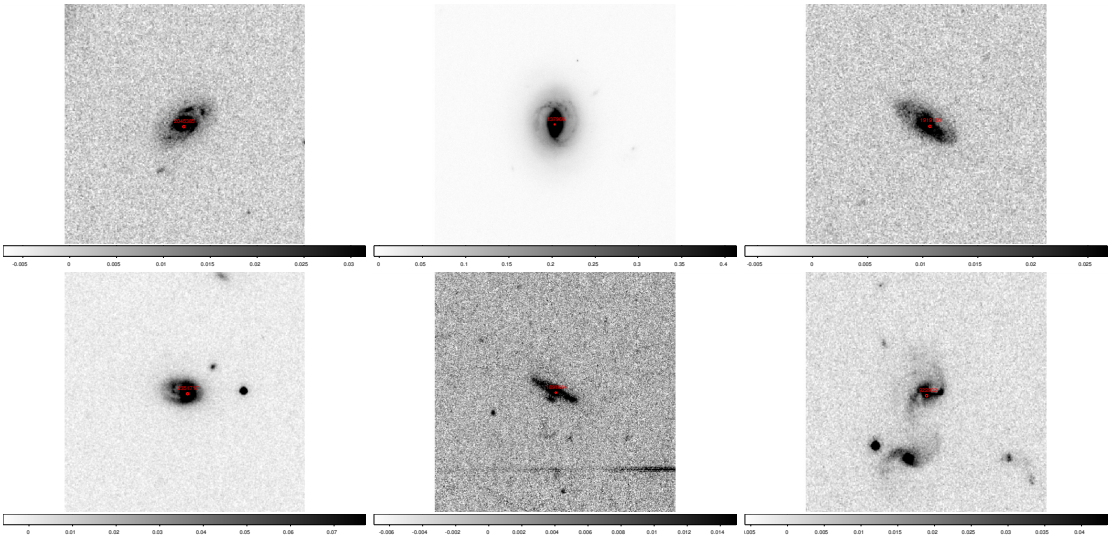

Figure 4.16: Type-2 AGN hosts classified as *bulge-dominated* and *intermediate-bulge*. From left to right XID: 2237, 2021, 323, 70, 292 and 5567.

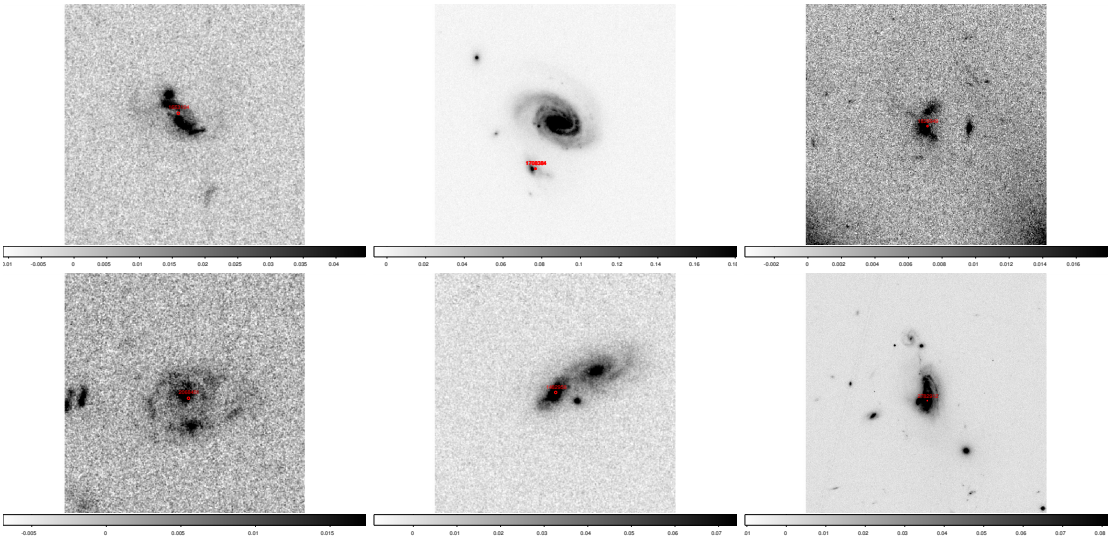

Figure 4.17: Type-2 AGN hosts classified as *possible mergers*. From left to right XID: 117, 217, 54451, 413, 5119 and 5112.

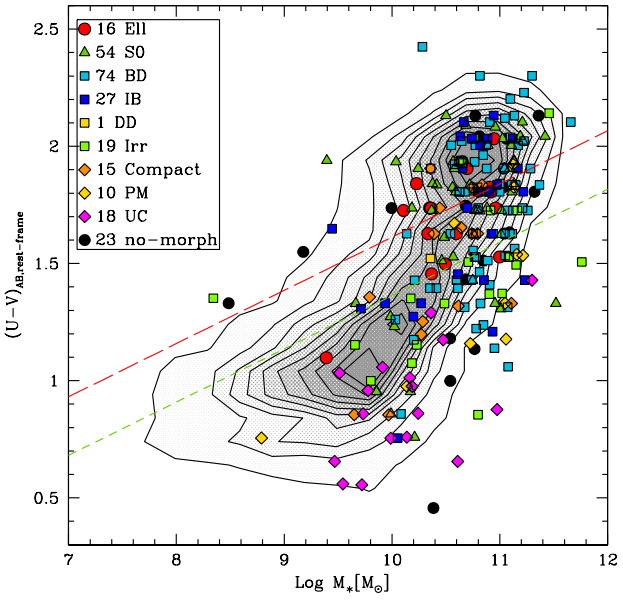

Figure 4.18: The morphology distribution (using the ZEST+ code) of the 234 AGN host-galaxies on the $(U - V)$ colour-mass diagram. The 23 sources without morphological information are also plotted. The $(U - V)$ color and stellar masses are computed using the SED-fitting code. We overplot the contours of about 18000 galaxies in *z*COSMOS (colours and stellar masses from *Hyperz*). The morphology classification is labeled as follow: elliptical (Ell), S0, bulge-dominated galaxy (BD), intermediate-bulge galaxy (IB), disk-dominated galaxy (DD), irregular (Irr), Compact, possible mergers (PM) and unresolved compact (UC). The red dashed line represents the red sequence cut defined by Borch et al. (2006), while the green short dashed line defines an approximate green valley region, both lines are calculated at redshift ~ 0.76, which is the average redshift of the main Type-2 sample.

Sources in the green-valley are approximately defined shifting this relation by 0.25 downward towards bluer colors. With these definitions, $\sim$ 40% (104/257) and $\sim$ 23% (60/257) of the total sample are included in the red-cloud and the green-valley, respectively. For all sources the Specific Star-Formation Rate (SSFR) is estimated, defined as the ratio of the SFR per unit of galaxy stellar mass (SSFR=SFR/M_*). The inverse of the SSFR, $SSFR^{-1}$, is called "growth time"

$$SSFR^{-1} = M_*/\dot{M}_*, \tag{4.3}$$

and corresponds to the time required for the galaxy to double its stellar mass, assuming its SFR remained constant. Actively star-forming galaxies are defined as sources with growth time smaller than the age of the Universe at their redshift ($SSFR^{-1} < t_{\rm Hubble}$), while sources with $SSFR^{-1}$ larger than the age of the Universe can be considered passive galaxies (see also Fontana et al. 2009; Brusa et al. 2009c). Figure 4.20 shows $SSFR^{-1}$ as a function of the stellar mass in three different redshift bins for the AGN host-galaxies in the red-sequence, in the green-valley and in the blue-coud and for the zCOSMOS galaxies in same redshift ranges. The horizontal lines mark the age of the Universe at the two redshift boundaries of the chosen intervals. At face value, almost all the sources in the red-sequence have $SSFR^{-1}$ larger than the age of the Universe at their redshift, which is consistent with passive galaxies. However, the value of $SSFR^{-1}$ has to be considered only as an approximate indication of the star-formation activity; in fact, there is some possible evidence of some residual star-formation, in our red-cloud galaxies, as witnessed by their host-galaxy morphologies. In the red-sequence 8 and 28 sources are classified as ellipticals and S0s, respectively; all together they represent 35% of the host-galaxy population in the red-sequence. About 25% is represented by disk galaxies (both bulge-dominated and

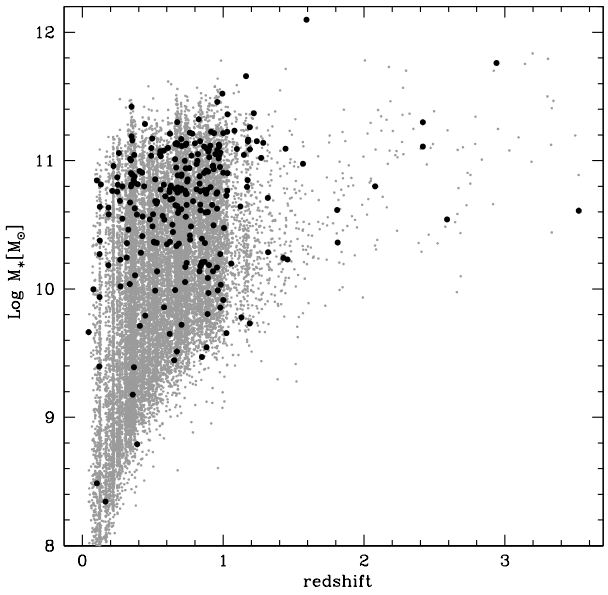

Figure 4.19: Distribution of the stellar masses as a function of redshift for the ∼ 18000 galaxies in zCOSMOS (*gray points*) and the 257 Type-2 AGN host-galaxies.

intemediate-bulge), which are probably still forming stars but not at high rates. In fact, 12 over 104 sources (∼ 12%) have a detection at 70μm and 5 have also a detection at 160μm (∼ 5%).

For these objects, the SFR inferred from the far-infrared detections is significantly higher than the SFR derived from the SED-fitting procedure. Indeed, a SED-fitting over the UV, optical and near-infrared bands is not always able to discriminate between the red continua of passive galaxies and those of dusty star-forming galaxies. Therefore, we decided to include another indicator in the present analysis broadly following the procedure described in Cardamone et al. (2010) (i.e., the $(U - V) - (V - J)$ color diagram). Near-infrared emission can distinguish between red-passive or dust-obscured galaxies: given a similar 0.5μm flux, a dusty population has more emission near ∼ 1μm than an older stellar population. A sub-sample of galaxies is selected in the same redshift range explored by Cardamone et al. (2010) (91 AGN host-galaxies with $0.8 \leq z \leq 1.2$). Fig. 4.21 shows both inactive galaxies and AGN host-galaxies in the same redshift range and the thresholds considered to divide galaxies in the red-sequence and in the green-valley (we consider an average redshift of 1 to define the threshold for the red-sequence and the green-valley). Thirty-one out of 91 AGN hosts are found to lie in the red-sequence (∼ 34%) and 26 in the green-valley (∼ 29%); while for galaxies about 32% and 21% lie in the red-sequence and green-valley, respectively. From a preliminary analysis of the rest frame $(U - V)$ against the rest-frame $(V - J)$ color (see Fig. 2 in Cardamone et al. 2010), we tentatively find that ∼ 6% of the AGN host-galaxies in the red-sequence and ∼ 27% of AGN host-galaxies in the green-valley are consistent with being dust-obscured starforming galaxies. These fractions for both AGN host-galaxies and inactive galaxies are reported in Table 4.2. The fractions of dust-obscured galaxies among the red-cloud and green-valley AGN in our sample, at $0.8 \leq z \leq 1.2$, are lower than those in the Cardamone et al. (2010) sample. However, the global fractions of AGN hosts, tentatively associated to passive galaxies, are very similar (∼ 50%) in the two samples. A more detailed

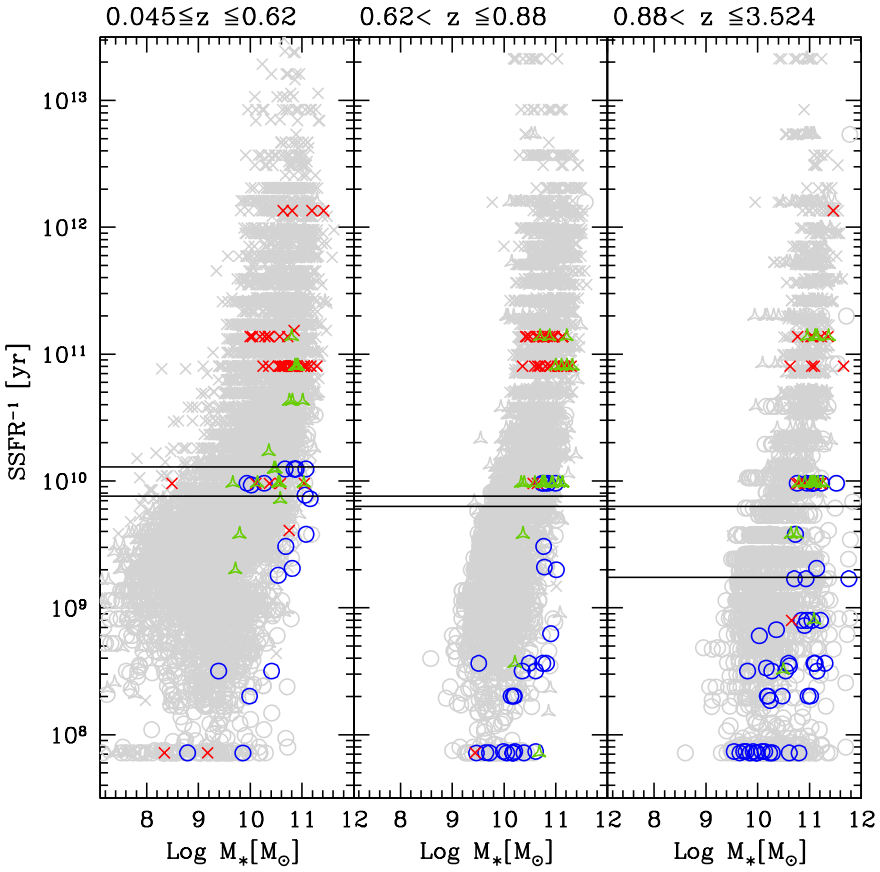

Figure 4.20: Inverse of the SSFR rate as a function of the stellar mass of the AGN host-galaxies in three different redshift bins for the zCOSMOS galaxies and for the Type-2 AGN sample in the red-sequence (red crosses), in the green-valley (green triangles) and in the blue-cloud (blue open circles). The horizontal lines mark the age of the Universe at the two redshift boundaries of the chosen intervals.

analysis of dust-corrected colors will be the subject of a future work on this sample (Lusso et al., in preparation).

4.5 Summary and Conclusions

A detailed analysis of the SEDs of 257 hard X–ray selected obscured AGN from the XMM-COSMOS survey is presented. All of them have spectroscopic redshifts, while for 112 sources an estimate of the column density from the X–ray spectral analysis is also available (112XMM sample). For obscured AGN, the nuclear luminosity is intercepted along the line of sight by the dusty torus postulated by the AGN unified schemes, reprocessing a significant amount of optical-UV emission in the infrared, so what we see in the optical-UV is mostly the light from the host-galaxy. On the one hand, this allows us to study the galaxy properties, on the other hand it makes difficult to estimate the nuclear bolometric power. A SED-fitting code has been

Table 4.2: AGN hosts and galaxies properties.

Sample	N	Red-sequence		Green-valley		Blue-cloud
$0.045 \leq z \leq 3.452$						
Type-2 AGN	257	104 (40%)	92 (88%) P 12 (12%) D	60 (23%)	49 (82%) P 11 (18%) D	93 (37%)
Galaxies	18040	5380 (29%)	4834 (91%) P 452 (9%) D	3822 (22%)	2434 (83%) P 654 (17%) D	8909 (49%)
$0.8 \leq z \leq 1.2$						
Type-2 AGN	91	31 (34%)	29 (94%) P 2 (6%) D	26 (29%)	19 (73%) P 7 (27%) D	34 (37%)
Galaxies	3750	1183 (32%)	1149 (97%) P 34 (3%) D	790 (21%)	550 (70%) P 240 (30%) D	1777 (47%)

Note – P=Passive, D=Dusty.

developed with the main purpose of disentagling the various contributions (starburst, AGN, host-galaxy emission) in the observed SEDs using a standard χ^2 minimization procedure. The code is based on a large set of starburst templates from Chary & Elbaz (2001) and Dale et al. (2001), and galaxy templates from the Bruzual & Charlot (2003) code for spectral synthesis models, while AGN templates are taken from Silva et al. (2004). These templates represent a wide range of SED shapes and luminosities and are widely used in the literature. The total (nuclear) AGN

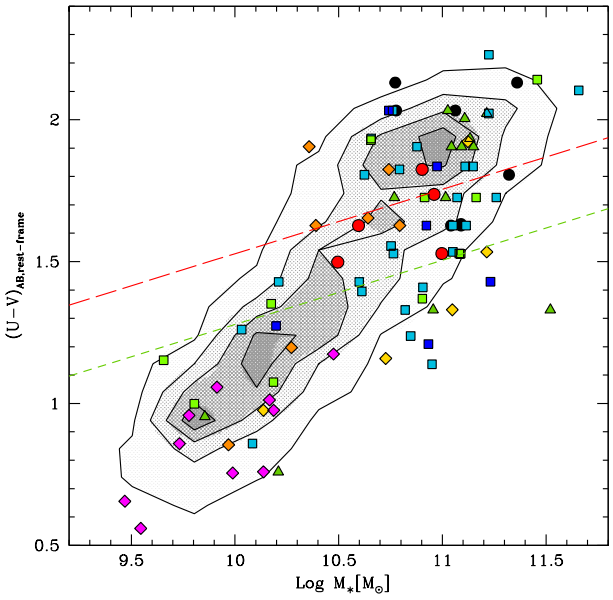

Figure 4.21: Distribution of the stellar masses as a function of of the rest-frame $(U - V)$ colors in the redshift range $0.8 \leq z \leq 1.2$. The red dashed line represents the red sequence cut defined by Borch et al. (2006), while the green short dashed line defines an approximate green valley region, both lines are calculated at redshift $\sim$ 1. The points are color coded as in Fig. 4.18.

bolometric luminosities are then estimated by adding the X–ray luminosities integrated over the 0.5-500 keV energy range to the infrared luminosity between 1 and 1000μm. The total X–ray luminosity is computed integrating the X–ray SED using the de-absorbed soft and hard X–ray luminosities. The SED is extrapolated to higher energies using the observed X–ray slope, and introducing an exponential cut-off at 200 keV. The total infrared luminosity is evaluated integrating the infrared AGN best-fit and then converted into the nuclear accretion disk luminosity applying the appropriate correction factors to account for the geometry and the anisotropy of the torus emission. The reprocessed IR emission is considered to be a good proxy of the intrinsic disk emission and this is supported by previous investigations (Pozzi et al. 2007; Gandhi et al. 2009; Vasudevan et al. 2010). In the distribution of the ratio $r = \mathrm{Log}\left(L_{12.3\ \mu m,\mathrm{obs}}/L_{12.3\ \mu m,\mathrm{predicted}}\right)$ (see Eq. 4.1) the majority of the objects are within 2σ of the r distribution. The tail outside 2σ and extending to high r includes 28 sources (with $r \gtrsim 0.5$) for which the predicted mid-infrared luminosity is significantly lower than observed. We call "low-r" AGN all sources within 2σ of the r distribution, while the "high-r" AGN sample is represented by the sources deviating more than 2 σ.
Our main observational findings are the following:

(1) The average observed SED is characterized by a flat X–ray slope, $\langle\Gamma = 1.12\rangle$, as expected for obscured AGN (not corrected for absorption), while in the optical-UV the observed light appears to be consistent with the host-galaxy emission. The average SED in the mid-infrared is more likely a combination of dust emission from star-forming region and AGN emission reprocessed by the dust.

(2) The full sample is splitted in four bins of different X–ray and infrared luminosities and redshift. The shapes of the average SEDs in the optical bands are approximately the same in all luminosity and redshift bins. There is a stronger host-galaxy contribution at lower luminosity/redshift bins, where the average SEDs have a typical galaxy shape. Moreover, there is a trend between X–ray and mid-infrared luminosity: the contribution of the AGN in the infrared (around $8 - 15\mu$m) is higher at higher X–ray luminosities.

(3) Type-2 AGN appear to have smaller bolometric corrections than Type-1 AGN. At the same hard X–ray luminosity, $43.30 \leq \mathrm{Log}\, L_{[2-10]\mathrm{keV}} \leq 44.30$, where both samples are well represented, we find that the median bolometric correction for Type-2 AGN (69 objects) is $\langle k_{\mathrm{bol}}\rangle \sim 16 \pm 1$, to be compared with a median bolometric correction $\langle k_{\mathrm{bol}}\rangle \sim 23 \pm 1$ for Type-1 AGN (167 objects). The two averages are statistically different at $\sim 5\ \sigma$ level and this is consistent with the results reported in Vasudevan et al. (2010).

(4) A clear separation in bolometric corrections for the low-r and the high-r samples is found. The relation provided by Gandhi and collaborators is valid for the majority of objects, while for 25% of the 112XMM sample SED-fitting procedure may underestimate the non-nuclear contribution. At a given hard X–ray luminosity ($43 \leq \mathrm{Log}\, L_{[2-10]\mathrm{keV}} \leq 44$) the low-$r$ sample has a median bolometric correction of $\langle k_{\mathrm{bol}}\rangle \sim 12 \pm 1$ (52 objects), to be compared with a median bolometric correction for the high-r sample of $\langle k_{\mathrm{bol}}\rangle \sim 36 \pm 3$ (17 objects). The two median values for k_{bol} are statistically different at $\sim 7.6\sigma$ level.

(5) Host-galaxies morphologies and the stellar masses indicate that obscured AGN are preferentially hosted in bulge-dominated galaxies with stellar masses greater than $10^{10} M_{\odot}$.

(6) The distribution of AGN hosts in the rest-frame $(U - V)$ – Log M_* plane is significantly different from that of normal galaxies over the same redshift range. AGN are found in massive galaxies with bluer colors than inactive galaxies of comparable stellar mass (no correction for the internal extinction has been applied to the $(U - V)$ colors). At stellar masses larger than $2.5 \times 10^{10} M_{\odot}$ AGN host-galaxies are bluer than the inactive galaxy population: $\langle U - V \rangle \sim 1.72$ with a dispersion of 0.29 for AGN host-galaxies (189 objects), while $\langle U - V \rangle \sim 1.78$ with a dispersion of 0.31 for inactive galaxies (6457 objects). The two mean values are statistically different at $\sim 3\sigma$ level.

(7) Almost all the sources in the red-sequence have $SSFR^{-1}$ larger than the age of the Universe at their redshift, which is consistent with passive galaxies. Following the same approach as in Cardamone and collaborators (i.e., combining the rest-frame $(U - V)$ vs Log M_* and the rest-frame $(U - V)$ vs $(V - J)$ color diagrams), we find that, consistently with their results, $\sim 50\%$ of AGN hosts lie in the passive region of this diagram. However, differently from Cardamone et al. (2010), only $\sim 27\%$ of AGN host-galaxies in the green-valley in our sample are consistent with dust-obscured sources.

Chapter 5

Models for spheroidal galaxies with a central SMBH

A one-zone evolutionary model is developed to study the co-evolution of supermassive black holes and their host galaxies, as a function of the accretion radiative efficiency, dark matter content, and cosmological infall of gas. In particular, the radiation feedback is computed by using the self-regulated Bondi accretion. The main properties of a set of simulations are also presented. The models are characterized by strong oscillations when the galaxy is in the AGN state with a high accretion luminosity. We found that these one-zone models are able to reproduce two important phases of galaxy evolution, namely an obscured-cold phase when the bulk of star formation and black hole accretion occur, and the following quiescent hot phase in which accretion remains highly sub-Eddington. A Compton-thick phase is also found in almost all models, associated with the cold phase. An exploration of the parameter space reveals that the closest agreement with the present-day Magorrian relation is obtained, independently of the dark matter halo mass, for galaxies with a low-mass seed black hole, and the accretion radiative efficiency $\simeq 0.1$. This Chapter is mainly based on: "*One-zone models for spheroidal galaxies with a central supermassive black-hole. Self-regulated Bondi accretion*"; Lusso E. & Ciotti L.; 2011, A&A, 525, A115.

5.1 Introduction

Elliptical galaxies invariably contain central supermassive black holes (SMBHs), and exists a tight relationship between the characteristic stellar velocity dispersion σ (or stellar mass M_*) of the host system and the SMBH mass $M_{\rm BH}$ (e.g., Magorrian et al. 1998b; Ferrarese & Merritt 2000b; Tremaine et al. 2002b; Yu & Tremaine 2002). These relations clearly indicate a co-evolution of the SMBHs and their host spheroids. Several investigations have been dedicated to this subject, either by using hydrodynamical simulations (e.g., Ciotti & Ostriker 1997, 2001, 2007; Ciotti et al. 2009, 2010) or one-zone models (e.g., Sazonov et al. 2005, hereafter SOCS; Ballero et al. 2008, Matteucci 2008). In some work, the effect of galaxy merging has also been taken into account (e.g., Hopkins et al. 2005, 2006). The main advantage of hydrodynamical models is that complex physical phenomena effects (such as shock waves, jets, radiation trans-

port, etc) can be taken into account. However, the computational time of the simulations force us to search for faster methods that allow a more systematic exploration of the parameter space, which is prohibitive with hydrodynamical simulations. In this framework, hydro-simulations can be used to set the acceptable range for parameters to be adopted in toy models (e.g., the duty cycle value, see Sect. 5.2.1), such as that used here, useful to identify the most interesting cases that can be simulated in detail with hydrodynamical codes.

The general idea behind one-zone models is to work with "average" equations that capture some aspect of a more complicated situation. In practice, some of the equations are exact (such as for example the mass and energy balance equation). On the other hand, some of the physical variables are volume or mass averaged (e.g., the mean gas and temperature of the interstellar medium, respectively), or finally computed at some fiducial radius of the assumed gas distribution. From this point of view, the specific galaxy and dark matter halo profiles do not enter directly into the code, but are needed to obtain realistic mean values to be used in the equations. A preliminary investigation of a physically based one-zone toy model has been done in SOCS, where it is shown that the final $M_{\rm BH}$ produced by feedback clearly reproduces the observed $M_{\rm BH}$-σ relation. The new models discussed here contain important improvements with respect to SOCS. First of all, the modelization of accretion onto SMBH. In this Thesis we examine how the effects of radiation pressure due to the Thomson electron scattering modify in a self-consistent way the spherical Bondi flow. Another improvement is the treatment of Type Ia supernova rates and mass losses due to the evolution of the galactic stellar population, the Kroupa (2001) initial mass function (IMF) coupled with the evolutionary prescription of Maraston (2005) is now adopted. Finally, the dark matter halo is now described by a finite-mass Jaffe (1983) distribution instead of a singular isothermal sphere.

In this scenario, the masses of central SMBH and the host galaxy grow in a dark matter halo, which is replenished by accretion of gas of cosmological origin. We follow star formation and the mass return from the evolving stellar populations is also considered. The combined effect of SNIa heating and radiative feedback, during episodes when the luminosity from the central SMBH approaches its Eddington limit, heats and drives much of the remaining gas out of the galaxy, limiting both future growth of the SMBH and future star formation to low levels. Merging phenomenon are not considered, and the study is restricted to the evolution of an isolated galaxy: it is well known that significant AGN activity may also be present in isolated systems, because of the large amounts of gas produced by passively evolving stellar populations (e.g., Mathews 1983; Ciotti et al. 1991; Bregman & Parriott 2009; Kaviraj et al. 2010; Cisternas et al. 2011). More specifically, the one-zone models discussed in this Chapter are developed as an alternative approach to study the "feedback modulated accretion flows" of Ciotti et al. (2009, 2010). There are two major differences between the present approach and hydro-simulations. The first, and most obvious, is the impossibility to resolve physical phenomena associated with specific length and timescales. The second is that heating feedback only is taken into account, while in the current version of the hydrodynamical code by Ciotti et al. (2009, 2010), both mechanical feedback, and radiation pressure are also considered. However, despite these shortcomings, with the present models we can attempt to simulate the process of galaxy formation, which is beyond the current possibilities of the hydro-simulations and at the same time we can explore the parameter space.

The evolutionary scenario addresses several key observational findings. First, that giant ellipticals are old – they end their period of vigorous star formation early in cosmic time, since the radiative output from the central SMBHs limits (in cooperation with the energetic input due to star formation) the gas content to be at levels for which ongoing star formation is minimal. Secondly, gas-rich, actively star-forming galaxies at redshift $z \sim 3$, including Lyman break galaxies and bright submillimeter SCUBA galaxies, generally exhibit AGN activity (Steidel et al. 2002; Alexander et al. 2003; Alexander 2009; Lehmer et al. 2005; Donley et al. 2010), indicating that their central SMBHs continue to grow. This suggests that the formation of a spheroid probably closely preceeds a quasar shining phase, as verified by spectroscopic observations indicating that quasars occupy metal-enriched environments (e.g., Hamann & Ferland 1999, Schawinski et al. 2009, Wild et al. 2010). The redshift evolution of the quasar emissivity and the star formation history of spheroids is thus expected to have evolved roughly in parallel since $z \sim 3$, which is also consistent with observations (e.g., Haiman et al. 2004, Heckman et al. 2004). Among the most important observational predictions of the model is the length of the so-called "obscured accretion phase" (e.g., Comastri 2004). This phase is defined as the period of time when a high column density is associated with a high accretion rate onto the central SMBH. We also study the relation between the duration of the obscured phase and the corresponding "cold phase" (defined by a low mass-weighted gas temperature), and how they depend on the adopted parameters. Finally, in a large set of models, how the final SMBH mass is related to the final stellar mass, is explored as a function of the dark matter halo mass, the amount of cosmological infall and the accretion rate of the gas, the SMBH accretion radiative efficiency, and finally the initial SMBH mass. Models are in close agreement with the observed Magorrian relation when high efficiencies ($\epsilon \sim 0.1$) and relatively low initial SMBH masses ($M_{\rm BH} \lesssim 10^6 M_\odot$) are assumed.

This Chapter is organized as follows. In Sect. 5.2, the physics adopted in the simulations is presented, with special emphasis on the differences from and improvements on SOCS. Section 5.3 is devoted to the description of the adopted self-regulated accretion model, while in Sect. 5.4 the findings are presented and discussed. The main results are summarized and discussed in Sect. 5.5, while several useful interpolating functions that are used to compute the stellar mass losses and the SNe Ia rate are presented in the Appendix C. A detailed treatment of the self-regulated Bondi accretion is given in Appendix D.

5.2 The model

The new models discussed here contain important improvements with respect to SOCS. First of all, the modelization of accretion onto SMBH. In this Thesis we examine how the effects of radiation pressure due to the Thomson electron scattering modify in a self-consistent way the spherical Bondi flow. Several aspects of this model were described in SOCS and Ciotti & Ostriker (2007), and only the relevant modifications are presented in the following.

5.2.1 The unchanged physics

For completeness, the aspects of the input physics that remain unchanged with respect to SOCS are briefly summarized. The differential equation for the gas mass balance is

$$\dot{M}_{\rm g} = \dot{M}_{\rm inf} - \dot{M}_* - f_{\rm Edd}\,\dot{M}_{\rm BH} - \dot{M}_{\rm esc}. \tag{5.1}$$

The first source term on the right-hand side (r.h.s.) describes the cosmological infall in a pre-existing (and time-independent) dark matter halo

$$\dot{M}_{\rm inf} = \frac{M_{\rm inf}}{\tau_{\rm inf}} e^{-t/\tau_{\rm inf}}, \tag{5.2}$$

where $M_{\rm inf}$ is the total gas mass accreted during the simulation (but in general not equal to the final stellar galaxy mass M_*), and $\tau_{\rm inf}$ is the characteristic infall timescale. A more appropriate description of the cosmological gas infall could be obtained by multiplying the r.h.s. of Eq. (5.2) by a factor $t/\tau_{\rm inf}$ (e.g., Johansson et al. 2009), so that the total infalling mass is unaffected, while the infall starts in a more gentle way. For completeness, some simulation with this different description are performed, and we found (as expected) that for reasonable values of $\tau_{\rm inf}$ the results are not much affected. Therefore, for consistency with SOCS we retain Eq. (5.2). The second source term is the net star-formation rate

$$\dot{M}_* = \dot{M}_*^+ - \dot{M}_*^{\rm w}, \tag{5.3}$$

where

$$\dot{M}_*^+ = \frac{\alpha_* M_{\rm g}}{\tau_*} \tag{5.4}$$

is the instantaneous star-formation rate, and $\dot{M}_*^{\rm w}$ is the mass return by the evolving stellar population (Appendix C.1); following SOCS, in the simulations α_* is fixed to be 0.3. The characteristic star-formation timescale τ_* is defined as

$$\tau_* = \max(\tau_{\rm dyn}, \tau_{\rm cool}), \tag{5.5}$$

where the dynamical timescale $\tau_{\rm dyn}$ is given by Eq. (5.18), and the mean gas cooling time $\tau_{\rm cool}$ is estimated to be

$$\tau_{\rm cool} = \frac{E}{\dot{E}_{\rm C}}. \tag{5.6}$$

In the equation above, $\dot{E}_{\rm C}$ is the fiducial cooling rate given by

$$\dot{E}_{\rm C} = n_{\rm e} n_{\rm p} \Lambda(T) = \left(\frac{\overline{\rho}_{\rm g}}{m_{\rm p}}\right)^2 \frac{X(1+X)}{2} \Lambda(T), \tag{5.7}$$

where $\overline{\rho}_{\rm g}$ is the instantaneous mean gas density (see Sect. 5.2.3),

$$\Lambda(T) = \frac{2.18 \times 10^{-18}}{T^{0.6826}} + 2.706 \times 10^{-47} T^{2.976}\ {\rm erg\,s^{-1}cm} \tag{5.8}$$

is the cooling function (Mathews & Bregman 1978; see also Ciotti & Ostriker 2001), and $X = 0.7$ is the hydrogen mass abundance (for simplicity a complete gas ionization is assumed). In agreement with Eqs. (5.6) and (5.7), the mean gas internal energy is

$$E = \frac{3\overline{\rho}_{\rm g} k_{\rm B} T}{2\mu m_{\rm p}}, \tag{5.9}$$

where $\mu = (0.25 + 1.5X + 0.25Y)^{-1} \simeq 0.62$ is the mean atomic weight. It follows that

$$\tau_{\rm cool} = \frac{8\pi r_{\rm g}^3 k_{\rm B} m_{\rm p}}{\mu X(X+1) M_{\rm g}} \frac{T}{\Lambda(T)}, \tag{5.10}$$

where $M_{\rm g}$ is the instantaneous value of the total gas mass and $r_{\rm g}$ is the gas distribution scale radius (Sect. 5.2.3). The third source term is the total accretion rate onto the SMBH

$$\dot{M}_{\rm BH} = \dot{M}_{\rm BH,acc} + \beta_{\rm BH,*} \dot{M}_*^+. \tag{5.11}$$

The first term describes gaseous accretion (Sect. 5.3), whereas the second term represents the contribution by the coalescence of stellar remnants of massive stars, as discussed in SOCS. The numerical coefficient $f_{\rm Edd} \approx 10^{-2} - 10^{-3}$ needs to be implemented in the one-zone code (which by definition is unable to model the different spatial scales of the problem) to represent the observed time variation of quasars. In practice, $f_{\rm Edd}$ represents the "duty-cycle", and its value is constrained by both observations (e.g. Yu & Tremaine 2002, Haiman et al. 2004) and simulations (Ciotti & Ostriker 2007, Ciotti et al. 2009, 2010). When the thermal energy of the interstellar medium (ISM) of the galaxy is high enough, the gas is able to escape from the dark matter potential well, at a fiducial escape rate computed as

$$\dot{M}_{\rm esc} = \begin{cases} \dfrac{M_{\rm g}}{\tau_{\rm esc}} & T \geqslant \eta_{\rm esc} T_{\rm vir}, \\ \\ 0 & T < \eta_{\rm esc} T_{\rm vir}. \end{cases} \tag{5.12}$$

The parameter $\eta_{\rm esc}$ is of the order of unity, while the expression for $T_{\rm vir}$ is given in the next section. Finally, the escape characteristic timescale is

$$\tau_{\rm esc} = \frac{2 r_{\rm g}}{c_{\rm s}}, \tag{5.13}$$

where $c_{\rm s}$ is the speed of sound and $r_{\rm g}$ is the scale length of the gas distribution (Sect. 5.2.3). Energy input into the ISM is provided by the thermalization of supernova ejecta (both SNII and SNIa). The treatment of SNII is the same as in SOCS, and the new numerical treatment of SNIa is described in Appendix C.2. Additional contributions to the ISM energetics come from the thermalization of red giant winds and radiative feedback due to accretion onto the SMBH. As in SOCS, the average quasar SED obtained from the CRB supplemented by information from individual objects is adopted. We recall that the UV and high energy radiation from a typical

quasar can photoionize and heat a low density gas up to an equilibrium Compton temperature ($T_C \approx 2 \times 10^7$ K) that exceeds the virial temperatures of giant ellipticals. Following SOCS, adiabatic cooling is also considered in the case of gas escaping and heating/cooling due to inflow/outflowing galactic gas. The gas temperature is therefore determined at each time-step by integrating the equation of the internal energy per unit volume

$$\dot{E} = \dot{E}_{H,SN} + \dot{E}_{H,w} + \dot{E}_{H,AGN} - \dot{E}_C + \dot{E}_{ad} + 3\frac{\dot{M}_{inf}\lambda v_{esc}^2 - \dot{M}_{esc}c_s^2}{16\pi r_g^3}, \tag{5.14}$$

where $\dot{E}_{H,SN}$ is the energy due to SNIa and SNII, $\dot{E}_{H,w}$ describes the thermalization of red giant winds, $\dot{E}_{H,AGN}$ is the AGN heating, $\dot{E}_{ad}$ is the adiabatic cooling in the case of galactic winds, and λ is a dimensionless parameter ($0.25 \leqslant \lambda \leqslant 1$). Finally, the gas is forced to remain above 10^4 K.

5.2.2 The dark matter halo

For simplicity, the dark matter (DM) halo in our model is the only contributor to the gravity of the galaxy. In addition, the gas and the stellar density distributions in the simulations are assumed to be proportional to the local (unevolving) DM density distribution, modeled as a Jaffe (1983) profile (Sect. 5.2.3)

$$\rho_h(r) = \frac{M_h}{4\pi}\frac{r_h}{r^2(r_h + r)^2}. \tag{5.15}$$

For a DM halo total mass M_h, the scale length r_h is fixed following Lanzoni et al. (2004). In that paper, 13 massive DM halos obtained from high-resolution cosmological N-body simulations were carefully analyzed. In particular, for each halo the "overdensity radius" r_Δ (sometimes called virial radius) was determined, and it was shown that r_Δ does not differ significantly from the true virial radius r_{vir} of the system (with a scatter $\lesssim 20\%$). Averaging over the 13 clusters reported in Table 2 in Lanzoni et al. (2004), we found that

$$M_h \cong 0.03 r_\Delta^3, \tag{5.16}$$

where M_h is in $10^9 M_\odot$ and r_Δ is in kpc units. For the Jaffe profile $r_{vir} = 2r_h$, and from Eq. (5.16) the scale-length r_h is linked to M_h by assuming $r_{vir} = r_\Delta$. The virial (3D) velocity dispersion associated with Eq. (5.15), is given by

$$\sigma_{vir}^2 = \frac{GM_h}{2r_h}. \tag{5.17}$$

The halo mean circular velocity is estimated as $v_c^2 = 2\sigma_{vir}^2$, and the dynamical time required in Eq. (5.5) is therefore given by

$$\tau_{dyn} = \frac{2\pi r_h}{v_c}. \tag{5.18}$$

5.2.3 The galaxy model

One of the new aspects of the model evolution investigated in this study is the time extent of the Compton thin and Compton-thick phases, as defined at the end of this section. In SOCS, the adopted gas density distribution was a singular isothermal sphere and the major drawback of this choice for the evaluation of average quantities is the divergence of the total mass. For this reason, a more realistic Jaffe density profile is now used, i.e., at each time the gas density distribution is assume to be

$$\rho_{\rm g}(r) = \frac{M_{\rm g}}{4\pi}\frac{r_{\rm g}}{r^2(r_{\rm g}+r)^2}, \tag{5.19}$$

where $r_{\rm g}$ is the gas scale radius and $M_{\rm g}$ is the instantaneous value of the total gas mass, obtained by integrating Eq. (5.1). For simplicity, $r_{\rm g} = r_{\rm h}$ during the whole simulation. However, it is possible to generalize the present approach and consider a time-dependent $r_{\rm g}$.

The mean gas density, which is needed in Eqs. (5.7) and (5.9), is evaluated to be the instantaneous mean value within the half-mass radius $r_{\rm g}$

$$\overline{\rho}_{\rm g} = \frac{3M_{\rm g}}{8\pi r_{\rm g}^3}, \tag{5.20}$$

while the virial gas temperature $T_{\rm vir}$ is obtained from the hydrostatic equilibrium and the Jeans equations solved in the gravitational potential of the DM halo neglecting the self-gravity of the gas. Simple algebra then shows that

$$T_{\rm vir} = \frac{\mu m_{\rm p} G M_{\rm h}}{6 k_{\rm B} r_{\rm g}}. \tag{5.21}$$

To quantify the relative importance of the optically thin and thick phases, the code computes the gas column density as

$$\langle N_{\rm H}\rangle = \frac{M_{\rm Pg}(R)}{2\pi R^2}, \tag{5.22}$$

where $M_{\rm Pg}(R)$ is the projected gas mass enclosed in a circle of radius R, and the factor of 2 at the denominator takes into account that only one side of the gas column actually obscures the center. Therefore, the fiducial column density depends not only on the total gas mass, but also on the aperture radius adopted. To simulate observational work (e.g. Risaliti et al. 1999), we decided to define R to be one hundredth of the effective radius $R_{\rm e}$*, i.e., in Eq. (5.22) $R \cong 0.0074 r_{\rm g}$. From Eq. (C.18)

$$\langle N_{\rm H}\rangle \cong 32.7\frac{M_{\rm g}}{r_{\rm g}^2}, \tag{5.23}$$

and $r_{\rm g}$ is fixed during the simulation, $\langle N_{\rm H}\rangle$ depends only on $M_{\rm g}$. The "thick" phase is defined with $\langle N_{\rm H}\rangle \geq 10^{24}$ cm^{-2}, while galaxies with column density $\langle N_{\rm H}\rangle \geq 10^{22}$ cm^{-2} are considered obscured.

*For the Jaffe model, $R_{\rm e} \cong 0.74 r_{\rm g}$.

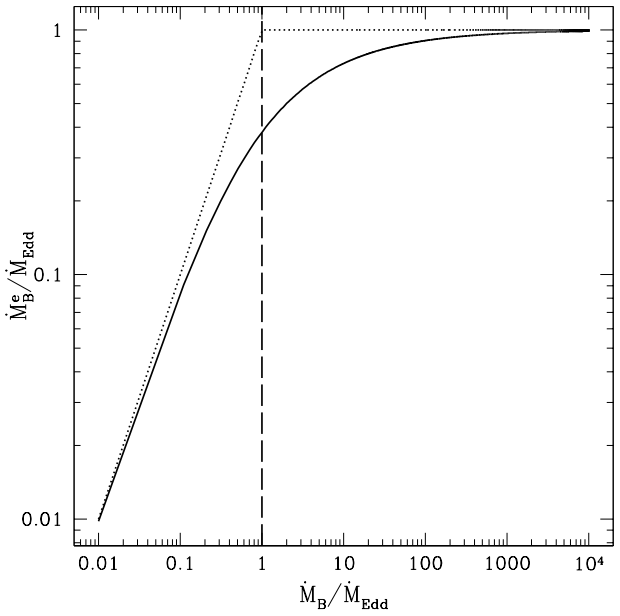

Figure 5.1: The self-regulated Bondi accretion rate $\dot{M}_{\rm B}^{\rm e}$ obtained from Eq. (5.31) is represented by the heavy solid line. The dotted line is the accretion rate determined by Eq. (5.25). Note how for very low and very high Bondi accretion rates $\dot{M}_{\rm B}$, the two prescriptions coincide.

5.2.4 The code

The simulations are performed by numerical integration of the previous evolutionary differential equations using a forward Euler scheme. The numerical code is based on the code developed in SOCS. The time step is defined as the minimum among the characteristic times associated with the different physical processes

$$\delta t = B \min\left(t_{\rm inf}, t_*, t_{\rm g}, t_{\rm BH}, t_{\rm E}\right), \tag{5.24}$$

where the different subscripts indicate the specific aspect of the physics involved and, in general, for a quantity X_i, $t_i \equiv X_i/|\dot{X}_i|$. The dimensionless coefficient $B \leq 1$ is used to improve the code accuracy. Several test simulations have been performed and $B \cong 0.1$ is found to lead a rapid convergence and excellent agreement with results obtained in SOCS, when used with their model galaxies and input physics.

5.3 Self-regulated Bondi accretion

As often assumed in the literature, the SMBH accretion rate is determined as the minimum between the Bondi accretion rate $\dot{M}_{\rm B}$ and Eddington limit $\dot{M}_{\rm Edd}$

$$\dot{M}_{\rm BH,acc} = \min(\dot{M}_{\rm Edd}, \dot{M}_{\rm B}). \tag{5.25}$$

In the previous formula, the Eddington accretion rate is

$$\dot{M}_{\rm Edd} \equiv \frac{L_{\rm Edd}}{\epsilon c^2}, \tag{5.26}$$

where $0.001 \lesssim \epsilon \lesssim 0.1$ is the accretion efficiency, and

$$L_{\rm Edd} = \frac{4\pi c G M_{\rm BH} \mu m_{\rm p}}{\sigma_{\rm T}} \tag{5.27}$$

is the Eddington luminosity and $\sigma_{\rm T}$ is the Thomson cross-section. The classical Bondi accretion rate is

$$\dot{M}_{\rm B} = \lambda_{\rm c} 4\pi\, G^2 M_{\rm BH}^2\, \rho_\infty c_{\rm s,\infty}^{-3}, \tag{5.28}$$

where ρ_∞ and $c_{\rm s,\infty}$ are the gas density and the speed of sound at infinity, respectively, and $\lambda_{\rm c}$ is a dimensionless coefficient of the order of unity (e.g., Bondi 1952, Krolik 1999). In Eq (5.28), radiative effects are not taken into account, so that in Eq. (5.25) there is a sharp transition between the pure hydrodynamical and radiation-dominated regimes. Fortunately, in the optical thin regime dominated by electron scattering, it is possible to extend the classical Bondi accretion solution and take into account the radiation pressure effects, so that the transition between Bondi-limited and Eddington-limited accretion can be described in a more consistent way. After solving this problem, we discovered that is had already been fully described by Taam et al. (1991) and Fukue (2001), and here the main features of the modified accretion model are summarized (see Appendix D for a detailed discussion). The result is obtained basically, by noting that in the optically thin regime the radiation pressure scales as $1/r^2$, thus reducing the effective gravitational force at each radius by the same amount. By imposing self-consistentcy, i.e. by requiring that the effective accretion rate $\dot{M}_{\rm B}^{\rm e}$ is determined by the effective gravity, one finally obtains the following expression for the modified coefficient

$$\lambda_{\rm c,eff} = \lambda_{\rm c} \left(1 - \frac{\dot{M}_{\rm B}^{\rm e}}{\dot{M}_{\rm Edd}}\right)^2 . \tag{5.29}$$

Therefore, the self-consistent Bondi accretion rate satisfies the equation

$$\dot{M}_{\rm B}^{\rm e} = \dot{M}_{\rm B} \left(1 - \frac{\dot{M}_{\rm B}^{\rm e}}{\dot{M}_{\rm Edd}}\right)^2 , \tag{5.30}$$

that can be solved for $\dot{M}_{\rm B}^{\rm e}$. After discarding the unphysical solution, we have

$$\dot{m} \equiv \frac{\dot{M}_{\rm B}^{\rm e}}{\dot{M}_{\rm Edd}} = \frac{1}{2}\left[2 + r - \sqrt{4r + r^2}\right], \quad r \equiv \frac{\dot{M}_{\rm Edd}}{\dot{M}_{\rm B}}. \tag{5.31}$$

For $r \to 0$ (high accretion rates) $\dot{m} \to 1$, so that $\dot{M}_{\rm B}^{\rm e}$ tends to the Eddington accretion, while for $r \to \infty$ (low accretion rates) $\dot{m} \to 0$. The full solution is indicated in Fig. 5.1 by the heavy solid line: note that Eq. (5.25) overestimates accretion onto SMBH in the range $0.1 \leqslant \dot{M}_{\rm B}/\dot{M}_{\rm Edd} \leqslant 100$.

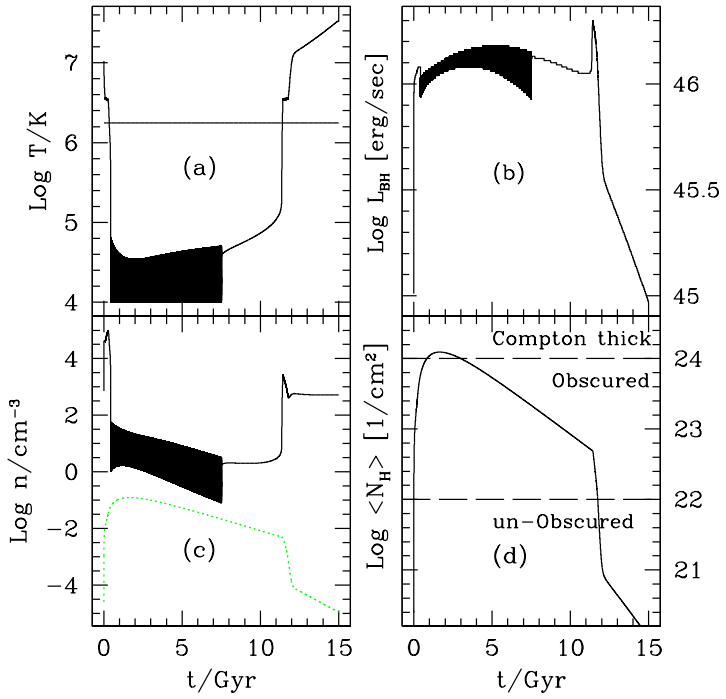

Figure 5.2: The time evolution of relevant quantities of the RM. *Panel a*: gas temperature; the virial temperature of the galaxy is the horizontal dashed line. *Panel b*: bolometric accretion luminosity. *Panel c*: gas density at the Bondi radius (black line) and the mean gas density (green dotted line). *Panel d*: mean gas column density $\langle N_{\rm H} \rangle$ at aperture radius of 0.088 kpc.

5.4 Results

In the following sections, the main properties of a set of simulations are addressed, focusing on three important issues and comparing the new results with those in SOCS. However, before discussing the whole set of the new models, in the next section the evolution of a representative model and three of its possible variants are presented in detail.

5.4.1 Reference model and some of its variants

Figure 5.2 shows the time evolution of important quantities of our galaxy reference model (RM). This model is characterized by a DM halo of total mass $M_{\rm h} = 4 \times 10^{11}\, M_\odot$, which corresponds to a halo scale length $r_{\rm h} = 11.86$ kpc and $R_{\rm e} = 8.83$ kpc, a fiducial circular velocity calculated according to Eq. (5.17) of ~ 270 km/sec, and a characteristic infall time 2 Gyr. The assumed total mass of the cosmological gas infall is $M_{\rm inf} = 10^{11}\, M_\odot$, corresponding to a dark-to-total mass ratio of 80% (provided that all the infalling gas forms stars). Other simulation parameters are $\alpha_* = 0.3$, $\beta_{\rm BH,*} = 1.5 \times 10^{-4}$, $\epsilon = 0.1$, $\eta_{\rm SN} = 0.85$, $\eta_{\rm esc} = 2$, and a stellar mass-to-light ratio of 5 (see Eq. [C.11]). As in SOCS, the initial SMBH mass is $10^8\, M_\odot$; the duty circle, $f_{\rm Edd}$, is fixed at 0.005.

As can be seen from the comparison of Fig. 5.2 with Figs. 7 and 8 in SOCS, the global evolution

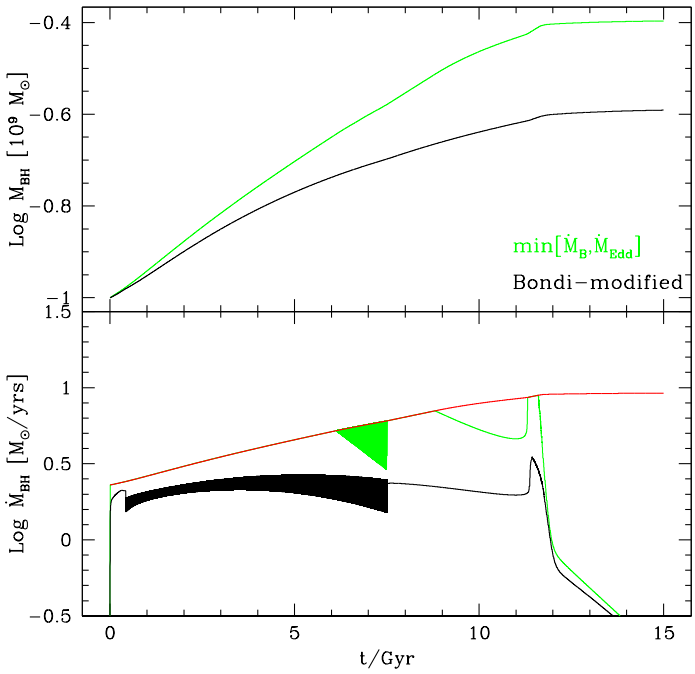

Figure 5.3: The SMBH accretion history of the RM. *Top panel*: time evolution of the SMBH mass as computed according to SOCS (green line) and with the Bondi-modified accretion (black line). *Bottom panel*: SMBH accretion rate from SOCS (green line) and from our work (black line). The red solid line is the Eddington accretion rate for the SOCS model.

of the new models is qualitatively very similar to those in SOCS. In particular, the time evolution of the model, from the beginning up to ~ 9 Gyrs, is characterized by a cold phase (the cold phase is defined as $T_{\rm gas} \leq 10^5$K) of high density and low temperature. The gas density at the Bondi radius remains between 1 and 10^2 particles per cm^3, while the mean gas density is $\sim 10^{-1} - 10^{-2}$ particles per cm^3. At the beginning of the cold phase, about 2.17 Gyrs are spent in the Compton-thick phase (see Fig. 5.2d). The remaining part of the cold phase is obscured, while the accretion luminosity remains high, at $L_{\rm BH} \gtrsim 10^{46}$ erg/sec. As soon as the mean gas density decreases (Fig. 5.2c green dotted line) the cooling becomes inefficient, the gas heating dominates, and the temperature increases to the virial temperature. The total duration of the cold phase is ~ 9 Gyr, which corresponds to a decrease in $\langle N_{\rm H} \rangle$ of about 2 orders of magnitude. The obscured phase lasts ~ 9.6 Gyr, while subsequently the galaxy is not obscured with an average column density around $\langle N_{\rm H} \rangle \sim 10^{20}$ cm^{-2}. The durations of the cold and the obscured phases are very similar, and indeed, the two phases are related. Until the gas density is high, the gas can radiate efficiently the energy input due to the AGN, and its temperature remains below 10^5 K. Because of this large amount of cold gas, the star formation proceeds at high rates, until most of the gas is consumed. At this point, the radiative cooling of the gas becomes inefficient and the heating due to the AGN causes the gas temperature to increase. The combined effects of the gas consumption and the increase temperature stop the star formation. A specific feature of the cold phase can be seen in Fig. 5.2, where characteristic temperature oscillations are apparent. These oscillations, already presented and discussed in SOCS, are due to the combined effect of gas cooling and AGN feedback. They terminate when the gas density falls below some threshold determined by the cooling function and because less and less gas is produced by stars and accreted by the

Table 5.1: Final properties of the RM and its variants at 15 Gyrs.

Model	M_*	$M_{\rm esc}$	$M_{\rm BH}$	$M_{\rm BH}/M_*$	$\log\langle N_{\rm H}\rangle$	$\Delta t^1_{\rm cold}$	$\Delta t^2_{\rm cold}$	$\Delta t_{\rm CT}$	$\Delta t_{\rm obs}$	$\Delta t_{\rm unobs}$
RM	93.22	6.56	0.256	2.75×10^{-3}	20.05	10.42	7.94	2.17	9.57	3.26
RM_1	92.47	6.62	0.945	1.02×10^{-2}	20.04	10.37	7.91	2.13	9.56	3.31
RM_2	42.65	7.21	0.214	5.01×10^{-3}	19.63	8.42	5.78	0.00	10.33	4.67
RM_3	192.97	6.69	0.321	1.67×10^{-3}	20.46	12.04	9.69	4.92	8.17	1.91
RM_4	90.59	5.55	0.288	3.18×10^{-3}	22.81	14.20	10.47	0.00	14.99	0.01

Note – All masses are in $10^9 M_\odot$ units. $M_{\rm BH}$ is the final black hole mass; M_* is the final stellar mass; $M_{\rm esc}$ is the total escaped gas mass. The average column density is in $\rm cm^{-2}$. $\Delta t_{\rm CT}$, $\Delta t_{\rm obs}$, and $\Delta t_{\rm unobs}$ represent the durations (in Gyr) of the Compton-thick phase, of the obscured phase, and the unobscured phase, respectively. Finally, $\Delta t^1_{\rm cold}$ and $\Delta t^2_{\rm cold}$ are the durations (in Gyr) measured assuming threshold temperatures of 10^5 K and 5×10^4 K, respectively.

galaxy, while SNIa heating declines less strongly. When the density is high (at early times), the cooling time is instead, very short, and AGN heating is radiated efficiently. The two competitive effects produce the temperature (and density) oscillations. In the hydro-simulations, the spatial and temporal structures of these oscillations is quite complicated, as feedback and cooling act on several different spatial and temporal scales (from a month to 10 Myr). In the one-zone models, the oscillations are instead dependent on the "duty-cycle" parameter $f_{\rm Edd}$ in Eq. (5.1), which is constrained by observational and theoretical studies (see Sect. 5.2.1).

To summarize, the observational properties of the RM would correspond to a system initially Compton-thick for $\sim$ 2.2 Gyrs, that then switches to an obscured phase for 9.6 Gyrs, while in the last 3.2 Gyrs the galaxy is unobscured. The SMBH accretion history is shown in Fig. 5.3, where it is compared to that predicted by the SOCS formulation in a model otherwise identical to the RM. The major difference between the two models is in the final value of $M_{\rm BH}$: in particular, Eq. (5.25) would predict a present-day $M_{\rm BH}$ a factor $\sim$ 1.5 higher than that for modified accretion. This is because the accretion in SOCS remains for almost all of the galaxy life, at the Eddington limit, while in the new treatment the self-regulation maintains the accretion at lower rates.
Before presenting the results of a global exploration of the parameter space, we focus on a few obvious questions. For example, what happens if all model parameters are fixed and only the radiative accretion efficiency is reduced? What happens if we increase or decrease the total mass of infalling gas? Or if we double the gas infalling time? Of course, these simple examples do not cover all the possible cases. However, these models will provide a guide as we investigate the parameter space. The relevant properties of the additional "reference" models are listed in Table 5.1.

The first variant of the RM model is model RM_1 obtained by reducing the radiative accretion efficiency from $\epsilon = 0.1$ to $\epsilon = 0.001$. Overall, this reduced efficiency model passes through the same evolutionary phases as model RM: an initial Compton-thick phase, followed by an obscured phase, and finally a low-density unobscured phase. The initial cold high density phase is also very similar to that of RM in Fig. 5.2. The most important and expected difference is in

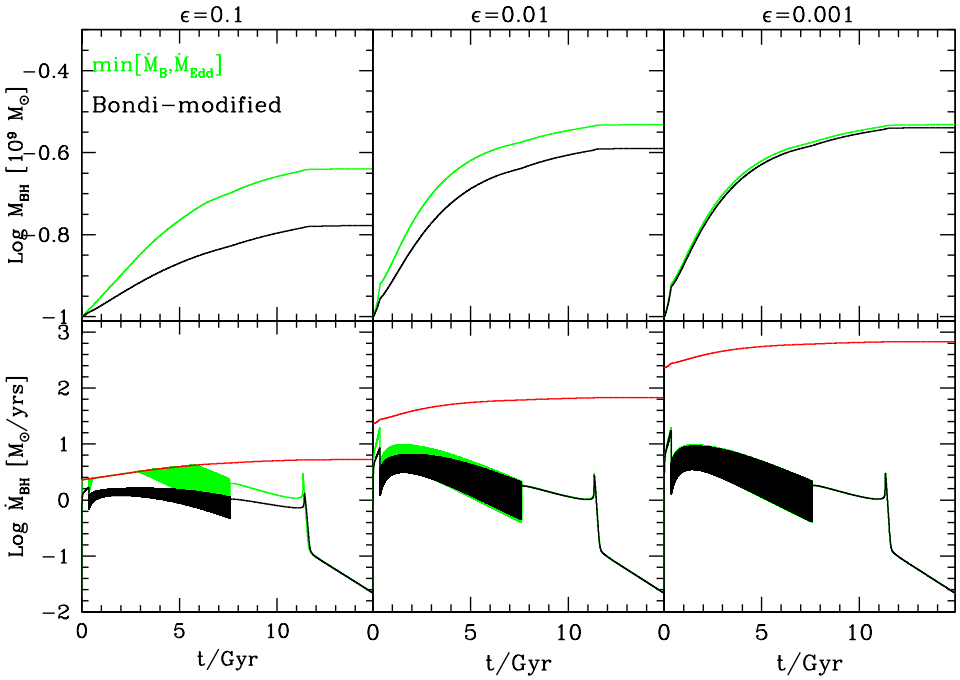

Figure 5.4: Evolution of the SMBH mass and accretion rate computed according to Eq. (5.25) (green line, SOCS) and Eq. (5.30) (black line) for a model with $M_{\rm inf} = 1.25 \times 10^{10} M_\odot$, $M_{\rm h} = 5 \times 10^{10} M_\odot$, and initial SMBH mass of $10^8 M_\odot$. From left to right: $\epsilon = 0.1$, $\epsilon = 0.01$, and $\epsilon = 0.001$. The red line represents the Eddington limit for the SOCS model.

the final mass of SMBH, which is higher by a factor of ≈ 3.5 than the RM. A reduction in the radiative efficiency also produces a slightly larger amount of escaped gas, because of the shorter cold phase. As a consequence, a larger amount of gas produced by the evolving stars is lost from the galaxy during the low-density, hot phase.

The effect of a reduction in $M_{\rm inf}$ is explored in model $\rm RM_2$, while all the others parameters are the same as in RM. Qualitatively, the evolution is again very similar to that of RM in Fig. 5.2. The main difference is the absence of the initial Compton-thick phase because of the lower gas density. Both the final stellar mass and final SMBH mass are lower than in model RM, as can be seen from Table 5.1. Overall, model $\rm RM_2$ does not display remarkable or unexpected properties. The only noticeable aspect is that the escaped mass is higher than in model RM, but this is again due to the shorter cold phase.

A complementary model to $\rm RM_2$ is $\rm RM_3$, where the value of $M_{\rm inf}$ is doubled while maintaining all the other parameters identical to those of model RM. The qualitative evolution is again similar to that of RM in Fig. 5.2, but, at variance with $\rm RM_2$, the Compton-thick phase is now present. Not surprisingly, the Compton-thick phase in model $\rm RM_3$ extends for a longer period (~ 5 Gyrs) than in the other variants of RM (see Table 5.1), and its total mass of new stars is also the highest. However, the total mass that escapes is not as high as one would expect, the infall mass being a factor of 2 higher than in the RM yet the escaped mass being almost the same. The main reason

for this behaviour is the very massive star formation, which is almost twice that of RM. Note that model RM_3 is the closest, in the RM family, to the galaxy models studied in the hydrodynamical simulations of Ciotti et al. (2009, 2010), as far as the final stellar mass and the final M_{BH} are concerned.
We finally discuss model RM_4, which is identical to model RM, but has twice as long an infall time. The main effects are the longest cold phase in RM family (see Table 5.1), and the absence of the initial Compton-thick phase. This latter characteristic is due to the time dilution of the infalling gas density, which prevents the possibility of reaching very high column density values. Overall, the final SMBH mass is not affected significantly by the extended infall phase, but its escaped gas masses is quite high because the total mass in new stars is (as expected) lower than in the RM model.
To summarize, these preliminary experiments have revealed that, at fixed dark matter halo, sensible variations in the input parameters (ϵ, M_{inf} and τ_{inf}) do not produce remarkable different results. The relevant differences are found mainly in the amount of star formation and the different durations of the cold and obscured phases, while the final SMBH mass appears to be mainly affected by the value of the radiative efficiency ϵ.

5.4.2 Exploring the parameter space

We now present the general results (summarized in Tables 5.2 and 5.3) of our examination of the parameter space. The SMBH initial mass in the models in Table 5.2 is $10^8 M_\odot$, while in Table 5.3 it is $10^5 M_\odot$. From the astrophysical point of view, the first choice mimics a scenario in which the central SMBHs are already quite massive at the epoch of galaxy formation, while in the second case the main growth occurs with galaxy formation. Each of the 5 main families of models (M_1, ..., M_5) consists of galaxy models characterized by the same dark halo mass, M_h, ranging from $10^{10} M_\odot$ (the M_1 family) up to $10^{12} M_\odot$ (the M_5 family). In each family, six models have been investigated with different values of infalling gas-to-dark matter ratio $\alpha = M_{inf}/M_h$, and finally different radiative efficiencies ϵ in the self-regulated Bondi accretion. In practice, in each family the effects of different total infalling gas mass and different efficiencies (spanning the commonly accepted range of values) are explored at fixed M_h.
Almost independently of M_h and the initial value of M_{BH}, some general trends can be recognize. For example in each group of 3 models characterized by identical parameters but decreasing ϵ, it is apparent how the total amount of stars formed decreases at decreasing ϵ, while the final M_{BH} increases. In the total mass budget of the galaxy, an important quantity is the total mass of gas ejected, M_{esc}. As expected, we find that massive galaxies, with larger infall gas masses also eject more mass. However, in all cases, the escaped gas mass is much lower than the final stellar mass, i.e., $\sim 10\%$ of it.
Finally, higher final gas masses are obtained, at fixed M_h, for higher M_{inf} and lower efficiencies, because of the less effective feedback. Note however that the product of ϵ and the mass accreted by the SMBH decreases with decreasing ϵ, i.e., even though the accreted mass is higher, the integrated energy output is lower, and so is the feedback effect[†].

[†]The higher SMBH masses account for the slightly lower final stellar masses. The mass conservation of the

A qualitative illustration of the effect of the reduction in ϵ on the SMBH accretion history is shown in Fig. 5.4. When the efficiency decreases, the final mass of the SMBH increases and, the corresponding evolution of identical models, but with the SOCS treatment, is indicated by the green line, i.e., where the accretion is determined by the minimum of $\dot{M}_{\rm B}$ and $\dot{M}_{\rm Edd}$. The differences in $M_{\rm BH}$ reduce with decreasing ϵ, because the Eddington accretion regime in the SOCS models (when the major differences from the Bondi-modified case are established), becomes less and less important, and $\dot{M}_{\rm B}^{\rm e}$ approches $\dot{M}_{\rm B}$.

All models have a transition phase from obscured to unobscured. The Compton-thick phase is present in almost all models that have a cold phase (18 of 30 simulations); however, in the less massive set of models (M_1) the Compton-thick phase is absent. This is consistent with the scenario in which the majority of the most massive black holes spend a significant amount of time growing in an earlier obscured phase (see Kelly et al. 2010; Treister et al. 2010).

Finally, the mean SMBH-to-star ratio is not far from the value inferred from the present-day Magorrian et al. (1998b) relation, though on the high mass side. This is not surprising, because of our use of a one-zone model. In any case, we emphasize that the SMBH feedback in the models was able to remove (in combination with star formation and/or gas escape) most of the infalling gas (which, if accreted onto the central SMBH in a cooling-flow like solution, would lead to the final SMBH masses being ~ 2 orders of magnitude higher than the observed ones).

Independent of the particular characteristics of the single models, Fig. 5.5 clearly illustrates that the final SMBH masses, in models with a quite high initial $M_{\rm BH}$ (Table 5.2), are higher than implied by the observed Magorrian relation. For this reason, other families of models are explored, in which the initial mass of the SMBH was reduced to $10^6 M_\odot$, $10^5 M_\odot$, and $10^3 M_\odot$. From Fig. 5.5, it is apparent how galaxy models with initial SMBH masses $\lesssim 10^6 M_\odot$ (circles) closely agree to within 1σ of the observed dispersion with observations, but only when the radiative efficiency is high, i.e. $\epsilon = 0.1$. It is even more remarkable that the final SMBH mass is proportional to the final M_*, as all the models started with the same initial SMBH mass. This strongly indicates that co-evolution is the most plausible explanation of the proportionality between M_* and $M_{\rm BH}$, in line with other observational evidence (e.g., see Haiman et al. 2004 and references therein).

To compare our present findings with those of a complementary hydrodynamical approach, in Fig. 5.5 the results of the high-resolution hydro-simulations developed by Ciotti et al. (2010, Table 1, Cols. 5 and 6) are plotted for a representative galaxy with stellar mass of $\sim 3 \times 10^{11} M_\odot$. The final $M_{\rm BH}$ are represented by crosses, and the different (luminosity weighted) radiative efficiencies are in the range $0.003 \leq \epsilon \leq 0.133$. Note that the crosses indicate almost all the hydrodynamical models that have been studied in detail so far, and this shows the importance of one-zone models as a complementary approach to exploring the parameter space. Also note that the final mass of the SMBHs, as computed in the hydrodynamical simulations, lead to an accurate reproduction of the Magorrian relation but the comparison with the one-zone models is delicate. In the hydrodynamical simulations (at variance with the one-zone models), the initial phases of galaxy formation are not simulated, and the focus is on the maintaining low SMBH masses in the presence of stellar mass losses that, if accreted onto the central SMBH as in an

code is quite remarkable, considering the amount of input physics involved ($M_{\rm inf} = M_* + M_{\rm esc} + M_{\rm BH}$).

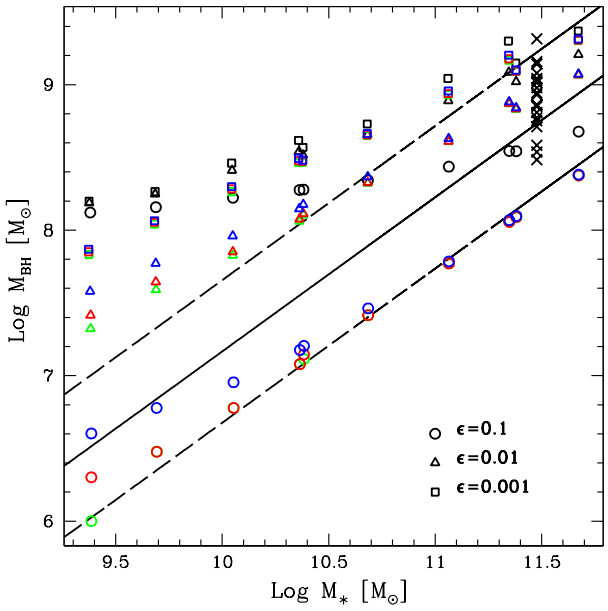

Figure 5.5: Final SMBH mass versus final stellar mass for all the explored models. The solid line is the Marconi & Hunt (2003) best-fit of the Magorrian (1998) relation, and the two dashed lines represent the associated 1-σ deviation. Different colors indicate different initial masses of the $M_{\rm BH}$, i.e. $10^3 M_\odot$ (green), $10^5 M_\odot$ (red, models in Table 5.3), $10^6 M_\odot$ (blue), and $10^8 M_\odot$ (black, models in Table 5.2). Different symbols identify the adopted value for radiative efficiency: $\epsilon = 0.1$ (circles), $\epsilon = 0.01$ (triangles), and $\epsilon = 0.001$ (squares). The black crosses are the hydrodynamical models in Table 1 of Ciotti et al. (2010).

undisturbed cooling flow, would produce a final BH mass of about a factor of ∼100 higher than the observed ones. For this reason, in the hydrodynamical models the galaxy is already assumed to have formed, and the initial mass of the SMBH is just slightly lower than the mass predicted by the Magorrian relation.

The optimal combination of parameters, in order to reproduce the Magorrian relation, is to assume a quite low initial SMBH mass and a quite high radiative efficiency. To show that this is really the case, few specific models are performed, with radiative efficiencies in a smaller range of values, obtaining the reproduction of the Magorrian relation. Galaxies with different initial $M_{\rm BH}$ seeds ($M_{\rm BH} = 10^3, 10^4, 10^5, 10^6 M_\odot$) have been simulated with radiative efficiencies in the range $\epsilon = 0.1 - 0.02$. The results are plotted in Fig. 5.6. Below Log $M_* = 10.5 M_\odot$ the relation is perfectly reproduced, above this stellar mass value there is a tendency to have BH masses below the local magorrian relation. In order to cover the region above $M_{\rm BH} = 10^8 M_\odot$ a radiative efficiency of the order of 0.01 or lower is required, as shown in Fig. 5.5.

5.5 Conclusions

This analysis is a natural extension of a previous paper by Sazonov et al. (2005). From a technical point of view, several aspects of the input physics have been improved. In particular, we have adopted a different description of the accretion rate, which now follows the self-consistent modified Bondi theory (Taam et al. 1991; Fukue 2001), instead of the minimum between the Eddington and the (classical) Bondi rate. Moreover, the SNIa rate is now computed using a high-precision multi-exponential approximation for the time-kernel in the convolution integral of the star formation rate, instead of the standard power-law. This avoids the need to store the entire star formation history and permits more rapid numerical simulations. The time-dependent

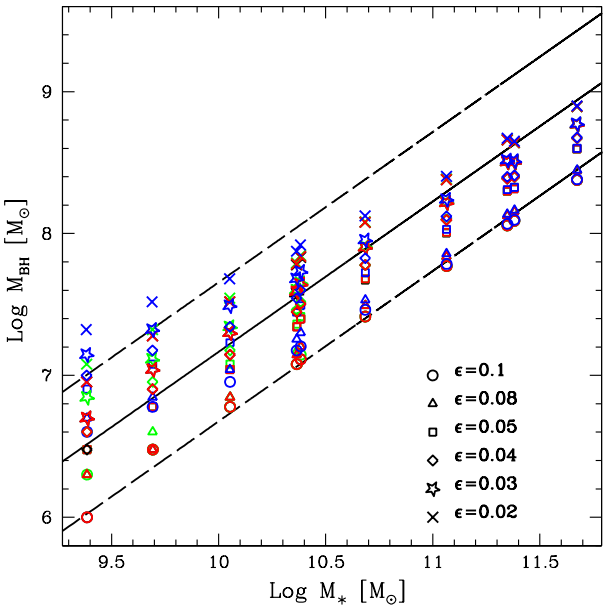

Figure 5.6: Final SMBH mass versus final stellar mass for models with efficiencies in the range $\epsilon = 0.1 - 0.02$. Different colors indicate different initial masses of the $M_{\rm BH}$, i.e. $10^3 M_\odot$ (green), $10^4 M_\odot$ (red), $10^5 M_\odot$ (blue), and $10^6 M_\odot$ (black). Different symbols identify the adopted value for radiative efficiency: $\epsilon = 0.1$ (circles), $\epsilon = 0.08$ (triangles), $\epsilon = 0.05$ (squares), $\epsilon = 0.04$ (diamonds), $\epsilon = 0.03$ (stars) and $\epsilon = 0.02$ (crosses).

mass return rate from the evolving stellar population is now computed using the Kroupa (2001) initial mass function and the mass return rate as a function of the stellar mass given by Maraston (2005), instead of the Ciotti et al. (1991) formulae. For the stellar mass-return rate, we also numerically implemented a multi-exponential fit. Finally, the dark-matter potential well (and the galaxy stellar distribution) are now described as Jaffe (1983) models.
From the astrophysical point of view, in addition to the standard outputs considered in SOCS (e.g. final SMBH mass, final stellar mass, etc), we now also focus on the duration of the "cold phase", of the "obscured phase", and the "Compton thick phase" as fiducially computed using the gas temperature and the column density of cold gas. The main parameters adopted to fix a model are the dark-matter halo mass (distributed to reproduce cosmological expectations), the amount of gas deemed to flow onto the dark matter halo, and finally the radiative accretion efficiency. As a separate parameter, the initial mass of the central SMBH is also considered. After some preliminary model exploration and verifying that the new treatment, when applied to the SOCS galaxy model reproduces the previous results, an extensively exploration of the parameter space is performed.
Our main results can be summarized as follows:

(1) Almost independently of the dark matter halo mass and the radiative efficiency, the computed galaxy models have an initial phase that extends for some Gyrs, in which the gas temperature is low and the gas density is high. These galaxies would be defined obscured quasars, where the gas column density is measured within an aperture radius of the order of $R_{\rm e}/100$.

(2) At late times, all the SMBHs are found to be in a low accretion state without much feedback, and the ISM is overall optically thin. The galactic ISM is at about the virial tem-

perature of the dark matter potential well and should be emitting in X-rays, as found for elliptical galaxies in the local universe.

(3) Interestingly, only a specific class of models, are found to agree with the observed Magorrian relation, i.e. only those with low initial SMBH masses ($\lesssim 10^6 M_\odot$) and high radiative accretion efficiency, $\epsilon \sim 0.1$. Higher initial SMBH masses, or lower radiative efficiencies lead to final SMBH masses that are too high. Therefore, this result implies that the seed SMBHs should be quite small, but that their mass accretion should occur mainly with high radiative efficiency, in agreement with observational findings.

(4) In addition, we have also shown how the self-regulated Bondi accretion recipe can be easily implemented in numerical codes, and how it leads to a lower SMBH mass accretion than the more common "on-off" Eddington regulation.

A series of final comments are in order. The first is that the presented one-zone models seem to be able to reproduce, without much fine tuning, two different phases of galaxy evolution, namely a first obscured phase where much of the SMBH accretion and star formation occurs, followed by a hot phase in which SMBH accretion is highly sub-Eddington and star formation is (almost) entirely absent. The robustness of the two-phase evolution, characterized both by one-zone and hydrodynamical simulations is mainly due to the combined effect of (1) the secular decrease in the mass return rate from the evolving stellar populations, (2) the time dependence of the SNIa heating (after the first Gyrs of evolution), and (3) the cooling function, which are identical in the hydrodynamical and the one-zone models. The increase in the specific ISM heating with increasing time, and that a substantial degassing occurs only when the gas temperature is roughly higher by a factor of ~ 4 than the virial temperature, leads to the appearance of the two phases in the two types of model.

The second is that to reproduce the present-day Magorrian relation, the optimal combination of parameters is a quite low initial SMBH mass and a quite high radiative efficiency. We propose that this represents a useful constrain of semi-analytical investigations (also in the context of high-z galaxy merging). As a side-product of this work, we also anticipate that the presented multi-exponential fit for stellar evolution and SNIa heating will be useful in both hydrodynamical and semi-analytical works.

Table 5.2: Final properties of models with self-regulated Bondi accretion with an initial SMBH mass of $10^8 M_\odot$. All masses are in units of $10^9 M_\odot$.

$M_{\rm inf}$	α	ϵ	M_*	$M_{\rm esc}$	$M_{\rm BH}$	$M_{\rm BH}/M_*$	$\log\langle N_{\rm H}\rangle$	$\Delta t^1_{\rm cold}$	$\Delta t^2_{\rm cold}$	$\Delta t_{\rm CT}$	$\Delta t_{\rm obs}$	$\Delta t_{\rm unobs}$
						$M_1 = 10$						
2.5	0.25	0.1	2.40	0.07	0.132	5.51×10^{-2}	18.95	10.74	8.39	0.00	11.29	3.71
2.5	0.25	0.01	2.38	0.07	0.154	6.45×10^{-2}	18.94	10.69	8.35	0.00	11.23	3.77
2.5	0.25	0.001	2.37	0.07	0.158	6.67×10^{-2}	18.94	10.68	8.35	0.00	11.22	3.78
5.0	0.5	0.1	4.88	0.07	0.144	2.95×10^{-2}	19.36	12.18	9.96	0.00	12.70	2.30
5.0	0.5	0.01	4.85	0.07	0.177	3.65×10^{-2}	19.35	12.13	9.92	0.00	12.64	2.36
5.0	0.5	0.001	4.84	0.07	0.184	3.80×10^{-2}	19.35	12.12	9.92	0.00	12.64	2.36
						$M_2 = 50$						
12.5	0.25	0.1	11.23	1.20	0.167	1.49×10^{-2}	19.43	10.51	8.11	0.00	11.45	3.55
12.5	0.25	0.01	11.12	1.21	0.257	2.32×10^{-2}	19.42	10.45	8.07	0.00	11.39	3.61
12.5	0.25	0.001	11.07	1.23	0.289	2.61×10^{-2}	19.42	10.45	8.06	0.00	11.38	3.62
25.0	0.5	0.1	24.10	0.79	0.190	7.90×10^{-3}	19.84	12.15	9.87	2.31	10.55	2.14
25.0	0.5	0.01	23.96	0.80	0.328	1.37×10^{-2}	19.83	12.10	9.84	2.29	10.51	2.20
25.0	0.5	0.001	23.92	0.80	0.370	1.55×10^{-2}	19.83	12.10	9.84	2.29	10.52	2.20
						$M_3 = 100$						
25.0	0.25	0.1	23.07	1.82	0.189	8.18×10^{-3}	19.64	10.53	8.11	0.00	11.51	3.49
25.0	0.25	0.01	22.91	1.83	0.346	1.51×10^{-2}	19.63	10.48	8.07	0.00	11.45	3.55
25.0	0.25	0.001	22.84	1.84	0.414	1.81×10^{-2}	19.63	10.48	8.07	0.00	11.45	3.55
50.0	0.5	0.1	48.34	1.51	0.220	4.55×10^{-3}	20.05	12.14	9.84	3.33	9.58	2.08
50.0	0.5	0.01	48.10	1.52	0.452	9.40×10^{-3}	20.04	12.09	9.80	3.32	9.55	2.14
50.0	0.5	0.001	48.00	1.53	0.536	1.12×10^{-2}	20.04	12.09	9.81	3.31	9.55	2.14
						$M_4 = 500$						
125.0	0.25	0.1	115.84	8.91	0.273	2.36×10^{-3}	20.11	10.37	7.87	2.51	9.33	3.15
125.0	0.25	0.01	115.38	8.87	0.776	6.73×10^{-3}	20.10	10.32	7.84	2.50	9.29	3.21
125.0	0.25	0.001	114.95	8.97	1.104	9.61×10^{-3}	20.10	10.32	7.84	2.48	9.31	3.21
250.0	0.5	0.1	240.57	9.03	0.349	1.45×10^{-3}	20.52	12.01	9.65	5.14	8.01	1.84
250.0	0.5	0.01	239.84	9.06	1.048	4.37×10^{-3}	20.51	11.98	9.63	5.13	7.98	1.89
250.0	0.5	0.001	239.42	9.12	1.407	5.88×10^{-3}	20.52	11.98	9.63	5.12	7.99	1.89
						$M_5 = 1000$						
250.0	0.25	0.1	222.85	26.74	0.350	1.57×10^{-3}	20.31	10.09	7.53	3.31	9.18	2.50
250.0	0.25	0.01	222.06	26.68	1.216	5.48×10^{-3}	20.30	10.05	7.51	3.30	9.08	2.61
250.0	0.25	0.001	220.80	27.16	1.994	9.03×10^{-3}	20.30	10.04	7.50	3.28	9.10	2.62
500.0	0.5	0.1	471.83	27.47	0.476	1.01×10^{-3}	20.72	11.85	9.44	5.78	7.77	1.45
500.0	0.5	0.01	470.52	27.66	1.613	3.43×10^{-3}	20.71	11.82	9.43	5.77	7.71	1.52
500.0	0.5	0.001	469.62	27.85	2.336	4.97×10^{-3}	20.71	11.83	9.43	5.77	7.72	1.52

Note – The halo mass $M_{\rm h}$ is $(10^{10}, 5\times10^{10}, 10^{11}, 5\times10^{11}, 10^{12})\ M_\odot$ for models M_1, M_2, M_3, M_4, and M_5, respectively. The total infall gas mass is $M_{\rm inf} = \alpha M_{\rm h}$. $M_{\rm BH}$ is the final SMBH mass (also with the contribution of the initial SMBH mass). M_* is the final stellar mass. $M_{\rm esc}$ is the total escaped gas mass. The average column density is in $\rm cm^{-2}$. $\Delta t_{\rm CT}$, $\Delta t_{\rm obs}$, and $\Delta t_{\rm unobs}$ represent the duration (in Gyrs) of the Compton-thick phase, the obscured phase, and the unobscured phase, respectively. Finally, $\Delta t^1_{\rm cold}$ and $\Delta t^2_{\rm cold}$ are the durations (in Gyr) measured assuming threshold temperatures of 10^5 K and 5×10^4 K, respectively.

Table 5.3: Final properties of models with self-regulated Bondi accretion with an initial SMBH mass of $10^5 M_\odot$. All masses are in units of $10^9 M_\odot$.

$M_{\rm inf}$	α	ϵ	M_*	$M_{\rm esc}$	$M_{\rm BH}$	$M_{\rm BH}/M_*$	$\log\langle N_{\rm H}\rangle$	$\Delta t^1_{\rm cold}$	$\Delta t^2_{\rm cold}$	$\Delta t_{\rm CT}$	$\Delta t_{\rm obs}$	$\Delta t_{\rm unobs}$
						$M_1 = 10$						
2.5	0.25	0.1	2.43	0.06	0.002	6.72×10^{-4}	18.98	10.94	8.50	0.00	11.51	3.49
2.5	0.25	0.01	2.41	0.07	0.026	1.06×10^{-2}	18.94	10.70	8.37	0.00	11.24	3.76
2.5	0.25	0.001	2.36	0.07	0.071	3.02×10^{-2}	18.93	10.64	8.31	0.00	11.18	3.82
5.0	0.5	0.1	4.93	0.07	0.003	6.39×10^{-4}	19.39	12.36	10.06	0.00	12.91	2.09
5.0	0.5	0.01	4.88	0.07	0.044	9.01×10^{-3}	19.35	12.11	9.90	0.00	12.62	2.38
5.0	0.5	0.001	4.81	0.07	0.113	2.35×10^{-2}	19.34	12.09	9.88	0.00	12.60	2.40
						$M_2 = 50$						
12.5	0.25	0.1	11.32	1.17	0.006	5.51×10^{-4}	19.45	10.61	8.16	0.00	11.55	3.45
12.5	0.25	0.01	11.23	1.19	0.071	6.36×10^{-3}	19.43	10.47	8.09	0.00	11.39	3.61
12.5	0.25	0.001	11.10	1.20	0.192	1.73×10^{-2}	19.42	10.44	8.06	0.00	11.37	3.63
25.0	0.5	0.1	24.19	0.78	0.014	5.60×10^{-4}	19.86	12.23	9.92	2.32	10.63	2.05
25.0	0.5	0.01	24.06	0.79	0.130	5.41×10^{-3}	19.83	12.09	9.84	2.32	10.48	2.21
25.0	0.5	0.001	23.90	0.79	0.297	1.24×10^{-2}	19.83	12.09	9.83	2.28	10.51	2.21
						$M_3 = 100$						
25.0	0.25	0.1	23.18	1.79	0.012	5.31×10^{-4}	19.65	10.60	8.14	0.00	11.58	3.42
25.0	0.25	0.01	23.06	1.81	0.119	5.16×10^{-3}	19.63	10.49	8.09	0.00	11.45	3.55
25.0	0.25	0.001	22.87	1.82	0.300	1.31×10^{-2}	19.63	10.47	8.07	0.00	11.44	3.56
50.0	0.5	0.1	48.44	1.50	0.026	5.42×10^{-4}	20.06	12.19	9.86	3.34	9.64	2.02
50.0	0.5	0.01	48.24	1.52	0.212	4.40×10^{-3}	20.04	12.08	9.80	3.33	9.52	2.15
50.0	0.5	0.001	48.00	1.52	0.452	9.42×10^{-3}	20.04	12.08	9.80	3.31	9.55	2.14
						$M_4 = 500$						
125.0	0.25	0.1	116.05	8.82	0.059	5.07×10^{-4}	20.12	10.39	7.88	2.52	9.35	3.13
125.0	0.25	0.01	115.67	8.85	0.407	3.52×10^{-3}	20.10	10.33	7.85	2.51	9.28	3.21
125.0	0.25	0.001	115.21	8.86	0.868	7.54×10^{-3}	20.10	10.32	7.84	2.49	9.29	3.22
250.0	0.5	0.1	240.70	9.02	0.123	5.10×10^{-4}	20.53	12.03	9.66	5.14	8.03	1.82
250.0	0.5	0.01	240.15	9.03	0.681	2.84×10^{-3}	20.51	11.97	9.63	5.14	7.97	1.89
250.0	0.5	0.001	239.57	9.06	1.238	5.17×10^{-3}	20.51	11.98	9.63	5.13	7.98	1.89
						$M_5 = 1000$						
250.0	0.25	0.1	222.92	26.81	0.114	5.12×10^{-4}	20.31	10.10	7.54	3.31	9.21	2.48
250.0	0.25	0.01	222.41	26.71	0.741	3.33×10^{-3}	20.30	10.05	7.51	3.31	9.08	2.61
250.0	0.25	0.001	221.73	26.64	1.504	6.78×10^{-3}	20.30	10.05	7.51	3.30	9.07	2.63
500.0	0.5	0.1	471.96	27.48	0.238	5.05×10^{-4}	20.72	11.86	9.45	5.78	7.78	1.44
500.0	0.5	0.01	471.01	27.55	1.167	2.48×10^{-3}	20.71	11.82	9.43	5.77	7.71	1.52
500.0	0.5	0.001	470.12	27.60	2.021	4.30×10^{-3}	20.71	11.82	9.43	5.77	7.71	1.52

Note – See Note in Table 5.2 for description.

Chapter 6

Concluding remarks and future perspectives

The structural parameters defining the AGN (e.g., bolometric luminosities, accretion rates) and the host-galaxy (e.g., stellar mass, SFR) global properties have been studied in this Thesis using a multiwavelength approach complemented by theoretical modeling. The Thesis aim is to seek answers to important questions, such as for how long the AGN shine as a luminous quasar, what is the distribution of the bolometric output and accretion rates, and how these are related to the host properties. In order to tackle these topics the work has been divided into three parts. In the following the main findings are reviewed, underlining the future perpectives of this research.

6.1 Nuclear properties of Type-1 AGN in XMM-COSMOS

The X-ray to optical properties of a sample of 545 X-ray selected Type-1 AGN, from the XMM-COSMOS survey, over a wide range of redshifts ($0.04 \leq z \leq 4.25$) and hard X-ray luminosities ($40.6 \leq \mathrm{Log}\, L_{[2-10]\mathrm{keV}} \leq 45.3$) is studied. The relationship between UV and X-ray luminosity, parameterized by the optical to X-ray spectral index, $\alpha_{\mathrm{ox}} = -\mathrm{Log}\,[L_{2\,\mathrm{keV}}/L_{2500\,\mathrm{\AA}}]/2.605$, and its dependence on redshift and luminosity were investigated. The α_{ox} parameter connects the two portions of the AGN broad-band spectrum dominated by the accretion power and, thus, it is expected to be a reliable tracer of the accretion properties and, in particular, of the relation between accretion disk emission, peaking in the UV, and coronal X-ray emission. In the past, it was widely adopted to compute the QSO contribution to the X-ray background and to estimate the X-ray luminosity function from optical counts (e.g., Zamorani et al. 1981; Avni & Tananbaum 1986, Silverman et al. 2005). These studies, based on *Einstein* observations, found a mean value of α_{ox} in the range $1.3-1.45$. Subsequently, many investigations have been performed (e.g., Yuan et al. 1998; Vignali et al. 2003; Strateva et al. 2005; Steffen et al. 2006; Just et al. 2007; Kelly et al. 2008; Gibson et al. 2008; Green et al. 2009 and Young et al. 2009), mainly based on large samples of optically selected Type-1 AGN with a high fraction of X-ray detections. These studies could not properly address the effect of the band selection (i.e. optical vs X-rays). For the first time the availability, in the XMM-COSMOS survey, of large samples of X-ray selected QSOs with a high quality photometric and spectroscopic coverage in the optical, opens the possibility for an

extended investigation of the α_{ox} distribution and its evolution. The sample size considered in this study is comparable to that of optically selected samples previously reported in the literature, but, to our knowledge, this is the largest, complete X-ray selected sample for which the study of the α_{ox} distribution is performed. The results presented here confirm and extend the previous findings to a large sample of X-ray selected AGN. The most important results are the following:

(i) The $L_{2\,keV} - L_{2500\,Å}$ correlation parametrized by $L_{2\,keV} \propto L^{\beta}_{2500\,Å}$ is confirmed, where $\beta = 0.760 \pm 0.022$. The best-fit slope agrees with previous studies based on optically selected samples, which found a value of β inconsistent with unity. The observed $L_{2\,keV} - L_{2500\,Å}$ correlation implies that more optical luminous AGN emit less X-rays per unit UV luminosity than less luminous AGN. This could be related to the hot corona covering factor, optical depth and electron temperatures. The interplay between hot electrons in a coronal gas and a colder accretion flow suggests that disk-corona parameters are strongly depending on the UV luminosity.

(ii) The mean value of α_{ox} for the full X-ray selected sample is $\langle\alpha_{ox}\rangle \sim 1.37 \pm 0.01$ with a dispersion around the mean of 0.18. We confirm the correlation between α_{ox} and $L_{2500\,Å}$ at $17\,\sigma$ significance level. The correlation becomes stronger if we take into account the effect of redshift using the partial correlation analysis ($\sim 21\,\sigma$). The slope of the best-fit relation between α_{ox} and $L_{2500\,Å}$ is consistent within $\sim 1.6\sigma$ with that obtained for an optically selected sample.

(iii) We found a very tight correlation between the α_{ox} values and the hard X-ray bolometric correction values. The $\alpha_{ox} - k_{bol}$ relation could be used as a practical tool to provide an accurate estimate ($\sim 20\%$ at 1σ) of the bolometric correction using only the α_{ox} value.

(iv) We found a correlation between both α_{ox} and k_{bol} and λ_{Edd}. The results for the $k_{bol} - \lambda_{Edd}$ relation and for $\alpha_{ox} - \lambda_{Edd}$ suggest that there is a connection between the broad-band emission, mostly in the UV, and the Eddington ratio, which is directly linked to the ratio between mass accretion rate, $\dot{M}_{acc}$, and Eddington accretion rate, $\dot{M}_{Edd}$.

6.2 Type-2 AGN: bolometric properties and host-galaxy connection

In this second part of the Thesis a detailed analysis of the SEDs of 257 hard X-ray selected obscured AGN from the XMM-COSMOS survey is presented. For obscured AGN the nuclear luminosity is intercepted along the line of sight by the dusty torus, reprocessing a significant amount of optical-UV emission in the infrared. The optical-UV part of the spectrum is dominated by the host-galaxy starlight. On the one hand, this allows us to obtain a better determination of the host-galaxy spectrum and luminosity, on the other hand it makes difficult to estimate the nuclear bolometric output as done with Type-1 AGN. A densely sampled SED over a broad wavelength interval is mandatory to extract useful information from SED fitting procedures, allowing to tightly constrain physical parameters from multi-component modeling and, in particular, to

properly disentangle the emission associated to stellar light from that due to accretion. The reprocessed IR emission could be a good proxy of the intrinsic disk emission (i.e., Pozzi et al. 2007, Vasudevan et al. 2010). The correlation between the intrinsic 2–10 keV X–ray emission and the infrared emission at 12.3μm discussed by Gandhi et al. (2009) has been used to compare the total observed luminosity at 12.3 μm to that predicted by the Gandhi relation (see Eq. [4.1]). The distribution of the ratio $r = \mathrm{Log}\left(L_{12.3\ \mu m,\mathrm{obs}}/L_{12.3\ \mu m,\mathrm{predicted}}\right)$ shows two peaks, one around zero for the majority of objects ($\sim$ 75% of 112XMM sample is within 2σ), the other at $r \simeq 0.7 - 0.8$, more than 2σ away from the main peak ($\sim$ 25% of the 112XMM sample). We called "low-r" all sources within 2σ of the r distribution, while "high-r" are all sources deviating by more than 2σ. Moreover, the host-galaxy morphologies, stellar masses and specific star-formation rates (SSFR, the ratio between the SFR and the galaxy stellar mass) are estimated. The inverse of the SSFR, $SSFR^{-1}$, called "growth time" (the time required for the galaxy to double its stellar mass assuming a constant SFR) is computed, combined with the host-galaxies colors, to investigate the properties of obscured AGN hosts with that of inactive galaxies. The most important findings are reported below:

(i) Type-2 AGN appear to have smaller bolometric corrections than Type-1 AGN. At the same hard X–ray luminosity we find a median bolometric correction $\langle k_{\mathrm{bol}} \rangle \sim 16 \pm 1$ for Type-2 AGN, to be compared with $\langle k_{\mathrm{bol}} \rangle \sim 23 \pm 1$ for Type-1 AGN. The two averages are statistically different at $\sim 5\ \sigma$ level and this is consistent with the results reported in Vasudevan et al. (2010). The $k_{\mathrm{bol}} - \lambda_{\mathrm{Edd}}$ and $\alpha_{\mathrm{ox}} - \lambda_{\mathrm{Edd}}$ relations suggest that there is a connection between the broad-band emission, mostly in the UV, and the Eddington ratio, which is directly linked to the ratio between mass accretion rate and the Eddington accretion rate. A higher λ_{Edd} corresponds to an enhanced optical-UV emission, which means a prominent big-blue bump and therefore a higher k_{bol}. A possible interpretation of the difference between the average bolometric corrections for Type-1 and Type-2 AGN could be referred to different mass accretion rates in Type-1 and Type-2 AGN. In this framework, Type-1 AGN would be higher-accreting objects than Type-2 AGN. This would be in contrast with the standard picture of AGN/host-galaxy co-evolution, in which obscured AGN are related with high accreting sources. However, most of our Type-2 AGN are at relatively low redshift ($0 < z < 1$) and low luminosities, hence, probably these sources are not related to the obscured AGN in the early stage of AGN/galaxy co-evolution.

(ii) A clear separation in bolometric corrections for the low-r and the high-r samples is present. At a given hard X–ray luminosity the low-r sample has a median bolometric correction of $\langle k_{\mathrm{bol}} \rangle \sim 12 \pm 1$, to be compared with a median bolometric correction for the high-r sample of $\langle k_{\mathrm{bol}} \rangle \sim 36 \pm 3$. The two median values for k_{bol} are statistically different at $\sim 7.6\sigma$ level. A likely explanation is that the SED-fitting for the 28 high-r Type-2 AGN overestimates the AGN emission in the infrared, which is probably due to star-forming processes. If the sources in the high-r AGN sample are more contaminated by the emission from star-forming region, the average bolometric correction for Type-2 AGN, excluding these sources, is even lower. This reinforces the idea of lower bolometric corrections for Type-2 AGN with respect to Type-1 AGN. Another possibility is that a significant fraction

of the bolometric luminosity can be dissipated in the circumnuclear region and in the host-galaxy (i.e., AGN-feedback), and, therefore, does not contribute to the observed bolometric luminosity.

(iii) The host-galaxies morphologies and the stellar masses indicate that obscured AGN are preferentially hosted in bulge-dominated galaxies with stellar masses greater than $10^{10} M_{\odot}$. The distribution of AGN hosts in the rest-frame $(U-V)$ – Log M_* plane shows a pronounced tail towards bluer colors: $\langle U-V \rangle \sim 1.72$ with a dispersion of 0.29 for AGN host-galaxies, while $\langle U-V \rangle \sim 1.78$ with a dispersion of 0.31 for inactive galaxies. The two mean values are statistically different at $\sim 3\sigma$ level.

(iv) If the SFRs derived from the SED-fitting procedure are used, we find that almost all the sources in the red-sequence have $SSFR^{-1}$ larger than the age of the Universe at their redshift, which is consistent with passive galaxies. Combining the rest-frame $(U-V)$ – Log M_* diagram with the $(U-V)$ vs $(V-J)$ diagram including the near-infrared band J, we have tried to to estimate the relative fraction of truly passive and dust-obscured hosts following the same approach as in Cardamone et al. (2010). For sources in the redshift range $0.8 \leq z \leq 1.2$, $\sim 50\%$ of AGN hosts lie in the passive region of the color-color diagram, the remaining have colors consistent with the presence of young stellar populations.

The mid and far-infrared parts of the SED are under-sampled with respect to the optical part. The ongoing Herschel survey over various fields at different depths ($100\mu m$ and $160\mu m$ in the COSMOS field) and the upcoming ALMA survey will allow us to gain an optimal multiwavelength coverage also in the far-infrared.
The sample of both Type-1 and Type-2 AGN will we extended by including fainter sources selected in Chandra-COSMOS and CDF-S. The limiting flux in CDF-S is about a factor 100 deeper than in the XMM-*Newton* (2×10^{-17}erg s^{-1}cm^{-2}) in the $0.5-2$ keV band and a factor of 10 deeper (1.3×10^{-16}erg s^{-1}cm^{-2}) in the $2-10$ keV band. Over the detected 462 X-ray point sources of the main 2Ms Chandra catalog, about 90% have an optical counterpart with photometric redshift, while about 60% have a reliable spectroscopic redshift. A sample containing up to ~ 1000 AGN selected from both large (i.e., COSMOS) and deep (i.e., CDF-S) X–ray surveys over a wide range of redshift, luminosities and obscuring column densities will be assembled. Moreover, given the excellent multiwavelength coverage from optical-UV to infrared and radio (e.g., GOODS, GEMS, MUSYC, Spitzer, VLA), a full SED will be available for these sources.

6.3 Evolution of spheroidal galaxies with SMBH

In the last part of the Thesis, the co-evolution of supermassive black holes and their host galaxies, as a function of the accretion radiative efficiency, dark matter content, and cosmological infall of gas is studied, from the theoretical point of view, using a one-zone evolutionary model. We focus on a scenario in which the masses of the central SMBH and the host galaxy grow in a dark matter halo, which is replenished by accretion of gas of cosmological origin. The evolution of star

formation is followed and also the mass return from the evolving stellar populations. Among the most important observational predictions of the model is the length of the so-called "obscured accretion phase". This phase is defined as the period of time when a high column density is associated with a high accretion rate onto the central SMBH. The relation between the duration of the obscured phase and the corresponding "cold phase" (defined by a low mass-weighted gas temperature), and how these phases depend on the adopted physical parameters are also studied. In this model, the obscured/unobscured AGN dichotomy is more related to two different phases of galaxy evolution, rather than to an orientation effect (i.e., unified model scheme). There are two major differences between the present approach and hydro-simulations. First, the impossibility to resolve physical phenomena associated with specific length and timescales. Second, only heating feedback is taken into account, while in the current version of the hydrodynamical code by Ciotti et al. (2009, 2010), both mechanical feedback, and radiation pressure are also considered. Despite these drawbacks, the present models attempt to simulate the process of galaxy formation exploring extensively the parameter space, which is beyond the current possibilities of the hydro-simulations. With this approach we are able to address several key points:

(i) The computed models have an initial phase that lasts for a few Gyrs, in which the gas temperature is low and the gas density is high, namely an obscured-cold-phase, when the bulk of star formation and black hole accretion occur. These galaxies would be defined obscured quasars, were we are able to measure their gas column density within an aperture radius of the order of $R_e/100$. This phase is followed by a quiescent hot phase in which accretion is highly sub-Eddington and the galaxy is unobscured.

(ii) At late times, all the SMBHs are found to be in a low accretion state without much feedback, and the ISM is overall optically thin. The galactic ISM is at about the virial temperature of the dark matter potential well and should be emitting in X-rays, as found for elliptical galaxies in the local universe.

(iii) Interestingly, we have found that only some specific classes of models, are able to reproduce the observed Magorrian relation, i.e. only those with low initial SMBH masses ($\lesssim 10^6 M_\odot$) and high radiative accretion efficiency, $\epsilon \sim 0.1$. Higher initial SMBH masses, or lower radiative efficiencies lead to final SMBH masses that are too high. Therefore, this result implies that the seed SMBHs should be relatively small, but that their mass accretion should occur mainly with high radiative efficiency, in agreement with observational findings.

In a future study, the assumption of a fixed gas density distribution will be relaxed, imposing a time dependence of $r_g(t)$ as a function of the gas thermal content at that given time. We expect that this additional ingredient will cause the models to become more sensitive to the adopted parameters. On the one hand by increasing the gas density during the cold phases (hence producing a stronger feedback by decreasing the value of the ionization parameter and increasing the mass accretion rate). On the other hand by decreasing the gas density during the hot phase, so reducing further the Eddington ratios at late times. We also expect that both the star-formation and accretion histories, as well as the durations of the obscured and Compton-thick phases, will be affected.

Appendices

Appendix A

Optical and X-ray properties of the total sample

Table A.1: Optical and X-ray properties of the total sample.

XID	Spectroscopic redshift	Photometric redshift	Log $L_{2500\ \text{Å}}$ [erg s^{-1}Hz^{-1}]	Log $L_{2\ \text{keV}}$ [erg s^{-1}Hz^{-1}]	α_{ox}	Log $L_{[2-10]\text{keV}}$ [erg s^{-1}]	$L_{\text{bol},1\mu\text{m}}$ [$L_{\odot}$]	k_{bol}	Class[a]
1	0.373	$0.37^{+0.03}_{-0.01}$	29.49	26.04	1.324	44.00	11.53	12.94	28
2	1.024	$1.05^{+0.03}_{-0.03}$	29.86	26.95	1.114	44.97	12.30	8.09	30
3	0.345	$0.36^{+0.02}_{-0.02}$	29.22	26.00	1.237	43.98	11.44	11.15	29
6	0.360	$0.32^{+0.02}_{-0.02}$	29.22	25.43	1.453	43.39	11.32	32.60	20
8	0.699	$0.71^{+0.01}_{-0.03}$	30.00	26.27	1.434	44.09	11.98	29.60	26
10	0.689	$0.68^{+0.02}_{-0.02}$	29.24	25.92	1.277	43.71	11.30	14.93	22
13	0.850	$0.84^{+0.02}_{-0.02}$	29.54	26.06	1.337	43.98	11.70	20.06	24
15	2.033	$2.01^{+0.03}_{-0.03}$	30.83	27.11	1.426	45.11	12.95	26.33	30
16	0.667	$0.61^{+0.03}_{-0.01}$	29.32	25.82	1.345	43.78	11.38	15.14	19
17	1.236	$1.28^{+0.02}_{-0.02}$	30.77	26.77	1.535	44.70	12.75	43.09	29
18	1.598	$1.45^{+0.05}_{-0.07}$	29.01	26.59	0.930	44.76	12.28	12.63	5
20	0.695	$0.69^{+0.03}_{-0.03}$	29.10	25.70	1.304	43.65	11.19	13.39	25
22	0.554	$0.55^{+0.01}_{-0.03}$	29.32	25.50	1.467	43.34	11.34	38.68	22
23	0.378	$0.37^{+0.03}_{-0.03}$	28.33	25.46	1.099	43.40	10.81	9.72	22
24	1.318	$1.35^{+0.03}_{-0.03}$	30.72	26.59	1.585	44.47	12.67	60.51	29
25	2.289	$2.28^{+0.02}_{-0.02}$	30.74	26.88	1.483	44.88	12.96	46.25	29
27	0.374	$0.38^{+0.02}_{-0.02}$	28.37	25.14	1.239	43.10	10.67	14.24	7
28	1.342	$1.38^{+0.06}_{-0.04}$	29.52	26.33	1.224	44.40	11.84	10.45	27
30	1.753	$1.78^{+0.02}_{-0.02}$	30.81	26.69	1.579	44.55	12.84	73.84	30
31	0.909	$0.90^{+0.02}_{-0.02}$	29.57	26.05	1.353	44.01	11.61	15.43	29
32	...	$1.04^{+0.08}_{-0.08}$	28.29	25.98	0.887	44.06	11.38	7.98	19
33	1.799	$1.77^{+0.03}_{-0.03}$	30.76	26.70	1.560	44.68	12.81	50.90	29
34	1.789	$1.77^{+0.03}_{-0.03}$	30.37	26.58	1.455	44.57	12.39	25.38	30
37	1.123	$1.10^{+0.04}_{-0.02}$	29.94	26.18	1.440	44.16	11.96	24.24	26
38	1.559	$1.55^{+0.03}_{-0.01}$	30.31	26.60	1.423	44.56	12.39	25.75	27
39	0.851	$0.86^{+0.02}_{-0.02}$	29.59	26.10	1.338	44.06	11.69	16.16	30
41	...	$1.03^{+0.05}_{-0.05}$	29.16	25.84	1.272	44.01	11.63	15.81	25
42	0.988	$1.02^{+0.02}_{-0.02}$	29.86	26.12	1.435	44.06	11.84	23.24	29
44	1.850	$1.86^{+0.04}_{-0.02}$	30.05	26.61	1.320	44.60	12.25	17.00	30
47	0.959	$0.95^{+0.05}_{-0.05}$	29.65	25.94	1.423	43.93	11.68	21.52	24

Table A.1: Optical and X-ray properties of the total sample – *continued.*

XID	Spectroscopic redshift	Photometric redshift	Log $L_{2500\,\text{Å}}$ [erg s^{-1}Hz^{-1}]	Log $L_{2\,\text{keV}}$ [erg s^{-1}Hz^{-1}]	α_{ox}	Log $L_{[2-10]\text{keV}}$ [erg s^{-1}]	$L_{\text{bol},1\mu\text{m}}$ [$L_\odot$]	k_{bol}	Class[a]
48	2.222	$2.23^{+0.03}_{-0.01}$	30.36	26.80	1.368	44.88	12.57	18.41	28
49	0.353	$0.37^{+0.03}_{-0.03}$	28.05	24.85	1.225	42.85	10.39	13.41	7
51	2.497	$2.47^{+0.03}_{-0.03}$	30.87	26.86	1.541	44.83	12.94	49.55	30
52	1.135	$1.16^{+0.02}_{-0.04}$	29.62	26.09	1.355	44.07	11.75	18.61	22
53	1.459	$1.47^{+0.03}_{-0.03}$	29.91	26.54	1.292	44.45	12.06	15.57	28
56	1.407	$0.53^{+0.01}_{-0.03}$	29.45	26.33	1.199	44.33	11.79	11.01	21
57	1.449	$1.44^{+0.02}_{-0.02}$	30.19	26.50	1.417	44.65	12.41	22.34	30
60	2.240	$2.25^{+0.03}_{-0.03}$	30.07	26.60	1.331	44.62	12.31	18.52	30
61	0.728	$0.73^{+0.03}_{-0.03}$	29.22	25.63	1.378	43.48	11.34	27.28	22
66	1.478	$1.48^{+0.02}_{-0.02}$	29.95	26.35	1.382	44.29	12.06	22.55	30
69	1.323	$1.39^{+0.05}_{-0.03}$	29.26	26.11	1.209	44.12	11.59	11.23	25
71	1.458	$1.45^{+0.05}_{-0.07}$	29.35	26.40	1.132	44.46	11.83	9.08	24
74	0.882	$0.89^{+0.03}_{-0.03}$	29.66	26.04	1.392	43.94	11.68	20.90	29
75	1.679	$1.67^{+0.03}_{-0.03}$	29.99	26.60	1.303	44.59	12.22	16.65	29
76	...	$2.50^{+0.06}_{-0.04}$	29.77	26.80	1.138	44.75	12.05	7.72	30
79	1.708	$1.75^{+0.03}_{-0.03}$	30.05	26.55	1.343	44.53	12.23	19.18	30
83	2.754	$2.74^{+0.02}_{-0.02}$	30.43	26.77	1.405	44.80	12.54	21.34	30
84	1.495	$1.52^{+0.02}_{-0.02}$	29.84	26.10	1.436	44.07	11.89	25.65	28
86	0.794	$0.81^{+0.03}_{-0.03}$	29.20	25.87	1.277	43.78	11.31	12.87	25
87	1.664	$1.67^{+0.03}_{-0.03}$	30.55	26.34	1.615	44.35	12.46	49.43	28
88	2.779	$2.74^{+0.04}_{-0.04}$	30.03	27.06	1.141	45.09	12.46	8.91	21
89	...	$1.45^{+0.03}_{-0.07}$	29.26	25.92	1.280	43.99	11.50	12.46	28
90	...	$1.40^{+0.08}_{-0.08}$	28.90	25.93	1.140	43.98	11.41	10.34	20
91	1.371	$1.42^{+0.04}_{-0.04}$	29.66	26.27	1.302	44.18	11.83	17.10	29
92	...	$0.95^{+0.07}_{-0.07}$	28.41	25.74	1.025	43.72	11.02	7.54	19
93	2.646	$2.65^{+0.03}_{-0.01}$	30.29	26.65	1.395	44.58	12.44	27.86	29
94	1.510	$1.54^{+0.02}_{-0.02}$	29.87	26.20	1.409	44.22	11.97	21.71	29
95	1.258	$1.24^{+0.04}_{-0.04}$	29.39	26.03	1.289	43.95	11.56	15.57	26
96	2.117	$2.13^{+0.03}_{-0.03}$	30.95	27.01	1.511	44.84	13.06	63.21	30
98	1.106	$1.03^{+0.03}_{-0.03}$	29.79	26.18	1.383	44.15	11.81	17.38	28
103	1.519	$1.54^{+0.02}_{-0.04}$	29.20	25.97	1.240	43.94	11.51	14.31	22
107	...	$1.53^{+0.03}_{-0.05}$	29.30	26.39	1.116	44.42	11.83	9.93	21
109	2.050	$2.06^{+0.02}_{-0.02}$	30.39	26.45	1.511	44.41	12.48	44.64	27
110	2.473	$2.46^{+0.02}_{-0.04}$	30.06	26.76	1.263	44.65	12.19	13.30	30
111	1.834	$1.83^{+0.03}_{-0.03}$	30.36	26.43	1.508	44.40	12.49	47.24	29
113	1.910	$1.97^{+0.03}_{-0.03}$	29.74	26.30	1.321	44.32	12.00	18.35	30
114	2.350	$2.33^{+0.03}_{-0.03}$	29.91	26.68	1.239	44.70	12.27	14.19	30
115	1.161	$1.34^{+0.02}_{-0.20}$	30.24	26.44	1.460	44.37	12.24	28.16	28
118	1.734	$1.74^{+0.04}_{-0.04}$	30.10	26.12	1.528	44.05	12.19	52.28	29
123	2.065	$2.09^{+0.07}_{-0.05}$	29.61	26.16	1.320	44.22	11.96	21.18	29
127	1.846	$1.82^{+0.04}_{-0.04}$	29.41	26.03	1.296	44.14	11.74	15.05	29
128	2.161	$2.17^{+0.03}_{-0.01}$	30.81	26.18	1.777	44.29	12.89	150.94	30
129	1.170	$1.12^{+0.04}_{-0.04}$	29.40	26.01	1.301	43.94	11.55	15.45	22
132	2.136	$2.13^{+0.05}_{-1.31}$	29.51	26.25	1.251	44.25	11.75	12.20	27
133	2.615	$2.61^{+0.03}_{-0.01}$	30.56	26.71	1.477	44.77	12.67	30.42	26
136	1.029	$1.06^{+0.04}_{-0.04}$	29.28	25.81	1.331	43.89	11.47	14.68	25
137	1.806	$1.82^{+0.02}_{-0.02}$	30.03	26.20	1.468	44.11	12.13	40.17	29
141	0.832	$0.83^{+0.03}_{-0.03}$	29.50	25.09	1.694	43.30	11.55	67.57	27
146	2.791	$2.77^{+0.03}_{-0.03}$	30.88	26.65	1.625	44.65	12.78	51.54	28
153	1.932	$1.95^{+0.03}_{-0.03}$	29.88	26.36	1.350	44.35	12.13	23.07	29
154	...	$0.59^{+0.05}_{-0.07}$	28.25	24.85	1.305	42.98	10.58	15.29	29
161	2.671	$2.66^{+0.02}_{-0.02}$	30.47	26.85	1.393	44.83	12.55	19.77	28
162	0.920	$0.91^{+0.03}_{-0.03}$	29.25	25.66	1.376	43.59	11.37	22.89	19
163	1.165	$1.18^{+0.08}_{-0.04}$	28.83	25.70	1.204	43.63	11.15	12.87	19
164	0.529	$0.51^{+0.03}_{-0.03}$	28.97	25.32	1.400	43.25	11.03	23.26	21
165	2.146	$1.83^{+0.37}_{-0.09}$	29.18	26.32	1.101	44.31	11.68	9.00	7
166	1.042	$1.07^{+0.03}_{-0.05}$	29.72	26.20	1.353	44.15	11.82	17.66	29
167	2.048	$2.11^{+0.07}_{-0.05}$	29.57	26.19	1.298	44.22	11.77	13.39	30
168	2.951	$2.92^{+0.02}_{-0.02}$	30.46	26.91	1.361	44.89	12.66	22.60	26
169	...	$2.45^{+0.05}_{-0.05}$	29.78	26.72	1.175	44.73	12.13	9.77	25
171	1.187	$1.22^{+0.04}_{-0.04}$	28.95	25.73	1.234	43.72	11.21	11.87	24

Table A.1: Optical and X-ray properties of the total sample – *continued.*

XID	Spectroscopic redshift	Photometric redshift	Log $L_{2500\ \text{Å}}$ [erg s^{-1}Hz^{-1}]	Log $L_{2\ \text{keV}}$ [erg s^{-1}Hz^{-1}]	α_{ox}	Log $L_{[2-10]\text{keV}}$ [erg s^{-1}]	$L_{\text{bol},1\mu\text{m}}$ [$L_\odot$]	k_{bol}	Class[a]
175	...	$1.54^{+0.04}_{-0.02}$	28.96	26.60	0.903	44.56	11.85	7.34	21
176	1.613	$1.62^{+0.02}_{-0.02}$	29.84	26.14	1.418	44.22	12.03	24.66	27
180	3.333	$3.37^{+0.03}_{-0.01}$	31.00	26.28	1.814	44.64	13.03	93.24	27
184	...	$0.92^{+0.04}_{-0.06}$	28.73	25.35	1.298	43.66	11.54	29.45	20
185	...	$1.11^{+0.05}_{-0.03}$	29.10	25.77	1.277	43.75	11.37	15.92	21
186	2.182	$2.22^{+0.04}_{-0.02}$	29.85	26.36	1.339	44.28	12.12	26.10	27
187	1.410	$3.30^{+0.04}_{-0.04}$	29.28	25.82	1.330	43.88	11.40	12.56	28
188	1.188	$1.23^{+0.03}_{-0.03}$	29.76	26.25	1.348	44.23	11.89	17.29	25
189	1.839	$1.54^{+0.04}_{-0.06}$	29.39	26.58	1.077	44.62	11.97	8.50	22
192	2.172	$2.16^{+0.04}_{-0.04}$	30.21	26.45	1.442	44.37	12.33	34.58	27
196	1.483	$1.50^{+0.02}_{-0.02}$	29.89	26.02	1.484	44.03	11.92	29.71	28
197	1.589	$1.56^{+0.04}_{-0.06}$	29.55	25.98	1.369	43.91	11.61	18.96	27
199	2.454	$2.42^{+0.02}_{-0.02}$	31.22	27.16	1.560	45.12	13.33	61.44	24
201	...	$1.27^{+0.07}_{-0.09}$	28.91	25.73	1.222	43.72	11.28	13.74	22
204	...	$1.18^{+0.10}_{-0.08}$	28.86	25.87	1.147	43.96	11.41	10.64	23
216	2.024	$2.00^{+0.02}_{-0.04}$	30.18	26.36	1.465	44.37	12.31	32.94	29
219	1.248	$1.24^{+0.04}_{-0.04}$	29.47	25.79	1.413	43.83	11.57	20.99	24
220	...	$2.14^{+0.04}_{-0.02}$	29.59	26.42	1.218	44.51	12.09	14.54	30
221	1.144	$1.11^{+0.07}_{-0.05}$	29.44	26.09	1.287	44.04	11.59	13.68	24
225	...	$0.74^{+0.08}_{-0.02}$	28.97	24.68	1.646	42.98	11.23	68.02	19
228	1.073	$2.04^{+0.02}_{-0.02}$	29.65	25.62	1.546	43.54	11.62	46.11	27
236	1.445	$1.45^{+0.03}_{-0.05}$	29.11	25.44	1.408	44.02	12.59	141.60	28
237	2.485	$2.52^{+0.04}_{-0.06}$	29.68	25.88	1.458	44.08	12.07	37.78	1
239	1.642	$1.65^{+0.01}_{-0.03}$	30.09	26.29	1.459	44.24	12.15	30.92	29
243	...	$0.98^{+0.14}_{-0.04}$	28.82	25.75	1.179	43.70	11.17	11.20	22
245	2.459	$2.38^{+0.02}_{-0.02}$	30.02	25.97	1.556	44.10	12.08	36.16	28
249	1.325	$1.20^{+0.08}_{-0.10}$	28.83	25.58	1.247	43.71	11.42	19.80	7
250	1.350	$2.55^{+0.03}_{-0.03}$	29.39	25.60	1.456	43.56	11.35	23.82	27
263	...	$1.72^{+0.12}_{-0.18}$	29.32	26.21	1.190	44.24	11.70	11.16	21
264	...	$1.59^{+0.15}_{-1.15}$	28.75	25.76	1.149	43.85	11.35	12.11	21
265	1.161	$1.18^{+0.14}_{-0.04}$	29.16	25.87	1.263	43.74	11.32	14.55	23
268	...	$0.97^{+0.05}_{-0.05}$	29.02	25.45	1.369	43.45	11.28	25.98	21
272	...	$1.99^{+0.07}_{-0.09}$	29.11	25.53	1.372	43.85	11.78	32.56	23
273	2.052	$2.05^{+0.05}_{-0.05}$	29.70	26.02	1.410	44.38	12.44	43.78	29
275	1.856	$1.87^{+0.03}_{-0.03}$	30.09	26.58	1.347	44.54	12.26	20.03	28
276	...	$2.62^{+0.02}_{-0.02}$	30.72	26.63	1.570	44.74	12.80	44.33	26
281	1.177	$1.20^{+0.06}_{-0.04}$	29.34	25.88	1.331	43.89	11.54	17.10	27
282	1.738	$1.73^{+0.05}_{-0.03}$	29.67	25.91	1.443	43.99	11.80	24.79	29
285	...	$2.05^{+0.03}_{-0.03}$	29.72	26.33	1.300	44.20	11.93	20.56	28
288	1.106	$1.09^{+0.05}_{-0.11}$	29.25	25.78	1.335	43.74	11.39	17.03	24
295	1.529	$1.54^{+0.02}_{-0.02}$	29.48	25.67	1.465	44.15	12.48	81.46	25
298	1.867	$1.88^{+0.10}_{-0.06}$	28.96	25.93	1.163	43.94	11.33	9.39	28
300	3.715	$3.53^{+0.03}_{-0.03}$	30.60	25.93	1.793	44.49	13.06	141.64	28
304	2.220	$1.67^{+0.07}_{-0.07}$	29.46	25.83	1.391	43.97	11.79	25.39	21
308	1.514	$1.53^{+0.03}_{-0.05}$	28.81	25.82	1.146	43.86	11.32	11.00	21
309	...	$1.77^{+0.05}_{-0.07}$	29.32	25.84	1.337	43.79	11.52	20.61	24
310	...	$2.67^{+0.01}_{-0.03}$	30.68	27.00	1.409	44.99	12.73	20.93	27
314	2.702	$2.70^{+0.12}_{-0.04}$	29.94	26.12	1.465	44.27	12.08	25.12	25
320	1.590	$1.56^{+0.06}_{-0.08}$	28.79	25.80	1.146	43.79	11.28	11.86	22
322	2.040	$2.01^{+0.05}_{-0.05}$	29.73	25.80	1.507	44.13	12.20	44.98	29
326	3.003	$3.06^{+0.04}_{-0.02}$	29.71	25.65	1.558	44.28	12.95	182.17	26
328	1.660	$1.65^{+0.05}_{-0.07}$	29.16	25.57	1.377	43.79	11.60	24.81	23
329	1.166	$1.15^{+0.03}_{-0.03}$	29.50	25.68	1.466	43.61	11.53	32.01	26
330	1.478	$2.15^{+0.05}_{-0.07}$	28.55	25.61	1.130	43.59	11.00	9.84	30
333	...	$3.07^{+0.07}_{-0.03}$	29.64	25.80	1.474	44.31	12.70	93.60	22
334	...	$1.96^{+0.08}_{-0.08}$	28.95	25.96	1.148	44.28	12.13	27.29	23
341	1.360	$1.41^{+0.05}_{-0.05}$	29.14	26.04	1.192	44.03	11.47	10.59	26
349	3.092	$3.09^{+0.03}_{-0.03}$	29.86	26.15	1.425	44.31	12.15	26.80	26
352	...	$0.20^{+0.02}_{-0.08}$	26.75	23.62	1.202	41.79	9.44	17.31	20
353	1.112	$1.43^{+0.05}_{-0.71}$	28.87	25.37	1.342	43.57	11.32	21.33	4

Table A.1: Optical and X-ray properties of the total sample – *continued.*

XID	Spectroscopic redshift	Photometric redshift	Log $L_{2500\,\text{Å}}$ [erg s^{-1}Hz^{-1}]	Log $L_{2\,\text{keV}}$ [erg s^{-1}Hz^{-1}]	α_{ox}	Log $L_{[2-10]\text{keV}}$ [erg s^{-1}]	$L_{\text{bol},1\mu\text{m}}$ [$L_\odot$]	k_{bol}	Class[a]
356	2.250	$2.04^{+0.06}_{-0.28}$	29.51	25.67	1.473	43.95	11.96	39.00	4
357	2.151	$2.15^{+0.05}_{-0.05}$	29.34	25.79	1.361	44.28	12.64	87.72	23
359	1.156	$1.12^{+0.02}_{-0.02}$	29.81	25.78	1.549	43.81	11.80	37.36	26
360	...	$1.85^{+0.11}_{-0.19}$	28.99	25.48	1.345	44.04	12.54	120.10	24
368	0.830	$0.81^{+0.03}_{-0.03}$	29.31	25.20	1.577	43.20	11.34	53.48	20
370	...	$1.93^{+0.03}_{-0.03}$	29.86	25.81	1.555	44.27	12.60	80.79	29
373	...	$2.42^{+0.04}_{-0.04}$	29.57	26.14	1.315	44.16	11.83	17.95	25
374	...	$1.14^{+0.28}_{-0.20}$	28.28	25.33	1.130	43.47	10.99	12.48	21
375	2.032	$2.05^{+0.03}_{-0.03}$	30.37	26.25	1.582	44.26	12.41	53.69	24
376	...	$2.78^{+0.10}_{-0.10}$	28.53	25.78	1.054	44.34	12.83	117.38	30
378	...	$0.82^{+1.36}_{-0.04}$	28.25	25.03	1.236	43.34	11.22	29.13	22
383	1.444	$1.43^{+0.03}_{-0.05}$	29.31	25.78	1.354	43.81	11.52	19.34	23
391	1.780	$1.76^{+0.04}_{-0.04}$	29.54	26.17	1.294	44.25	11.79	13.15	29
395	...	$2.98^{+0.04}_{-0.04}$	29.73	26.24	1.343	44.31	11.96	16.90	30
397	2.235	$2.26^{+0.06}_{-0.04}$	29.88	25.78	1.571	44.24	12.56	79.54	29
399	...	$1.08^{+0.04}_{-0.06}$	28.55	25.55	1.150	43.61	11.05	10.38	20
400	...	$0.80^{+0.30}_{-0.12}$	27.53	25.15	0.912	43.28	10.71	10.47	21
402	...	$1.08^{+0.10}_{-0.14}$	28.42	25.32	1.188	43.47	11.06	14.79	20
404	1.800	$0.71^{+1.07}_{-0.03}$	29.67	25.99	1.412	43.82	11.71	29.72	19
410	...	$1.08^{+0.06}_{-0.08}$	28.85	25.27	1.371	43.36	11.06	19.32	22
415	...	$1.56^{+0.44}_{-0.08}$	28.96	25.26	1.420	43.71	11.95	66.11	24
425	...	$2.64^{+0.02}_{-0.02}$	30.24	26.18	1.556	44.33	12.31	36.66	30
430	0.889	$0.81^{+0.05}_{-0.05}$	28.44	25.14	1.269	43.29	11.01	19.96	19
435	...	$2.08^{+0.14}_{-0.26}$	29.39	25.42	1.526	44.26	13.56	772.61	28
436	1.817	$1.79^{+0.03}_{-0.09}$	30.41	26.32	1.568	44.27	12.39	51.01	30
449	2.134	$1.72^{+0.12}_{-0.22}$	28.69	26.02	1.024	44.13	11.61	11.48	5
453	...	$2.83^{+0.07}_{-0.07}$	29.91	26.72	1.226	44.65	12.06	9.90	28
456	...	$1.93^{+0.05}_{-0.05}$	29.20	25.74	1.327	43.97	11.70	20.69	28
458	...	$1.71^{+1.35}_{-0.09}$	28.98	25.55	1.316	43.95	12.01	44.49	28
460	2.982	$2.99^{+0.03}_{-0.07}$	29.98	25.90	1.566	44.22	12.33	48.79	27
462	2.047	$2.06^{+0.04}_{-0.06}$	29.84	26.00	1.475	44.04	11.97	32.72	25
467	...	$1.01^{+1.89}_{-0.05}$	28.00	25.64	0.903	43.68	10.98	7.53	19
484	1.310	$2.42^{+0.04}_{-0.02}$	29.30	25.32	1.530	43.48	11.33	26.91	30
496	1.220	$1.26^{+0.04}_{-0.10}$	29.82	26.04	1.453	43.97	11.86	29.64	27
498	2.490	$2.47^{+0.03}_{-0.03}$	30.21	26.20	1.540	44.38	12.35	35.52	30
504	3.651	$3.65^{+0.03}_{-0.03}$	30.18	26.55	1.392	44.36	11.99	16.31	28
512	2.727	$2.73^{+0.03}_{-0.03}$	30.45	26.16	1.646	44.26	12.55	75.59	27
525	...	$2.49^{+0.03}_{-0.03}$	29.89	26.35	1.358	44.24	12.01	22.64	30
530	...	$0.21^{+1.75}_{-0.03}$	26.63	23.70	1.122	42.28	10.83	137.78	26
531	...	$1.77^{+0.05}_{-0.07}$	29.06	25.75	1.268	44.08	11.98	30.54	23
541	...	$2.65^{+0.01}_{-0.61}$	30.61	25.57	1.936	44.13	12.86	203.48	28
558	1.451	$1.45^{+0.03}_{-0.03}$	30.02	26.21	1.463	44.09	12.16	45.16	29
567	1.935	$1.95^{+0.03}_{-0.03}$	29.87	26.11	1.445	44.13	12.05	31.66	30
569	1.528	$1.54^{+0.02}_{-0.02}$	29.35	25.54	1.460	43.72	11.59	28.35	26
1151	3.345	$3.40^{+0.02}_{-0.02}$	30.43	26.43	1.536	44.68	12.62	33.74	29
1461	1.656	$1.53^{+0.05}_{-0.07}$	29.02	26.12	1.110	44.18	11.65	11.19	6
1467	2.522	$2.56^{+0.02}_{-0.02}$	29.97	25.87	1.573	44.33	12.66	81.28	30
1548	1.796	$1.76^{+0.04}_{-0.04}$	29.36	25.79	1.367	43.36	11.53	55.70	27
1559	2.046	$1.76^{+0.22}_{-0.26}$	29.07	25.58	1.342	43.88	11.81	32.70	4
2013	1.246	$1.24^{+0.02}_{-0.04}$	29.59	26.54	1.167	44.57	11.93	8.92	30
2016	0.345	$0.32^{+0.02}_{-0.02}$	29.65	25.49	1.596	43.48	11.55	45.62	29
2020	1.506	$1.52^{+0.06}_{-0.02}$	30.85	26.75	1.573	44.63	12.87	65.82	29
2036	0.971	$0.97^{+0.05}_{-0.03}$	29.23	26.23	1.151	44.23	11.60	8.88	30
2040	0.521	$0.51^{+0.01}_{-0.03}$	28.59	25.57	1.159	43.53	10.89	8.84	24
2046	1.800	$1.77^{+0.03}_{-0.01}$	30.45	26.87	1.371	44.87	12.60	20.51	30
2051	0.668	$0.68^{+0.02}_{-0.02}$	29.52	26.11	1.311	44.02	11.58	13.62	30

Table A.1: Optical and X-ray properties of the total sample – *continued.*

XID	Spectroscopic redshift	Photometric redshift	Log $L_{2500\,\text{Å}}$ [erg s^{-1}Hz^{-1}]	Log $L_{2\,\text{keV}}$ [erg s^{-1}Hz^{-1}]	α_{ox}	Log $L_{[2-10]\text{keV}}$ [erg s^{-1}]	$L_{\text{bol},1\mu\text{m}}$ [$L_\odot$]	k_{bol}	Class[a]
2058	0.967	$1.02^{+0.04}_{-0.04}$	29.94	26.34	1.380	44.30	11.97	17.79	30
2071	0.876	$0.94^{+0.02}_{-0.04}$	29.65	25.90	1.440	43.93	11.70	22.71	27
2072	...	$1.60^{+0.02}_{-0.02}$	29.74	26.37	1.293	44.41	12.11	19.27	29
2074	...	$0.59^{+0.01}_{-0.03}$	29.58	25.43	1.595	43.43	11.59	54.68	19
2080	1.315	$1.33^{+0.03}_{-0.03}$	29.91	26.30	1.385	44.20	11.96	22.02	26
2081	...	$0.92^{+0.02}_{-0.02}$	29.33	26.16	1.217	44.16	11.57	10.01	27
2083	...	$1.23^{+0.03}_{-0.02}$	29.54	26.32	1.234	44.29	11.75	10.94	28
2093	2.506	$2.48^{+0.02}_{-0.02}$	31.11	26.94	1.599	44.95	13.19	66.85	26
2096	...	$2.32^{+0.02}_{-0.02}$	29.83	26.94	1.110	44.95	12.38	10.24	29
2105	1.509	$1.58^{+0.02}_{-0.02}$	30.06	26.47	1.376	44.38	12.26	29.66	29
2117	1.185	$1.20^{+0.04}_{-0.02}$	29.74	26.59	1.208	44.59	11.99	9.63	28
2119	0.482	$0.45^{+0.01}_{-0.03}$	29.13	25.57	1.366	43.41	11.15	21.06	26
2128	...	$1.38^{+0.02}_{-0.04}$	29.88	26.36	1.353	44.37	12.03	17.66	25
2138	1.551	$1.54^{+0.02}_{-0.02}$	30.15	26.58	1.371	44.54	12.24	19.01	28
2147	2.029	$2.04^{+0.02}_{-0.04}$	30.52	27.00	1.348	44.76	12.68	31.75	29
2148	1.510	$1.54^{+0.02}_{-0.02}$	29.37	26.09	1.259	44.19	11.75	14.03	29
2166	...	$0.97^{+0.03}_{-0.05}$	29.42	26.18	1.244	44.18	11.64	10.84	27
2169	1.776	$1.78^{+0.04}_{-0.04}$	30.09	26.40	1.416	44.31	12.17	27.98	30
2178	1.517	$1.54^{+0.02}_{-0.02}$	30.12	26.51	1.386	44.43	12.19	22.38	30
2187	1.301	$1.84^{+0.02}_{-0.02}$	29.83	26.01	1.465	43.91	11.88	35.14	28
2199	0.853	$0.85^{+0.03}_{-0.03}$	29.66	26.11	1.362	44.10	11.75	17.03	27
2200	1.849	$1.85^{+0.03}_{-0.01}$	30.42	26.52	1.499	44.47	12.39	31.88	28
2202	1.516	$1.51^{+0.03}_{-0.01}$	30.34	26.00	1.666	43.97	12.39	100.25	29
2204	1.188	$1.20^{+0.10}_{-0.14}$	28.77	26.05	1.044	44.02	11.33	7.78	20
2207	...	$0.74^{+0.02}_{-0.02}$	29.12	25.65	1.333	43.58	11.21	16.20	27
2209	2.055	$2.05^{+0.03}_{-0.03}$	30.80	26.68	1.581	44.67	12.85	58.92	29
2211	1.248	$1.21^{+0.03}_{-0.03}$	29.37	26.14	1.239	44.19	11.68	11.87	28
2216	1.516	$1.53^{+0.03}_{-0.03}$	29.81	26.31	1.343	44.25	11.94	18.90	25
2217	1.171	$1.17^{+0.03}_{-0.05}$	29.32	26.10	1.236	44.12	11.57	10.80	26
2219	...	$0.80^{+0.04}_{-0.04}$	28.34	25.66	1.028	43.69	11.14	10.69	19
2228	1.120	$1.09^{+0.03}_{-0.11}$	29.06	26.29	1.064	44.24	11.52	7.22	25
2232	1.641	$1.61^{+0.03}_{-0.03}$	29.51	26.03	1.336	44.12	11.77	17.38	25
2234	0.692	$0.70^{+0.06}_{-0.02}$	28.55	25.34	1.232	43.33	10.91	14.47	21
2239	...	$0.58^{+0.02}_{-0.02}$	29.54	25.03	1.732	43.43	11.89	110.89	23
2244	1.916	$1.94^{+0.02}_{-0.02}$	30.11	26.58	1.356	44.53	12.19	17.63	28
2248	0.910	$0.78^{+0.02}_{-0.04}$	28.93	25.56	1.295	43.55	11.15	15.07	20
2261	1.234	$1.26^{+0.04}_{-0.04}$	29.82	26.03	1.456	44.02	11.87	27.29	30
2265	2.274	$2.27^{+0.03}_{-0.01}$	30.81	26.54	1.637	44.60	12.85	67.39	28
2276	2.215	$2.24^{+0.02}_{-0.04}$	30.09	26.30	1.455	44.27	12.28	39.04	25
2280	0.930	$1.31^{+0.17}_{-1.01}$	28.26	25.54	1.042	43.66	11.08	10.02	28
2309	...	$0.74^{+0.02}_{-0.04}$	28.87	25.46	1.311	43.36	11.05	18.80	21
2333	1.618	$1.64^{+0.02}_{-0.02}$	30.28	26.23	1.556	44.23	12.39	55.20	29
2334	1.597	$1.63^{+0.03}_{-0.03}$	29.57	26.11	1.330	43.99	11.72	20.60	26
2335	1.360	$1.36^{+0.02}_{-0.02}$	30.19	26.25	1.513	44.17	12.24	45.63	29
2340	0.977	$0.98^{+0.04}_{-0.04}$	29.41	25.86	1.361	43.79	11.43	16.76	30
2342	1.171	$1.19^{+0.03}_{-0.03}$	29.87	26.09	1.451	44.04	11.90	27.74	29
2344	2.389	$2.37^{+0.03}_{-0.03}$	30.54	26.55	1.529	44.47	12.66	59.10	29
2359	1.406	$1.39^{+0.07}_{-0.09}$	29.09	26.12	1.140	44.31	11.93	15.83	21
2361	2.181	$2.20^{+0.02}_{-0.02}$	30.20	26.52	1.415	44.51	12.28	22.72	30
2391	...	$1.56^{+0.02}_{-0.06}$	30.10	26.09	1.540	44.18	12.15	35.88	27
2394	3.333	$3.35^{+0.03}_{-0.05}$	29.73	26.57	1.214	44.63	12.10	11.19	29
2396	1.600	$1.63^{+0.01}_{-0.03}$	30.59	25.79	1.844	43.95	12.60	170.14	29
2397	1.200	$1.22^{+0.04}_{-0.04}$	29.36	25.80	1.367	43.94	11.65	19.49	22
2407	3.093	$0.92^{+0.06}_{-0.02}$	30.64	27.09	1.365	45.08	12.78	18.85	24
2410	1.167	$1.18^{+0.06}_{-0.06}$	29.00	25.58	1.315	43.67	11.33	17.35	21
2421	3.104	$3.11^{+0.01}_{-0.03}$	30.65	26.72	1.508	44.75	12.66	31.01	30

Table A.1: Optical and X-ray properties of the total sample – *continued.*

XID	Spectroscopic redshift	Photometric redshift	Log $L_{2500\,\text{Å}}$ [erg s^{-1}Hz^{-1}]	Log $L_{2\,\text{keV}}$ [erg s^{-1}Hz^{-1}]	α_{ox}	Log $L_{[2-10]\text{keV}}$ [erg s^{-1}]	$L_{\text{bol},1\mu\text{m}}$ [$L_\odot$]	k_{bol}	Class[a]
2422	...	$0.80^{+0.04}_{-0.14}$	28.76	25.26	1.342	43.39	11.10	19.64	19
2433	1.433	$1.43^{+0.03}_{-0.03}$	29.31	26.20	1.191	44.22	11.65	10.43	28
2435	0.730	$0.72^{+0.02}_{-0.02}$	28.99	25.37	1.390	43.42	11.09	17.74	27
2484	...	$0.50^{+0.02}_{-0.02}$	28.18	25.05	1.200	43.10	10.70	15.21	19
2488	1.432	$1.45^{+0.03}_{-0.05}$	29.08	26.08	1.151	44.03	11.45	9.99	25
2504	...	$1.99^{+0.05}_{-0.05}$	29.37	26.27	1.188	44.26	11.76	11.94	24
2509	...	$1.75^{+0.19}_{-0.09}$	28.91	26.23	1.028	44.32	11.70	9.16	21
2514	...	$1.43^{+0.09}_{-0.11}$	28.65	25.95	1.036	44.05	11.45	9.65	21
2522	1.536	$1.56^{+0.04}_{-0.04}$	30.40	26.59	1.462	44.67	12.54	27.91	25
2528	...	$2.05^{+0.11}_{-0.09}$	29.52	25.90	1.389	44.17	11.97	23.87	28
2546	1.101	$0.88^{+0.04}_{-0.04}$	28.88	25.65	1.238	43.66	11.19	12.75	6
2554	...	$2.55^{+0.05}_{-0.03}$	29.83	26.45	1.297	44.49	12.04	13.79	28
2557	1.230	$2.27^{+0.03}_{-0.03}$	29.41	25.81	1.382	43.77	11.50	20.84	28
2602	...	$3.40^{+0.74}_{-0.78}$	29.35	26.20	1.209	44.42	12.08	17.54	25
2609	...	$1.75^{+0.03}_{-0.03}$	29.72	26.22	1.341	44.15	11.80	17.16	30
2613	2.008	$1.88^{+0.02}_{-0.02}$	31.23	26.21	1.926	44.20	13.12	322.41	28
2637	1.609	$1.64^{+0.04}_{-0.04}$	29.71	25.78	1.509	43.90	11.80	30.40	27
2650	...	$2.42^{+0.04}_{-0.04}$	29.56	26.75	1.079	44.80	12.19	9.34	30
2651	0.979	$0.95^{+0.05}_{-0.05}$	29.34	25.78	1.367	43.74	11.58	26.57	22
2703	2.281	$2.27^{+0.03}_{-0.03}$	30.25	26.57	1.413	44.55	12.45	30.41	29
2749	...	$2.87^{+0.03}_{-0.03}$	30.82	26.69	1.588	44.97	13.06	46.68	28
2750	1.798	$1.77^{+0.03}_{-0.03}$	29.31	26.25	1.174	44.18	11.70	12.68	28
2754	...	$1.22^{+0.04}_{-0.08}$	28.68	25.29	1.301	43.30	11.01	19.51	20
2792	...	$2.00^{+0.04}_{-0.06}$	29.33	25.95	1.300	44.02	11.66	16.83	28
2799	...	$1.26^{+0.04}_{-0.04}$	29.73	26.03	1.421	44.26	12.11	26.74	30
2810	1.257	$0.30^{+0.02}_{-0.02}$	28.73	25.63	1.191	43.66	11.14	11.53	29
2812	2.181	$2.26^{+0.02}_{-0.02}$	31.26	26.17	1.953	44.44	13.23	238.23	28
2845	1.782	$1.77^{+0.03}_{-0.05}$	29.22	26.12	1.190	43.99	11.42	10.30	28
2922	2.076	$2.11^{+0.03}_{-0.03}$	29.85	25.86	1.532	43.85	11.93	46.54	27
2979	...	$2.37^{+0.03}_{-0.03}$	30.13	25.80	1.661	44.03	12.15	50.71	30
5008	0.754	$0.61^{+0.03}_{-0.01}$	29.11	25.20	1.499	43.26	11.32	44.40	7
5013	1.826	$1.80^{+0.02}_{-0.02}$	29.81	26.01	1.457	44.13	11.94	24.58	28
5020	...	$1.21^{+0.03}_{-0.03}$	29.40	25.45	1.518	43.73	11.71	36.63	26
5031	1.824	$1.83^{+0.03}_{-0.03}$	29.69	25.70	1.531	43.85	11.82	36.02	29
5035	1.226	$1.20^{+0.12}_{-0.06}$	28.89	26.13	1.061	44.09	11.42	8.05	21
5038	1.299	$1.26^{+0.04}_{-0.04}$	28.92	25.35	1.370	43.75	11.91	54.76	4
5049	1.139	$1.13^{+0.03}_{-0.03}$	29.61	25.29	1.658	43.52	11.68	56.24	24
5061	1.784	$1.78^{+0.02}_{-0.02}$	30.20	26.59	1.385	44.62	12.41	23.45	28
5071	1.539	$1.55^{+0.03}_{-0.03}$	29.26	25.70	1.369	43.98	11.86	29.02	27
5078	1.899	$1.90^{+0.02}_{-0.02}$	30.73	26.22	1.733	44.33	12.69	88.29	30
5082	1.888	$1.89^{+0.01}_{-0.03}$	30.92	26.92	1.536	44.89	12.96	44.79	29
5095	1.215	$1.21^{+0.07}_{-0.05}$	28.97	25.67	1.266	43.81	11.45	16.56	20
5096	...	$1.54^{+0.02}_{-0.02}$	29.76	26.30	1.327	44.33	12.00	18.11	29
5099	...	$1.98^{+0.04}_{-0.02}$	29.92	26.28	1.395	44.73	12.96	65.23	29
5102	...	$1.03^{+0.07}_{-0.05}$	28.90	26.12	1.066	44.16	11.55	9.21	21
5121	0.196	$0.22^{+0.02}_{-0.02}$	28.43	24.48	1.517	42.41	10.58	57.32	7
5125	1.023	$1.03^{+0.03}_{-0.03}$	29.20	25.19	1.536	43.49	11.53	42.22	21
5133	0.658	$0.63^{+0.01}_{-0.03}$	30.02	26.16	1.479	44.05	11.95	30.18	30
5135	...	$1.19^{+0.09}_{-0.09}$	28.83	25.77	1.173	43.81	11.21	9.61	25
5138	...	$2.14^{+0.02}_{-0.04}$	30.21	26.66	1.364	44.64	12.44	24.04	30
5140	...	$2.15^{+0.39}_{-0.71}$	28.66	25.57	1.182	44.11	12.55	105.60	22
5149	...	$1.56^{+0.22}_{-0.48}$	28.47	25.45	1.161	43.70	11.46	21.66	19
5150	0.518	$0.51^{+0.01}_{-0.03}$	29.98	26.18	1.459	44.07	11.92	26.75	28
5151	...	$0.74^{+0.02}_{-0.02}$	29.62	26.22	1.307	44.16	11.70	13.53	27
5158	0.431	$1.44^{+0.12}_{-0.08}$	28.06	24.46	1.383	42.21	10.03	24.90	19
5162	3.524	$3.54^{+0.04}_{-0.04}$	29.99	26.23	1.442	44.46	12.31	26.85	30

Table A.1: Optical and X-ray properties of the total sample – *continued.*

XID	Spectroscopic redshift	Photometric redshift	Log $L_{2500\,\text{Å}}$ [erg s^{-1}Hz^{-1}]	Log $L_{2\,\text{keV}}$ [erg s^{-1}Hz^{-1}]	α_{ox}	Log $L_{[2-10]\text{keV}}$ [erg s^{-1}]	$L_{\text{bol},1\mu\text{m}}$ [$L_\odot$]	k_{bol}	Class[a]
5163	1.407	$1.45^{+0.03}_{-0.03}$	30.54	26.76	1.450	44.67	12.61	33.60	28
5165	...	$2.95^{+0.05}_{-0.03}$	29.77	26.41	1.291	44.56	12.19	16.23	26
5166	1.567	$1.57^{+0.03}_{-0.03}$	29.36	26.07	1.262	44.02	11.54	12.57	27
5170	...	$2.75^{+0.01}_{-0.03}$	29.94	26.57	1.294	44.68	12.30	15.86	29
5172	...	$1.31^{+0.03}_{-0.05}$	29.06	25.39	1.408	43.92	12.38	111.16	28
5173	1.856	$1.86^{+0.02}_{-0.02}$	30.00	26.59	1.307	44.63	12.20	14.46	30
5179	2.258	$2.23^{+0.03}_{-0.02}$	29.75	25.89	1.480	44.16	12.11	34.15	28
5180	1.343	$1.38^{+0.02}_{-0.02}$	29.84	25.87	1.523	44.05	12.03	36.19	29
5188	0.766	$2.19^{+0.03}_{-0.03}$	29.11	26.24	1.101	44.26	11.67	9.79	28
5189	1.579	$1.59^{+0.01}_{-0.03}$	30.38	25.86	1.735	44.27	12.67	94.22	27
5192	...	$1.95^{+0.69}_{-0.93}$	28.40	26.09	0.886	44.10	11.42	8.11	22
5199	3.609	$3.60^{+0.02}_{-0.02}$	30.18	26.44	1.432	44.62	12.38	22.31	30
5201	...	$0.75^{+0.03}_{-0.03}$	28.36	25.09	1.252	43.20	10.80	15.27	21
5204	2.665	$2.67^{+0.03}_{-0.03}$	30.04	26.17	1.486	44.44	12.37	32.46	29
5206	...	$1.23^{+0.09}_{-0.07}$	28.84	25.65	1.226	43.87	11.60	20.52	19
5212	1.413	$1.43^{+0.03}_{-0.05}$	29.69	26.43	1.251	44.43	11.91	11.74	28
5214	...	$1.48^{+0.04}_{-0.06}$	29.03	25.83	1.227	43.55	11.25	19.26	25
5218	...	$2.71^{+0.05}_{-0.03}$	29.95	26.25	1.419	44.35	12.07	19.84	29
5219	3.304	$3.25^{+0.03}_{-0.03}$	30.29	26.34	1.517	44.45	12.37	31.82	26
5226	1.613	$1.62^{+0.02}_{-0.02}$	30.01	26.32	1.418	44.31	12.10	23.62	29
5240	...	$1.43^{+0.03}_{-0.05}$	29.47	26.74	1.046	44.70	12.02	7.94	26
5243	...	$1.52^{+0.04}_{-0.14}$	29.04	25.76	1.259	43.81	11.37	13.87	21
5248	0.217	$0.31^{+0.01}_{-0.03}$	28.71	24.04	1.793	42.25	10.75	120.61	22
5250	...	$1.45^{+0.03}_{-0.03}$	29.88	26.38	1.343	44.41	11.97	13.89	28
5254	1.271	$1.27^{+0.03}_{-0.05}$	29.50	25.81	1.414	43.73	11.54	24.61	25
5257	1.111	$1.11^{+0.03}_{-0.03}$	30.31	26.26	1.553	44.19	12.26	44.56	28
5261	0.376	$0.37^{+0.03}_{-0.01}$	29.17	25.71	1.330	43.64	11.29	16.93	24
5272	0.850	$0.82^{+0.04}_{-0.02}$	29.28	25.94	1.282	43.85	11.43	14.31	24
5273	...	$2.50^{+0.02}_{-0.02}$	30.78	26.77	1.541	44.74	12.84	47.66	30
5277	1.679	$1.68^{+0.02}_{-0.02}$	29.72	26.26	1.329	44.27	11.85	14.55	28
5280	1.108	$1.04^{+0.04}_{-0.04}$	29.25	25.83	1.310	43.80	11.49	18.85	20
5286	...	$1.09^{+0.05}_{-0.05}$	28.93	25.71	1.234	43.81	11.35	13.18	20
5290	1.882	$1.90^{+0.02}_{-0.02}$	30.01	26.29	1.424	44.34	12.14	23.84	29
5293	...	$2.14^{+0.04}_{-0.04}$	29.56	26.14	1.314	44.19	11.80	15.44	30
5304	...	$1.00^{+1.62}_{-0.02}$	29.60	26.59	1.156	44.63	12.04	9.80	24
5305	...	$2.50^{+0.06}_{-0.12}$	29.01	25.60	1.306	44.00	12.09	46.38	25
5306	...	$0.92^{+0.06}_{-0.04}$	28.73	25.40	1.277	43.46	11.02	14.03	24
5315	1.574	$1.67^{+0.07}_{-0.29}$	28.97	25.32	1.404	43.64	11.71	45.16	6
5317	2.030	$2.03^{+0.03}_{-0.03}$	30.99	26.47	1.733	44.46	13.01	135.71	29
5320	0.340	$0.42^{+0.02}_{-0.02}$	28.34	25.16	1.224	43.07	10.60	13.01	7
5326	...	$0.95^{+1.41}_{-0.17}$	28.36	25.28	1.180	43.57	11.36	23.35	27
5329	...	$1.09^{+0.09}_{-0.05}$	29.12	25.85	1.255	43.87	11.30	10.49	28
5330	...	$2.18^{+0.02}_{-0.02}$	30.15	26.53	1.390	44.53	12.31	22.73	28
5331	3.038	$3.04^{+0.02}_{-0.02}$	30.87	26.75	1.583	44.65	12.85	59.66	28
5339	2.519	$2.52^{+0.04}_{-0.04}$	29.66	26.03	1.393	44.11	11.83	19.77	30
5345	...	$3.29^{+0.05}_{-0.03}$	30.02	26.25	1.446	44.37	12.13	21.80	30
5359	...	$1.28^{+0.06}_{-0.06}$	29.22	25.39	1.468	43.97	12.58	154.44	23
5361	...	$1.26^{+0.04}_{-0.06}$	29.32	25.80	1.353	43.91	11.64	20.37	20
5363	2.387	$2.39^{+0.03}_{-0.03}$	29.80	26.03	1.447	44.35	12.36	39.00	30
5373	...	$2.08^{+0.04}_{-0.04}$	29.79	26.12	1.412	44.10	11.89	23.45	28
5378	2.082	$2.13^{+0.03}_{-0.03}$	29.89	26.43	1.330	44.41	12.09	18.15	29
5382	3.465	$3.45^{+0.03}_{-0.07}$	29.95	25.61	1.666	44.36	13.42	440.81	30
5384	...	$2.25^{+0.03}_{-0.03}$	30.63	26.98	1.401	44.94	12.81	28.32	29
5387	1.573	$1.54^{+0.02}_{-0.02}$	29.72	25.72	1.533	43.80	11.74	33.45	27
5394	0.878	$0.81^{+0.03}_{-0.03}$	29.29	25.50	1.455	43.57	11.52	33.51	19
5396	1.669	$1.68^{+0.02}_{-0.02}$	30.12	26.68	1.323	44.70	12.33	16.55	28

Table A.1: Optical and X-ray properties of the total sample – *continued.*

XID	Spectroscopic redshift	Photometric redshift	Log $L_{2500\,\text{Å}}$ [erg s^{-1}Hz^{-1}]	Log $L_{2\,\text{keV}}$ [erg s^{-1}Hz^{-1}]	α_{ox}	Log $L_{[2-10]\text{keV}}$ [erg s^{-1}]	$L_{\text{bol},1\mu\text{m}}$ [$L_\odot$]	k_{bol}	Class[a]
5397	1.470	$1.47^{+0.03}_{-0.03}$	29.54	26.35	1.224	44.49	12.07	14.67	24
5402	2.238	$2.27^{+0.03}_{-0.05}$	29.93	25.78	1.590	44.03	12.14	49.19	28
5404	1.334	$1.36^{+0.02}_{-0.04}$	29.66	26.27	1.303	44.25	11.85	15.26	26
5415	0.906	$0.91^{+0.03}_{-0.03}$	29.75	25.34	1.692	43.49	11.71	62.98	27
5416	...	$0.55^{+0.05}_{-0.05}$	28.90	25.57	1.279	43.55	11.06	12.34	28
5417	...	$2.05^{+0.05}_{-1.35}$	30.29	26.00	1.647	44.21	12.35	53.16	29
5420	...	$0.63^{+1.69}_{-0.63}$	27.36	24.79	0.988	43.02	10.68	17.53	29
5425	...	$1.40^{+0.06}_{-0.06}$	29.19	25.63	1.368	43.92	11.80	29.18	23
5428	...	$1.61^{+0.05}_{-0.05}$	29.06	25.63	1.315	43.76	11.43	17.86	23
5429	0.346	$0.52^{+0.02}_{-0.02}$	28.06	24.78	1.260	42.72	10.38	17.44	6
5431	2.027	$2.00^{+0.02}_{-0.02}$	29.64	26.06	1.374	44.12	11.93	24.81	29
5434	2.402	$2.40^{+0.02}_{-0.02}$	30.03	26.67	1.290	44.65	12.24	14.83	28
5437	1.447	$1.44^{+0.02}_{-0.04}$	29.51	25.73	1.452	43.79	11.66	28.58	25
5452	...	$1.92^{+0.06}_{-0.06}$	28.96	25.96	1.151	44.03	11.42	9.38	28
5453	0.728	$0.72^{+0.02}_{-0.02}$	28.97	25.39	1.374	43.75	11.78	40.82	25
5457	...	$0.70^{+0.04}_{-0.02}$	28.51	24.80	1.423	43.15	11.17	40.44	21
5464	1.623	$1.59^{+0.05}_{-0.03}$	29.48	25.76	1.429	44.04	11.92	29.02	25
5468	0.795	$0.80^{+0.02}_{-0.02}$	29.82	26.15	1.407	43.99	11.81	25.10	28
5476	0.703	$1.47^{+0.03}_{-0.03}$	29.21	25.61	1.382	43.48	11.33	27.33	4
5478	...	$2.76^{+0.02}_{-0.04}$	29.79	25.86	1.510	44.11	12.08	35.93	30
5479	...	$1.43^{+0.21}_{-0.21}$	28.26	25.49	1.063	43.61	11.07	11.09	19
5482	...	$3.33^{+0.07}_{-0.07}$	29.70	26.21	1.339	44.35	11.98	16.53	30
5483	...	$2.83^{+0.01}_{-0.03}$	30.57	26.11	1.709	44.29	12.58	75.09	30
5485	1.092	$9.00^{+0.00}_{-0.00}$	29.54	26.21	1.276	44.15	11.70	13.63	-99
5492	...	$2.39^{+0.01}_{-0.03}$	30.80	26.73	1.562	44.86	12.92	44.21	30
5501	...	$0.95^{+0.03}_{-0.03}$	29.46	26.25	1.231	44.26	11.71	10.81	30
5503	1.294	$1.30^{+0.02}_{-0.04}$	30.07	26.55	1.348	44.49	12.13	16.91	30
5505	1.855	$1.87^{+0.05}_{-0.05}$	29.51	26.25	1.251	44.20	11.75	13.76	27
5506	...	$1.13^{+0.07}_{-0.83}$	28.74	25.12	1.390	43.23	11.01	23.23	21
5507	0.905	$0.89^{+0.03}_{-0.03}$	28.97	25.60	1.295	43.58	11.26	18.23	22
5510	1.480	$1.49^{+0.03}_{-0.03}$	29.57	26.54	1.161	44.62	12.04	10.25	27
5514	...	$2.87^{+0.03}_{-0.05}$	29.54	25.65	1.493	44.33	13.15	254.18	27
5515	...	$1.57^{+0.37}_{-0.07}$	28.89	25.39	1.344	43.94	12.44	120.04	28
5518	2.686	$2.70^{+0.04}_{-0.02}$	29.94	26.29	1.399	44.40	12.13	20.66	29
5520	1.182	$1.13^{+0.07}_{-0.09}$	28.94	25.21	1.431	43.48	11.42	33.97	20
5521	...	$0.88^{+0.06}_{-0.06}$	28.84	25.35	1.339	43.22	11.01	23.52	21
5523	1.087	$0.99^{+0.05}_{-0.07}$	29.26	25.58	1.412	43.56	11.39	25.85	22
5529	...	$0.92^{+0.08}_{-0.06}$	29.27	25.98	1.260	43.87	11.40	12.90	23
5531	1.530	$1.54^{+0.02}_{-0.02}$	29.89	25.86	1.545	43.91	11.98	45.63	30
5532	...	$2.11^{+0.07}_{-0.07}$	29.19	25.64	1.363	43.83	11.56	20.28	26
5541	...	$2.36^{+0.02}_{-0.02}$	29.71	26.18	1.352	44.45	12.27	25.52	30
5544	1.889	$1.89^{+0.03}_{-0.03}$	30.57	26.32	1.630	44.26	12.59	82.78	29
5554	...	$2.41^{+0.03}_{-0.03}$	30.32	26.20	1.583	44.27	12.29	40.56	30
5555	...	$1.14^{+0.20}_{-0.12}$	28.38	25.19	1.223	43.37	11.01	16.63	19
5560	1.035	$1.04^{+0.04}_{-0.04}$	29.46	25.34	1.582	43.72	11.91	58.63	23
5561	...	$2.11^{+0.01}_{-0.03}$	30.53	26.44	1.570	44.20	12.63	102.22	29
5563	...	$3.41^{+0.55}_{-3.27}$	29.17	26.44	1.048	44.51	11.85	8.28	21
5566	0.837	$0.83^{+0.03}_{-0.05}$	29.14	25.76	1.298	43.75	11.30	13.59	24
5575	2.408	$2.40^{+0.02}_{-0.02}$	29.90	26.60	1.269	44.55	12.12	14.18	29
5577	0.987	$0.98^{+0.02}_{-0.04}$	29.60	25.89	1.425	43.95	11.70	21.40	27
5581	2.668	$2.63^{+0.05}_{-0.03}$	29.77	26.09	1.412	44.20	11.89	18.55	28
5583	3.499	$3.49^{+0.03}_{-0.03}$	30.41	26.13	1.644	44.34	12.43	47.18	26
5584	...	$2.67^{+0.21}_{-2.51}$	29.48	26.21	1.254	44.36	11.90	13.10	27
5592	3.745	$3.78^{+0.04}_{-0.04}$	30.17	26.51	1.404	44.55	12.15	15.24	30
5598	1.702	$1.01^{+0.11}_{-0.05}$	29.07	25.73	1.281	43.91	11.56	16.95	20
5600	1.955	$2.00^{+0.02}_{-0.02}$	30.51	26.48	1.550	44.45	12.54	47.21	28

Table A.1: Optical and X-ray properties of the total sample – *continued.*

XID	Spectroscopic redshift	Photometric redshift	Log $L_{2500\,\text{Å}}$ [erg s^{-1}Hz^{-1}]	Log $L_{2\,\text{keV}}$ [erg s^{-1}Hz^{-1}]	α_{ox}	Log $L_{[2-10]\text{keV}}$ [erg s^{-1}]	$L_{\text{bol},1\mu\text{m}}$ [$L_\odot$]	k_{bol}	Class[a]
5602	...	$0.40^{+1.84}_{-0.02}$	27.43	24.34	1.189	42.50	10.06	13.73	27
5606	4.166	$4.01^{+0.05}_{-0.05}$	30.03	26.45	1.373	44.43	12.09	17.45	27
5607	1.359	$1.36^{+0.02}_{-0.02}$	30.06	25.62	1.706	43.86	12.11	67.78	29
5608	...	$2.13^{+0.21}_{-0.07}$	28.84	26.11	1.046	44.57	12.81	66.31	28
5609	1.343	$1.34^{+0.04}_{-0.04}$	29.43	26.00	1.315	43.92	11.56	17.05	25
5615	2.005	$2.02^{+0.02}_{-0.02}$	30.72	26.57	1.596	44.55	12.81	69.77	29
5617	0.103	$0.22^{+0.02}_{-0.02}$	28.18	24.16	1.543	42.19	10.42	64.25	7
5624	...	$2.11^{+0.05}_{-0.55}$	29.19	26.33	1.096	44.34	11.71	9.14	26
5625	...	$2.75^{+0.03}_{-0.03}$	29.99	26.61	1.296	44.54	12.23	18.74	29
5627	1.337	$1.37^{+0.03}_{-0.03}$	30.08	26.05	1.547	44.09	12.08	36.84	30
10083	...	$1.23^{+0.05}_{-0.05}$	29.16	25.85	1.268	43.99	11.56	14.53	25
10158	1.980	$2.00^{+0.02}_{-0.02}$	30.34	25.98	1.675	44.22	12.49	70.74	27
10168	...	$1.54^{+0.04}_{-0.04}$	29.39	25.62	1.449	43.98	12.04	43.87	25
10183	...	$2.97^{+0.03}_{-0.03}$	29.64	25.64	1.538	44.15	12.56	97.59	30
10257	...	$1.60^{+0.08}_{-0.14}$	29.08	25.36	1.428	43.73	11.81	46.57	21
10332	...	$2.22^{+0.16}_{-0.22}$	29.15	26.49	1.021	43.79	11.61	25.35	28
10360	...	$2.82^{+0.04}_{-0.04}$	29.59	25.87	1.427	44.03	11.87	26.61	26
10388	0.776	$2.23^{+0.03}_{-0.03}$	28.87	25.22	1.400	43.30	11.01	19.37	29
10690	...	$3.10^{+0.04}_{-0.04}$	29.62	25.93	1.418	44.20	12.08	28.63	27
10709	2.095	$2.11^{+0.03}_{-0.03}$	29.83	25.65	1.607	43.85	11.97	50.60	28
10719	...	$1.70^{+0.02}_{-0.02}$	29.76	25.73	1.547	44.00	11.98	36.08	28
10829	...	$1.46^{+0.34}_{-0.18}$	28.68	25.54	1.207	43.86	11.74	28.92	20
10852	...	$2.43^{+0.03}_{-0.03}$	29.64	26.20	1.322	44.57	12.61	41.76	30
10875	...	$0.04^{+0.02}_{-0.02}$	25.74	22.25	1.342	40.63	8.73	47.34	20
10889	1.960	$2.03^{+0.03}_{-0.03}$	31.43	26.91	1.736	44.80	13.44	170.15	28
10911	...	$2.05^{+0.07}_{-0.05}$	30.01	25.84	1.603	43.97	12.16	59.40	20
30012	...	$2.31^{+0.07}_{-0.13}$	29.26	25.62	1.400	44.10	12.41	78.23	23
30366	...	$1.66^{+0.02}_{-0.02}$	29.98	25.53	1.706	43.91	12.16	67.61	28
30370	...	$0.68^{+0.42}_{-0.12}$	27.35	24.65	1.035	43.36	12.29	324.11	19
30587	...	$0.75^{+0.05}_{-0.05}$	28.51	24.85	1.403	42.94	10.69	21.69	21
30687	1.478	$1.49^{+0.05}_{-0.03}$	29.36	25.33	1.544	43.66	11.76	48.09	27
30699	...	$2.05^{+0.03}_{-0.03}$	29.79	25.82	1.523	44.00	12.02	40.09	29
30874	...	$1.60^{+0.02}_{-0.02}$	30.04	26.34	1.420	44.66	12.60	33.80	30
30942	...	$2.08^{+0.28}_{-0.22}$	28.80	25.73	1.180	43.93	11.58	16.73	23
31234	...	$2.14^{+0.18}_{-0.06}$	29.51	25.84	1.409	44.10	11.91	24.85	29
53037	...	$2.32^{+0.08}_{-0.72}$	29.06	26.38	1.029	44.72	12.62	30.03	30
53249	2.335	$2.32^{+0.08}_{-1.24}$	29.09	25.45	1.397	44.12	12.93	246.71	23
53283	1.223	$1.25^{+0.03}_{-0.03}$	29.69	25.44	1.631	43.50	11.70	60.41	27
53329	...	$2.58^{+0.02}_{-0.02}$	29.82	25.83	1.531	44.15	12.23	46.52	27
53339	...	$0.71^{+1.17}_{-0.03}$	27.96	24.83	1.199	43.03	10.74	19.66	19
53340	1.130	$1.15^{+0.05}_{-0.05}$	29.25	25.73	1.353	44.35	13.04	186.72	26
53352	...	$2.62^{+0.22}_{-0.10}$	29.21	25.70	1.346	44.20	12.56	87.48	21
53357	...	$2.64^{+0.02}_{-0.02}$	30.71	25.88	1.854	44.24	12.77	130.55	30
53374	...	$1.16^{+0.18}_{-0.10}$	28.86	25.83	1.164	44.04	11.69	17.02	22
53379	...	$2.40^{+0.02}_{-0.02}$	30.01	26.41	1.379	44.56	12.29	20.46	28
53537	1.067	$1.12^{+0.04}_{-0.02}$	30.72	26.85	1.484	44.75	12.69	33.55	29
53577	...	$1.10^{+0.06}_{-0.04}$	29.85	26.53	1.274	44.53	12.03	12.07	28
53584	1.797	$1.78^{+0.06}_{-0.10}$	29.29	25.85	1.324	44.07	11.85	23.37	23
53610	...	$1.68^{+0.06}_{-0.04}$	29.36	25.54	1.464	43.79	11.69	30.18	23
53614	...	$1.44^{+0.04}_{-0.10}$	29.14	25.25	1.493	43.69	11.92	64.36	27
53659	...	$1.19^{+0.03}_{-0.03}$	29.99	25.85	1.590	43.93	11.98	43.23	25
53675	...	$0.51^{+0.11}_{-0.21}$	27.47	24.40	1.179	42.45	10.03	14.58	21
53678	...	$0.66^{+0.04}_{-0.02}$	28.38	25.06	1.273	43.51	11.72	61.90	22
53686	2.614	$2.56^{+0.02}_{-0.02}$	30.72	26.60	1.582	44.65	12.79	52.97	26
53700	1.600	$1.67^{+0.13}_{-0.21}$	29.07	25.48	1.378	43.68	11.47	23.57	20
53720	...	$1.99^{+0.07}_{-0.11}$	29.88	25.55	1.660	43.80	11.94	52.62	30
53723	...	$2.13^{+0.11}_{-0.11}$	29.14	25.68	1.328	43.93	11.73	24.43	21
53724	...	$2.05^{+0.03}_{-0.03}$	29.93	25.91	1.543	44.23	12.30	44.74	29
53737	...	$1.19^{+1.13}_{-0.05}$	27.91	25.14	1.064	43.53	11.57	42.72	19

Table A.1: Optical and X-ray properties of the total sample – *continued.*

XID	Spectroscopic redshift	Photometric redshift	Log $L_{2500\,\text{Å}}$ [erg s^{-1}Hz^{-1}]	Log $L_{2\,\text{keV}}$ [erg s^{-1}Hz^{-1}]	α_{ox}	Log $L_{[2-10]\text{keV}}$ [erg s^{-1}]	$L_{\text{bol},1\mu\text{m}}$ [$L_\odot$]	k_{bol}	Class[a]
53749	2.384	$2.36^{+0.04}_{-0.04}$	29.50	25.74	1.443	43.90	11.75	27.39	28
53755	...	$1.79^{+0.43}_{-1.29}$	28.81	25.31	1.344	43.97	12.72	217.73	24
53831	1.556	$1.56^{+0.02}_{-0.02}$	30.82	26.96	1.481	44.81	12.86	43.50	29
53840	...	$1.27^{+0.07}_{-0.07}$	28.72	26.05	1.026	44.13	11.55	10.09	19
53970	...	$2.48^{+0.06}_{-1.70}$	29.79	25.70	1.571	44.04	12.13	46.56	28
54129	0.631	$1.13^{+0.09}_{-0.05}$	28.05	24.58	1.334	43.04	11.32	73.68	22
54137	1.983	$1.97^{+0.03}_{-0.03}$	30.06	25.71	1.670	44.14	12.50	86.61	27
54140	...	$2.14^{+0.06}_{-0.04}$	29.46	26.40	1.174	44.36	11.90	13.11	29
54202	2.102	$2.11^{+0.03}_{-0.03}$	30.46	26.78	1.410	44.83	12.71	28.95	29
54204	1.356	$1.36^{+0.02}_{-0.02}$	30.25	25.47	1.835	43.85	12.37	127.14	29
54263	1.160	$1.17^{+0.03}_{-0.03}$	29.51	26.69	1.082	44.75	12.09	8.44	25
54280	...	$0.92^{+0.04}_{-0.04}$	28.89	25.43	1.328	43.58	11.27	18.94	23
54294	1.560	$1.54^{+0.02}_{-0.02}$	29.68	26.21	1.333	44.35	12.02	18.10	29
54308	1.711	$1.71^{+0.03}_{-0.03}$	29.78	25.95	1.469	44.18	12.10	31.88	29
54309	...	$2.57^{+0.03}_{-0.03}$	30.32	26.04	1.646	44.32	12.42	47.85	28
54318	...	$2.09^{+5.91}_{-0.45}$	28.29	25.96	0.893	44.12	11.57	10.91	22
54330	...	$1.95^{+0.05}_{-0.03}$	29.59	25.67	1.504	43.77	11.71	33.37	28
54333	...	$2.14^{+0.04}_{-0.02}$	29.91	26.28	1.393	44.31	12.13	24.91	30
54355	2.011	$1.99^{+0.03}_{-0.03}$	30.66	26.56	1.575	44.57	12.72	54.06	24
54358	...	$0.87^{+0.29}_{-0.87}$	27.54	24.91	1.009	43.04	10.46	9.96	29
54359	...	$1.55^{+0.05}_{-0.07}$	29.05	26.08	1.141	44.28	11.91	16.53	21
54370	...	$0.38^{+1.10}_{-0.02}$	27.55	24.45	1.189	42.84	10.89	43.32	19
54374	...	$2.11^{+0.97}_{-0.71}$	28.47	25.61	1.097	44.12	12.48	87.53	22
54376	2.203	$0.79^{+0.05}_{-0.03}$	29.58	26.27	1.272	44.41	12.04	16.49	25
54392	...	$2.53^{+0.03}_{-0.03}$	30.26	26.34	1.505	44.60	12.57	35.79	26
54405	...	$1.86^{+0.04}_{-0.04}$	29.46	25.72	1.438	43.87	11.67	24.23	30
54409	...	$0.78^{+0.12}_{-0.30}$	27.90	24.94	1.135	43.08	10.58	11.85	22
54424	...	$0.31^{+2.33}_{-0.31}$	26.46	24.15	0.887	42.16	9.34	5.74	29
54430	...	$1.08^{+1.28}_{-0.90}$	27.99	25.12	1.099	43.39	11.12	20.44	23
54431	...	$1.26^{+0.82}_{-0.14}$	28.72	25.22	1.343	43.66	11.89	65.01	20
54439	4.251	$4.25^{+0.05}_{-0.05}$	29.60	26.07	1.354	44.46	12.52	43.72	30
60001	...	$2.00^{+0.08}_{-0.12}$	29.18	26.04	1.205	44.51	12.75	66.77	23
60002	...	$1.83^{+1.21}_{-0.93}$	28.87	25.59	1.259	43.89	11.73	26.65	28
60004	...	$2.49^{+0.03}_{-0.03}$	30.00	26.33	1.407	44.60	12.48	28.99	30
60013	...	$1.98^{+0.10}_{-1.18}$	29.22	25.40	1.465	44.02	12.70	182.15	25
60020	...	$2.64^{+0.02}_{-0.02}$	30.20	25.73	1.714	44.10	12.39	75.45	27
60105	...	$2.05^{+0.03}_{-0.03}$	29.86	25.89	1.524	44.26	12.39	51.72	26
60107	...	$1.51^{+0.03}_{-0.03}$	29.50	25.74	1.443	44.11	12.18	44.88	25
60131	3.328	$3.48^{+0.02}_{-0.04}$	30.79	25.85	1.898	44.20	12.70	121.80	30
60164	...	$1.34^{+0.04}_{-0.04}$	29.57	25.72	1.479	43.90	11.79	30.14	25
60186	...	$3.39^{+0.05}_{-3.17}$	30.36	27.52	1.090	44.81	12.71	30.28	23
60229	...	$0.17^{+0.03}_{-0.03}$	26.75	23.85	1.111	42.20	10.14	33.08	22
60243	...	$0.99^{+0.15}_{-0.19}$	28.27	25.10	1.215	43.33	11.04	19.39	19
60247	...	$2.48^{+0.02}_{-0.04}$	30.05	25.73	1.658	43.91	12.13	63.64	30
60304	...	$2.35^{+0.83}_{-0.85}$	28.40	25.51	1.111	44.14	12.81	179.89	19
60311	...	$3.33^{+0.03}_{-0.07}$	30.39	26.62	1.445	44.57	12.35	23.00	30
60315	...	$2.09^{+0.05}_{-0.03}$	29.70	25.98	1.427	44.41	12.62	62.26	29
60368	...	$1.55^{+0.03}_{-0.03}$	29.19	25.32	1.486	43.48	11.40	31.56	25
60414	...	$1.75^{+0.07}_{-1.25}$	29.60	25.56	1.548	43.71	11.72	39.52	29
60415	...	$2.78^{+0.04}_{-0.10}$	29.83	25.80	1.544	44.29	12.61	80.82	28
60421	...	$1.60^{+0.70}_{-0.20}$	28.40	25.27	1.202	43.71	11.90	59.93	20
60434	0.634	$0.58^{+0.04}_{-0.04}$	28.47	25.22	1.248	43.70	12.05	85.28	7
60440	...	$1.78^{+0.06}_{-1.26}$	29.43	26.32	1.194	43.63	11.70	44.53	26
60446	...	$0.34^{+0.04}_{-0.02}$	27.42	23.99	1.317	42.19	9.90	19.79	21
60466	...	$2.81^{+0.01}_{-0.03}$	30.34	25.87	1.717	44.21	12.46	67.57	30

[a] The SED model of the best-fit template is coded from 1 to 30, as detailed in S09.

Appendix B

Properties of the Type-2 AGN sample

Table B.1: Properties of the Type-2 AGN sample.

XID	Redshift	Log $\langle N_{\rm H}\rangle$ [cm^{-2}]	Log $L_{[2-10]\rm keV}$ [erg s^{-1}]	Log $L_{\rm bol}$ [erg s^{-1}]	$k_{\rm bol}$	Log M_* [M$_\odot$]	SFR [$M_\odot$/yrs]	$M_{\rm U}$	$M_{\rm V}$	Morphological class[a]
67	0.367	$20.48^{G}_{-20.90}$	42.80	43.84	10.97	9.39	7.73	-18.67	-19.77	0
65	0.979	$21.71^{+21.37}_{-21.83}$	43.84	44.89	11.17	10.27	58.94	-20.57	-21.77	7
64	0.686	$21.40^{+21.28}_{-21.51}$	43.55	44.59	10.81	10.35	70.90	-20.17	-21.56	10
63	0.355	...	42.98	44.32	21.88	10.89	6.23	-20.61	-22.13	2
54	0.350	...	42.58	43.42	6.83	11.19	0.11	-20.57	-22.62	12
45	0.121	$21.34^{+21.15}_{-21.52}$	41.90	42.92	10.62	9.40	0.00	-16.76	-18.70	1
43	1.162	$21.79^{+21.64}_{-21.93}$	44.24	45.29	11.12	11.66	5.66	-21.28	-23.38	2
41	0.962	$22.11^{+22.13}_{-22.52}$	44.06	45.17	13.03	9.99	135.80	-21.44	-22.20	8
19	0.659	$20.70^{+20.30}_{-20.95}$	43.68	44.85	15.01	11.01	51.39	-21.57	-22.88	1
4	0.132	$20.70^{+20.48}_{-20.85}$	42.85	43.78	8.54	10.81	1.53	-19.64	-21.36	1
117	0.936	$22.21^{+21.20}_{-22.64}$	43.48	45.60	132.11	11.21	205.57	-21.81	-23.34	23
116	0.874	$21.26^{+20.90}_{-21.46}$	43.50	44.63	13.46	10.60	4.11	-20.19	-21.81	0
112	0.762	...	43.65	44.89	17.23	10.94	0.64	-20.00	-22.13	3
104	0.623	$21.81^{+21.67}_{-21.91}$	44.09	45.16	11.71	11.21	2.02	-20.16	-22.26	1
101	0.927	...	43.71	44.80	12.25	10.96	0.66	-21.25	-22.99	0
100	0.270	...	42.60	43.68	11.97	10.23	0.00	-19.14	-20.98	0
99	0.730	$21.08^{+20.78}_{-21.30}$	43.55	44.88	21.58	10.05	157.57	-21.61	-22.36	11
85	1.001	$20.90^{G}_{-21.32}$	43.47	44.93	28.55	9.91	110.99	-20.33	-21.39	8
81	0.915	$21.89^{+21.79}_{-21.99}$	44.12	45.10	9.46	11.22	1.22	-20.40	-22.63	2
70	0.688	$23.25^{+23.07}_{-23.41}$	44.01	45.61	39.74	10.61	555.45	-20.87	-22.32	3
152	0.895	...	43.77	44.89	13.25	9.97	129.72	-21.09	-21.95	7
150	0.740	$22.10^{+21.82}_{-22.39}$	43.30	44.27	9.27	10.66	0.56	-19.38	-21.28	3
147	2.941	21.95^{G}_{G}	44.89	46.71	66.01	11.76	339.50	-23.05	-24.55	6
143	0.732	$22.26^{+21.85}_{-22.56}$	43.62	44.66	10.91	11.12	0.96	-20.75	-22.78	3
142	0.498	...	42.92	43.88	9.11	10.49	2.47	-19.30	-20.92	1
134	0.625	...	42.98	44.00	10.42	10.70	0.62	-19.48	-21.38	0
122	2.418	$23.05^{+22.79}_{-23.31}$	44.89	46.02	13.66	11.11	351.89	-22.26	-23.59	7
121	0.502	$21.20^{+20.95}_{-21.38}$	43.01	44.01	9.86	10.58	0.47	-19.19	-21.10	1
120	0.552	$22.18^{+22.10}_{-22.26}$	43.73	45.13	24.82	11.05	11.66	-19.81	-21.93	2
119	0.891	$21.26^{+21.04}_{-21.34}$	44.07	45.27	15.72	10.60	108.90	-20.68	-22.11	2
194	1.456	$22.74^{+22.39}_{-22.99}$	44.21	45.54	21.35	10.23	236.46	-20.83	-21.99	5
193	0.731	...	43.40	44.84	27.35	10.17	207.00	-21.30	-22.25	1
191	0.346	$22.18^{+21.98}_{-22.38}$	43.01	44.16	14.20	10.80	0.78	-20.04	-21.84	2

Table B.1: Properties of the Type-2 AGN sample. – *continued.*

XID	Redshift	Log $\langle N_{\rm H}\rangle$ [cm^{-2}]	Log $L_{[2-10]\rm keV}$ [erg s^{-1}]	Log $L_{\rm bol}$ [erg s^{-1}]	$k_{\rm bol}$	Log M_* [M$_\odot$]	SFR [$M_\odot$/yrs]	$M_{\rm U}$	$M_{\rm V}$	Morphological class[a]
177	0.339	...	42.66	43.86	15.62	10.67	3.79	-20.68	-21.99	2
174	0.740	...	43.43	44.52	12.37	10.20	79.10	-20.52	-21.69	2
173	1.028	...	44.04	45.71	47.00	10.76	6.07	-20.91	-22.44	2
172	0.891	$21.30^{+21.00}_{-21.46}$	43.33	44.78	28.19	10.08	164.72	-21.36	-22.22	2
170	0.934	...	43.43	44.83	25.30	10.93	50.60	-21.89	-23.10	3
158	0.703	$22.48^{+22.13}_{-22.70}$	43.35	44.36	10.24	11.17	1.83	-20.66	-22.56	3
157	0.185	$21.69^{+21.08}_{-21.86}$	42.06	43.31	17.98	10.63	0.03	-19.18	-21.22	3
230	0.734	$22.43^{+21.93}_{-22.87}$	43.40	44.61	16.30	10.94	9.07	-21.05	-22.67	2
229	0.864	$22.21^{+21.80}_{-22.47}$	43.78	44.85	11.76	11.11	1.60	-20.21	-22.21	1
222	0.337	...	42.49	43.75	18.39	10.04	0.08	-18.34	-20.27	1
217	0.660	...	43.41	45.54	136.69	11.13	14.10	-20.92	-22.75	23
214	0.864	...	43.28	44.39	12.94	10.77	6.12	-20.32	-22.04	1
212	0.931	$23.37^{+23.21}_{-24.32}$	44.13	45.54	25.45	10.50	96.79	-20.21	-21.71	0
206	0.673	...	43.39	44.73	21.60	10.65	4.62	-19.11	-21.13	2
203	0.374	...	42.68	43.68	9.97	10.11	1.33	-18.66	-20.39	0
202	1.319	...	44.22	46.00	61.12	10.29	268.73	-20.67	-21.92	7
198	0.895	...	43.75	44.90	14.06	11.07	12.31	-21.08	-22.80	2
277	0.695	...	43.32	44.62	20.29	10.77	19.18	-21.52	-22.65	...
274	0.678	...	43.22	44.59	23.44	10.89	0.56	-20.16	-22.19	11
269	0.836	...	43.49	44.78	19.74	11.15	1.76	-20.61	-22.52	1
257	0.490	...	42.98	44.49	32.97	11.10	1.56	-19.58	-21.78	2
255	0.187	...	42.05	57.13	...	10.58	3.98	-19.25	-21.17	2
253	0.480	...	42.83	44.39	36.35	10.54	3.63	-20.05	-21.68	2
252	1.238	...	43.96	45.89	86.16	11.15	446.46	-21.87	-23.36	5
242	0.838	...	43.21	45.10	78.23	10.17	208.15	-20.09	-21.44	5
234	0.644	...	43.35	45.32	92.77	10.44	0.20	-19.96	-21.69	7
231	1.428	...	43.93	45.14	16.30	10.24	93.84	-21.58	-22.44	8
352	0.165	$21.15^{G}_{-21.59}$	41.61	43.17	35.80	8.34	3.05	-15.51	-16.86	5
345	1.813	...	44.14	45.49	22.29	10.36	34.22	-20.41	-21.70	8
339	0.518	...	43.02	44.38	23.18	9.99	48.09	-19.68	-20.95	1
323	0.839	$22.27^{+22.12}_{-22.40}$	43.94	45.20	17.81	10.61	128.95	-20.82	-22.21	2
302	0.186	...	41.81	43.48	47.35	10.18	0.11	-19.31	-21.05	1
297	0.439	...	42.82	43.96	13.86	10.80	0.46	-20.85	-22.59	2
296	0.570	...	42.85	43.95	12.68	10.57	3.86	-20.42	-21.95	1
293	0.445	$22.16^{+22.08}_{-22.25}$	43.48	44.90	25.92	11.28	2.40	-20.95	-22.85	2
292	0.618	$22.77^{+22.51}_{-22.96}$	43.62	44.87	17.56	10.76	13.95	-19.45	-21.27	3
283	1.030	$21.30^{+20.95}_{-21.53}$	43.87	44.90	10.59	10.90	8.33	-20.35	-22.18	0
442	0.922	$22.47^{+21.86}_{-22.98}$	43.43	45.07	43.86	10.66	56.68	-19.21	-21.13	5
417	0.340	...	43.24	44.42	15.18	11.01	2.41	-20.43	-22.06	1
413	1.023	$23.56^{+23.34}_{-23.92}$	44.24	45.31	11.64	10.73	14.03	-21.68	-22.83	23
411	0.952	$22.36^{+21.94}_{-22.55}$	43.93	45.03	12.53	10.74	5.76	-19.95	-21.77	7
399	1.189	$21.72^{+21.38}_{-22.03}$	43.76	44.78	10.32	9.73	73.16	-20.48	-21.34	8
398	0.745	...	43.04	44.20	14.62	10.84	0.50	-20.64	-22.47	7
385	0.350	$22.21^{+21.75}_{-22.64}$	42.85	44.43	38.04	10.82	0.81	-18.57	-20.87	2
382	0.740	...	43.19	44.50	20.09	10.74	5.73	-21.15	-22.58	2
371	0.901	...	43.49	44.94	28.45	11.03	0.77	-20.51	-22.54	1
364	0.764	...	43.26	44.64	24.21	11.22	2.05	-21.08	-22.89	3
2191	0.621	...	43.10	44.47	23.64	9.65	61.91	-20.29	-21.15	7
2081	1.566	...	44.72	45.80	12.16	10.97	468.39	-23.36	-24.24	8
2076	0.735	$21.88^{+21.84}_{-21.92}$	44.18	45.39	16.28	10.75	153.76	-21.06	-22.49	1
2050	1.031	$21.89^{+21.78}_{-21.99}$	44.78	45.88	12.59	11.36	1.67	-21.05	-23.18	...
2043	0.668	$22.00^{+21.89}_{-22.23}$	43.82	45.00	15.19	11.14	1.00	-20.48	-22.61	2
2028	1.592	$21.86^{+21.79}_{-21.94}$	45.01	46.60	38.93	12.10	130.50	-22.44	-24.56	8
2021	0.104	$22.43^{+22.38}_{-22.48}$	42.75	43.86	12.86	10.85	0.46	-19.41	-21.37	2
1533	0.123	...	41.33	56.73	...	10.27	1.94	-20.28	-21.61	3
1429	0.356	$21.54^{+21.45}_{-21.61}$	43.54	44.81	18.32	11.16	19.82	-21.08	-22.62	23
507	0.879	...	43.32	44.34	10.46	10.74	0.40	-19.80	-21.83	3
2353	1.122	$22.27^{+21.57}_{-22.59}$	43.92	44.95	10.82	10.64	11.53	-19.95	-21.60	7
2352	0.659	...	43.03	44.85	65.59	9.99	132.89	-21.13	-21.99	1
2289	0.833	$22.56^{+22.32}_{-22.80}$	43.68	45.19	32.32	10.82	181.49	-21.54	-22.87	2
2246	0.899	...	43.74	44.85	12.77	10.19	76.31	-21.09	-22.06	8
2237	0.944	$22.44^{+22.32}_{-22.58}$	44.09	45.25	14.30	11.05	141.12	-21.40	-22.93	2
2220	0.995	...	43.82	45.51	49.15	11.52	34.59	-23.41	-24.74	1

Table B.1: Properties of the Type-2 AGN sample. – *continued.*

XID	Redshift	Log $\langle N_{\rm H} \rangle$ [cm^{-2}]	Log $L_{[2-10]\rm keV}$ [erg s^{-1}]	Log $L_{\rm bol}$ [erg s^{-1}]	$k_{\rm bol}$	Log M_* [M$_\odot$]	SFR [$M_\odot$/yrs]	$M_{\rm U}$	$M_{\rm V}$	Morphological class[a]
2218	0.248	...	42.35	43.68	21.25	10.76	1.34	-19.80	-21.42	1
2213	0.957	...	43.67	44.91	17.40	10.17	43.75	-20.87	-21.89	8
2210	0.968	$22.82^{+22.61}_{-23.02}$	43.86	45.10	17.36	11.02	10.83	-20.94	-22.66	1
2195	0.425	$21.20^{+21.08}_{-21.32}$	43.13	44.66	33.76	10.41	81.44	-20.32	-21.72	2
2439	0.736	$21.78^{+21.45}_{-21.92}$	43.32	44.87	35.25	10.74	5.72	-20.55	-22.17	7
2429	0.870	$22.43^{+22.07}_{-22.69}$	43.54	44.38	6.89	10.36	0.28	-18.63	-20.54	7
2425	1.173	...	43.91	45.63	52.29	10.85	88.29	-21.80	-23.03	2
2422	0.832	...	43.50	44.66	14.33	10.14	68.08	-20.96	-21.94	23
2416	0.518	...	43.00	44.27	18.62	10.68	15.88	-20.40	-21.84	...
2413	0.839	...	43.70	45.00	19.61	10.76	0.42	-19.85	-21.88	2
2408	1.270	$22.98^{+22.73}_{-23.23}$	43.86	45.83	92.48	11.02	521.81	-21.96	-23.34	6
2407	0.928	$21.61^{+21.40}_{-21.76}$	43.90	45.15	17.89	10.14	186.17	-21.80	-22.56	8
2387	0.899	$21.96^{+21.56}_{-22.34}$	43.64	44.86	16.34	11.09	12.83	-21.42	-23.05	9
2370	0.639	$22.34^{+22.06}_{-22.63}$	43.32	44.30	9.52	10.50	0.23	-18.90	-21.03	1
2570	0.368	$23.18^{+22.96}_{-23.40}$	43.13	44.39	17.87	11.04	1.38	-20.35	-22.25	1
2547	0.763	22.39^{G}_{G}	43.17	43.96	6.17	10.42	0.19	-19.58	-21.42	1
2544	0.826	$23.28^{+22.98}_{-23.61}$	44.10	44.88	5.97	11.32	2.61	-21.34	-23.15	...
2538	0.623	...	42.99	58.35	...	10.78	6.27	-20.65	-22.27	3
2529	0.373	$22.43^{+22.27}_{-22.62}$	42.67	43.78	12.83	10.63	0.53	-19.61	-21.42	2
2519	0.972	...	43.79	45.13	21.91	11.04	11.47	-21.30	-22.93	...
2501	0.447	...	42.80	43.76	9.17	9.79	1.63	-18.73	-20.09	7
2473	0.865	...	43.92	45.56	43.97	10.90	128.33	-21.53	-22.90	5
2448	0.530	...	42.74	44.04	19.63	10.14	1.43	-19.04	-20.67	2
2440	1.175	$22.26^{+22.01}_{-22.52}$	43.70	44.67	9.39	11.15	1.02	-21.42	-23.25	2
5014	0.213	$23.37^{+23.21}_{-23.53}$	43.18	44.21	10.59	10.76	0.72	-19.95	-21.75	1
5006	2.417	$24.08^{+23.81}_{-24.39}$	44.61	46.80	154.41	11.30	545.22	-22.43	-23.86	8
2860	0.671	...	43.09	44.43	21.86	9.51	8.92	-19.17	-20.21	8
2855	0.554	...	42.75	44.52	58.92	11.07	9.53	-21.68	-22.99	2
2668	0.886	$23.22^{G}_{-23.63}$	44.07	45.38	20.74	10.77	0.43	-19.58	-21.71	...
2655	0.674	...	43.23	44.66	27.11	11.30	2.48	-19.78	-22.08	10
2651	0.978	$21.36^{+21.00}_{-21.59}$	43.73	45.23	31.89	10.95	111.87	-22.36	-23.49	2
2639	0.956	...	43.77	44.61	6.85	10.62	0.52	-19.60	-21.41	2
2608	0.125	24.18^{G}_{G}	43.07	82.39	...	10.64	0.00	-19.87	-21.81	2
2579	0.267	...	42.13	57.48	...	10.69	0.00	-19.13	-21.22	1
5093	0.556	...	43.12	44.58	29.34	10.77	0.74	-19.37	-21.38	2
5081	0.766	...	44.17	45.64	29.22	10.39	337.72	-23.34	-23.80	...
5077	0.326	$21.34^{+20.78}_{-21.66}$	42.38	57.68	...	10.46	2.33	-19.54	-21.06	1
5075	0.221	$21.76^{+21.36}_{-22.06}$	42.15	43.36	16.03	10.96	0.00	-19.86	-21.94	1
5068	0.409	$22.63^{+22.38}_{-22.91}$	42.69	43.47	5.97	9.71	2.59	-18.32	-19.63	3
5064	0.679	$22.77^{+22.09}_{-23.84}$	43.23	44.21	9.55	10.59	0.49	-19.52	-21.33	1
5047	0.252	$22.80^{+22.41}_{-23.38}$	42.73	43.82	12.28	10.81	0.05	-19.63	-21.67	...
5041	0.527	23.09^{G}_{G}	43.47	44.74	18.33	10.67	0.58	-18.80	-20.90	3
5036	0.704	$22.86^{+22.56}_{-23.12}$	43.49	44.69	16.03	10.89	0.97	-19.66	-21.67	1
5034	0.508	$23.15^{G}_{-28.00}$	43.06	44.11	11.36	10.37	2.44	-19.32	-21.04	1
5139	0.749	...	43.32	44.73	25.78	10.85	7.45	-21.44	-22.87	3
5132	0.317	$21.26^{+20.95}_{-21.49}$	42.47	43.83	23.00	10.36	1.33	-18.84	-20.36	4
5128	0.775	$22.40^{G}_{-28.00}$	43.27	44.11	7.00	11.04	1.36	-20.34	-22.24	2
5126	1.006	$22.18^{+21.91}_{-22.38}$	43.63	45.43	63.49	10.48	148.29	-21.20	-22.38	8
5119	0.387	...	42.70	43.85	14.19	10.58	5.31	-19.41	-21.08	23
5118	0.349	...	42.37	43.24	7.42	11.42	0.19	-21.15	-23.19	12
5112	0.260	...	43.22	44.57	22.35	11.06	14.76	-21.56	-22.74	23
5104	0.702	...	43.11	44.38	18.47	10.88	0.55	-21.05	-22.79	1
5101	0.424	$22.97^{+22.70}_{-23.32}$	43.06	44.10	10.91	10.91	1.00	-19.40	-21.51	2
5094	0.738	$21.88^{+21.57}_{-22.19}$	43.30	44.49	15.46	11.13	0.00	-21.40	-23.25	1
5235	0.800	$21.71^{+21.59}_{-21.79}$	44.07	45.32	17.47	11.13	0.99	-21.08	-23.01	1
5227	0.677	$21.96^{+20.90}_{-22.32}$	43.33	44.83	31.09	10.79	6.46	-20.37	-22.10	1
5225	0.958	$21.61^{+21.20}_{-21.95}$	43.35	44.52	14.80	10.75	14.88	-20.53	-22.08	2

Table B.1: Properties of the Type-2 AGN sample. – *continued.*

XID	Redshift	Log $\langle N_{\rm H}\rangle$ [cm^{-2}]	Log $L_{[2-10]\rm keV}$ [erg s^{-1}]	Log $L_{\rm bol}$ [erg s^{-1}]	$k_{\rm bol}$	Log M_* [M$_\odot$]	SFR [$M_\odot$/yrs]	$M_{\rm U}$	$M_{\rm V}$	Morphological class[a]
5224	0.911	$22.67^{+22.19}_{-22.97}$	43.62	44.92	19.86	10.79	6.48	-20.08	-21.90	2
5196	0.817	$21.26^{+20.78}_{-21.51}$	43.30	44.53	16.76	11.00	10.37	-21.49	-23.02	0
5193	0.980	$21.45^{+21.11}_{-21.67}$	43.66	44.71	11.14	9.85	99.77	-20.50	-21.46	1
5190	0.667	$21.46^{+21.11}_{-21.69}$	43.22	44.24	10.51	10.95	0.64	-20.31	-22.34	0
5182	0.668	...	42.86	43.62	5.72	10.33	2.25	-19.53	-21.16	0
5162	3.524	$22.48^{G}_{-22.86}$	44.82	45.96	13.75	10.61	567.01	-23.30	-23.95	8
5153	0.787	$22.89^{+22.68}_{-23.06}$	43.94	46.04	124.41	10.68	671.81	-20.16	-21.91	9
5343	0.652	$21.90^{+21.73}_{-22.05}$	43.34	44.62	19.05	9.44	38.81	-17.36	-19.01	3
5336	0.390	$22.04^{+21.75}_{-22.26}$	42.52	43.75	16.93	8.79	8.58	-18.45	-19.20	23
5319	0.811	$22.41^{+22.03}_{-22.71}$	43.64	44.67	10.72	10.97	0.69	-20.98	-22.82	3
5318	0.394	$22.84^{G}_{-23.65}$	42.57	43.87	19.83	10.82	0.81	-19.47	-21.48	3
5308	1.285	...	44.40	45.70	20.19	11.14	67.00	-21.34	-22.90	2
5307	0.675	...	43.65	44.61	9.08	10.75	5.89	-20.58	-22.20	2
5288	1.000	$22.22^{+21.93}_{-22.43}$	43.78	45.61	67.71	11.21	17.09	-20.53	-22.55	1
5285	2.590	...	44.46	45.55	12.31	10.54	109.39	-21.85	-22.85	9
5272	0.850	...	43.82	44.95	13.39	10.21	219.41	-21.98	-22.74	1
5255	1.057	...	43.58	44.78	15.74	10.20	78.25	-20.21	-21.48	3
5435	0.079	...	41.55	42.84	19.68	10.00	0.07	-18.84	-20.58	...
5432	0.820	...	43.24	44.72	29.82	11.05	11.72	-21.32	-22.95	2
5427	1.177	$23.58^{+23.38}_{-23.84}$	44.22	45.38	14.50	11.16	15.18	-21.30	-23.03	5
5412	1.190	...	43.68	59.05	...	11.09	336.41	-21.61	-23.13	5
5411	0.676	...	43.16	44.18	10.44	11.13	0.00	-21.10	-23.04	1
5401	0.558	$22.20^{G}_{-22.66}$	43.30	44.88	37.73	11.03	11.29	-20.68	-22.51	...
5388	0.705	...	43.20	44.40	15.86	10.78	28.87	-21.26	-22.48	2
5385	0.868	...	43.36	44.47	12.96	10.21	44.53	-19.71	-21.14	2
5372	0.734	...	42.94	44.27	21.11	10.56	3.81	-19.50	-21.33	1
5370	0.582	$21.11^{+20.70}_{-21.36}$	43.68	44.72	10.84	10.54	19.13	-20.78	-21.96	...
5502	0.530	$21.73^{+21.28}_{-22.18}$	42.93	44.06	13.62	10.68	0.60	-19.74	-21.55	2
5500	0.364	...	44.45	45.14	4.87	10.85	5.66	-20.51	-22.02	...
5493	0.623	...	43.31	44.35	10.91	10.37	6.13	-19.87	-21.32	0
5490	0.983	...	43.69	44.64	8.75	10.03	17.88	-19.68	-20.94	2
5484	0.608	$22.00^{+21.88}_{-22.12}$	43.48	44.46	9.54	11.10	0.00	-20.72	-22.76	2
5481	0.812	...	43.57	44.49	8.43	10.78	0.44	-19.89	-21.92	...
5474	0.639	...	43.07	44.06	9.85	10.70	0.37	-20.60	-22.34	3
5447	0.271	...	42.30	43.60	19.82	10.02	1.13	-18.81	-20.04	1
5443	0.284	$23.07^{+22.90}_{-23.24}$	43.15	43.85	4.98	10.55	0.44	-18.81	-20.81	2
5440	0.678	...	43.01	58.44	...	11.12	13.86	-21.20	-22.93	2
10498	1.189	...	43.57	44.85	19.23	11.26	18.98	-21.55	-23.27	2
10239	0.838	$21.79^{+21.40}_{-22.08}$	43.50	44.51	10.35	10.66	0.33	-19.89	-21.82	2
5626	0.489	...	43.59	44.97	24.22	11.04	1.36	-20.33	-22.24	...
5623	1.130	$21.41^{+21.08}_{-21.61}$	43.79	44.97	15.37	9.78	81.39	-20.29	-21.25	8
5587	0.882	...	43.45	44.55	12.39	9.55	47.60	-20.93	-21.49	8
5572	0.581	...	42.97	44.30	21.44	9.86	100.43	-20.51	-21.46	1
5567	0.772	$21.38^{+20.30}_{-21.84}$	43.10	58.58	...	10.49	84.04	-20.70	-22.03	5
5542	0.103	$21.59^{+21.45}_{-21.76}$	41.82	42.65	6.75	8.48	0.03	-15.82	-17.15	...
5537	0.315	$21.72^{+21.58}_{-21.85}$	42.49	43.54	11.27	10.24	0.22	-18.35	-20.25	1
5525	2.079	...	44.45	46.03	38.26	10.80	877.10	-23.17	-24.02	5
54514	0.707	23.64^{G}_{G}	43.87	45.52	45.31	11.11	1.62	-20.82	-22.63	1
54510	0.884	...	43.61	44.87	18.30	11.09	1.54	-20.47	-22.38	1
54502	0.248	...	42.06	57.40	...	10.87	0.92	-20.21	-22.02	2
54490	0.908	...	43.56	44.75	15.35	11.11	13.58	-21.48	-23.11	2
54461	0.979	...	43.92	44.97	11.16	11.06	0.84	-20.60	-22.63	...
54377	0.358	$21.92^{+21.58}_{-22.20}$	42.66	43.80	13.74	9.18	20.95	-17.00	-18.55	...

Table B.1: Properties of the Type-2 AGN sample. – *continued.*

XID	Redshift	Log $\langle N_{\rm H}\rangle$ [cm^{-2}]	Log $L_{[2-10]\rm keV}$ [erg s^{-1}]	Log $L_{\rm bol}$ [erg s^{-1}]	$k_{\rm bol}$	Log M_* [M$_\odot$]	SFR [$M_\odot$/yrs]	$M_{\rm U}$	$M_{\rm V}$	Morphological class[a]
54055	1.028	...	43.68	45.31	42.14	11.22	17.48	-20.55	-22.58	2
53922	0.850	...	43.37	45.52	139.79	9.47	41.01	-20.45	-21.10	8
30676	0.850	...	43.39	44.65	18.34	10.39	2.56	-19.67	-21.30	7
10674	0.496	...	42.94	44.48	34.89	11.17	1.85	-20.36	-22.37	2
60142	0.972	...	43.41	44.31	7.90	11.11	0.94	-21.32	-23.16	2
60109	0.729	...	43.06	44.15	12.40	10.77	0.42	-20.16	-22.09	2
60047	1.023	...	43.44	44.73	19.60	9.66	63.17	-19.40	-20.55	5
60026	1.809	...	44.02	45.58	35.85	10.62	118.59	-21.06	-22.38	7
60024	1.147	...	43.62	44.78	14.49	11.04	1.38	-20.35	-22.25	1
54545	0.518	...	43.12	44.40	19.23	10.85	0.89	-19.57	-21.58	...
54535	0.370	...	42.51	57.81	...	10.87	0.93	-19.62	-21.63	2
54534	0.959	...	43.51	44.94	27.11	11.08	12.61	-21.71	-23.23	5
54520	0.889	...	43.40	44.21	6.52	9.80	20.06	-20.01	-21.01	5
54517	0.124	...	41.62	56.74	...	10.38	0.00	-19.52	-21.36	1
60305	0.346	...	42.38	43.79	25.72	10.90	0.99	-20.29	-22.10	3
60274	1.097	...	43.48	45.92	277.26	11.09	154.26	-21.20	-22.83	9
60211	0.511	...	42.78	43.92	13.70	10.36	0.17	-19.75	-21.49	0
60205	0.969	...	43.56	45.51	89.71	11.12	13.85	-20.60	-22.52	23
60193	0.589	...	43.04	44.01	9.36	10.72	0.38	-20.35	-22.19	1
60188	1.442	...	43.83	59.26	...	11.09	12.92	-21.43	-23.06	2
60185	0.529	...	42.72	44.44	52.58	10.36	0.28	-18.63	-20.54	2
60183	0.285	...	42.44	44.31	74.54	10.80	0.78	-20.04	-21.84	...
60161	0.417	...	42.46	43.41	8.83	10.28	0.14	-17.45	-19.87	2
60152	0.579	...	42.95	44.84	77.39	10.81	31.66	-20.83	-22.29	10
140	0.045	$21.57^{+21.36}_{-21.74}$	41.06	42.37	20.37	9.66	0.48	-18.76	-20.09	1
60494	0.661	...	43.01	44.64	42.75	10.78	6.25	-20.94	-22.47	2
60486	0.661	...	43.08	43.88	6.37	10.65	0.33	-19.88	-21.81	0
60454	1.169	...	43.48	44.63	14.10	10.79	6.49	-20.68	-22.31	7
60430	0.123	...	41.28	56.73	...	9.94	0.90	-19.44	-20.77	3
60426	0.833	...	43.36	44.41	11.08	10.88	0.94	-19.93	-21.84	2
60403	1.000	...	43.39	45.07	48.61	10.91	111.25	-21.41	-22.82	2
60364	0.602	...	42.82	43.78	9.17	10.35	0.16	-19.72	-21.46	0
60354	0.880	...	43.18	44.62	27.17	10.92	8.74	-21.01	-22.63	3
60353	1.317	...	43.70	45.55	70.57	10.71	30.24	-20.42	-21.93	6
70133	0.894	...	43.74	44.69	8.77	10.91	8.57	-20.68	-22.41	5
70096	0.842	...	43.27	44.34	11.82	10.19	76.11	-20.78	-21.86	5
70095	0.346	...	42.36	43.39	10.85	11.00	0.00	-21.08	-22.92	2
70077	0.406	...	42.92	43.77	6.95	10.92	1.03	-20.34	-22.14	0
70015	1.218	...	43.59	59.08	...	11.37	1.70	-21.97	-23.80	2
60082	0.780	...	43.19	44.24	11.30	11.21	1.18	-21.87	-23.61	2
54451	0.967	...	43.69	45.08	24.82	11.05	11.66	-22.22	-23.55	23
5073	0.926	$21.66^{+21.52}_{-21.78}$	43.69	44.51	6.63	10.96	9.42	-21.99	-23.32	1
2622	1.080	$22.00^{+21.65}_{-22.30}$	43.56	44.78	16.58	11.23	17.80	-22.38	-23.81	3
2239	0.579	$22.40^{+22.16}_{-22.62}$	43.55	44.78	17.14	11.08	31.49	-22.86	-23.92	10
70136	0.728	$22.70^{+22.55}_{-22.84}$	43.73	44.67	8.68	11.00	1.24	-20.53	-22.34	2
70137	0.704	...	43.25	44.91	45.02	9.72	73.37	-21.38	-21.94	8
70139	0.427	...	42.81	44.36	35.25	10.57	0.27	-19.66	-21.59	1
70154	0.702	...	43.02	44.30	19.31	10.62	0.30	-19.80	-21.73	10
70177	0.958	...	43.34	44.40	11.57	11.46	0.21	-20.94	-23.08	5
70212	0.629	...	42.84	44.05	16.19	10.80	0.79	-20.05	-21.85	11
70220	0.373	...	42.34	43.73	24.54	10.83	0.83	-20.10	-21.91	1

[a] The morphological classification of the Type-2 AGN hosts is coded from 0 to 23: 0 = elliptical, 1 = S0; 2 = bulge-dominated; 3 = intermediate-bulge; 4 = disk-dominated; 5 = irregular; 6 = compact/irregular; 7 = compact; 8 = unresolved/compact; 9 = blended; 10 = bulge-dominated/close-companion; 11 = intermediate-bulge/close-companion; 12 = S0/close-companion; 23 = possible mergers. G= Galactic column density, 2.5×10^{20} cm^{-2}.

Appendix C

Interpolating functions for stellar evolution

C.1 Stellar mass losses

The general expression for the stellar mass-return rate from an evolving stellar population is

$$\dot{M}_*^{\rm w}(t) = \int_0^t \dot{M}_*^+(t')W_*(t-t')\mathrm{d}t', \tag{C.1}$$

where $\dot{M}_*^+$ is the instantaneous star-formation rate and $W_*(t-t')$ is the normalized stellar death rate for a stellar population of age $t-t'$. For an initial mass function (IMF) of unitary total mass and age t,

$$W_*(t) = \mathrm{IMF}[M_{\rm TO}(t)]|\dot{M}_{\rm TO}(t)|\Delta M^{\rm w}[M_{\rm TO}(t)], \tag{C.2}$$

where $M_{\rm TO}(t)$ is the mass of stars entering the turn-off at time t, and $\Delta M^{\rm w}$ their mass loss. Following Ciotti & Ostriker (2007), we assume that

$$\Delta M^{\rm w} = \begin{cases} 0.923M - 0.48, & 0.08 \leqslant M \leqslant 8.5 \\ M - 1.4, & 8.5 < M \leqslant 40 \\ M/2, & M > 40. \end{cases} \tag{C.3}$$

In our models, we adopt a Kroupa (2001) IMF, with a minimum mass of 0.08 $M_\odot$ and a maximum mass of 100 $M_\odot$, while $\dot{M}_{\rm TO}(t)$ is taken from Maraston (2005)

$$\begin{aligned} \log M_{\rm TO}(t) \cong 2.982 + 0.213\log t - 0.108(\log t)^2 + \\ 0.006(\log t)^3. \end{aligned} \tag{C.4}$$

In the formula above, t is in yrs and $M_{\rm TO}$ in solar masses. The main computational problem posed by the evaluation of the integral in Eq. (C.1) is that, in principle, the entire history of $\dot{M}_*^+(t')$ must be stored, which requires a prohibitively large amount of memory and computational time. In the special case of an exponential time dependence of W_*, this problem can be fortunately avoided, as shown in Ciotti & Ostriker (2001, 2007). In the present case, W_* is not an exponential function,

Table C.1: Multi-exponential expansion parameters (in Gyrs) for stellar mass losses and SNIa rate. Note that for SNIa the coefficients a_i are dimensionless.

Stellar mass return				SNIa			
a_0	16.38	b_0	1.93	a_0	0.18	b_0	7.43
a_1	1.93	b_1	0.19	a_1	3.22×10^{-2}	b_1	1.00
a_2	0.38	b_2	0.03	a_2	7.15×10^{-3}	b_2	0.22
a_3	–	b_3	–	a_3	1.84×10^{-3}	b_3	5.79×10^{-2}
a_4	–	b_4	–	a_4	5.22×10^{-4}	b_4	1.72×10^{-2}
a_5	–	b_5	–	a_5	1.34×10^{-4}	b_5	5.28×10^{-3}

being more similar to a power law. However, we assume that a fit in terms of exponentials has been obtained, i.e.

$$W_*(t) = \sum_i \frac{e^{-\frac{t}{b_i}}}{a_i}, \tag{C.5}$$

where the timescales a_i and b_i are known. From the above equation and Eq. (C.1), it follows that

$$\dot{M}_*^{\rm w}(t) = \sum_i \frac{F_i(t)}{a_i} \tag{C.6}$$

where

$$F_i(t) \equiv \int_0^t \dot{M}_*^+(t') e^{-\frac{t-t'}{b_i}} \mathrm{d}t'. \tag{C.7}$$

We divide the integral into

$$F_i(t) = \int_{t-\delta t}^t \dot{M}_*^+(t') e^{-\frac{t-t'}{b_i}} \mathrm{d}t' + \int_0^{t-\delta t} \dot{M}_*^+(t') e^{-\frac{t-t'}{b_i}} \mathrm{d}t', \tag{C.8}$$

where δt represents the last time-step. The evaluation of the first integral can be done by using a simple trapezoidal rule and only the values of $\dot{M}_*^+$ at t and $t-\delta t$ are required. The second integral is transformed by adding and subtracting δt in the exponential term, and simple algebra finally shows that

$$F_i(t) = \frac{\delta t}{2}\left[\dot{M}_*^+(t) + e^{-\frac{\delta t}{b_i}} \dot{M}_*^+(t-\delta t)\right] + e^{-\frac{\delta t}{b_i}} F_i(t-\delta t). \tag{C.9}$$

Therefore, the introduction of the multi-exponential fit allow us to compute the instantaneous mass return rate at time t just by storing the values of the F_i functions at the previous time-step. We performed a non-linear fit of the tabulated values of Eq. (C.2) (obtained with the exact formulae). We found that an acceptable approximation over the entire Hubble time is obtained with the coefficients in the first row of Table C.1 (with a percentage error of at most of 10% and only at very late times, when the mass return rate of a stellar population is negligible).

C.2 SN Ia

In a given simple stellar population, the total (i.e. volume-integrated) energy release by SNIa is

$$L_{\rm SN}(t) = E_{\rm SN} R_{\rm SN}(t), \tag{C.10}$$

where $E_{\rm SN} = 10^{51}$ erg is the fiducial energy released by SNIa event and $R_{\rm SN}$ is the SNIa rate. From Eqs. (11)-(12) in Ciotti & Ostriker (2007), the SNIa rate for a stellar population of mass M_* can be written as

$$R_{\rm SN}(t) = \frac{1.6\times10^{-13}}{\Upsilon_{\rm B\odot}} \frac{M_*}{M_\odot} \left(\frac{t}{t_{\rm H}}\right)^{-s} \qquad [\rm yrs^{-1}], \tag{C.11}$$

where we adopt a stellar mass-to-light ratio $\Upsilon_{\rm B\odot} = 5$, $\theta_{\rm SN} = 1$, $h = 0.7$, $t_{\rm H} = 13.7$ Gyrs, and $s = 1.1$. In our model with a star formation rate of $\dot{M}_*$, it follows that in each time-step an amount $\dot{M}_*\delta t$ of stars is added to the galaxy body. Therefore, the instantaneous total rate of SNIa explosion at time t is

$$R^{\rm T}_{\rm SN}(t) = \frac{1.6\times10^{-13}}{\Upsilon_{\rm B\odot} M_\odot} \int_0^t \dot{M}_*(t') \left(\frac{t-t'}{t_{\rm H}}\right)^{-1.1} {\rm d}t'. \tag{C.12}$$

We expanded the dimensionless power-law kernel in the integral above again using a (dimensionless) multi-exponential function, so that all the considerations in Sect. C.1 hold and in particular Eq. (C.9). The functions F_i now contain new values of b_i (in units of $\rm Gyrs^{-1}$). The parameters of the multi-exponential fit (with percentual errors $< 3\%$ over 13.7 Gyrs) are listed in the second row of Table C.1. Therefore,

$$L_{\rm SN}(t) = \frac{1.6\times10^{38}}{\Upsilon_{\rm B\odot} M_\odot} \sum_i \frac{F_i}{a_i} \qquad {\rm erg\ s^{-1}} \tag{C.13}$$

and finally, the average SNIa heating per unit time and unit volume, needed in the gas energy equation is

$$\dot{E}_{\rm H,SNIa} = \frac{3L_{\rm SN}(t)}{8\pi r_{\rm g}^3}, \tag{C.14}$$

where again we use half-mass values.

C.3 Column density for the Jaffe model

In our model the gas density at each computation time is assumed to be proportional to $\rho_{\rm h}$ and given by Eq. (5.19). In general, we consider a spheroid having a radius r and a gas density distribution $\rho_{\rm g}(r)$. Using cartesian coordinates we can write the radius r as $r^2 = x^2 + y^2 + z^2$. We

evaluate the surface density along an axis, for istance z, as

$$\Sigma(z) = \int_{-\infty}^{+\infty} \rho_{\rm g}(r)\mathrm{d}z \tag{C.15}$$

the sphere is symmetric along z so

$$\int_{-\infty}^{+\infty} \rho_{\rm g}(r)\mathrm{d}z = 2\int_{0}^{+\infty} \rho_{\rm g}(r)\mathrm{d}z.$$

Consider a circle having a radius R laid in the plain (x, y), so $R = \sqrt{x^2 + y^2}$ and conseguently $z = \sqrt{r^2 - R^2}$, the differential is $\mathrm{d}z = r\mathrm{d}r/\sqrt{r^2 - R^2}$ and for $z = 0 \Rightarrow r = R$. The corresponding projected gas distribution is

$$\Sigma_{\rm g}(R) \equiv 2\int_{R}^{\infty} \frac{\rho_{\rm g}(r) r \mathrm{d}r}{\sqrt{r^2 - R^2}}. \tag{C.16}$$

We note that the projected density formally diverges for $R \to 0$, so that, to estimate a realistic value of the column density we need to compute a mean value of the projected density within a fiducial aperture. The explicit formulae for $\Sigma_{\rm g}(R)$, and the associated projected mass encircled with R, $M_{\rm Pg}(R)$, are given in Jaffe (1983). In particular, to estimate $\langle N_{\rm H}\rangle$ in Eq. (5.22) we consider $M_{\rm Pg}(R)$

$$\begin{aligned} M_{\rm Pg}(R) &= 2\pi \int_{0}^{R} R' \, \Sigma_{\rm g}(R')\mathrm{d}R' = \\ &= M_{\rm g} - 4\pi \int_{R}^{\infty} r\rho_{\rm g}(r)\sqrt{r^2 - R^2}\mathrm{d}r. \end{aligned} \tag{C.17}$$

Integration of equation (C.17) yields

$$\frac{M_{\rm Pg}(R)}{M_{\rm g}} = \tilde{R}\begin{cases} \dfrac{\pi}{2} - \dfrac{\tilde{R}\,\mathrm{arcsech}\tilde{R}}{\sqrt{1-\tilde{R}^2}}, & 0 < \tilde{R} < 1; \\ \\ \dfrac{\pi}{2} - \dfrac{\tilde{R}\,\mathrm{arcsec}\tilde{R}}{\sqrt{\tilde{R}^2-1}}, & \tilde{R} > 1; \end{cases} \tag{C.18}$$

where $\tilde{R} \equiv R/r_{\rm g}$ and $M_{\rm Pg}(r_{\rm g}) = (\pi/2 - 1)M_{\rm g}$.

Appendix D

Self-regulated Bondi accretion: detailed treatment

In the Bondi (1952) treatment of stationary, spherically simmetric accretion of ionized gas onto SMBH (or more in general onto a central gravitating body of mass M), where magnetic field and self-gravity of the gas are negleted, the flow is suppose to be optically thin, so that the resulting solution is purely hydrodynamical, and radiative feedback effects are not considered. However, it is well known that the effects of the radiation pressure due to Thomson electron scattering may become important on the accreting gas. In this scenario the accreting flow have an upper limit rate: the accretion rate $\dot{M}_{\rm Edd}$

$$\dot{M}_{\rm Edd} \equiv \frac{L_{\rm Edd}}{\epsilon c^2}, \tag{D.1}$$

where ϵ is the efficiency of accretion in the range of value $0.001 \leqslant \epsilon \leqslant 0.1$ and $L_{\rm Edd}$ is the Eddington luminosity

$$L_{\rm Edd} = \frac{4\pi c G M_{\rm BH} \mu m_{\rm p}}{\sigma_{\rm T}}, \tag{D.2}$$

$\mu m_{\rm p}$ is the mass per electron and $\sigma_{\rm T}$ the Thomson cross-section. Here, we show how to generalize Bondi accretion to the case of radiation pressure (for a full treatment see Lusso & Ciotti 2011). The basic equations for such accretion flow are two: the continuity equation and the equation of motion. The continuity equation is

$$\frac{\partial \rho}{\partial t} + \nabla \cdot (\rho \mathbf{v}) = 0, \tag{D.3}$$

where ρ is the gas density and $\mathbf{v}$ is the infall gas velocity. For a steady ($\partial\rho/\partial t = 0$) and spherically simmetric flow ($v_\phi = v_\theta = 0, \rho = \rho(r)$, only the radial component is considered) we have

$$\frac{1}{r^2}\frac{\rm d}{{\rm d}r}(r^2 \rho v_r) = 0. \tag{D.4}$$

Integrating the previous equation we get

$$\dot{M} = 4\pi r^2 \rho v_r, \tag{D.5}$$

where the constant is the mass accretion rate $\dot{M}$ crossing each spherical shell.

The Euler equation is

$$\rho\frac{\partial \mathbf{v}}{\partial t} + \rho\mathbf{v}\cdot\nabla\mathbf{v} = -\nabla P + \mathbf{f}_{\rm ext} \tag{D.6}$$

where $\rho\mathbf{v}\cdot\nabla\mathbf{v}$ is the momentum, P is the pressure, and $\mathbf{f}_{\rm ext}$

$$\mathbf{f}_{\rm ext} = \mathbf{F}_{\rm g} + \mathbf{F}_{\rm rad}, \tag{D.7}$$

represents the external force on the fluid and is the sum of the gravitational force, $\mathbf{F}_{\rm g}$, while $\mathbf{F}_{\rm rad}$ takes into account the effects of the radiation pressure. In absence of vorticity (guaranteed by the Kelvin theory) the advective term can be written as

$$\mathbf{v}\cdot\nabla\mathbf{v} = \frac{\nabla v_r^2}{2}. \tag{D.8}$$

When integrating Eq. (D.6) along the radial streamline, the integral

$$\omega \equiv \int_r^\infty \frac{{\rm d}P}{\rho}, \tag{D.9}$$

can be shown to be the gas specific *enthalpy*. Using a politropic equation with index γ

$$\frac{P}{P_\infty} = \left(\frac{\rho}{\rho_\infty}\right)^\gamma, \tag{D.10}$$

where ρ_∞ and P_∞ is the density and the pressure at the infinity, Eq. (D.9) can be written in term of the sound speed

$$c_{\rm s}^2(r) \equiv \left(\frac{\partial P}{\partial \rho}\right)_S = c_{\rm s,\infty}^2\left(\frac{\rho}{\rho_\infty}\right)^{\gamma-1}, \tag{D.11}$$

so that

$$\omega = \frac{c_{\rm s,\infty}^2}{(\gamma-1)}\left[1-\left(\frac{\rho}{\rho_\infty}\right)^{\gamma-1}\right], \tag{D.12}$$

where $c_{\rm s,\infty}$ is the sound speed at the infinity. The sum of the (radial) gravitational force and the radiation pressure can be written as

$$F_{\rm g} + F_{\rm rad} = \frac{\rho GM}{r^2} - \frac{\rho GM}{r^2}\frac{L}{L_{\rm Edd}} = \frac{\rho GM}{r^2}\left(1-\frac{L}{L_{\rm Edd}}\right) \tag{D.13}$$

Therefore, in presence of electron scatteringin the optically thin regime, the gas experiences an *effective gravity* of reduced gravitational constant

$$G_{\rm eff} = G\left(1-\frac{\dot{M}}{\dot{M}_{\rm Edd}}\right). \tag{D.14}$$

Consequently, the *effective gravitational potential* produced by the central SMBH is

$$\Phi_{\rm eff} = -\frac{G_{\rm eff} M_{\rm BH}}{r}. \tag{D.15}$$

The Bernoulli equation (or conservation of energy) for a streamline reaching the infinity is then

$$\frac{v_r^2}{2} + \Phi_{\rm eff} + \omega = 0. \tag{D.16}$$

After normalization of v_r and ρ as follows

$$\tilde{\upsilon} = \frac{v_r}{c_{\rm s,\infty}} \quad , \quad \tilde{\rho} = \frac{\rho}{\rho_\infty}, \tag{D.17}$$

and putting Eq. (D.12) into Eq. (D.16), we have

$$\frac{\tilde{\upsilon}^2}{2} + \frac{1}{\gamma - 1}\left(\tilde{\rho}^{\gamma-1} - 1\right) = -\frac{\Phi_{\rm eff}}{c_{\rm s,\infty}^2}. \tag{D.18}$$

We can write the right-side hand of Eq. (D.18) as

$$-\frac{\Phi_{\rm eff}}{c_{\rm s,\infty}^2} = \frac{GM}{c_{\rm s,\infty}^2 r}\left(1 - \frac{\dot{M}}{\dot{M}_{\rm Edd}}\right) = \frac{1}{x}\left(1 - \frac{\dot{M}}{\dot{M}_{\rm Edd}}\right) \tag{D.19}$$

where $x = r/R_{\rm B}$ and $R_{\rm B} = GM/c_{\rm s,\infty}^2$ is the Bondi radius. From Eq. (D.5), using previous results, we have an equation very similar to the classical Bondi accretion rate given by

$$\dot{M} = \frac{4\pi\rho_\infty G^2 M^2}{c_{\rm s,\infty}^3} x^2 \tilde{\rho}\tilde{\upsilon} \tag{D.20}$$

where the normalized accretion rate is a function of the accretion rate: $\lambda = \lambda(\dot{M})$

$$\lambda_{\rm c} = x^2 \tilde{\rho}\tilde{\upsilon} = \frac{\dot{M} c_{\rm s,\infty}^3}{4\pi G^2 M^2 \rho_\infty}. \tag{D.21}$$

Introducing now the Mach number as $\mathcal{M} = \upsilon/c_{\rm s}$ and normalizing it using equations (D.17), we can write

$$\mathcal{M} = \frac{\tilde{\upsilon}}{\tilde{\rho}^{(\gamma-1)/2}}. \tag{D.22}$$

Rewriting Eq. (D.21) including $\mathcal{M}$ and taking off $\tilde{\upsilon}$ we have

$$\tilde{\upsilon} = \left(\frac{\lambda}{x^2}\right)^{(\gamma-1)/(\gamma+1)} \mathcal{M}^{2/(\gamma+1)}. \tag{D.23}$$

Using Eqs. (D.22) and (D.23), Eq. (D.18) became

$$\mathcal{M}^{\frac{4}{(\gamma+1)}}\left(\frac{1}{2}+\frac{1}{(\gamma-1)\mathcal{M}^2}\right)=$$

$$=\left(\frac{x^2}{\lambda}\right)^{\frac{2(\gamma-1)}{(\gamma+1)}}\left(\frac{1}{\gamma-1}+\frac{1}{x}\right)-\lambda^{-\frac{2(\gamma-1)}{(\gamma+1)}}x^{\frac{(3\gamma-5)}{(\gamma+1)}}\frac{\dot{M}}{\dot{M}_{\rm Edd}} \tag{D.24}$$

where in the right hand we have only x and λ terms and in the left hand we have $\mathcal{M}$ terms. Defining

$$\Lambda=\left(\frac{1}{\lambda}\right)^{2(\gamma-1)/(\gamma+1)} \tag{D.25}$$

we have

$$g(\mathcal{M})=\Lambda F(x) \tag{D.26}$$

with

$$F(x)\equiv f(x)-x^{(3\gamma-5)/(\gamma+1)}\frac{\dot{M}}{\dot{M}_{\rm Edd}}. \tag{D.27}$$

We can compute the minimum value of x as $dF(x)/dx=0$ so

$$x_{\rm min}=\frac{5-3\gamma}{4}\left(1-\frac{\dot{M}}{\dot{M}_{\rm Edd}}\right) \tag{D.28}$$

and putting it into Eq. (D.26)

$$\frac{\gamma+1}{2(\gamma-1)}=\Lambda_{\rm c,eff}F(x_{\rm min}) \tag{D.29}$$

from $\Lambda_{\rm c,eff}$ we can compute the effective normalized accretion rate

$$\lambda_{\rm c,eff}=\left(\frac{1}{2}\right)^{(\gamma+1)/2(\gamma-1)}\left(\frac{5-3\gamma}{4}\right)^{-(5-3\gamma)/2(\gamma-1)}\left(1-\frac{\dot{M}}{\dot{M}_{\rm Edd}}\right)^2=$$

$$=\lambda_{\rm c}\left(1-\frac{\dot{M}}{\dot{M}_{\rm Edd}}\right)^2 \tag{D.30}$$

where $\lambda_{\rm c}$ is the classical normalized accretion rate derived by Bondi (1952). We can define the effective Bondi accretion using Eq. (D.20)

$$\dot{M}=4\pi R_{\rm B}^2\rho_\infty c_{\rm s,\infty}\lambda_{\rm c}\left(1-\frac{\dot{M}}{\dot{M}_{\rm Edd}}\right)^2=\dot{M}_{\rm B}\left(1-\frac{\dot{M}}{\dot{M}_{\rm Edd}}\right)^2. \tag{D.31}$$

The second order equation above for $\dot{M}$ has two solutions. Rejecting the unphysical solution, and introducing $\dot{m}=\dot{M}/\dot{M}_{\rm Edd}$ and $\alpha=\dot{M}_{\rm Edd}/\dot{M}_{\rm B}$, we finally obtain

$$\dot{m}=\frac{1}{2}\left[2+\alpha-\sqrt{4\alpha+\alpha^2}\right]. \tag{D.32}$$

Bibliography

Adelman-McCarthy, J. K. & et al. 2005, VizieR Online Data Catalog, 2267, 0

Akritas, M. G. & Siebert, J. 1996, MNRAS, 278, 919

Alexander, D. M. 2009, in Astronomical Society of the Pacific Conference Series, Vol. 419, Astronomical Society of the Pacific Conference Series, ed. S. Jogee, I. Marinova, L. Hao, & G. A. Blanc, 381–+

Alexander, D. M., Bauer, F. E., Brandt, W. N., et al. 2003, AJ, 125, 383

Allen, C. W. 1976, Astrophysical Quantities, ed. Allen, C. W.

Anderson, S. F. & Margon, B. 1987, ApJ, 314, 111

Antonucci, R. 1993, ARA&A, 31, 473

Avni, Y. & Tananbaum, H. 1982, ApJ, 262, L17

Avni, Y. & Tananbaum, H. 1986, ApJ, 305, 83

Ballero, S. K., Matteucci, F., Ciotti, L., Calura, F., & Padovani, P. 2008, A&A, 478, 335

Bechtold, J., Siemiginowska, A., Shields, J., et al. 2003, ApJ, 588, 119

Bell, E. F., Wolf, C., Meisenheimer, K., et al. 2004, ApJ, 608, 752

Bianchi, S., Fonseca Bonilla, N., Guainazzi, M., Matt, G., & Ponti, G. 2009, ArXiv e-prints

Böhringer, H., Matsushita, K., Churazov, E., Ikebe, Y., & Chen, Y. 2002, A&A, 382, 804

Bolzonella, M., Miralles, J., & Pelló, R. 2000, A&A, 363, 476

Bondi, H. 1952, MNRAS, 112, 195

Bondi, M., Ciliegi, P., Schinnerer, E., et al. 2008, ApJ, 681, 1129

Borch, A., Meisenheimer, K., Bell, E. F., et al. 2006, A&A, 453, 869

Brandt, W. N., Laor, A., & Wills, B. J. 2000, ApJ, 528, 637

Bregman, J. N. & Parriott, J. R. 2009, ApJ, 699, 923

Brusa, M., Civano, F., & Comastri, A. 2009a, Submitted

Brusa, M., Civano, F., Comastri, A., et al. 2010, ApJ, 716, 348

Brusa, M., Comastri, A., Gilli, R., et al. 2009b, ApJ, 693, 8

Brusa, M., Comastri, A., Mignoli, M., et al. 2003, A&A, 409, 65

Brusa, M., Fiore, F., Santini, P., et al. 2009c, A&A, 507, 1277

Brusa, M., Zamorani, G., Comastri, A., et al. 2007, ApJS, 172, 353

Bruzual, G. & Charlot, S. 2003, MNRAS, 344, 1000

Bundy, K., Georgakakis, A., Nandra, K., et al. 2008, ApJ, 681, 931

Calzetti, D., Armus, L., Bohlin, R. C., et al. 2000, ApJ, 533, 682

Capak, P., Aussel, H., Ajiki, M., et al. 2008, VizieR Online Data Catalog, 2284, 0

Capak, P., Aussel, H., Ajiki, M., et al. 2007, ApJS, 172, 99

Cappelluti, N., Brusa, M., Hasinger, G., et al. 2009, A&A, 497, 635

Cappelluti, N., Hasinger, G., Brusa, M., et al. 2007, ApJS, 172, 341

Cappi, M., Matsuoka, M., Comastri, A., et al. 1997, ApJ, 478, 492

Cardamone, C. N., Urry, C. M., Schawinski, K., et al. 2010, ApJ, 721, L38

Carroll, B. W. & Ostlie, D. A. 1996, An Introduction to Modern Astrophysics, ed. Carroll, B. W. & Ostlie, D. A.

Chabrier, G. 2003, ApJ, 586, L133

Chanan, G. A. 1983, ApJ, 275, 45

Chary, R. & Elbaz, D. 2001, ApJ, 556, 562

Ciliegi, P., Zamorani, G., Hasinger, G., et al. 2003, A&A, 398, 901

Cimatti, A., Daddi, E., Mignoli, M., et al. 2002, A&A, 381, L68

Ciotti, L., D'Ercole, A., Pellegrini, S., & Renzini, A. 1991, ApJ, 376, 380

Ciotti, L. & Ostriker, J. P. 1997, ApJ, 487, L105+

Ciotti, L. & Ostriker, J. P. 2001, ApJ, 551, 131

Ciotti, L. & Ostriker, J. P. 2007, ApJ, 665, 1038

Ciotti, L., Ostriker, J. P., & Proga, D. 2009, ApJ, 699, 89

Ciotti, L., Ostriker, J. P., & Proga, D. 2010, ApJ, 717, 708

Cisternas, M., Jahnke, K., Inskip, K. J., et al. 2011, ApJ, 726, 57

Comastri, A. 2004, in Astrophysics and Space Science Library, Vol. 308, Supermassive Black Holes in the Distant Universe, ed. A. J. Barger, 245–+

Corbin, M. R. 2000, ApJ, 536, L73

Cowie, L. L. & Barger, A. J. 2008, ApJ, 686, 72

Dale, D. A. & Helou, G. 2002, ApJ, 576, 159

Dale, D. A., Helou, G., Contursi, A., Silbermann, N. A., & Kolhatkar, S. 2001, ApJ, 549, 215

Dickinson, M., Papovich, C., Ferguson, H. C., & Budavári, T. 2003, ApJ, 587, 25

Donley, J. L., Rieke, G. H., Alexander, D. M., Egami, E., & Pérez-González, P. G. 2010, ApJ, 719, 1393

Elvis, M., Civano, F., Vignali, C., et al. 2009, ApJS, 184, 158

Elvis, M., Wilkes, B. J., McDowell, J. C., et al. 1994, ApJS, 95, 1

Feigelson, E. D. & Nelson, P. I. 1985, ApJ, 293, 192

Ferrarese, L. & Merritt, D. 2000a, ApJ, 539, L9

Ferrarese, L. & Merritt, D. 2000b, ApJ, 539, L9

Finoguenov, A., Guzzo, L., Hasinger, G., et al. 2007, ApJS, 172, 182

Fontana, A., Santini, P., Grazian, A., et al. 2009, A&A, 501, 15

Fukue, J. 2001, PASJ, 53, 687

Fukugita, M., Ichikawa, T., Gunn, J. E., et al. 1996, AJ, 111, 1748

Gallagher, S. C., Brandt, W. N., Sambruna, R. M., Mathur, S., & Yamasaki, N. 1999, ApJ, 519, 549

Gandhi, P., Horst, H., Smette, A., et al. 2009, A&A, 502, 457

Gaskell, C., Goosmann, R., Antonucci, R., & Whysong, D. 2004, in Astronomical Society of the Pacific Conference Series, Vol. 311, AGN Physics with the Sloan Digital Sky Survey, ed. G. T. Richards & P. B. Hall, 61

Genzel, R., Burkert, A., Bouché, N., et al. 2008, ApJ, 687, 59

Gibson, R. R., Brandt, W. N., & Schneider, D. P. 2008, ApJ, 685, 773

Gilli, R., Comastri, A., & Hasinger, G. 2007, A&A, 463, 79

Granato, G. L. & Danese, L. 1994, MNRAS, 268, 235

Green, P. J., Aldcroft, T. L., Richards, G. T., et al. 2009, ApJ, 690, 644

Green, P. J., Schartel, N., Anderson, S. F., et al. 1995, ApJ, 450, 51

Haardt, F. & Maraschi, L. 1991, ApJ, 380, L51

Haardt, F. & Maraschi, L. 1993, ApJ, 413, 507

Haardt, F., Maraschi, L., & Ghisellini, G. 1994, ApJ, 432, L95

Haiman, Z., Ciotti, L., & Ostriker, J. P. 2004, ApJ, 606, 763

Hamann, F. & Ferland, G. 1999, ARA&A, 37, 487

Hasinger, G., Cappelluti, N., Brunner, H., et al. 2007, ApJS, 172, 29

Hatziminaoglou, E., Pérez-Fournon, I., Polletta, M., et al. 2005, AJ, 129, 1198

Heckman, T. M., Kauffmann, G., Brinchmann, J., et al. 2004, ApJ, 613, 109

Hewett, P. C. & Foltz, C. B. 2003, AJ, 125, 1784

Hopkins, P. F., Hernquist, L., Cox, T. J., et al. 2005, ApJ, 630, 705

Hopkins, P. F., Hernquist, L., Cox, T. J., et al. 2006, ApJS, 163, 1

Hopkins, P. F., Hernquist, L., Cox, T. J., & Kereš, D. 2008, ApJS, 175, 356

Hopkins, P. F., Richards, G. T., & Hernquist, L. 2007, ApJ, 654, 731

Hornschemeier, A. E., Brandt, W. N., Garmire, G. P., et al. 2001, ApJ, 554, 742

Horst, H., Gandhi, P., Smette, A., & Duschl, W. J. 2008, A&A, 479, 389

Horst, H., Smette, A., Gandhi, P., & Duschl, W. J. 2006, A&A, 457, L17

Isobe, T., Feigelson, E. D., Akritas, M. G., & Babu, G. J. 1990, ApJ, 364, 104

Isobe, T., Feigelson, E. D., & Nelson, P. I. 1986, ApJ, 306, 490

Jaffe, W. 1983, MNRAS, 202, 995

Jahnke, K., Bongiorno, A., Brusa, M., et al. 2009, ApJ, 706, L215

Jahnke, K., Sánchez, S. F., Wisotzki, L., et al. 2004, ApJ, 614, 568

Jogee, S., Barazza, F. D., Rix, H., et al. 2004, ApJ, 615, L105

Johansson, P. H., Naab, T., & Ostriker, J. P. 2009, ApJ, 697, L38

Just, D. W., Brandt, W. N., Shemmer, O., et al. 2007, ApJ, 665, 1004

Kauffmann, G. & Haehnelt, M. 2000, MNRAS, 311, 576

Kauffmann, G., Heckman, T. M., Tremonti, C., et al. 2003a, MNRAS, 346, 1055

Kauffmann, G., Heckman, T. M., Tremonti, C., et al. 2003b, MNRAS, 346, 1055

Kaviraj, S., Schawinski, K., Silk, J., & Shabala, S. S. 2010, ArXiv e-prints

Kellermann, K. I., Sramek, R., Schmidt, M., Shaffer, D. B., & Green, R. 1989, AJ, 98, 1195

Kelly, B. C., Bechtold, J., Trump, J. R., Vestergaard, M., & Siemiginowska, A. 2008, ApJS, 176, 355

Kelly, B. C., Vestergaard, M., Fan, X., et al. 2010, ApJ, 719, 1315

Koekemoer, A. M., Aussel, H., Calzetti, D., et al. 2007, ApJS, 172, 196

Kormendy, J. & Richstone, D. 1995, ARA&A, 33, 581

Koski, A. T. 1978, ApJ, 223, 56

Koss, M., Mushotzky, R., Veilleux, S., & Winter, L. 2010, in American Institute of Physics Conference Series, Vol. 1248, American Institute of Physics Conference Series, ed. A. Comastri, L. Angelini, & M. Cappi, 453–454

Kriss, G. A. & Canizares, C. R. 1985, ApJ, 297, 177

Krolik, J. H. 1999, Active galactic nuclei : from the central black hole to the galactic environment, ed. J. H. Krolik

Kroupa, P. 2001, MNRAS, 322, 231

La Franca, F., Franceschini, A., Cristiani, S., & Vio, R. 1995, A&A, 299, 19

Lanzoni, B., Ciotti, L., Cappi, A., Tormen, G., & Zamorani, G. 2004, ApJ, 600, 640

Lavalley, M., Isobe, T., & Feigelson, E. 1992, in Astronomical Society of the Pacific Conference Series, Vol. 25, Astronomical Data Analysis Software and Systems I, ed. D. M. Worrall, C. Biemesderfer, & J. Barnes, 245

Lawrence, A. & Elvis, M. 1982, ApJ, 256, 410

Le Floc'h, E., Aussel, H., Ilbert, O., et al. 2009, ApJ, 703, 222

Lehmer, B. D., Brandt, W. N., Alexander, D. M., et al. 2005, AJ, 129, 1

Lilly, S. J., Le Brun, V., Maier, C., et al. 2009, ApJS, 184, 218

Lilly, S. J., Le Fèvre, O., Renzini, A., et al. 2007, ApJS, 172, 70

Lusso, E. & Ciotti, L. 2011, A&A, 525, A115+

Lusso, E., Comastri, A., Vignali, C., et al. 2010, A&A, 512, A34

Lutz, D., Maiolino, R., Spoon, H. W. W., & Moorwood, A. F. M. 2004, A&A, 418, 465

Maccacaro, T., Gioia, I. M., Wolter, A., Zamorani, G., & Stocke, J. T. 1988, ApJ, 326, 680

Magorrian, J., Tremaine, S., Richstone, D., et al. 1998a, AJ, 115, 2285

Magorrian, J., Tremaine, S., Richstone, D., et al. 1998b, AJ, 115, 2285

Mainieri, V., Hasinger, G., Cappelluti, N., et al. 2007a, ApJS, 172, 368

Mainieri, V., Hasinger, G., Cappelluti, N., et al. 2007b, ApJS, 172, 368

Maiolino, R., Marconi, A., & Oliva, E. 2001, A&A, 365, 37

Maraston, C. 2005, MNRAS, 362, 799

Marconi, A. & Hunt, L. K. 2003, ApJ, 589, L21

Marconi, A., Risaliti, G., Gilli, R., et al. 2004, MNRAS, 351, 169

Mathews, W. G. 1983, ApJ, 272, 390

Mathews, W. G. & Bregman, J. N. 1978, ApJ, 224, 308

Matteucci, F. 2008, ArXiv e-prints

McCracken, H. J., Radovich, M., Iovino, A., et al. 2008, VizieR Online Data Catalog, 2286, 0

Menci, N., Fontana, A., Giallongo, E., & Salimbeni, S. 2005, ApJ, 632, 49

Merloni, A., Bongiorno, A., Bolzonella, M., et al. 2010, ApJ, 708, 137

Merloni, A., Rudnick, G., & Di Matteo, T. 2004, MNRAS, 354, L37

Mo, H., van den Bosch, F. C., & White, S. 2010, Galaxy Formation and Evolution, ed. Mo, H., van den Bosch, F. C., & White, S.

Morrison, R. & McCammon, D. 1983, ApJ, 270, 119

Nandra, K., Georgakakis, A., Willmer, C. N. A., et al. 2007, ApJ, 660, L11

Nemmen, R. S. & Brotherton, M. S. 2010, MNRAS, 408, 1598

Nenkova, M., Sirocky, M. M., Nikutta, R., Ž. Ivezić, & Elitzur, M. 2008, ApJ, 685, 160

Perola, G. C., Puccetti, S., Fiore, F., et al. 2004, A&A, 421, 491

Peterson, B. M. 1997, An Introduction to Active Galactic Nuclei, ed. Peterson, B. M.

Peterson, B. M., Ferrarese, L., Gilbert, K. M., et al. 2004, ApJ, 613, 682

Polletta, M., Tajer, M., Maraschi, L., et al. 2007, ApJ, 663, 81

Pozzi, F., Vignali, C., Comastri, A., et al. 2010, A&A, 517, A11+

Pozzi, F., Vignali, C., Comastri, A., et al. 2007, A&A, 468, 603

Prescott, M. K. M., Impey, C. D., Cool, R. J., & Scoville, N. Z. 2006, ApJ, 644, 100

Prevot, M. L., Lequeux, J., Prevot, L., Maurice, E., & Rocca-Volmerange, B. 1984, A&A, 132, 389

Puccetti, S., Vignali, C., Cappelluti, N., et al. 2009, ApJS, 185, 586

Richards, G. T., Fan, X., Schneider, D. P., et al. 2001, AJ, 121, 2308

Richards, G. T., Hall, P. B., Vanden Berk, D. E., et al. 2003, AJ, 126, 1131

Richards, G. T., Lacy, M., Storrie-Lombardi, L. J., et al. 2006, ApJS, 166

Risaliti, G., Maiolino, R., & Salvati, M. 1999, ApJ, 522, 157

Rovilos, E. & Georgantopoulos, I. 2007, A&A, 475, 115

Salvato, M., Hasinger, G., Ilbert, O., et al. 2009, ApJ, 690, 1250

Sandage, A. & Visvanathan, N. 1978, ApJ, 225, 742

Sanders, D. B., Phinney, E. S., Neugebauer, G., Soifer, B. T., & Matthews, K. 1989, ApJ, 347, 29

Sanders, D. B., Salvato, M., Aussel, H., et al. 2007, ApJS, 172, 86

Sazonov, S. Y., Ostriker, J. P., Ciotti, L., & Sunyaev, R. A. 2005, MNRAS, 358, 168

Scarlata, C., Carollo, C. M., Lilly, S., et al. 2007, ApJS, 172, 406

Schawinski, K., Lintott, C. J., Thomas, D., et al. 2009, ApJ, 690, 1672

Schinnerer, E., Sargent, M. T., Bondi, M., et al. 2010, ApJS, 188, 384

Schlegel, D. J., Finkbeiner, D. P., & Davis, M. 1998, ApJ, 500, 525

Scoville, N., Aussel, H., Benson, A., et al. 2007, ApJS, 172, 150

Silva, L., Granato, G. L., Bressan, A., & Danese, L. 1998, ApJ, 509, 103

Silva, L., Maiolino, R., & Granato, G. L. 2004, MNRAS, 355, 973

Silverman, J. D., Green, P. J., Barkhouse, W. A., et al. 2005, ApJ, 618, 123

Silverman, J. D., Lamareille, F., Maier, C., et al. 2009, ApJ, 696, 396

Silverman, J. D., Mainieri, V., Lehmer, B. D., et al. 2008, ApJ, 675, 1025

Soifer, B. T., Boehmer, L., Neugebauer, G., & Sanders, D. B. 1989, AJ, 98, 766

Springel, V., Di Matteo, T., & Hernquist, L. 2005, MNRAS, 361, 776

Stalin, C. S., Petitjean, P., Srianand, R., et al. 2009, ArXiv e-prints

Steffen, A. T., Strateva, I., Brandt, W. N., et al. 2006, AJ, 131, 2826

Steidel, C. C., Hunt, M. P., Shapley, A. E., et al. 2002, ApJ, 576, 653

Stickel, M., Lemke, D., Klaas, U., et al. 2000, A&A, 359, 865

Strateva, I., Ž. Ivezić, Knapp, G. R., et al. 2001, AJ, 122, 1861

Strateva, I. V., Brandt, W. N., Schneider, D. P., Vanden Berk, D. G., & Vignali, C. 2005, AJ, 130, 387

Surace, J. A., Shupe, D. L., Fang, F., et al. 2005, in Bulletin of the American Astronomical Society, Vol. 37, American Astronomical Society Meeting Abstracts, 1246–+

Sutherland, W. & Saunders, W. 1992, MNRAS, 259, 413

Szokoly, G. P., Bergeron, J., Hasinger, G., et al. 2004, ApJS, 155, 271

Taam, R. E., Fu, A., & Fryxell, B. A. 1991, ApJ, 371, 696

Tadhunter, C. & Tsvetanov, Z. 1989, Nature, 341, 422

Tananbaum, H., Avni, Y., Branduardi, G., et al. 1979, ApJ, 234, L9

Taniguchi, Y., Scoville, N., Murayama, T., et al. 2007, ApJS, 172, 9

Treister, E., Urry, C. M., Schawinski, K., Cardamone, C. N., & Sanders, D. B. 2010, ApJ, 722, L238

Tremaine, S., Gebhardt, K., Bender, R., et al. 2002a, ApJ, 574, 740

Tremaine, S., Gebhardt, K., Bender, R., et al. 2002b, ApJ, 574, 740

Trump, J. R., Impey, C. D., Elvis, M., et al. 2009, ApJ, 696, 1195

Trump, J. R., Impey, C. D., Gabor, J. M., et al. 2007, in Astronomical Society of the Pacific Conference Series, Vol. 373, The Central Engine of Active Galactic Nuclei, ed. L. C. Ho & J.-W. Wang, 726

Urry, C. M. & Padovani, P. 1995, PASP, 107, 803

Vanden Berk, D. E., Richards, G. T., Bauer, A., et al. 2001, AJ, 122, 549

Vasudevan, R. V. & Fabian, A. C. 2007, MNRAS, 381, 1235

Vasudevan, R. V. & Fabian, A. C. 2009, MNRAS, 392, 1124

Vasudevan, R. V., Fabian, A. C., Gandhi, P., Winter, L. M., & Mushotzky, R. F. 2010, MNRAS, 402, 1081

Vignali, C., Brandt, W. N., & Schneider, D. P. 2003, AJ, 125, 433

Wild, V., Heckman, T., & Charlot, S. 2010, MNRAS, 405, 933

Wilkes, B. J. & Elvis, M. 1987, ApJ, 323, 243

Wilkes, B. J., Tananbaum, H., Worrall, D. M., et al. 1994, ApJS, 92, 53

Wilkins, S. M., Trentham, N., & Hopkins, A. M. 2008, MNRAS, 385, 687

Wilson, A. S., Braatz, J. A., Heckman, T. M., Krolik, J. H., & Miley, G. K. 1993, ApJ, 419, L61+

Wolf, C., Meisenheimer, K., Kleinheinrich, M., et al. 2004, A&A, 421, 913

Young, M., Elvis, M., & Risaliti, G. 2009, ApJS, 183, 17

Yu, Q. & Tremaine, S. 2002, MNRAS, 335, 965

Yuan, W., Siebert, J., & Brinkmann, W. 1998, A&A, 334, 498

Zakamska, N. L., Strauss, M. A., Krolik, J. H., et al. 2003, AJ, 126, 2125

Zamorani, G., Henry, J. P., Maccacaro, T., et al. 1981, ApJ, 245, 357

Zheng, W., Kriss, G. A., Telfer, R. C., Grimes, J. P., & Davidsen, A. F. 1997, ApJ, 475, 469

If I could be who you wanted
all the time